

# Probabilistic Safety Assessment of Offshore Wind Turbines



Final Report

7<sup>th</sup> February 2015

Cover: Wind turbines on the ocean © Zentilia

---

Research Project: Probabilistic Safety Assessment  
of Offshore Wind Turbines (PSA)  
Probabilistische Sicherheitsbewertung  
von Offshore-Windenergieanlagen (PSB)

Sponsored by: Ministry for Science and Culture in Lower Saxony  
Niedersächsisches Ministerium für Wissenschaft und Kultur

Support Code: GZZM2547

Research Period: 01.12.2009 – 30.11.2014

Coordination: Dr.-Ing. habil. Michael Hansen (Institute of Concrete Construction)

Homepage: [www.psb.uni-hannover.de](http://www.psb.uni-hannover.de)

All institutes are members of ForWind and belong to the Leibniz Universität Hannover:

Institute of Concrete Construction  
*Prof. Dr.-Ing. Steffen Marx*

Institute of Building Materials Science  
*Prof. Dr.-Ing. Ludger Lohaus*

Franzius Institute for Hydraulic, Estuarine and Coastal Engineering  
*Prof. Dr.-Ing. habil. Torsten Schlurmann*

Institute for Geotechnical Engineering  
*Prof. Dr.-Ing. Martin Achmus*

Institute for Steel Construction  
*Prof. Dr.-Ing. Peter Schaumann*

Institute of Structural Analysis  
*Prof. Dr.-Ing. habil. Raimund Rolfes*

Institute for Drive Systems and Power Electronics  
*Prof. Dr.-Ing. Axel Mertens / Prof. Dr.-Ing. Bernd Ponick*

Institute of Electric Power Systems  
*Prof. Dr.-Ing. habil. Lutz Hofmann*

Institute of Machine Design and Tribology  
*Prof. Dr.-Ing. Gerhard Poll*

Institute of Turbomachinery and Fluid Dynamics  
*Prof. Dr.-Ing. Jörg Seume*

---

## Content

1	Objective .....	1
2	Executive summary .....	2
2.1	Safety of Offshore Wind Turbines (WP 1).....	2
2.2	Action Effects of Wind and Waves (WP 2).....	2
2.3	Soil (WP 3).....	3
2.4	Foundation and Support Structure (WP 4).....	3
2.5	In Situ Assembly (WP 5).....	4
2.6	Monitoring of mechanical Components (WP 6).....	5
2.7	Diagnostic Systems for Electronic Systems (WP 7).....	5
2.8	Reliability of the Grid Connection (WP 8) .....	6
3	Summary .....	7
3.1	Safety of Offshore Wind Turbines (WP 1).....	7
3.2	Action Effects of Wind and Waves (WP 2).....	7
3.3	Soil (WP 3).....	9
3.4	Foundation and Support Structure (WP 4).....	9
3.5	In Situ Assembly (WP 5).....	10
3.6	Monitoring of mechanical Components (WP 6).....	11
3.7	Diagnostic Systems for Electronic Systems (WP 7).....	12
3.8	Reliability of the Grid Connection (WP 8) .....	13
4	Work packages.....	15
4.1	Safety of Offshore Wind Turbines (WP 1).....	15
4.2	Action Effects of Wind and Waves (WP 2).....	29
4.3	Soil (WP 3).....	46
4.4	Foundation and Support Structure (WP 4).....	56
4.5	In Situ Assembly (WP 5).....	85
4.6	Monitoring of mechanical Components (WP 6).....	95
4.7	Diagnostic Systems for Electronic Systems (WP 7).....	109
4.8	Reliability of the Grid Connection (WP 8) .....	120
5	Exploitation of results.....	138
5.1	Follow-up projects .....	138

- 5.2 Publication List ..... 141
- 5.3 Academical Theses ..... 145
- 6 References ..... 151
  - 6.1 Safety of Offshore Wind Turbines (WP 1)..... 151
  - 6.2 Action Effects of Wind and Waves (WP 2)..... 153
  - 6.3 Soil (WP 3)..... 155
  - 6.4 Foundation and Support Structure (WP 4)..... 156
  - 6.5 In Situ Assembly (WP 5)..... 158
  - 6.6 Monitoring of mechanical Components (WP 6)..... 159
  - 6.7 Diagnostic Systems for Electronic Systems (WP 7)..... 160
  - 6.8 Reliability of the Grid Connection (WP 8) ..... 160

# 1 Objective

Electricity from offshore wind turbines (OWTs) will have a large impact on tomorrow's energy policy. In 2010 the first German offshore wind farm *Alpha Ventus* was built in the North Sea.

The design, construction, and deployment as well as the operation of offshore wind farms raise new questions and challenges for both government and industry.

What are the reasons for questioning existing design concepts for these structures? There are different commonly used design concepts in engineering standards. However, these design concepts are based on insufficiently research data. Nowadays, more information about loads and the structural behavior of OWTs is available.

This interdisciplinary project is expected to answer the central question of the design process: What is the probability of failure in the current design of offshore wind turbines? By using probabilistic methods, the probabilities of failure can be calculated and possibilities for optimizing the structural design may be detected. Besides determining safety factors for civil engineering, safety and reliability assessments of the mechanical and electronic components of OWTs will also be carried out.



Figure 0.1: Research Platforms [1.60]

The previously mentioned first German offshore wind park *Alpha Ventus* was built in the test field near the location of the research platform *FINO 1*. Environmental parameters for offshore structures such as the design wave and wind velocities

were measured using existing research platforms as shown in Figure 0.1. Based on these data, loads for the structures can be calculated. They can also be measured at some measurement platforms.

The institutes of the Leibniz Universität Hannover (LUH) involved in this research project belong to three different faculties; cf. Figure 0.2. All project partners are members of *ForWind*, the Center for Wind Energy Research jointly run by the universities in Oldenburg, Hanover, and Bremen.

Faculty of Civil Engineering and Geodetic Science	Faculty of Mechanical Engineering	Faculty of Electrical Engineering and Computer Science
FI Franzius Institute of Hydraulics, Waterways and Coastal Engineering	TFD Institute of Turbomachines and Fluid Dynamics	IEH Institute of Electric Power Systems / Electric Power Engineering Section
IFB Institute of Building Materials Science	IMKT Institute of Machine Elements and Engineering Design	IAL Institute of Drive Systems and Power Electronics
IFS Institute of Steel Construction		-AS Electrical Machines and Drive Systems Section
IFMA Institute of Concrete Construction		-LE Power Electronics and Drive Control Section
IGBE Institute of Soil Mechanics, Foundation Engineering and Waterpower Engineering	Leibniz Universität Hannover	
ISD Institute of Structural Analysis	ForWind Zentrum für Windenergieforschung	

Figure 0.2: Project Partners

The general aim of this research project is to analyze the entire structure of OWTs with respect to their levels of safety. Many of the presented results are based on previously gained knowledge from other research projects such as *GIGAWIND* ([www.gigawind.de](http://www.gigawind.de)).

The involved institutes work on different work packages (WP) and use the same methodology and tools as set out in WP 1.

WP 1 Safety of OWT	IFMA/IFS/ISD
WP 2 Action effects (wind and waves)	TFD/FI
WP 3 Soil	IGBE
WP 4 Foundation and tower	IFMA/IFS/ISD
WP 5 Manufacturing of supporting structure	IFB
WP 6 Monitoring of mechanical components	IMKT
WP 7 Diagnosis of electrical components	IAL-AS
WP 8 Reliability of grid connection	IAL-LE/IEH

Figure 0.3: Work Packages

## 2 Executive summary

### 2.1 Safety of Offshore Wind Turbines (WP 1)

#### 2.1.1 Abstract

For onshore constructions, historically established target reliability levels exist. An ongoing discussion deals with the target reliability of components of offshore wind turbines and the OWTs themselves. There is still no agreement on the acceptable possibility of failure or the so-called reliability index.

In the WPs different methods for reliability analysis are used to reach their respective objectives. Some objectives and assumptions are quite similar for each WP. Therefore, it was decided to translate these assumptions into principles. Thus, a database with justified parameters was created.

#### 2.1.2 Objective

The objective of this research project is to obtain a design approach for offshore wind turbines by using a holistic probability analysis to obtain the probability of failure. About 30 researchers in three faculties are involved in the project. These researchers worked on individual and team objectives. They used similar methods and a joint database as set out in WP 1.

In the field of wind energy and particularly for OWTs, there is no international consensus regarding the target reliability index. A reliability index is commonly used for the design of structural components and also entire structures. Expressions for the reliability of structures are included in different standards which will be revised soon. The reliability of offshore structures, in particular, is critically dependent on their availability and accessibility. These topics are part of the work done in this project.

### 2.2 Action Effects of Wind and Waves (WP 2)

#### 2.2.1 Abstract

Aerodynamic wind loads and hydrodynamic wave loads are essential input parameters for probabilistic investigations of offshore wind turbines. Therefore, in this work package, characteristic parameters of the loads and the resistance of OWTs are determined. The common database of wind and wave measurements *FINO 1* is used. The work at the Institute of Turbomachinery and Fluid Dynamics (TFD) is focused on uncertain parameters caused by the complex flow environments as well as geometric deviations and material imperfections of the rotor blades. The work at the Franzius Institute for Hydraulic, Estuarine and Coastal Engineering (FI) is focused on the sensitivity of wave-breaking probability and significant sea state parameters, and their uncertainties dependent on influencing parameters and determination methods.

#### 2.2.2 Objective

Offshore wind turbines operate in a complex, unsteady flow environment which causes fluctuating aerodynamic loads. Unsteady flow environments are by definition characterized by a high degree of uncertainty. In addition, manufacturing tolerances and material imperfections also cause uncertainties in the design process. The rotor blades of wind turbines are long, slender, and flexible structures, and future rotor blades will tend to become even longer and more slender. The consideration of uncertainties and aeroelastic phenomena becomes increasingly important for the fatigue strength of these structures and overall performance of OWTs. In order to consider uncertainties in the design phase of OWTs, probabilistic design methods can be used. The objective is to determine the effect of wind field parameters on extreme and fatigue

loads of offshore wind turbines. The probabilities of failure due to fatigue loads in the blade root are estimated and a modeling approach for geometric and structural uncertainties of rotor blades is developed.

Extreme hydrodynamic loads on OWTs result principally from breaking waves, which cause severe impact on offshore structures and induce singular stresses as well as vibration and therefore discrete degradation of the support structure. For an efficient design of OWTs, dominant and significant sea state parameters as well as wave-breaking probabilities must be considered, whose influencing factors vary strongly in the natural sea state environment. In a first step, design wave heights and occurrence of wave trains in the North Sea were analyzed with a statistical analysis of extreme events. They served as input parameters for the subsequent two-dimensional laboratory and numerical experiments, in which the wave-breaking probability was analyzed to quantify its scatter. Factors considered were the significant wave height, peak period, water depth, record length, and the random phase angle distribution.

## **2.3 Soil (WP 3)**

### **2.3.1 Abstract**

Within a geotechnical design procedure, uncertainties due to environmental impacts and variable soil properties have to be taken into account. This is generally done by applying partial safety factors to the actions and the resistances. By performing reliability-based design, it is possible to relate the deterministic design in terms of applied partial safety factors to a failure probability or safety.

In this work package, in a first step uncertainty sources within a reliability-based design were quantified, and different approaches to establish a subsoil model were shown. In addition, results from reliability-based design studies

regarding axially and laterally loaded OWT foundation piles were presented.

### **2.3.2 Objective**

Several offshore wind farms are planned to be installed in the German North Sea in the near future.

For moderate water depths (up to 30m) monopile foundations were found to be suitable to transfer the environmental loads into the subsoil. For greater water depths tripod, tripile, or jacket support structures were used. The acting load is resisted mainly by skin friction of the quasi-axially loaded foundation piles.

Uncertainties within the design of these foundation piles are usually taken into account by applying partial safety factors to the loads and the resistances. This procedure is known in the literature as the Load Resistance Factor Design (LRFD). According to Eurocode 0, the LRFD belongs to the Level 1 reliability-based design method and should establish a certain safety level in a system as a function of prescribed damage fault classes.

However, the safety in terms of a failure probability cannot be proven within the LRFD. Further, the magnitude of uncertainty sources is not captured by the LRFD, and this is an issue that strongly affects the safety of a system.

By using a complete reliability design method, the impact of uncertainties on the safety and design can be evaluated in a more accurate way.

The aim of this work package is to quantify uncertainties and model procedures regarding geotechnical reliability-based design as well as to determine their impact on the LRFD for axially and laterally loaded offshore foundation piles.

## **2.4 Foundation and Support Structure (WP 4)**

### **2.4.1 Abstract**

Within this work package, advanced design and optimization of support

structures for offshore wind turbines are evaluated with respect to the probabilistic safety concept. Therefore, critical limits for the design are identified. Uncertainties as well as the scatter of action effects and resistances are considered by applying probabilistic methods.

Measurement-based offshore data are analyzed in order to estimate relevant design parameters for offshore wind turbines. For the probabilistic design, finite element models of offshore wind turbines are created. A probabilistic determination of the ultimate axial capacity for foundation piles is carried out in cooperation with work package 3. The dynamic behavior of an offshore wind turbine with a monopile substructure is examined, taking probabilistic influences of various model input parameters into account. The joints of a jacket substructure are also designed according to probabilistic design procedures.

## 2.4.2 Objectives

Relevant failure types are identified and analyzed for different support structures of OWTs. These investigations are carried out on OWTs with monopile and jacket substructures, because these types of substructures are the most commonly used and the most relevant substructures installed in the German Exclusive Economic Zone.

The limit states for both the semi-probabilistic as well as the probabilistic safety concept were considered. Limit states of the semi-probabilistic safety concept stipulated in standards for OWTs are adapted for the probabilistic design.

For the probabilistic design, stochastic descriptions of both action effects and resistances are required. Based on offshore data obtained from the measurement platform *FINO 1*, design parameters were identified. Finite element models of support structures were developed to calculate and evaluate the dynamic response of OWTs. Probabilistic modeling of soil properties was carried out

in accordance with WP 3. Fatigue loads were determined and the scatter of fatigue resistances was evaluated.

Probabilities of failure were determined within the probabilistic reliability assessment of OWTs. For this purpose, suitable methods such as the Monte Carlo simulation were used.

Applying the methods described in this report for the probabilistic safety concept, economic optimization of the structural design of OWTs was performed.

## 2.5 In Situ Assembly (WP 5)

### 2.5.1 Abstract

Grouted joints are tube-in-tube connections, with the gap between pile and sleeve filled with grout. The grout material could be concrete, mortar or cement paste. High-performance mortars are generally used for the grouted joints of offshore wind turbines in Germany.

Grouted joints connect the piles, which are driven into the seabed, with the upper part of the supporting structure. Accordingly, this kind of connection plays a crucial role in ensuring the stability and durability of the supporting structure. Experiences from previously erected wind farms have shown that the design and completion of grouted joints are challenging as well as cost intensive if failures do occur.

As opposed to the precast and quality-monitored parts of the support structure, grouted joints have to be constructed under harsh offshore conditions. Therefore, quality control of the in-situ work is greatly complicated by the design and the environmental exposure of the connection. The connection represents a black box, and only assumptions can be made for the in-situ material properties of the grout. Therefore, it is necessary to apply high safety factors.

A deeper knowledge of the risk factors of the in-situ construction and the in-situ material properties are required for the optimization of grouted joints.

## 2.5.2 Objective

The objective of this work package named “Supporting Structure Production In Situ” is the determination of risk factors for the construction of grouted joints and the in-situ material behavior of grout materials. Furthermore, concepts used to minimize possible defects before and during the execution are to be developed.

## 2.6 Monitoring of mechanical Components (WP 6)

### 2.6.1 Abstract

Technical systems are subjected to damage mechanisms with stochastic distributions of the failure probability. Therefore, the exact time of failure of mechanical components in the drivetrain of offshore wind turbines, for example due to rolling fatigue of the bearings in the gearbox, cannot be predicted. The use of condition and load monitoring systems combined with the basic understanding of damage mechanisms allows for the early detection of damage in mechanical components and consequently their timely repair to prevent expensive secondary damage and downtimes.

Work package 6 deals with the development and evaluation of analysis methods for vibration-based condition monitoring systems, the evaluation of experimental vibration pickups as well as the examination of force sensors for screw connections suitable for monitoring the forces on bearings and other structural components.

### 2.6.2 Objective

The number of installed wind turbines as well as the power of new turbines is increasing dramatically in light of the renewed focus in energy policy on renewable energies. In addition, an increasing number of wind turbines are being installed or will be installed in near and far offshore locations. Offshore wind

turbines are more difficult to access, which results in longer downtimes in cases of component failures which require repairs.

Damage in the mechanical drivetrain of wind turbines, for example on rolling element bearings, cannot be prevented or even predicted with sufficient warning. Therefore, the aim of work package 6 is the development and optimization of monitoring and diagnostic systems for OWTs capable of ensuring reliable operation and efficient maintenance of the system by force monitoring and early detection of damage. Such systems should also provide data during experimental studies on single components of the OWT drivetrain.

## 2.7 Diagnostic Systems for Electronic Systems (WP 7)

### 2.7.1 Abstract

This work package deals with early fault detection in wind turbine generators. The main types of faults and damage in electrical machines cause characteristic changes in the electromagnetic air-gap field, whose dependency on position and time was investigated in previous works at Institute for Drive Systems and Power Electronics, Electrical Machines and Drive Systems (IAL-AS). Using sensors such as search coil systems, the spatial dependence acts as a filter supporting the detection of a fault or defect, because of the large distance between the signal in normal operation and in the case of a fault, as well as the identification of the type of fault by signal frequency.

### 2.7.2 Objective

In theory, the sensor signals are assumed to be zero in faultless wind turbines. In real applications, the signal fluctuation and the reachable ratio of the signal at fault as well as the signal of faultless generators have to be evaluated. Further, the influence of the generator type (doubly fed induction generator, permanent magnet synchro-

nous generator, etc.) as well as the influence of power electronic components on the reliability of the failure diagnosis has to be examined. For this reason, two diagnostic systems are being designed and the recorded data are evaluated. Based on the results, appropriate design criteria are developed for this kind of diagnostic system.

## **2.8 Reliability of the Grid Connection (WP 8)**

### **2.8.1 Abstract**

Regarding the reliability of offshore wind turbines, both the electrical system and the grid connection constitute important parts for analysis. In this work package the Institute for Drive Systems and Power Electronics and the Institute of Electric Power Systems were collaborating. The overall aim was to evaluate different grid connection topologies with respect to their reliability from a probabilistic point of view. The two institutes focused on the generator and its frequency converter, and on the grid connection, respectively.

In the first part of this WP the probabilistic reliability model of the entire electrical system was implemented by the Institute of Power Systems. In the second part, the Institute for Drive Systems and Power Electronics analyzed reliability models for power electronics within the grid connection.

The operation and grid connection of large offshore wind farms (OWFs) in Germany are particularly challenging, because of the long distances of the OWF to the nearest point of common coupling due to the protection of coastal areas and of the Wadden Sea. Long distances from the offshore substations to the substations on land have to be bridged with submarine cables. In the German North Sea, this is usually done by high-voltage direct current transmission (HVDC).

Due to specific concepts, a fault-free condition of OWF grids is an N-0 operation

and thus counts as an endangered operation, considering grid security standards of supply grids. Due to the very poor accessibility of the equipment, which is also strongly affected by the weather, any possible damage, failure and its consequences must be considered in the project planning process.

### **2.8.2 Objective**

In the field of electrical power supply the reliability of the system plays an important role. For the investor, the breakdown of a wind turbine always means financial losses because of the costs of repairs and the loss of (financial) compensation for energy fed into the grid. In the field of OWTs in particular, a breakdown inevitably leads to long downtimes as repair times are longer due to limited accessibility. It is well known that for higher-power wind turbines, the number of system failures of the electrical parts increase. Thus, it is very important to investigate the reliability of the electrical systems of large (offshore) wind turbines and their grid connections. Wind is an important stochastic input factor that determines load cycles and stress of the wind turbine. The issues mentioned in this section constitute the motivation to examine the system from a probabilistic point of view.

In order to consider the effects of stochastically arising or time-variant environment effects such as wind, weather, and aging of the equipment, reliability investigations with stochastic models had to be developed. The models had to consider the influences of these parameters sufficiently accurately in order to estimate the probable failure behavior with the desired reliability. To solve this problem, various suitable reliability analysis and condition assessment methods exist. Depending on the type of question to be answered, both analytical and simulation methods can be used.

## 3 Summary

### 3.1 Safety of Offshore Wind Turbines (WP 1)

There is still no predefined target reliability in the standards for onshore and offshore wind turbines. In a discussion within a panel of experts for the BSH (Bundesamt für Seeschifffahrt und Hydrographie) standard "Design", work group "Safety level", it was concluded that only a risk analysis for optimal safety and reliability of offshore wind turbines is of real importance. Within such a risk analysis, existing failure probabilities have to be considered with their (economic) consequences of failure. A target reliability index  $\beta = 3.3$  ( $P_{f,annual} = 5 \cdot 10^{-4}$ ) was proposed. However, the standardized and predefined sensitivity factors  $\alpha_E = -0.7$  and  $\alpha_R = 0.8$  are no longer valid because of the dominant wind load. It became apparent that there exists no reasonable basis for reducing the present safety level and associated safety elements of OWTs. Thus, holistic investigations for OWTs such as that carried out in this project are necessary for developing further approaches.

The aim of two supplementary workshops was to discuss the approaches and assumptions with representatives from industry and to get to know their interests in this matter. Thus, the main focus was on finding realistic approaches to determine the input variables for WPs. Critical limit states for the design and possible load and damage scenarios were discussed. The financial losses due to damage or break down and the inclusion of public interest were mentioned. It became clear that the failure of a single OWT appears to be of rather minor concern. The failure of a whole wind park, however, would be considered a major event. A failure of this kind could be related to structural design, for example if the towers or the foundations of all OWTs were damaged by a catastrophic event or an inherent

systematic failure in the design. On the other hand, failure of the electrical components and the grid connection could lead to big financial losses. Generally, electrical systems are planned with a known (N-1) reliability, meaning that each part is designed redundantly. In OWTs, however, there is no (N-1) reliability. For these electrical systems, it is not common to keep reserve components for all parts, such as cables and transformers. This is very risky, because for offshore structures the failure of low-cost modules can lead to very high costs for maintenance and repair.

In conclusion, the workshops clarified the interests of the industry and allowed for the validation of assumptions and input values for the present investigations.

Within this project it was not feasible to use one software package only, because the objectives of the WPs differ too much. In some cases, tools programmed in-house are necessary and useful. In other cases, the different software products could not be linked. Thus, in WP 4 for example, the loads of wave and wind were examined separately. Additionally, soil specifications and probabilistic methods were also considered. Nonlinear examinations such as these are very computationally expensive, and it is necessary to make smart assumptions.

At the end of this project we had learned much about how sensitive the results are to the chosen input parameters. For predefined approaches some results for the structural components but no general statements are available.

The individual results of all the WPs are presented in the following chapters.

### 3.2 Action Effects of Wind and Waves (WP 2)

In this work package, the wind speed measurements of the *FINO 1* offshore research platform were analyzed based on the 10-min-mean wind data of the cup anemometers. Aside from low wind

speeds, the measured turbulence intensities are lower compared to the values in the standards of the International Electrotechnical Commission (IEC). In order to obtain robust results, the wind shear exponent was determined with a nonlinear regression analysis over all cup anemometers at different heights. The measured mean wind shear exponent is very similar to the recommended value in the IEC standards. However, a strong dependency on wind speed was observed in the measured data.

Aeroelastic simulations were performed for standard and site-specific wind field parameters. The simulations, which were based on the design requirements of the support structure and on the site-specific wind field parameters, yield both significantly lower fatigue and less extreme loads than the IEC recommendations for the rotor design during normal power production. The lifetime probability of failure due to blade root fatigue loads were estimated by means of FORM (First Order Reliability Method) and MCS (Monte Carlo Simulation). It was shown that the site-specific failure probabilities are significantly lower than those obtained from calculations based on the IEC standard. Clearly, the requirements in the IEC standard 61400-3 are very conservative for rotor blade design.

The investigations into geometric uncertainties show that variations of the airfoil geometry lead to significant scatter of the lift and drag coefficients, therefore affecting the rotor blade loads. In contrast, the effects on the power and annual energy production are almost negligible, irrespective of the assumptions made.

The effect of structural uncertainties in the rotor blades (modeled by a spatial random field approach) on the full-system mode shapes and natural frequencies was investigated. The results show significant scatter of the natural frequencies of the rotor modes and the torsional drivetrain mode, which can lead to increased risk of

resonance with the 3P harmonics of the rotational speed.

For the hydrodynamic analysis, the following conclusions can be drawn from the set of test runs in the experimental and numerical wave tank.

Firstly, the initial steepness of the sea spectrum has a great influence on the number of breaking waves in the time series. Here, a change in the peak period  $T_P$  has a greater influence than a change in the significant wave height  $H_S$ .

Secondly, the randomness of the phase angle distribution, and hence the randomness of the wave sequence in the time series, has a significant influence on the number of breaking waves; different realizations of the same energy density spectra in the time domain did not produce the same numbers of breaking waves in the experiments. There are two possible reasons for that: Either the record length was too short (50–100 waves) or a model time series cannot represent all possible time series from one sea spectrum. Therefore, a first series of numerical simulations was conducted, which resulted in the following conclusion: For the investigated sea spectrum, a minimum sample size of approximately 75 test runs (corresponding to approximately 3,750 single waves) is necessary for determining a stable mean value for the time to breaking onset  $t_{br}$  and the distance to breaking onset  $x_{br}$ . Further investigations for varying sea spectra will be part of future work. The development of an analytical detection method to find wave breaking in a time series showed that not a single parameter but a combination of parameters is required to detect a wave breaking in a time series. Currently, the most promising approach is to use a combination of minimum surface elevation, instantaneous frequency (and its derivations), and crest-front steepness. The introduction of an enhanced wave-steepness parameter will be part of future work.

### 3.3 Soil (WP 3)

This work package covers the geotechnical reliability-based design for mainly axially and laterally loaded offshore foundation piles. Therefore, as a first step soil uncertainties, uncertainties regarding the evaluation of soil properties as well as uncertainties regarding the reliability design process had to be quantified. Furthermore, the influence of the defined uncertainties on the geotechnical design within the partial safety factor approach had to be investigated and evaluated. The safety of a deterministically designed system by application of prescribed partial safety factors was to be determined also.

The declared aims for all these targets could be reached.

Within the development of WP 3, uncertainties for cohesive and non-cohesive soil in terms of commonly used soil properties, uncertainties regarding the estimation of soil properties as well as information concerning the spatial soil structure were specified. Additionally, different approaches regarding the implementation of a stochastic subsoil model were presented, since such a model also has a non-negligible impact on the results.

The influence of the reliability-based design on the deterministic design procedure in terms of safety was also investigated for both categories of offshore foundation piles, namely monopiles and axially loaded piles.

It can be concluded that the desired safety for monopiles is achieved within the deterministic design process. Regarding the influence of variable properties, the influence of the acting load on the safety is at least as great as that of the variability of the soil properties.

Regarding the design of mainly axially loaded piles, a full relationship between deterministic and reliability-based design for two common design methods, namely the API method (by the American Petroleum Institute API) and ICP method, was developed. Here the safety of a

deterministic design system can be obtained as a function of the applied partial safety factors.

### 3.4 Foundation and Support Structure (WP 4)

The design of offshore wind turbines is regulated by standards and guidelines as recommended by the approving authorities. These standards for the design of offshore wind turbines are usually based on the semi-probabilistic safety concept. The design of offshore wind turbines is based on numerical modeling and investigations.

In probabilistic design, the probability of failure of the considered components for a period of one year has to be calculated by evaluating the probabilistic distributions of both effects and resistances. For both the semi-probabilistic safety concept and the probabilistic safety concept, the failure of a structural component is defined as its exceeding a limit state. In particular, for offshore wind turbines which are affected by heavily scattering loads during their lifetime, advanced structural design and optimization solutions can be found within the probabilistic safety concept.

Within work package 4, the advanced design and optimization of support structures for offshore wind turbines are evaluated with respect to the probabilistic safety concept. Uncertainties as well as the scatter of design-relevant parameters are described by their respective underlying probability distributions. Adequate probabilistic methods for the determination are used. Both action effects and resistances relevant to offshore wind turbines are considered within work package 4.

Critical limit states for the structural design of offshore wind turbines are identified. Finite element models of offshore wind turbines are developed for further investigations using the probabilistic safety concept. Within work

package 4, only monopile and jacket substructures are investigated.

Environmental actions on offshore wind turbines and their respective scatter are analyzed with respect to offshore data measured at the *FINO 1* measurement platform. Relevant design parameters for offshore wind turbines are found from the underlying probability distributions. Recommendations are made in order to adequately estimate underlying probability distributions as well as design parameters of extreme offshore conditions using comparatively short measurement periods. The dynamic behavior of an offshore wind turbine with a monopile substructure is examined. The scatter of various parameters used for modeling the structure as well as the external conditions is taken into account. Material properties, geometrical data, and soil conditions for the foundation are described by their respective probability distributions. Robustness analyses are carried out in order to estimate the first and second natural bending frequencies of a support structure of an offshore wind turbine with a monopile substructure, in dependence of the scatter of the input parameters. The analyses show that especially the soil and the water depth have a significant impact on the dynamic behavior of the entire structure. Linear correlations and coefficients of determination are used to quantify the influence of the model parameters. It is shown that a small variation of just a single input parameter significantly affects the resulting coefficients of determination. At this point in time, no statement can be made about which parameter is the most dominant. However, parameters responsible for the variation in the results and parameters of less importance were detected. Nevertheless, the scatter of the natural bending frequencies of the investigated support structure is comparatively small.

The probabilistic design for the ultimate axial capacity for foundation piles of a jacket substructure is carried out in

cooperation with work package 3 "Soil". Using the design load cases as stipulated in the relevant standards, the extreme event of a one-year storm is considered. The scatter of wind- and wave-induced axial forces on the foundation piles is estimated on the basis of the underlying probability distributions describing the respective extreme wind and wave. The stochastic description of the axial load capacity of the foundation piles is calculated in work package 3. The annual probability that the axial load capacity of the foundation piles is exceeded by the acting axial loads is calculated by using a Monte Carlo simulation, a commonly used procedure in reliability analyses. The calculated values of the probability of failure lie within the range recommended by relevant standards and guidelines.

Fatigue design is important for substructures of offshore wind turbines such as jackets and tripods. The joints of a jacket substructure are designed using probabilistic fatigue design. Here, the stochastic description of the highest stresses, which occur very rarely, is important as these stresses govern the fatigue design. The peak-over-threshold method can be applied to describe the distribution of the very high stress ranges. In general, the analyses show that the probabilistic design is very sensitive to the underlying probability distributions. Hence, the accuracy of the applied probabilistic distributions has to be ensured by precise data analyses. Under- or overestimation of the probability of failure is possible, which may result in increased economic risk during the lifetime of offshore wind turbines.

### **3.5 In Situ Assembly (WP 5)**

Important influences of offshore conditions on the material properties of grout and on the in-situ assembly of this material were found. The influencing factors were analyzed and separated into four groups: grout material, application method,

offshore conditions, and the type of construction.

The main influences are the diverse temperature conditions, wind and waves. Furthermore, the large length of the grout hoses and the length and size of grout lines, the environmental exposure of the grouted joint, and the size of the gap between pile and sleeve are all important variables.

With this knowledge in mind, a basic PHA was carried out. The analysis included a system design analysis, an analysis of undesirable system states, failures, evaluation of risks, and recommended corrective actions for the in-situ assembly. Top and basic events were determined for a fault tree analysis (FTA) within the PHA. Two fault trees were designed; firstly, a minor failure, for example extended filling times, and secondly, a major failure, for example an incompletely filled grouted joint. The probability of failure was determined for both events.

A probability of failure of about 26% was determined for the top event “NCR” (extended filling time). The second fault tree with the top event “defective grouted joint” has a probability of failure of about 22%. Here, installation of the grout seal was the most important basic event. The probability of failure for a “defective grouted joint” could be reduced by improving the quality of the grout seal and the grout lines.

A laboratory testing facility was set up for evaluating the influence of different failure modes on the material behavior of the grout. Typical failure modes were simulated and analyzed, for example a temporarily blocked grout line and a “stinger operation” as a repair action for a defective grouted joint. The experimental simulation of the temporarily blocked grout line showed a reduction in the mean value of the compressive strength of between 10% and 39%. The reduction of the mean value of the compressive strength for the repair action “stinger operation” ranged from 17% to 59%.

### 3.6 Monitoring of mechanical Components (WP 6)

The exact time of failure of drivetrain components in wind turbines cannot be predicted with satisfactory accuracy. Damage on bearings due to rolling fatigue as a result of repetitive over-rolling with high contact pressures is distributed stochastically. The calculation of bearing lifetime according to DIN 26281 only yields a failure probability and – despite modifications applied to the calculation methods and intense research – general statements about the damage mechanism of rolling fatigue. The influence of other damage mechanisms relevant to the operation of large-size bearings in wind applications, such as harmful slip, white etching cracks (WEC), or the passage of damaging currents, cannot be calculated or have never been investigated sufficiently.

Offshore wind turbines are less accessible than onshore turbines because of their location in open water. In addition, maintenance and repair of damage are made more difficult due to the fact that the turbines are not accessible by ship for a large part of the year because of critical wave heights. Therefore, financial losses as a consequence of long downtimes in the event of failures are accompanied by higher costs for the transport of components by ship or even helicopter. For this reason, maintenance costs make up a larger share of the operation costs of OWTs compared to onshore turbines.

Therefore, condition monitoring systems are needed to detect failures in the drivetrains of wind turbines reliably and at an early stage, so that expensive secondary damage to other mechanical components can be avoided and maintenance can be scheduled effectively. However, use of these systems is made increasingly difficult by changes in the drivetrain layout developed to increase the power density of wind turbines.

Thus, the aim of this work package was to develop and optimize monitoring and diagnosis systems for large-size bearings for different modern types of drivetrains in OWTs. The work included investigations on an analysis method for vibration-based condition-monitoring systems, experimental vibration pickups, and sensors to examine and monitor preload forces of screw connections.

A condition-monitoring system that records and analyzes mechanical vibrations was installed and tested on a large-size bearing test rig and an onshore turbine. The analysis method had previously been tested successfully on smaller bearings. It uses a Hilbert transformation to create an envelope curve without the use of filters. An increase in the level of damage-related vibrations could successfully be related to indentations from particles in a test bearing of the large-size bearing test rig. The analyses of recordings from the wind turbine gear box showed a distinct pattern in the order spectrum of one bearing, which could signal emerging damage. The wind turbine will be monitored further, and the measuring system will be enhanced.

When experimental vibration pickups, capable of measuring vibrations as closely as possible to rolling element bearings, were used, component tests and basic investigations showed more sensitive transmission behavior. Influences on the sensor output and the measuring chain were identified and analyzed.

Different washers coated with a piezoresistive sensor layer were utilized to perform basic tests. Screw connections suitable for bolted large-size bearings showed satisfactory laboratory results regarding transfer curve and statistic deviation. However, further investigations and developments are required to quantify or reduce the effect of influences on the output signal.

### **3.7 Diagnostic Systems for Electronic Systems (WP 7)**

Due to the increasing use of renewable energy, early fault detection in wind turbine generators is becoming more and more important. In units with restricted accessibility – offshore wind turbines in particular – early detection of faults is necessary to avoid subsequent damage and long downtimes. This work package focuses on early fault detection in electrical machines using search coil systems. All important types of faults and damage in electrical machines, such as interturn faults, short-circuit faults, or rotor eccentricities, result in characteristic changes of the magnetic air-gap field. These changes can be used to detect a fault by placing search coils in the stator slots. Based on the voltage induced in these coils, they can be used to identify the type of fault from the induced frequency. Search coil systems are particularly suitable for the detection of interturn faults and eccentricities, since these faults have little or no influence on the quantities at the terminals of a machine, and are therefore not easy to detect from the outside.

Three generator types are commonly used in wind energy plants. Besides doubly fed induction machines and salient pole synchronous machines, permanent magnet synchronous machines have seen increasing use over the past years. Initially, a search coil system was designed for use in a doubly fed induction generator, and its ability to detect interturn faults and even turn-to-turn faults and eccentricities was shown. In theoretical considerations it is assumed that no voltage is induced in the search coil system during normal operation of the system. In reality, however, residual eccentricities and other asymmetries due to manufacturing and mounting tolerances cannot be avoided. In order to evaluate the influence of residual eccentricities on fault detection, the signal-to-noise ratio

was examined. Based on previous research of search coil systems for synchronous machines, the special challenges of the design of search coil systems for permanent magnet synchronous machines with high pole pair/slot number combinations are determined, and their ability to detect winding faults and eccentricities is shown. To minimize the complexity of the search coil system as well as to improve fault detection, the conclusions drawn from the stator-fixed system are transferred to the design of a rotor-fixed search coil system.

### 3.8 Reliability of the Grid Connection (WP 8)

This work package deals with the electrical system's lifetime and the reliability of offshore wind parks. On the one hand the converter lifetime is addressed (IAL-LE), while on the other hand a reliability analysis for a complete wind park grid is performed (IEH).

A converter lifetime analysis for so-called doubly-fed induction generator (DFIG) - based wind turbines was performed at the IAL-LE. In a first step, a steady-state model for a specific wind turbine is developed. For each wind speed stator, rotor and grid currents/voltages are predicted. An electrothermal model for the converter module is implemented. In this way, the lifetime temperature swings that are harmful to the power module are predicted. To get an idea of the lifetime consumption, wind speed data in the German North Sea measured over one year are used as input. Several operating points are identified as lifetime critical. The gained results only apply to steady-state operation. This restriction can be overcome by using dynamic models. Therefore, in the second part of this project, a dynamic model of the DFIG wind turbine is developed. Extensive literature research yields several possible mechanical descriptions of the DFIG turbine. A dynamic speed control strategy

is set up to track the point of maximum power in these mechanical power coefficient curves. A specific description is found to best. This dynamic model is implemented in *MATLAB Simulink* as a simulation tool. The simulation of the dynamic junction temperature offers the possibility to examine the lifetime consumption in a more practice-relevant way.

Reliability assessments are important techniques for the analysis, conception, and eventually the safe operation of offshore wind farms. An optimum design of OWFs requires not only analytical financial calculations of the expected electrical losses, but also detailed modeling of the entire wind farm management system. For this calculation, two different simulation approaches were presented at the IEH, in addition to an overview of the analytical procedures. The Markov chain Monte Carlo method (MCMC) and the Monte Carlo simulation method (MCS) for reliability assessment of OWTs, presented in this work package, use the specific advantages of analytical considerations for aspects in the simulation environment in each case. Furthermore, after introducing characteristics of reliability considerations and the basic principles of analytical and simulative methods, possibilities for extensive modeling of the required equipment and influencing factors are discussed. The stochastic dependence of the accessibility of a wind farm and the failure probability of its equipment on the variable wind conditions and the time-variant condition of the wind farm are considered in a comprehensive model. The simulation models for maintenance and repair modes developed in this WP, as well as their emphasis on damage and losses, form a good basis for future calculations. Thus, particularly with the Monte Carlo simulation tool developed in this WP, a very detailed study of reliability characteristics of any OWT topology is possible. Estimates about fault times and

economic yields can be obtained a priori. Various concepts for maintenance or interconnection of wind power plants within an OWP (offshore wind park) can be compared. This system can be extended to any control system because of its modular design. At the same time, a simplified implementation can be developed by also considering the analytically based MCMC method. This approach is mainly used as a reference or in cases where accurate modeling is not or no longer possible.

The input parameters of the investigations can be chosen freely for both the individual reliability characteristics of the equipment as well as for the site-specific and climatic conditions.

A simple comparison of different equipment for case studies and investment analyses is possible by discretizing equipment models on the relevant failure and repair rates. Thus, a basis for a program for an extensive reliability evaluation of arbitrary OWFs is developed and its function is shown with different examples.

## 4 Work packages

### 4.1 Safety of Offshore Wind Turbines (WP 1)

Institute of Concrete Construction

Michael Hansen, Boso Schmidt

#### 4.1.1 Abstract

For onshore structures, target reliability levels established historically are stipulated in relevant design standards. An ongoing discussion deals with the target reliability of components of offshore wind turbines and the OWTs themselves [1.30]. There is still no agreement on the acceptable possibility of failure or the so-called reliability index.

In the WPs different methods for reliability analysis are used to reach their respective objectives. Some objectives and assumptions are quite similar for each WP. Therefore, it was decided to translate these assumptions into principles. Thus, a database with justified parameters was created.

#### 4.1.2 Objective

The objective of this research project is to obtain a design approach for offshore wind turbines by using a holistic probability analysis to obtain the probability of failure. About 30 researchers in three faculties are involved in the project. These researchers worked on individual and team objectives. They used similar methods and a joint database as set out in WP 1.

In the field of wind energy and particularly for OWTs, there is no international consensus regarding the target reliability index. A reliability index is commonly used for the design of structural components and also structures themselves. Expressions for the reliability of the structure are included in DIN 61400-1 [1.7] and EC0 [1.8] and will be revised soon. In addition, the reliability of offshore structures is critically dependent on their availability and accessibility; see Figure 1.1.

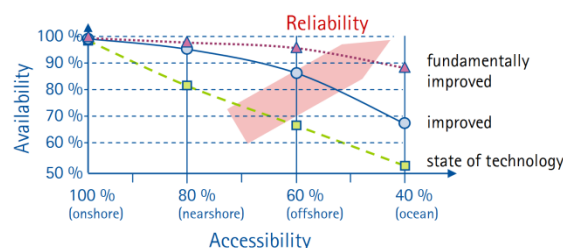


Figure 1.1: Relationship between reliability, availability, and accessibility for offshore wind turbines; cf. [1.45]

#### 4.1.3 Approach

Reliability analyses represent an appropriate approach for the development of civil engineering standards; cf. [1.15]. With such analyses, characteristic values and safety factors for predefined safety classes can be determined. Unlike in deterministic examinations, random parameters are taken into account in probabilistic methods. Thus, statements about the occurrence frequency of several limit states are possible. The importance and sensitivity of the included parameters can also be evaluated.

In the actual design of OWT structures, random parameters are substituted by characteristic loads and safety factors. These values are generally taken from building standards or from guidelines for onshore wind turbines; for example [1.3] [1.4]. In probabilistic examinations, the essential design parameters ought to include their statistical values to obtain safe and efficient structures. Previous research projects have dealt with the failure probabilities of wind turbine components, for example blade fails or tower fails. The current project focuses on the entire tower and the tower-foundation interaction.

The economy of structures and buildings depends on the investment costs (construction costs) and the costs of failure; see Figure 1.2. The failure of OWTs can concern the whole structure or just single parts of the electrical or mechanical components. In a holistic design concept, the relevant risks and follow-up costs of environmental damage

have to be considered. The risk  $R$  given in Eq. (1.1) has to be lower than the socially justifiable limited risk  $R_{lim}$ . This limit risk may be obtained from different approaches, for example those listed in [1.59] or [1.27].

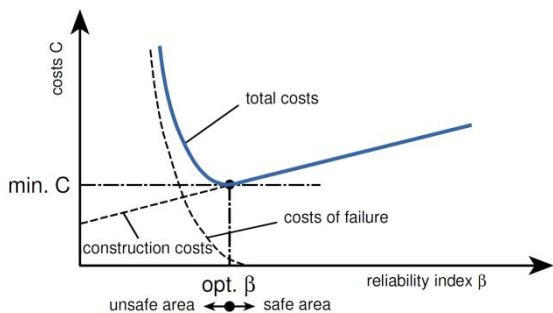


Figure 1.2: Development of costs, cf. [1.28] [1.56] [1.57]

$$R = V_f \cdot P_f \leq R_{lim} \quad (1.1)$$

where:

- R risk
- $V_f$  consequences of failure
- $P_f$  probability of failure
- $R_{lim}$  limited risk

A probabilistic approach for OWTs is suitable for classifying the reliability of the analyzed structures. Thus, it should be possible to optimize the reliability and economic investment of OWTs.

### Reliability Modeling

#### Uncertainties

In reliability analysis, several kinds of uncertainties have to be considered; see Figure 1.3. Uncertainties modeled by stochastic variables are divided into four groups. Inherent uncertainties are related to the randomness of a quantity (for example the expected wave height or annual maximum wind speed). Model uncertainties are related to imperfect knowledge or idealizations of the mathematical or physical models used for the uncertainty (for example distribution fittings, models for bearing behavior). Furthermore, there are dimensional uncertainties related to imperfect dimensions (for example geometrical

quantities) and statistical uncertainties related to the limited sample sizes of observed quantities. Human errors are not included, because they cannot be estimated with probability methods.

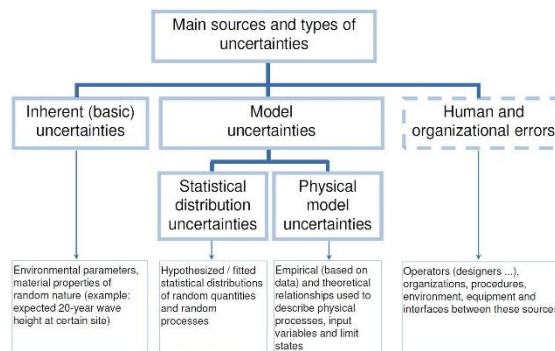


Figure 1.3: Uncertainties; cf. [1.28] [1.37]

#### Reliability Methods

Various reliability analysis methods are used. These methods are different with regard to their degree of precision (level of sophistication, [1.28]). The semi-probabilistic method, also called partial safety concept and introduced internationally by [1.8] and nationally by [1.6], is a so-called Level I method, in which characteristic values of actions and resistances are used to obtain design values by multiplication with partial factors. The partial safety factors are calculated with Level II methods.

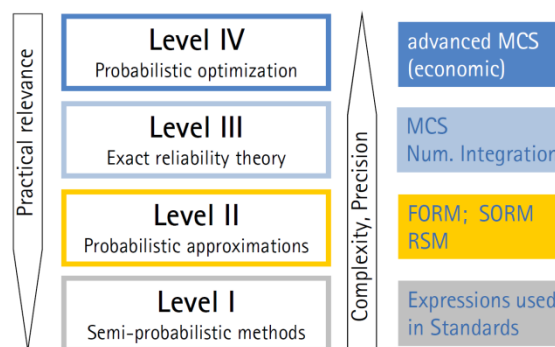


Figure 1.4: Methods for probabilistic analysis and levels of sophistication; cf. [1.28]

#### FORM, SORM, ARSM, MCS

The Level II methods (for example FORM/SORM: first/second order reliability method) are based on the mean average

value and the statistical spread, which are two characteristics of random distributions of mechanic parameters (basic values). More accurate results are achieved by applying Level III methods such as numeric integration or the Monte Carlo method (MCM). To perform stochastic optimization and robust design optimization, sampling methods (for example ISPUD: importance sampling using design point or LHS: Latin hypercube sampling) or the adaptive response surface method (ARSM) are used; cf. [1.28], [1.36].

By applying approximation procedures such as FORM, it is possible to carry out comparisons and sensitivity analyses of different structures. Based on the probability of failure, the Hasofer-Lind second moment reliability index and the sensitivity factors of actions and resistances, it is possible to obtain approximate values for the safety elements, such as the partial safety factors ([1.28], [1.52], [1.53], [1.56], [1.57]). To make any statement about the probability of failure of the structure, more precise probability methods are needed. To determine non-linear limit state functions or to carry out non-linear calculations of the structure, the MCM or the ARSM can be used.

More detailed explanations about reliability methods are given in [1.28], [1.34].

### *Fault, Event and Decision Trees*

Two important tools for probabilistic safety investigations and quality management are fault tree analysis (FTA) and event tree analysis (ETA). FTA is based on failure of a system, which can be attributed to the malfunction of its subsystems. These malfunctions are caused by the failure of the subsystem components. The result of these considerations is represented as the so-called fault tree, which indicates the logical links between the failure of the components and the system. In the fault tree, only the states "functioning/secure" and "failure/insecure" are considered. These states are associated with

occurrence probabilities. The probability of failure of the system follows from the mathematical evaluation of the fault tree on the basis of the component malfunction, the probabilities for the occurrence of action effects, and gross errors (human errors).

For successful employment of FTA, first of all it is necessary to perform a systems analysis. In a systems analysis, a system is divided into subsystems and components. After mutual dependencies of the components have been analyzed, the investigation is limited to the critical operating states. Hence, the critical states of the system must be identified which can be done with a worst-case analysis. A worst-case analysis should consider the following aspects; cf. [1.17]:

- Stipulation of the extent of damage on a five-step scale
- Specifications of the damage duration
- Averting mechanisms

In Table 1.1 an overview of the use and the objectives of some quality management technologies (QM technologies) is shown. Some of these processes are also used in current probabilistic tools [1.36].

*Table 1.1: Methods and objectives of some preventive QM technologies*

Methods	Objective target
FMEA Failure mode and effect analysis	Early fault detection and implementation of counteractions Systematic improvement of products and processes (risk reduction)
FTA Fault tree analysis	Identification of failure sources Development and application of particular corrective actions
ETA Event tree analysis	Analysis of possible sequential events
DoE Design of experiments	Systematic design of experiments to determine influence parameters
Six Sigma	Product and process development for minimized nonconformity to a target value Investigation of process quality

Further details of these processes are found in [1.17]. Decision trees for risk investigations are dealt with in [1.20] and [1.14].

### System Reliability

Two types of logical component arrangements can be distinguished: the *series system* and the *parallel system*. In reality, however, the logical description of a system failure corresponds better to the model of a series system with parallel subsystems, or to the equivalent form of a parallel system with series subsystems. The status of a system is defined by the characteristics of its components. The discretization of the system into components does not necessarily correspond to the subdivision into mechanical elements, since the status of a mechanical element depends on the characteristics of its critical locations (e.g. plastic hinges). The subdivision of a system into components also depends on the type of loading (line load, concentrated load etc.). Therefore, a mechanical element has several components and can be considered as a subsystem.

#### Series systems

In a *series system*, system failure can be expressed as the failure of one of its components ("or" link). This can be illustrated by representing the series system as a chain system without redundancy. All components equally share the task fulfilled by the system as a whole. The probability of failure of a series system corresponds to the set union of the failure probability of its  $m$  components; cf. Eq. (1.2).

$$\begin{aligned} P_{f, Sys(ser)} &= P\left(\bigcup_{i=1}^m [g_i(x) \leq 0]\right) \\ &= P\left(\bigcup_{i=1}^m F_i\right) = 1 - P\left(\bigcap_{i=1}^m \bar{F}_i\right) \end{aligned} \quad (1.2)$$

Eq. (1.3) represents trivial boundaries for rough estimates of the failure probability of series systems. The left-hand boundary in Eq. (1.3) represents the exact value for uncorrelated components.

$$\max[P(F_i)] \leq P_{f, Sys(ser)} \leq \sum P(F_i) \quad (1.3)$$

This interval can be reduced further by using elementary bars, the so-called *Ditlevsen Bounds*; see Eq. (1.4) and (1.5).

$$P_{f, Sys(ser)}^{lower} \geq \min \left\{ \begin{array}{l} 1 \\ P(F_1) + \sum_{i=2}^m \left[ P(F_i) - \max_{j<i} P(F_i \cap F_j) \right] \end{array} \right\} \quad (1.4)$$

$$P_{f, Sys(ser)}^{upper} \leq P(F_1) + \sum_{i=2}^m \max_{j<i} \left\{ \begin{array}{l} 0 \\ P(F_i) - P(F_i \cap F_j) \end{array} \right\} \quad (1.5)$$

#### Parallel system

A *parallel system* fails if all  $m$  limit states are exceeded. Therefore, all of its components, including the strongest element, must fail ("and" link). Two types of parallel systems can be differentiated. Parallel systems with passive redundancy contain components which are used only if other components have already failed. Parallel systems with active redundancy only include components which are effective. The failure of a component triggers the redistribution of partial functionalities to more resilient components, but does not cause system failure.

The probability of failure of a parallel system with active redundancy can be expressed as the average value of the failure probabilities of its components according to Eq. (1.6), with Eq. (1.7) representing trivial boundaries for it. The left-hand boundary represents the exact value for uncorrelated components.

$$P_{f, Sys(par)} = P\left(\bigcap_{i=1}^m [g_i(x) \leq 0]\right) = P\left(\bigcap_{i=1}^m F_i\right) \quad (1.6)$$

$$\prod P(F_i) \leq P_{f, Sys(par)} \leq \min[P(F_i)] \quad (1.7)$$

### Codes and Guidelines

A brief history and general comparison of different guidelines, which may be used for the design of OWT support structures, are given in [1.35], [1.44], [1.51]. These guidelines have been developed by

organizations such as the International Electrotechnical Commission (IEC), Germanischer Lloyd (GL), Det Norske Veritas (DNV), the International Organization for Standardization (ISO), and the American Petroleum Institute (API). DNV has been a part of Germanischer Lloyd (GL) since 2014.

In [1.44], the guidelines developed by the API and the IEC are compared in general terms regarding the extent of their applicability and fundamental differences for OWT support structure design. The API and IEC guidelines are also compared with respect to their levels of reliability, which is inherent in their design methodologies for monopiles.

The limitation of target reliability levels has evolved with the economic optimization of structures cf. [1.15], [1.48], [1.52], [1.53]. The target failure probability for OWTs has to be predefined in standards. Wind turbine structures are unmanned and carry much less risk to human life than onshore structures. Therefore, they may be designed to a lower safety class. The characteristic loads in codes are given as 50-year values [1.2] or 100-year values [1.1]. Furthermore, the design of wind turbine structures is expected to be governed by wind turbine loads, which are of another nature than wave loads. However, wave loads are assumed to govern for structures designed according to [1.1].

During revision of [1.2] in 2007, different examinations were carried out. It was concluded with consensus in the wind industry that the minimum requirements for structural safety are identical on land and offshore [1.51].

#### Reference Periods

The calculated probability of failure  $P_f$  and the reliability index  $\beta$  can be very sensitive to changes in the stochastic model, in particular in the range of very low failure probabilities. Therefore, a conditional probability is formulated in dependence of the value of  $\beta$ . This probability is only valid

if a great number of basic conditions (for example distribution type of the base variables) are considered. Thus, a comparison of the probability or the value of  $\beta$  is appropriate only if it refers to the same theoretical model or to the same assumptions [1.50]. This applies particularly to the influence factor of time. Due to time-dependent influences and material properties, the probability of failure is also time dependent. If the probability of failure is used as a safety factor, it is vital to stipulate a reference period also. With regard to the uncertainties concerning the statistical information, the shortest possible reference periods need to be chosen. If time-dependent properties have a dominant influence on the resistance parameters or equations (for example fatigue), however, it is unfavorable to have short reference periods.

Reference periods for characteristic values are specified with regard to the intended life of the structure or the assumed duration of the design situation. In [1.8], a period of 50 years is stipulated as a planning value for the design working life of buildings and common supporting structures. Values for the service life of systems for energy generation are shown in [1.56]; cf. also Table 1.2.

*Table 1.2: Service life of different structures; cf. [1.56]*

Technical life [year]	Electricity from ...
40	Coal
25	Gas
40	Nuclear
50	Hydro
20	Wind (onshore)
?	Wind (offshore)

An approximate conversion of the reliability index  $\beta$  between different reference periods [1.6] can be carried out with Eq. (1.8).

$$\Phi(\beta_n) \approx [\Phi(\beta_1)]^n \quad (1.8)$$

#### Target Reliability Levels

In the relevant design codes, specifications relating to target reliability levels can be found only indirectly. In present semi-probabilistic verification formats, defined partial safety factors are included for stress demand and resistance variables. The product of these two safety elements is the global safety factor, which was stipulated in previous standards and was considered exclusively on the resistance side. The partial safety factors determined by probabilistic Level II calculations (for example FORM) and calibrated with Level III methods (for example Monte Carlo method, numeric integration) were calibrated for the existing safety level, which is not constant.

The modern partial safety concept registers the uncertainties at their origin. This means that there are safety factors to increase the design loads and to decrease the design resistances. This often leads to different results compared to the global safety concept. This can be caused by the weighting and statistical scatter of the detailed parameters for the different actions, model assumptions, and building materials. A target reliability based on the global safety concept is hence uneconomical, and also unsafe in some cases. Thus, the stipulation of an appropriate target reliability value in dependence on the type of structure and its environmental exposure is important for a safe and economic design of wind turbines (WT).

Target reliabilities for different countries are found in existing standards. Therefore, any new design approach should not yield very different results to the ones obtained with current design standards. The IABSE Working Commission 1 carried out a comparative study of the reliability targets of a number of existing codes; cf. Table 1.3 and [1.58].

In Germany the target reliability and the reliability index are 4.2 (reference period one year) and 3.8 (reference period 50 years), respectively.

*Table 1.3: Target reliability indices  $\beta$  for a one- year reference period stipulated in international codes; cf. [1.58]*

Reliability index $\beta$	3,0	3,5	4,0	4,5	5,0
Argentina					
Canada					
China					
Denmark					
Estonia					
Germany					
Holland					
South Africa					
Spain					
Sweden					
UK					
USA					

Target reliability levels for wind turbines have been formulated in [1.49] using theoretical cost-benefit analyses. In [1.56], specific values for different structural parts of a WT are mentioned. Critical statements about the previous target values of the reliability levels for WTs are given in [1.46]. A comparison with similar guidelines of the oil and gas industry [1.10] clearly shows their main differences; cf. Table 1.4.

*Table 1.4: Target reliability indices  $\beta$  (probability of failure  $P_f$ ) for support structures according to [1.8] and [1.15], and values for offshore support structures of the oil and gas industry [1.10] for a one-year reference period*

Relative expenses to increase safety	Failure consequences		
	Low (cf. RC1)	Medium (cf. RC2)	High (cf. RC3)
High (A)	3,1 ( $1 \cdot 10^{-3}$ ) *3	3,3 ( $5 \cdot 10^{-4}$ ) *2	3,7 ( $1 \cdot 10^{-4}$ ) *1
Medium (B)	3,7 ( $1 \cdot 10^{-4}$ )	4,2 ( $1 \cdot 10^{-5}$ ) *1	4,4 ( $5 \cdot 10^{-6}$ )
Low (C)	4,2 ( $1 \cdot 10^{-5}$ )	4,4 ( $5 \cdot 10^{-6}$ )	4,7 ( $1 \cdot 10^{-6}$ ) *4

\*1  $\beta=4,0$  ( $P_f = 3 \cdot 10^{-5}$ ) for manned non-evacuated structures (L1) [1.10]  
 \*2  $\beta=3,3$  ( $P_f = 5 \cdot 10^{-4}$ ) for manned evacuated structures (L2) [1.10]  
 \*3  $\beta=3,1$  ( $P_f = 1 \cdot 10^{-3}$ ) for unmanned structures (L3) [1.10]  
 \*4  $\beta=4,7$  ( $P_f = 1 \cdot 10^{-6}$ ) target reliability for structural members (RC2) acc. to [1.8]

Considering the stipulations of onshore building standards [1.6], [1.8], a smaller target reliability could be used for unmanned OWTs. Furthermore, there is a certain logic to this argument, because the reliability of these OWT structures is not relevant for the general public.

Rather, the target reliability values should be defined by the operators who suffer a commercial loss in the event of failure of an OWT. For a lower reliability index, higher failure probabilities are assumed. Because of low failure consequences, a classification into reliability class RC1 would be appropriate.

#### *Safety, Consequence and Reliability Classes*

In civil engineering there are different kinds of structures. Due to the different fail options, structural failures and especially structural collapse have to be assessed individually. Therefore, safety classes or reliability classes (RC) are defined for the consideration of risk. Different reliability indices  $\beta$  are thus stipulated for the three reliability classes for the ultimate limit state (ULS) and the serviceability limit state (SLS); see Table 1.5.

The basic principles formulated within the framework of the European construction standards are published in [1.8]. These values are understood as minimum requirements for general cases and are based on calibrations according to the design guidelines of different countries. In the present case, logarithmic normal distributions and Weibull distributions were used to describe the resistance variables and the model uncertainty, and normal distributions were used to describe permanent actions and extreme value distributions for variable actions.

*Table 1.5: Reliability indices  $\beta$  for different reliability classes (RC)*

Reference period	1 year			50 years		
	1	2	3	1	2	3
Ultimate Limit State (ULS)	4,2 <sup>(2,5)</sup>	4,7 <sup>(1,2)</sup> 4,2 <sup>(3)</sup>	5,2 <sup>(2,4)</sup>	3,2 <sup>(2)</sup> 3,3 <sup>(4)</sup>	3,8 <sup>(1,2,4)</sup>	4,4 <sup>(2)</sup> 4,3 <sup>(4)</sup>
Serviceability Limit State (SLS)	2,5 <sup>(5)</sup>	3,0 <sup>(1)</sup> 2,9 <sup>(2)</sup>	3,5 <sup>(4)</sup>	1,0 <sup>(4)</sup>	1,5 <sup>(1,2,4)</sup>	2,0 <sup>(4)</sup>

(1) DIN 1055-100 [1.6] (2) EN1990 [1.8] (3) JCSS [1.15] (4) JCSS [1.14]

The stipulation of the required reliability by way of a reliability index  $\beta$  is determined not only from national experience and requirements. The

selected mechanical and probabilistic modeling, in particular, influences the reliability index as well as the projected service life. Therefore, the necessary reliability index (target reliability) is to serve mainly as a basis for the development of consistent design regulations, but not as an explicit specification of the existing probability of failure.

Three consequence classes (CC) and reliability classes (RC) with corresponding required reliabilities are stipulated in dependence on possible consequences listed in [1.8] (Tables B.1 and B.2). The levels of danger and the loss of human lives or real values are low for RC1 and high for RC3.

*Table 1.6: Recommendation for minimum values of the reliability index  $\beta$*

Reliability class	Minimum value of $\beta$ ( $P_f$ ) for the reference period of ...				
	1 year	20 years	30 years	50 years	100 years
RC3	5,2 (1·10 <sup>-7</sup> )	4,6 (2·10 <sup>-6</sup> )	4,5 (3·10 <sup>-6</sup> )	4,3 (8·10 <sup>-6</sup> )	4,3 (1·10 <sup>-5</sup> )
RC2	4,7 (1·10 <sup>-6</sup> )	4,0 (3·10 <sup>-5</sup> )	4,0 (4·10 <sup>-5</sup> )	3,8 (7·10 <sup>-5</sup> )	3,7 (1·10 <sup>-4</sup> )
RC1	4,2 (1·10 <sup>-5</sup> )	3,5 (3·10 <sup>-4</sup> )	3,4 (4·10 <sup>-4</sup> )	3,3 (5·10 <sup>-4</sup> )	3,0 (1·10 <sup>-3</sup> )

A conversion of the failure probabilities from a reference period of one year to a reference period of 50 years is possible with Eq. (1.9); cf. also Eq. (1.8).

$$\begin{aligned}
 P_{f,50} &= \Phi(-\beta_{50}) = 1 - \Phi(\beta_{50}) \\
 &= 1 - [\Phi(\beta_1)]^{50} \\
 &= 1 - [1 - \Phi(\beta_1)]^{50} \quad (1.9) \\
 &= 1 - (1 - P_{f,1})^{50} \\
 &\approx 50 \cdot P_{f,1}
 \end{aligned}$$

In *Figure 1.5* the dependencies of the reliability indices on the reference period for the different reliability classes are shown graphically; cf. [1.30]. Thus, reliability indices can also be derived for WT planning periods of 20 or more years.

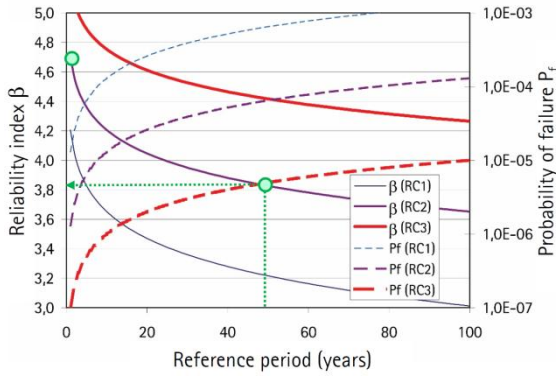


Figure 1.5: Dependence of the reliability index on the reference period; cf. [1.30]

### Partial Safety Factors

For practical applications, a constant reliability index  $\beta$  is used, and constant values of the FORM sensitivity factors  $\alpha_E$  and  $\alpha_R$  are defined in order to reduce the bandwidth of possible solutions to a single case. In [1.6], the fixed values for  $\alpha_E$  and  $\alpha_R$  are -0.7 and 0.8, respectively, if  $\beta = 3.8$  for these sensitivity factors and condition (1.10) is met.

$$0.16 < \frac{\sigma_E}{\sigma_R} < 7.6 \quad (1.11)$$

Otherwise, the sensitivity factors have to be calculated with different parameters; cf. [1.25], [1.28].

### Factors for Actions

The characteristic and design values of the variable actions depend on the reference period. For the design values of the variable actions in the ULS, a reference period  $n = 50$  years is generally used. These variable actions are generally Gumbel distributed; cf. Eq. (1.12), [1.25] and especially Chapter 2 of this report

$$Q_{d,50,RC2} = m_{Q,50} \cdot \left[ 1 - 0.7797 \cdot v_{Q,50} \cdot \left( 0.5772 + \ln \left[ -\ln \left( \Phi \left[ (0.7 \cdot 3.8) \right] \right) \right] \right) \right] \quad (1.12)$$

$$Q_{d,50,RC2} = m_{Q,50} \cdot \left[ 1 - c(RC2) \cdot v_{Q,50} \right] = m_{Q,50} \cdot \left[ 1 - 3.87 \cdot v_{Q,50} \right]$$

For WTs with smaller reference periods, the determining equation for the design value could be modified. The design value of the variable actions is determined with Eq. (1.13) for a reference period of 20 years for reliability class RC2 with  $\beta = 4.0$ . For reliability class RC1 with  $\beta = 3.5$  and the same reference period of 20 years, Eq. (1.14) applies. A constant sensitivity factor  $\alpha_E = 0.7$  is assumed in this case.

$$Q_{d,20,RC2} = m_{Q,20} \cdot \left[ 1 - 0.7797 \cdot v_{Q,20} \cdot \left( 0.5772 + \ln \left[ -\ln \left( \Phi \left[ (0.7 \cdot 4.0) \right] \right) \right] \right) \right] \quad (1.13)$$

$$= m_{Q,20} \cdot \left[ 1 - c(RC2) \cdot v_{Q,20} \right]$$

$$= m_{Q,20} \cdot \left[ 1 + 4.20 \cdot v_{Q,20} \right]$$

$$Q_{d,20,RC1} = m_{Q,20} \cdot \left[ 1 - 0.7797 \cdot v_{Q,20} \cdot \left( 0.5772 + \ln \left[ -\ln \left( \Phi \left[ (0.7 \cdot 3.5) \right] \right) \right] \right) \right] \quad (1.14)$$

$$= m_{Q,20} \cdot \left[ 1 - c(RC1) \cdot v_{Q,20} \right]$$

$$= m_{Q,20} \cdot \left[ 1 + 3.40 \cdot v_{Q,20} \right]$$

For the three reliability classes RC1 to RC3, the dependencies of the design values of the variable actions  $Q_d$  on the reference period are depicted in Figure 1.6. The coefficient  $c$  (RC) used in Eqs. (1.12) - (1.14) is shown for each case. To determine the characteristic values of the variable actions, however, the reference period  $n = 50$  years is used for imposed loads (95% fractile), and  $n = 1$  year is used for the environmental actions such as wind loads (98% fractile).

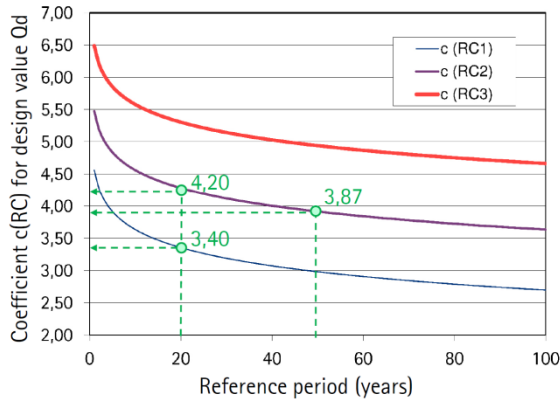


Figure 1.6: Dependence of the design values of the variable actions on the reliability classes and reference periods

Hence, Eq. (1.15) applies to imposed loads, while Eq. (1.16) is used for wind loads. For detailed information see [1.28], A.9.1.

$$Q_{k,il,50} = m_{Q,50} \cdot \left[ 1 - 0.7797 \cdot v_{Q,50} \cdot \left( 0.5772 + \ln \left[ -\ln \left( \Phi [0.95] \right) \right] \right) \right] \quad (1.15)$$

$$= m_{Q,50} \cdot [1 + 1.87 \cdot v_{Q,50}]$$

$$Q_{k,wf,1} = m_{Q,1} \cdot \left[ 1 - 0.7797 \cdot v_{Q,1} \cdot \left( 0.5772 + \ln \left[ -\ln \left( \Phi [0.98] \right) \right] \right) \right] \quad (1.16)$$

$$= m_{Q,1} \cdot [1 + 2.59 \cdot v_{Q,1}]$$

For a stipulated partial safety factor, the reference periods of the design values and the characteristic values must agree. The characteristic values of the environmental actions are determined with Eq. (1.17) for the normal reference period  $n = 50$  years.

For WTs with a reference period of 20 years, the characteristic value of the wind loads can be determined with Eq. (1.18).

$$Q_{k,wf,50} = m_{Q,1} \cdot \left[ 1 - 0.7797 \cdot v_{Q,1} \cdot \left( 0.5772 + \ln \left[ -\ln \left( \Phi [0.98^{50}] \right) \right] - \ln(50) \right) \right] \quad (1.17)$$

$$= m_{Q,50} \cdot \left[ 1 - 0.46 \cdot v_{Q,50} \right]$$

$$Q_{k,wf,20} = m_{Q,1} \cdot \left[ 1 - 0.7797 \cdot v_{Q,1} \cdot \left( 0.5772 + \ln \left[ -\ln \left( \Phi [0.98^{20}] \right) \right] - \ln(20) \right) \right] \quad (1.18)$$

$$= m_{Q,20} \cdot [1 - 0.26 \cdot v_{Q,20}]$$

The partial safety factor of the actions is calculated as the ratio of the design value and the characteristic value. In this way, the partial safety factor is also dependent on the reference period and the reliability class. In [1.6] the partial safety factor  $\gamma_f$  is stipulated for variable actions acting unfavorably, independent of the size of the coefficient of variation, such as the 98% fractile with  $\gamma_Q = 1.50$ .

For OWTs, different partial safety factors apply. The partial safety factors for ULS verifications according to Table 1.7 are taken from [1.9].

Table 1.7: Partial safety factors for actions  $\gamma_f$  according to [1.9]

Unfavorable loads			Favorable loads
N	A	T	
Normal	Abnormal	Transport and erection	All design situations
1.35	1.10	1.50	0.90

Similar specifications are defined in the guidelines of the Deutsches Institut für Bautechnik (DIBt) [1.3], [1.4] and Germanischer Lloyd (GL) [1.11], [1.12], [1.13]. The differences between both

publications are highlighted in color and boldface type in Table 1.8.

*Table 1.8: Partial safety factors  $\gamma_f$  for the actions for ULS verifications [1.4]*

Source of loading	Unfavorable loads				Favorable loads
	Type of design situation				All design situations
	N Normal	E Extreme	A Ab- normal	T Transport and erection	
Environmental	1,20	1,35	1,10	1,50	0,90
Operational	1,20	1,35	1,10	1,50	0,90
Gravity	<b>1,10/1,35*</b>	<b>1,10/1,35*</b>	1,10	1,25	<b>0,90</b>
Other initial forces	<b>1,20</b>	<b>1,25</b>	1,10	<b>1,30</b>	0,90
Thermal	–	1,35	–	–	<b>0,90</b>

\* in the mass is not determined by weighing

Smaller safety factors may also be applied to the actions if their magnitudes are determined by measurements or with numeric analyses verified by measurements with a very high level of confidence. This kind of work is described in Chapter 2 of this report.

#### *Resistance Factors*

The characteristic value of the yield stress  $f_{yk}$  of the reinforcing steel corresponds to the 5% fractile of the statistical distribution. For verification purposes, the partial safety factor is determined for reinforcing bars according to Eq. (1.19).

$$\begin{aligned}\gamma_R &= \exp\left(\left[0.8 \cdot 3.8 - \Phi^{-1}(0.05)\right] \cdot v_R\right) \\ &= \exp(1.395 \cdot v_R)\end{aligned}\quad (1.19)$$

The partial safety factor  $\gamma_S = 1.15$  stipulated in [1.5] also applies to the coefficient of variation of the yield stress of reinforcing bars  $v_S = 10\%$ .

A partial safety factor  $\gamma_C = 1.50$  is stipulated in [1.5] for concrete strength classes up to C50/60. For precast elements (PE) produced in a works-related and continuously monitored manufacturing plant, this factor may be reduced to  $\gamma_{C,PE} = 1.35$ . The unfavorable scatter of all influence variables is generally taken into account by the coefficients of variation  $v_R \approx 0.29$  and  $v_{R,PE} \approx 0.22$  (cf. [1.28]).

#### *Factors for Model Uncertainties*

Model uncertainties have to be taken into account within all probabilistic assessments. Unfortunately, however, there is a lack of knowledge regarding these model uncertainties. For normal structural behavior and ultimate limit state design, failure cases are known and feasible assumptions are available in the literature; cf. [1.27]. The structural behavior of WTs and OWTs can be simulated reasonably well. However, there is less information available about cases of structural collapse. To understand model uncertainties, a comparison of the theoretical and the experimentally determined load-bearing behavior is necessary. The model uncertainties can be estimated with standardized methods; cf. [1.8] Annex D and [1.28].

The model uncertainties are very important for probabilistic assessments, because they can only be formulated with great scatter. The coefficient of variation of model uncertainties is generally much greater than that of other input parameters. Therefore, the so-called model factor governs probabilistic calculations. Within the present calculations, model uncertainties were only used for the soil model in Chapters 3 and 4.

#### *Correlation and Combination of Actions and Action Effects*

Within limit state verification, there are often several variable actions of different origins. In conservative design, load modeling is carried out over extreme value distributions in the reference period, because the probability of two extreme values occurring simultaneously is relatively small.

Many approaches for developing factors for conservative design are based on a proposal from *Turkstra* [1.55]. According to this document, several variable actions occurring simultaneously are to be combined in such a way that the governing variable action (main action) takes its extreme value with respect to a specified

time period. The other variable actions (accompanying actions) are applied with their respective value at that point in time. Every variable action is assumed in turn to be the governing action. Thus, the number of load combinations depends directly on the number of variable actions acting simultaneously. For the design, the most unfavorable load combination governs. The variable actions are assumed to be independent of each other. However, this approach neglects the fact that the most unfavorable situation can occur at a time at which none of the participating actions exhibits a maximum value.

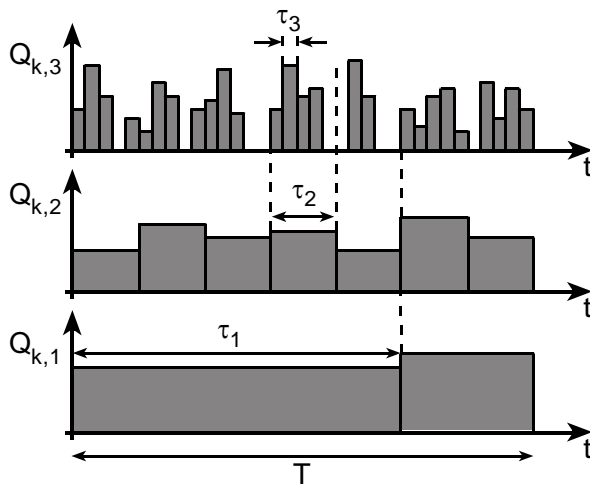


Figure 1.7: Loads within reference period  $T$  (Borges-Castanheta); cf. [1.28]

Based on the proposal by *Turkstra*, a modified approach was proposed by the Joint Committee on Structural Safety (JCSS) according to *Borges-Castanheta* (Figure 1.7), which is also called *design-value method* [1.15]. According to this method, the reference period  $T$  of every time-variant action first has to be divided into a number of elementary time periods of similar duration  $\tau_i$ , so that the extreme values of the actions in consecutive periods can be considered as independent. In addition, the conservative assumption is made that the value of its intensity  $Q_{k,i}$  is constant during the elementary time period  $\tau_i$  (basic period). This assumption also applies to

constantly variable actions. It should be noted that the shorter basic periods are integral dividers of the next larger basic periods ( $\tau_i = n \cdot \tau_2 = m \cdot \tau_3$ ). After the period lengths have been sorted in ascending order ( $\tau_3 < \tau_2 < \tau_1$ ), the necessary combinations can be found according to Eq. (1.19), with the help of the probability distributions of the actions and their extreme values  $F_{i,\max}(Q_{k,i})$ ; cf. [1.25], [1.28].

The distribution function of the extreme values  $F_{Q,\max}(Q_{k,i})$  can be calculated from the number of load changes  $N_i$  and their distribution function  $F_i(Q_{k,i})$  in the basic period  $\tau_i$ , using Eq. (1.20).

$$F_{Q,\max}(Q_{k,i}) = [F_i(Q_{k,i})]^{N_i} \quad (1.20)$$

$$F_{Q,\max}(Q_{k,i}) = (1 - P_i [1 - F_i(Q_{k,i})])^{N_i} \quad (1.21)$$

The factor  $\psi_{0,i}$  for combined loads is calculated with Eq. (1.22) ([1.24]-[1.26], [1.14]).

$$\begin{aligned} \psi_{0,i} &= \frac{F_{Q,\max}^{-1}[\Phi(0.4 \cdot \beta_c)]^{N_i}}{F_{Q,\max}^{-1}[\Phi(\beta_c)]^{N_i}} \\ &= \frac{F_{Q,\max}^{-1}(\exp[-N_i \cdot \Phi(0.4 \cdot \beta_c)])}{F_{Q,\max}^{-1}[\Phi(0.7 \cdot \beta)]} \end{aligned} \quad (1.22)$$

$$\beta_c = -\Phi\left[\frac{\Phi(\alpha_E \cdot \beta)}{N_i}\right] \quad N_i = \frac{T}{\tau_i} \quad (1.23)$$

The factor  $\psi_{0,i}$  depends on the longest basic period  $\tau_1$  of the independent actions considered, the reference period  $T$ , and the applicable distribution. Some basic periods  $\tau_i$  or different loads are given in Table 1.9. The planned service life of the support structure is generally chosen as the reference period  $T$ ; cf. Figure 1.7.

Table 1.9: Basic periods  $\tau_1$  for independent actions; cf.[1.25], [1.26]

Load	Distribution	Basic period $\tau_1$	$N_1 = T/\tau_1$
Dead weight	Normal	50 years	1
Imposed load	Gumbel	5 years	10
Snow	Continental climate	0,25 years	200
	Maritime climate	0,125 years	400
Wind	Gumbel	$\approx 0,008$ years	6000

For different basic periods  $\tau_1$  of the loads, the factors can be determined with Eq. (1.21), using a Gumbel distribution according to Eq. (1.24).

$$F_{Q_{max}}^{-1}(a) = 1 - 0.7797 \cdot v_{Q,T} \cdot \left( 0.5772 + \ln[-\ln(a)] \right) \quad (1.24)$$

### Reliability Modeling of OWT

Reliability investigations are generally very expensive to carry out. A great number of calculations have to be performed to obtain predictions regarding the probability of failure. Thus, appropriate methods and programs have to be chosen to perform suitable and efficient analyses.

Each OWT is modeled as a system of different components which are divided into two groups: structural members such as tower and foundation (WP 3-5) or blades (WP 2), as well as mechanical components (WP 6) and electrical components (WP 7 and 8). For the structural members, limit state equations can be formulated, defining failure or unacceptable behavior. The parameters in these equations have to be modeled using stochastic variables. In this project, the uncertainties of the stochastic parameters and models were determined from available measurement data.

For OWTs, physical problems are very complex; the wave-structure-foundation interaction causes many problems in the design. Moreover, there are a large number of possible failure sources that have to be considered along with their complex interactions. In Figure 1.8 a

simplified flow chart of the development procedure is shown.

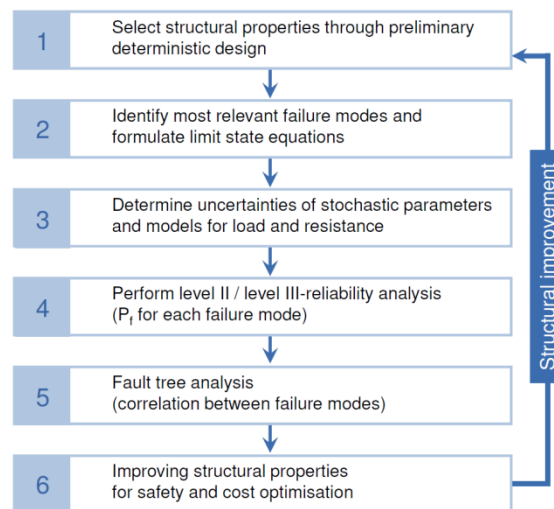


Figure 1.8: Flow chart of probabilistic OWT assessment [1.38]

In this project, the reliability of the mechanical and electrical components is estimated by using classical reliability models, for example FMEA (failure mode and effect analysis) or FTA (failure tree analysis).

### Reunification of WPs

#### Information and Assumptions

In WP 1 one objective target is to unite the methodology of all WPs. Therefore, regular meetings with all involved persons were held about every ten weeks after the start of the project. Short presentations by persons of each WP ensured that individual approaches could be discussed. Thus, common assumptions based on a coordinated method of investigation were found. These assumptions were clarified and validated during two workshops held in 2012; cf. Annual Report 2012 [1.39], paragraph 2.1.3.

#### Bilateral Discussions

The progress of each WP was evaluated in bilateral discussions between WP1 and the other WPs. The goal and purpose of these dialogues were to develop commonalities between the used methods and input variables in the different WPs. The networking of each WP within the

whole project was also examined. With this approach, possible cooperations could be forged and similar work carried out in different WPs could be detected.

#### Software

At the start of this project, software was evaluated for use in the research. As a result, the software *optiSlang*<sup>®</sup> [1.36] was bought and made available to all project partners. In a workshop all participants were informed about the content and possibilities of this software. However, only few project partners used this software in this project. Some project partners created their own tools instead. For the examination of statistical parameters the software *RCP Statrel* was used.

### 4.1.4 Results

There is still no predefined target reliability in the standards for onshore and offshore wind turbines. A panel of experts for the BSH standard "Design", work group "Safety level", met in Hanover in March 2012 [1.18]. The participants work either for manufacturers, research institutions, or certifiers. They met to discuss current and future approaches to safety elements of wind-loaded structures and their foundations. As a result, it was concluded that only a risk analysis for optimal safety and reliability of offshore wind turbines may be of real importance. Within such a risk analysis, existing failure probabilities have to be merged with their (economic) consequences of failure. A target reliability index  $\beta = 3.3$  ( $P_{f,annual} = 5 \cdot 10^{-4}$ ) was proposed. However, standardized sensitivity factors  $\alpha_E = -0.7$  and  $\alpha_R = 0.8$  as stipulated in EC 0 [1.8] are no longer valid because of the dominant wind load. It became apparent that no reasonable basis exists to reduce the present safety level and associated safety elements of OWTs. Thus, holistic investigations for OWTs such as those carried out in this project are necessary for developing further approaches.

Further to the research in the work packages, two workshops were held in Hanover in May and June 2012 [1.42], [1.43]. The aim of these events was to discuss the current approaches and assumptions with representatives from industry and to get to know their interests in this matter. Thus, the main focus was on finding realistic approaches to determine the input variables for all WPs. Critical limit states and possible scenarios were discussed. The financial losses in case of failure and public interest were also discussed. It became clear that the failure of a single OWT appears to be of rather minor concern. Failure of a whole wind park, however, would be considered a major event. A failure of this kind could be related to structural design, for example, if the towers or the foundation of all OWTs were damaged by a catastrophic event or an inherent systematic failure in the design. On the other hand, failure of the electrical components and the grid connection could lead to big financial losses. Generally, electrical systems are planned with a known N–1 reliability, meaning that each part is designed redundantly. In OWTs, however, there is no N–1 reliability. For these electrical systems, it is not common to keep reserve components for all parts, such as cables and transformers. This is very risky, because for offshore structures the failure of low-cost modules can lead to very high costs for maintenance and repair.

In conclusion, the workshops clarified the interests of industry and enabled the validation of assumptions and input values for the present investigations.

In this section, the methods used in the different WPs are summarized step by step. Although there are great differences between the methods used in each WP, similarities can also be found.

WP 1 is characterized by the common use of methodical approaches and existing databases. A central database, which was updated and extended regularly, was

used. The required statistical values for probabilistic determination of failure probabilities could be obtained from this database. In civil engineering, these necessary data are statistical values of the resistance and the loads.

Considering support structures and their environmental conditions, soil parameters are also essential. These parameters are highly dependent on the OWT location. The database also contains an overview of the statistical values for the location of the research platform *FINO 1* [1.21]

In addition to the material and soil properties, the component dimensions are also important. To obtain these properties, data from other research projects such as *GIGAWIND* [1.22] were also used.

The statistical distributions of essential load parameters for OWTs are hardly known. To determine the statistical values of these input parameters, the meteorological and hydrological measurements from the research platform *FINO 1*

were used. For the statistical analysis of the loads on an OWT, it is important to use a distribution which represents a suitable approximation of a dataset or the associated histogram. In civil engineering, the range of low occurrence probability is important. Thus, the upper quantiles of a probability distribution are important for determining the reliability. In civil engineering, the Gumbel distribution as a distribution of extreme values can be used to appropriately describe climate loads. Further distribution types are the Weibull or the Rayleigh distribution.

For the design of OWT support structures, the current 50-year extreme values of wind and wave loads are combined in a conservative manner. Using wind and sea state data from the measuring platforms in the North Sea and the Baltic Sea, the interaction of wind and waves has been analyzed stochastically; cf. [1.19] and [1.29].

## 4.2 Action Effects of Wind and Waves (WP 2)

*Action Effects of Wind:*

**Institute of Turbomachinery and Fluid Dynamics (TFD)**

Benedikt Ernst, Jörg Seume

*Action Effects of Waves:*

**Franzius-Institute for Hydraulic, Estuarine and Coastal Engineering (FI)**

Mayumi Wilms, Arndt Hildebrandt, Torsten Schlurmann

### 4.2.1 Abstract

Aerodynamic wind loads and hydrodynamic wave loads are essential input parameters to consider during probabilistic investigations of offshore wind turbines (OWT). Therefore, in this work package characteristic parameters of the loads and the resistance of OWTs are determined. The common database of wind and wave measurements *FINO 1* is used. The work at the TFD is focused on uncertain parameters caused by the complex flow environments as well as geometric deviations and material imperfections of the rotor blades. The work at the FI is focused on the sensitivity of wave-breaking probability and significant sea state parameters, and their uncertainties dependent on influencing parameters and determination methods.

### 4.2.2 Objective

Offshore wind turbines operate in a complex unsteady flow environment which causes fluctuating aerodynamic loads. Unsteady flow environments are by definition characterized by a high degree of uncertainty. In addition, manufacturing tolerances and material imperfections also cause uncertainties in the design process. The rotor blades of wind turbines are long, slender, and flexible structures and future rotor blades will tend to become even longer and more slender. The consideration of uncertainties and aero-elastic phenomena becomes increasingly

important with regard to fatigue strength of these structures and overall performance of OWTs.

In order to consider uncertainties in the design phase of OWTs, probabilistic design methods can be used. The objective is to determine the effect of wind field parameters on extreme and fatigue loads of an offshore wind turbine. The probabilities of failure due to fatigue loads in the blade root are estimated and a modeling approach for geometric and structural uncertainties of rotor blades is developed.

Extreme hydrodynamic loads on OWTs result principally from breaking waves, which cause severe impact on offshore structures and induce singular stresses as well as vibration and therefore discrete degradation of the support structure. For an efficient design of OWTs dominant and significant sea state parameters as well as wave-breaking probabilities must be considered, which influencing factors vary strongly in the natural sea state environment. In a first step, design wave heights and occurrence of wave trains in the North Sea have been analyzed on the basis of statistical analysis of extreme events. They serve as input parameters for the subsequent two-dimensional laboratory and numerical experiments, which analyzed the wave-breaking probability to quantify its scatter. Factors considered here are the significant wave height, peak period, water depth, record length, and the random phase angle distribution.

### 4.2.3 Approach (TFD)

In the IEC standards 61400-1 [2.2] and -3 [2.3], several Design Load Cases (DLC) are defined for Offshore Wind Turbines (OWT). In the present study, the focus is on the turbine response in an operating state, DLC 1.1 and DLC 1.2 in particular. Both are defined for normal operation conditions between the cut-in and cut-out wind speed ( $v_{in} \leq v \leq v_{out}$ ), and are used to analyze extreme loads (DLC 1.1) and fatigue loads (DLC 1.2).

The wind speed measurements at the *FINO 1* research platform are analyzed in order to investigate the effect of site-specific wind field parameters in comparison to requirements given in the IEC standard. Based on this analysis, 3D turbulent stochastic wind fields are generated, and the response of an OWT model is then computed with aeroelastic simulation software.

The analysis of the results is focused on the edgewise and flapwise blade root bending moments. The fatigue loads are analyzed by means of the damage-equivalent load-range approach while the extreme loads are determined by means of two statistical extrapolation methods: a Peak Over Threshold (POT) extrapolation method, and a method based on Average Conditional Exceedance Rates (ACER). A First Order Reliability Method (FORM) and a Monte Carlo Simulation (MCS) are used to estimate the failure probability.

In order to investigate the effect of variations of material and/or geometric properties a Latin hypercube sampling is performed. Due to the fact that the cross-sectional parameters of the rotor blades do not vary independently from each other, a spatial random field approach is used.

#### 4.2.4 Results (TFD)

##### Analysis of *FINO 1* wind speed measurements

For the design of wind turbines as well as for the calculations of the loads and the power output, the wind profile and the turbulence intensity are of special interest. In the standards IEC 61400-1 [2.2] and IEC 61400-3 [2.3], the wind profile can be described, by the so called power law profile:

$$v(z) = v_{hub} \left( \frac{z}{z_{hub}} \right)^\alpha \quad (2.1)$$

with mean horizontal wind speed  $v(z)$  at height  $z$  above the ground (here: 40 m), mean horizontal wind speed  $v_{hub}$  at hub

height  $z_{hub}$  (here: 90 m), and wind shear exponent  $\alpha$ . The IEC standards], [2.3] recommend that a wind shear exponent of 0.14. For DLC 1.1 and 1.2 the Normal Turbulence Model (NTM) has to be used for aeroelastic load simulations. In both IEC standards, the turbulence intensity  $TI$  is defined as the standard deviation  $\sigma_v$  of the horizontal wind speed related to the mean wind speed  $v$ :

$$TI = \frac{\sigma_v}{v} \quad (2.2)$$

For the rotor and nacelle assembly of OWT the standard deviation of the horizontal wind speed is defined as [2.2]

$$\sigma_v = I_{15}(0.75 \cdot v_{hub} + 5.6 \text{ m/s}) \quad (2.3)$$

For the support structure, the offshore turbulence intensity is defined based on an approximation of the 90% percentile of the standard deviation of the horizontal wind speed [2.3]:

$$\sigma_{v90} = \frac{v_{hub}}{\ln(z_{hub}/z_0)} + 1.28 \cdot 1.44 \text{ m/s} \cdot I_{15} \quad (2.4)$$

where  $z_0$  is the surface roughness length and  $I_{15}$  is the average turbulence intensity at hub height at 15 m/s wind speed (here: 0.12). The surface roughness length  $z_0$  has to be solved iteratively with the following equation [2.3]:

$$z_0 = \frac{A_c}{g} \left[ \frac{\kappa \cdot v_{hub}}{\ln(z_{hub}/z_0)} \right]^2 \quad (2.5)$$

$A_c$  is the Charnock parameter with  $A_c = 0.011$  for open sea,  $\kappa$  is the von-Karman parameter with  $\kappa = 0.4$  and  $g$  is the acceleration of gravity.

In order to allow a comparison taking into account site-specific wind field parameters, the wind speed measurements of the *FINO 1* offshore research platform were analyzed for the period between

January 2004 and December 2010. The investigation was based on 10 min mean wind data from the *FINO 1* cup anemometers at 90 m height. Due to wind direction fluctuations, the given standard deviation of the cup anemometers is not exactly the standard deviation of the horizontal wind speed, though close to it [2.36]. In order to calculate the 90th percentiles of the turbulence intensities, the *FINO 1* data was subdivided into 1 m/s wind speed bins. In Figure 2.1 the measured 90th percentile turbulence intensity is compared with the proposed turbulence intensity in the IEC standard 61400-3 [2.3]. ‘IEC C onshore’ denotes the normal turbulence model which can be used for the design of the rotor and nacelle assembly, while ‘IEC C offshore’ denotes the turbulence conditions for the design of the support structure. For both relations, a reference turbulence intensity  $TI_{15} = 0.12$  was used in accordance with the IEC standard. Except in cases of wind speeds lower than 4 m/s, the measured turbulence intensities lie below the IEC-values.

The wind shear exponent at the *FINO 1* platform was calculated for two cases by means of rearranging Equation (2.1). First, only the mean horizontal wind speeds on two different heights were considered. These are the hub height of the OWT model ( $z_{hub} = 90m$ ) and a height near the lower end of the rotor plane ( $z = 40m$ ). Second, a nonlinear regression over all cup anemometers from 33 m to 100 m height was performed. The hub height of the OWT model is the reference height and a Levenberg-Marquardt algorithm was used for the regression ensuring more robust wind speed exponents. In the first case, the measured mean wind shear exponent is  $\alpha = 0.09$  and in the second case it is  $\alpha = 0.138$ , which is close to the recommended value ( $\alpha = 0.14$ ) in the IEC standard [2.21]. However, both cases are strongly dependent on wind speed (see Figure 2.2). Further discussions are given in [2.15].

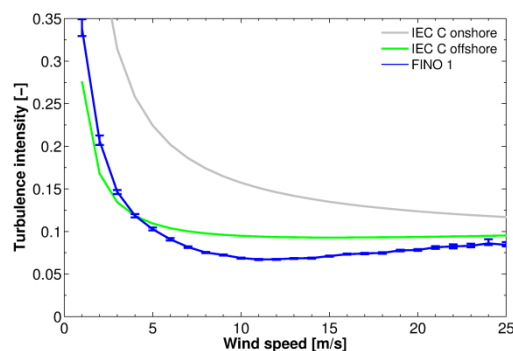


Figure 2.1: 90% percentile of the measured turbulence intensity depending on wind speed at 90 m height [2.15]

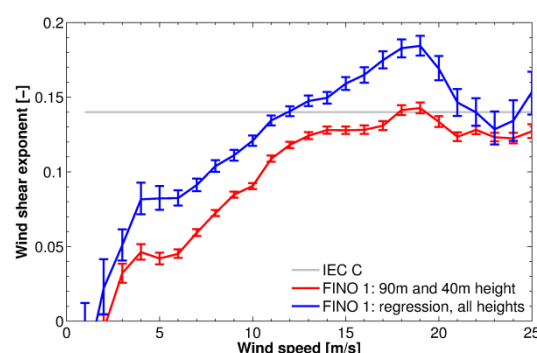


Figure 2.2: Mean value of the measured wind shear exponent depending on wind speed [2.15]

### Aeroelastic load simulations

The NREL 5 MW reference wind turbine model [2.22] was used to investigate the effect of the turbulence intensity and wind shear on the loads of an OWT. The OWT model has a rotor diameter of 126 m and a hub height of 90 m. It is a pitch-regulated turbine which can operate at variable speed. The rated wind speed is 11.4 m/s, and the maximum rotor speed is 12.1 m/s. For the aeroelastic simulations three dimensional stochastic wind fields were generated by means of TurbSim [2.21]. Between cut-in wind speed  $v_{in}=3$  m/s and cut-out wind speed  $v_{out}=25$  m/s, wind fields with 12 different mean wind speeds (3 m/s, 5 m/s, ..., 25 m/s) for each with 30 different random seeds were created. The aeroelastic design code FAST [2.23] was used for the load simulations. The simulation time is 660 sec including 60 sec run-in time. There are two different

variations based on the wind shear exponent analysis of the *FINO 1* data. In the following, the first one is denoted as '*FINO 1 V1*' and the second as '*FINO 1 V2*'. Further information about the simulation set up is given in [2.15].

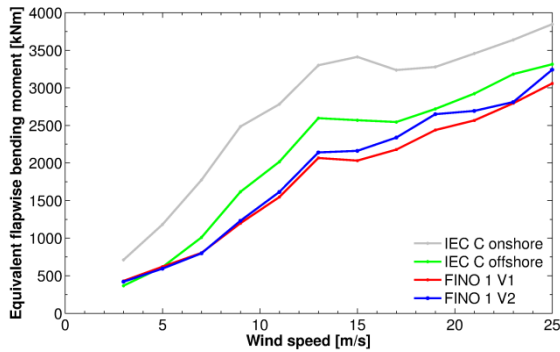


Figure 2.3: Mean value of the damage-equivalent flapwise bending moment [2.15]

### Fatigue loads

The fatigue loads were analyzed by means of the damage-equivalent load-range approach. For the time series, rainflow counting was used to determine the amplitudes  $R_i$  and the corresponding number of load cycles  $n_i$ . Based on the IEC standard 61400-13 [2.4], the damage-equivalent load is defined as

$$R_{eq} = \left( \frac{\sum_i R_i^m \cdot n_i}{n_{eq}} \right)^{1/m} \quad (2.6)$$

where  $m$  is the Wöhler curve exponent and  $n_{eq}$  is the equivalent number of load cycles. The damage-equivalent flapwise and edgewise bending moments at the blade root were calculated with  $m = 10$  and  $n_{eq} = 600$  for each 10 min time series. This results in an equivalent frequency of 1 Hz. The edgewise bending moment is mainly caused by gravity forces and less by turbulence intensity and wind shear. In contrast to this, there are significant differences in flapwise bending moments caused by the wind fields based on the IEC standard and the *FINO 1* data. As an example, the mean values of the damage-equivalent flapwise bending moments of 30 simulations are shown in Figure 2.3.

Furthermore, it is shown that the bending moments are more affected by turbulence intensity than by the wind shear exponent [2.15].

### Extreme loads

The IEC standards [2.2], [2.3] require the determination by statistical extrapolation of extreme loads in an operating state with a recurrence period of 50 years. Ernst and Seume [2.15] use a Peak Over Threshold extrapolation (POT) method, which is also recommended by the IEC standards [2.2], [2.3], and a method based on Average Conditional Exceedance Rates (ACER). In case of the POT method, the threshold is the mean value plus 1.4 times the standard deviation ( $\mu + 1.4\sigma$ ). The aggregation of the peaks uses the "aggregation before fitting" procedure and a three parameter Weibull distribution is used to fit the local distributions. The ACER method is a novel extrapolation method, which was developed by Naess [2.27] and Gaidai [2.26]. In order to determine the extreme loads on wind turbines it was already applied in [2.35]. To ensure that the extracted peaks are independent, the independency is tested by Blum's test [2.9] and the sample correlation coefficient. For more background information refer to [2.15].

The characteristic extreme loads obtained by the POT method are generally larger than with the ACER method. Furthermore, the characteristic of the long-term exceedance distributions differ significantly (compare Figure 2.4 and Figure 2.5) due to differences of the POT and ACER methods themselves, as well as the different distribution functions used. In [2.15] it is shown that the data fits of the POT method are worse in comparison to fits of the ACER method. Due to this, it is assumed that the characteristic loads obtained by means of the ACER method are more plausible. However, in both cases the simulations based on the IEC standards yield higher characteristic loads when compared to simulations based on

the *FINO 1* data. Based on the existing simulation database, an extensive parameter study was performed in terms of the short-term distribution function, the optimal threshold, the number of extracted peaks, and the number of required simulation time series [2.24]. It was shown that 30 simulations for each mean wind speed are sufficient for the POT and ACER method.

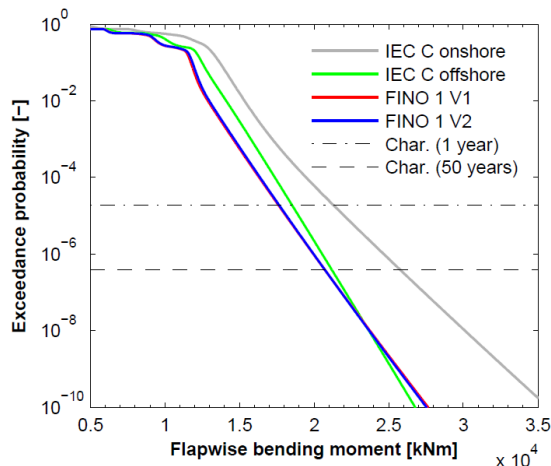


Figure 2.4: Long-term exceedance probability distribution of the blade root flapwise bending moment calculated by means of the POT method [2.15]

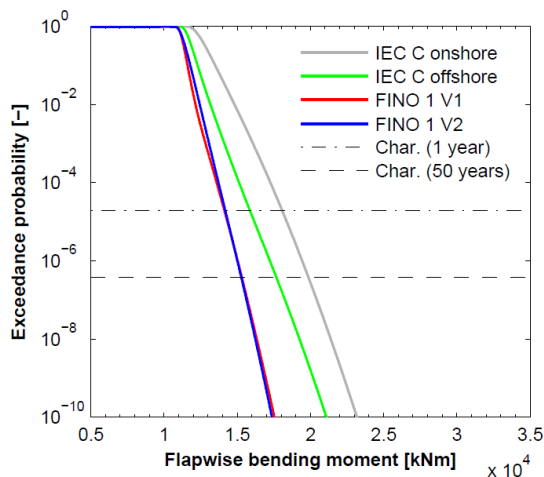


Figure 2.5: Long-term exceedance probability distribution of the blade root flapwise bending moment calculated by means of the ACER method [2.15]

### Probability of failure

In order to calculate the failure probability of the rotor blades due to fatigue loads in

DLC 1.2, the limit state function is defined as

$$Z(\underline{x}) = R(\underline{x}) - S(\underline{x}). \quad (2.7)$$

The resistance  $R(\underline{x})$  and the load  $S(\underline{x})$  depend on a vector of stochastic parameters  $\underline{x}$  (wind speed, turbulence, wind shear, fatigue strength ...). If the load  $S(\underline{x})$  is larger than the resistance  $R(\underline{x})$ , or  $Z(\underline{x}) < 0$ , the component fails. The probability of failure is then defined as

$$p_f = P(Z(\underline{x}) < 0) = \int_{Z(\underline{x}) < 0} f(\underline{x}) d\underline{x} \quad (2.8)$$

where  $f(\underline{x})$  is the probability density function (cf. [2.37]). The integral can be calculated by means of a Monte Carlo Simulation (MCS) or with the First Order Reliability Method (FORM).

According to [2.37], the dimension of moments (Nm) and the approach of damage-equivalent loads for  $T = 20$  years life were used in the present study for both the resistance  $R$ , as well as the load  $S$ . Formally  $R$  and  $S$  may be functions of all components of  $\underline{x}$ . To simplify, more natural dependencies were assumed. The fatigue resistance is defined without a specific section modulus (see [2.37]):

$$R(\underline{x}_R) = q_0 x_{dim} x_{\Delta\sigma_A} SRF \gamma_f \gamma_m S_{avg}(\underline{x}_{char}). \quad (2.9)$$

The parameter  $q_0$  takes into account the variation in fatigue strength due to load sequence effects,  $x_{dim}$  describes the variation in material dimensions, and  $x_{\Delta\sigma_A}$  is the parameter for the variation in constant amplitude fatigue strength. Simulations were performed for 11 wind speeds (4, 6, ..., 24 m/s), each with 10 different random seeds in order to determine the average characteristic load  $S_{avg}(\underline{x}_{char})$ . In doing so, the characteristic site conditions ( $U_{avg}$ ,  $T_{15}$ ,  $\alpha$ ) were fixed and chosen based on the wind turbine class I C according to [2.2] and the *FINO 1*

measurement data. The load  $S(\underline{x})$  depends on the average wind speed  $U_{avg}$ , the Weibull shape parameter  $b$ , the turbulence intensity  $TI$ , the wind shear exponent  $\alpha$ , the air density  $\rho$ , and the yaw error  $Y$ :

$$S(\underline{x}_S) = S(U_{avg}, b, TI, \alpha, \rho, Y). \quad (2.10)$$

In contrast to the previous analysis of the fatigue loads (see Equation (2.6) and Figure 2.3), here a modified definition of the damage-equivalent loads was used, which takes the mean load level into account:

$$R_{eq} = \left[ \sum_i \frac{n_i}{n_{eq}} \left( \frac{R_i}{1 - \frac{R_{mi}}{UTL}} \right)^m \right]^{1/m} \quad (2.11)$$

$R_{mi}$  is the mean load level of the amplitude  $R_i$  and  $UTL$  is the ultimate tensile load. For further information refer to [2.37], [2.19]. The life time damage-equivalent load can then be calculated as follows

$$L_{eq} = \left[ \frac{1}{n_{eq,L}} \int R_{eq}(u)^m n_{eq} p(u) n_T du \right]^{1/m} \quad (2.12)$$

here  $n_{eq,L}$  is the life time number of load cycles, the probability of the load cases is described by the probability of wind speeds  $p(u)$ , and  $n_T$  is the number of short time periods in the total life time [2.34].

In the present study a First Order Reliability Method (FORM) and a Monte Carlo Simulation (MCS) were used to estimate the failure probability. For both methods many realizations/variations of the stochastic vectors  $\underline{x}_S$  and  $\underline{x}_R$  have to be simulated. In case of the site-specific wind parameters in  $\underline{x}_S$ , for each realization several aeroelastic simulations are required. Here, a Latin Hypercube Sampling (LHS) was performed to determine the effect of  $\underline{x}_S$  on the loads. The uncertain parameters used in this investigation are listed in Table 2.1. 50

samples were created for each wind speed bin, resulting in 550 generated wind fields and aeroelastic simulations. Based on these simulations, 1 million data sets were created randomly to calculate the life time damage-equivalent load  $L_{eq}$ . In Table 2.2, the resulting mean values and standard deviations of the life time damage-equivalent flapwise bending moment at the blade root are given for 'IEC C onshore' and 'FINO 1 V2'.

Table 2.1: Overview of the uncertain parameters used in the calculations; \* limit is set to +/- 4°

Parameter	Dist.	Mean	Std.	CoV
$U_{avg}$ [m/s]	N	IEC C,		0.05
$b$	N			0.015
$TI$	N	FINO 1		0.1
$\alpha$	N	V2		0.1
$\rho$ [kg/m <sup>3</sup> ]	N	1.225		0.1
$Y$ [°]	N*	0	1	
$q_0$	LN	1		0.1
$\underline{x}_R$ $X_{\Delta\sigma A}$	LN	1.163		0.07
$X_{dim}$	N	1		0.05

Table 2.2: Life time damage-equivalent flapwise bending moment  $L_{eq,flap}$

	Mean	Std
IEC C onshore	4452.2 kNm	253.8 kNm
FINO 1 V2	2958.8 kNm	214.53 kNm

For the analysis of the limit state function (equation 7) the life time damage-equivalent load  $L_{eq}$  was used which was assumed to be normally distributed. The FORM converges after 64 and 56 design evaluations of the limit state equation, respectively. For the MCS 10000 design evaluations are performed. The resulting life time failure probabilities of the blade root in flapwise direction are given in Table 2.3. For the calculation based on the 'IEC C onshore' data, the failure probabilities are in the same order of magnitude. If the site-specific wind speed data 'FINO 1 V2' is considered, the failure probability is significantly lower. In case of the MCS, the 10000 design evaluations

are not sufficient to estimate the failure probability.

The estimated failure probabilities for the 'IEC C onshore' conditions are also of the same order of magnitude as the standard calculation given in [2.37]. In order to reduce the simulation effort [2.37] as well as [2.17] used response surfaces with first and second order polynomials to approximate the loads  $S(\underline{x})$ . In doing so, the results highly depend on the quality of the approximation model. However, in the present investigations the estimated failure probabilities highly depend on the quality of the fitted load distribution. Due to this, the absolute failure probabilities should be considered with caution and should be used only for relative comparisons. In future work, each design should be evaluated by means of a series of aeroelastic simulations.

Table 2.3: Lifetime failure probability of the blade root in flapwise direction

	FORM	MCS
IEC C onshore	$3.1 \cdot 10^{-4}$	$4.9 \cdot 10^{-4}$
FINO 1 V2	$9.3 \cdot 10^{-8}$	0

### Effect of airfoil geometry variations

Geometric variations in rotor blades can arise from manufacturing tolerances and operational wear. In order to investigate the effect of airfoil geometry variations on the lift and drag coefficients as well as the loads and the performance of an OWT, a Latin hypercube sampling was used to vary characteristic parameters simultaneously. These parameters are the maximum thickness  $t$ , the location of the maximum thickness  $x_t$ , the maximum camber  $w$ , the location of the maximum camber  $x_w$ , and the trailing edge thickness  $t_{TE}$  (see Figure 2.6).

All parameters are normalized with respect to the chord length and varied relatively with respect to the corresponding parameter of the baseline geometry. Aside from the variation of the trailing edge thickness, all variations are described by a truncated normal distribution with a mean

value of 0% and a standard deviation of 10%. The lower and upper limits are set to  $\pm 5\%$ , respectively. The trailing edge thickness is very small and therefore also relative changes of  $\pm 5\%$  would be negligible. Due to this, a standard deviation of 66.67% is assumed and the lower and upper limits are set to  $\pm 100\%$ . For all the airfoils of the 5 MW OWT, the lift and drag coefficients were calculated by means of the panel code XFOIL [2.11], and the load and performance simulations were performed with FAST [2.23].

The variations in the airfoil geometry lead to a significant scatter of the lift and drag coefficients (see for example Figure 2.7), which also affects the damage-equivalent flapwise bending moments. In contrast, the effects on the power and the annual energy production are almost negligible with regard to the assumptions made.

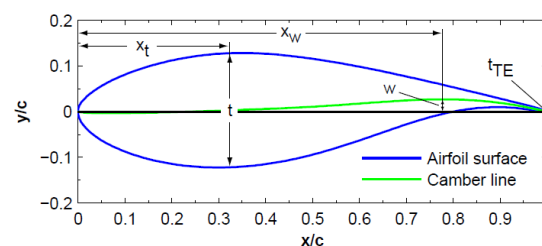


Figure 2.6: Geometry parameters of the DU25 profile [2.12]

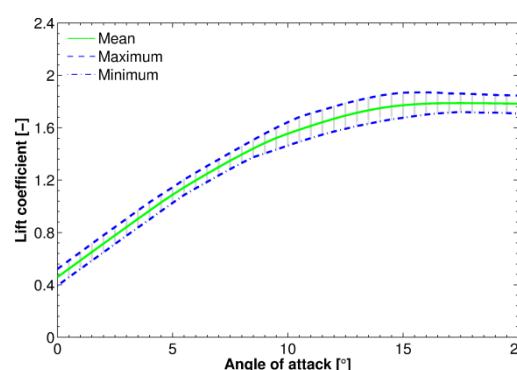


Figure 2.7: Lift coefficients of the varied DU25 profile geometries [2.12]

### Structural uncertainty of rotor blades

Structural uncertainties can arise due to imperfections in the composite materials, which can be caused by variations of the fiber and matrix material properties, or the

fiber volume ratio etc., or due to tolerances in the non-automated manufacturing process. In order to investigate the effect of structural uncertainties on the full-system mode shapes and natural frequencies of an OWT, the distributed blade mass density (BMassDen), cross-sectional flapwise (FlpStff) and edgewise stiffness (EdgStff) were varied relatively with respect to the corresponding baseline parameters (cf. Figure 2.8). The relative variations are described by a normal distribution ( $\mu = 0\%$ ,  $\sigma = 10\%$ ) and the relative parameter variations were created simultaneously by means of a Latin hypercube sampling. It is assumed that the three parameters are independent from each other. However, there is a spatial dependency of the cross-sectional parameters along the blade radius (length). In order to investigate this, three different types of spatial variations were examined. First, it is assumed that the relative variations are uniformly distributed along the blade. Second, it is assumed that the parameters of a cross-section vary independently from other cross-sections. Third, it is assumed that the variations of the structural parameters are spatially correlated.

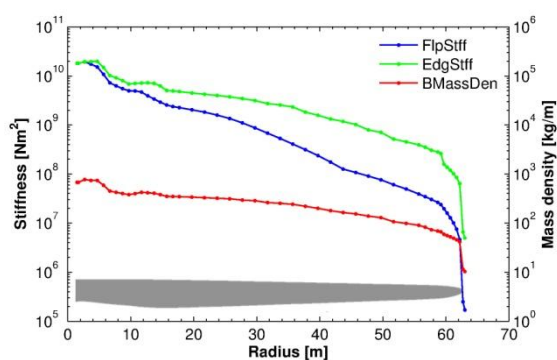


Figure 2.8: Blade mass density and cross-sectional stiffness parameters of the 5 MW OWT model [2.14] (data based on [2.21])

The variations of the spatially correlated structural properties were modeled by a random field approach. The dependency structure between the random field values at different locations is described by the

covariance matrix, which is based on an inverse-exponential correlation function with three different correlation lengths  $b$ : 10%, 50%, and 100% of the total blade length  $L$ . Finally, the random fields were created by means of the Karhunen-Loeve expansion which uses a spectral representation of the random field [2.16]. In the case of a spatially uniform variation, the structural parameters are varied constantly along the rotor blade length. The spatially independent variation leads to completely random variations along the blade length, causing local extreme fluctuations. These local fluctuations are damped if spatially correlated parameters are assumed. In case of a small correlation length, the correlation function quickly tends to zero and the spatial random field is weakly correlated. For an increasing correlation length, the correlation increases and the variations along the blade become smoother, see e.g. [2.14], [2.13].

In order to investigate the effect of these structural parameter variations on the eigenfrequencies of the rotor blade and the full-system natural frequencies of the OWT model, a tool chain/simulation process was developed based on MATLAB, BModes [2.7], and FAST [2.23]. BModes uses a finite-element approach to calculate the mode shapes and eigenfrequencies of the rotor blade. The resulting scatter (coefficient of variation - COV) of the eigenfrequencies in the first three blade modes at standstill (without rotation), caused by the different types of spatial parameter variations, is shown in Figure 2.9. It can be seen that the highest COV is caused by the spatially uniform variation of the blade parameters, while the spatially independent variation leads to the lowest COV. In this case, the effect of local variances can be compensated for, which leads to minimal variations in the eigenfrequencies. In terms of spatially correlated parameter variations an increasing correlation length leads to an increasing COV. This behavior can also be

observed in the natural frequencies of the rotor modes. For a correlation length  $b = 0.1L$ , the COV is approximately an average of the two extremes, i.e. the spatially uniform and spatially independent variations. Based on this,  $b = 0.1L$  seems to be a reasonable assumption on which to base subsequent studies.

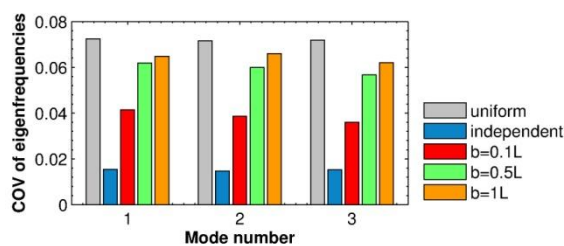


Figure 2.9: Coefficient of variation of the blade eigenfrequencies at standstill [2.14]

For the design of the OWT it is necessary to consider aeroelastic effects on the entire structure, because the drivetrain and tower-nacelle subsystem of an OWT are not solely affected by the vibration of a single blade, instead these components “feel” the modes of the entire rotor. In order to determine the system natural frequencies of the OWT model, the aeroelastic code FAST [2.23] was used to create the linearized state-space model, then a multi-blade coordinate transformation was performed to capture the cumulative dynamics of all blades in a fixed (non-rotating) frame of reference [2.8]. The system natural frequencies and mode shapes were then calculated by means of eigenanalysis.

The OWT model is a variable speed wind turbine. Due to this, the effect of structural uncertainty had to be investigated for different rotational speeds. Figure 2.10 shows the Campbell diagram with the first 11 modes. The grey shaded regions indicate the inter-quantile range containing the middle 95% of all values. It is shown that the effect on the tower modes (mode 1 and 2) is very small, but there is a high frequency scatter of the rotor modes. The variation of the blade structural parameters also affects the drivetrain

torsional mode (mode 3), which can lead to an increased risk of resonance with the 3P harmonics of the rotational speed.

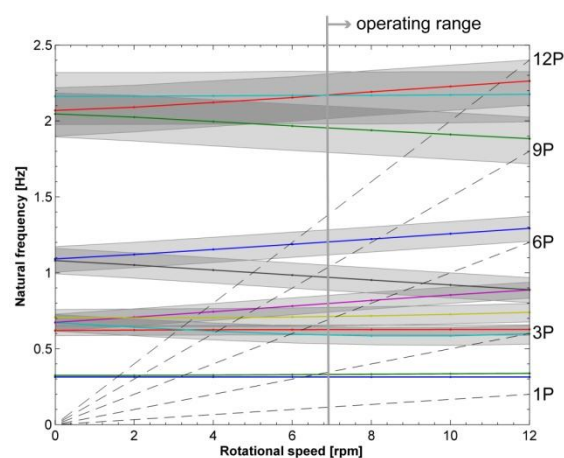


Figure 2.10: Campbell diagram of the OWT model [2.13]

#### 4.2.5 Approach (FI)

Several authors have investigated the statistical properties of wave-breaking by different approaches: the experimental methods with field or controlled laboratory measurements (with contact or remote-sensing measurements), numerical simulations, or analytical methods. For a convenient overview see [2.5] and [2.28].

To investigate the wave-breaking probability, a criterion to define the breaking onset of a wave crest has to be chosen. Furthermore, for an efficient testing and analysis, an automatable method to detect wave-breaking has to be developed.

Common wave-breaking criteria are: geometric criterion (wave steepness, ratio of wave height to wave length), kinematic criterion (ratio particle velocity to phase velocity), and dynamic criterion (ratio downward particle acceleration to gravity). Based on the wave-breaking criteria and which phase of the breaking process shall be analyzed, the detection method has to be chosen.

#### Analysis of FINO 1 data

As mentioned in the objective, firstly, the sea state data at FINO 1 have been analyzed to extract the required input parameters for the subsequent laboratory

and numerical experiments. Results can be found in [2.29] and in [2.30]. The *FINO 1* data have been analyzed on the basis of statistical analysis of extreme events to determine the design wave and design wave height according to [2.1]. To investigate the sensitivity of the determination process, the sampling method and the distribution functions for extreme waves have been varied. Used sampling methods have been: peaks-over-threshold and n-days maxima method. The latter method is a modified version of the annual maxima method with shorter time spans than a year to increase the sample size. Used distribution functions have been: Gumbel (extreme value distribution type I), Weibull and Gamma.

#### **Detection of wave-breaking**

To conduct the experiments efficiently, a detection method has been searched which determines automatically the number of wave-breaking in a test. For this, two detection methods have been compared with each other: a remote-sensing, optical method, and an analytical method.

#### **Remote-sensing, optical method**

For the remote-sensing method, a video-imagery based system has been developed to detect automatically whitecaps in videos taken in a laboratory environment. Whitecaps are here defined as a breaking wave. Several aspects need to be considered: starting with the used cameras, their configuration and calibration aspects, illumination, and other environmental influences. There are a few image-processing techniques for detection of whitecap coverage which basically all work on grayscale-images and the application of thresholds, see [2.32], [2.33] and [2.25].

The advantages of remote-sensing methods are: no interference with the test area, and spatial measurement of a large area. The disadvantages of the method are: high sensitivity to environmental influences, and a limitation on the

exclusive detection of whitecapping (which is an already developed breaker and not the breaking onset).

#### **Analytical method**

Because of those disadvantages of the optical method, an analytical detection method based on the analysis of time series of water surface elevations has been tested. Due to the complex and intermittent nature of wave-breaking, the theoretical techniques found in literature are often semi-empirical and use a time-frequency analysis technique, like the Hilbert transform, to identify wave-breaking in a time series. Griffin et al. generated breaking waves of varying intensity and used the phase time method, which is based on the Hilbert transform, to determine the location of breaking, see [2.18]. They showed that steep, non-breaking waves have a nearly constant instantaneous frequency. The instantaneous frequency increases when a breaking wave approaches the breaking point. More details to these methods, especially to the Hilbert transform, may be found in [2.5] and [2.20]. Furthermore, geometrical parameters like steepness, crest-front and -rear steepness, skewness, and asymmetry are considered and their evolution towards the breaking onset point is investigated.

#### **Scatter of wave-breaking probability**

##### *Physical model tests*

To investigate the sensitivity of wave-breaking probability to the input conditions, model tests were carried out in the wave flume of the Franzius-Institute (WKS) with its overall dimensions of 110 m length, 2.2 m width and 2.0 m height. The piston type wave maker is hydraulically driven and capable of generating regular and irregular waves with wave heights up to 0.35 m while using a stroke of up to  $\pm 0.30$  m by a water depth of up to 1.2 m. In the rear part of the flume, a beach is installed as a passive wave absorber in order to minimize reflections. For the tests, the water surface elevation were

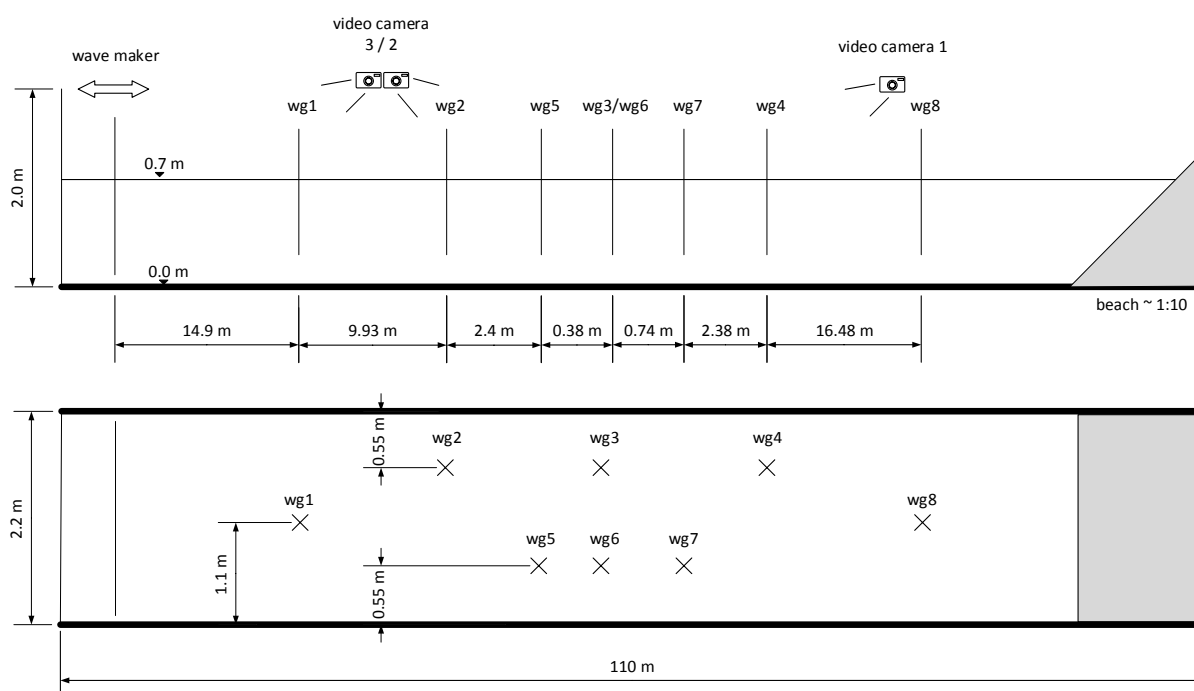


Figure 2.11: Sketch of the experimental setup in the WKS wave flume. Top: side view of setup. Bottom: top view of setup. wg: wave gauge

measured using eight capacitive type wave gauges installed along the flume and covering a testing area of 45 m. As additional measurement equipment, three video cameras were installed to record the tests and to determine the wave-breaking in post-processing. A sketch of the test setup is given in Figure 2.11.

The cameras 1 and 2 were installed with such a viewing direction, so that they faced wave gauges WG2 to WG7, see Figure 2.12 and Figure 2.13, and camera 3 faced WG1 and the wave paddle.



Figure 2.12: View direction of video camera 1 in the WKS wave flume

Wave gauge WG1 was used to determine the incident wave spectrum. The position of testing area in the flume is a compromise between minimal distance to the wave maker (at least 5 times maximum wave length) and maximum distance to the beach (to avoid wave reflections in the testing area).



Figure 2.13: View direction of video camera 2 in the WKS wave flume

#### Test program and procedure

The test program meets the condition for intermediate water and is carried out in a length scale of 1:40, which is a compromise between possible wave generation and possible water depths.

After the wave gauges and the video cameras were installed, the flume was filled to still water level.

A test program with 15 tests were compiled, see Table 2.4. As a spectrum, a narrow-band JONSWAP spectrum with enhancement factor  $\gamma = 3.3$  were used. By means of the random phase angle  $\phi$ , the sea spectrum is transformed to a water surface elevation time series by linear superposition of a number of sinusoidal wave components with different frequencies and phases. Five sets of random phase angle distributions (uniformly distributed between 0 and  $2\pi$ ) have been generated before the tests and stored. That way, the wave spectrum, characterized with significant wave height  $H_S$  and peak period  $T_P$ , could be transformed repeatedly to time domain and resulting in the same wave train every time with the same sequence of individual waves.

Table 2.4: Compilation of conducted model tests

#	$d$ [m]	$T_P$ [s]	$H_S$ [m]	nw	$\phi$
1	0.7	1.7	0.200	50	<b>a</b>
2	0.7	1.7	0.200	50	a
3	0.7	1.7	0.200	50	<b>b</b>
4	0.7	1.7	0.200	50	b
5	0.7	1.7	0.200	50	a
6	0.7	1.7	0.200	50	<b>c</b>
7	0.7	1.7	<b>0.225</b>	50	a
8	0.7	1.7	<b>0.250</b>	50	a
9	0.7	1.7	0.200	50	<b>d</b>
10	0.7	1.7	0.200	50	<b>e</b>
11	0.7	<b>1.9</b>	0.200	50	a
12	0.7	<b>2.2</b>	0.200	50	a
13	0.7	1.7	0.200	<b>100</b>	a
14	0.7	1.7	0.200	100	a
15	<b>0.8</b>	1.7	0.200	50	a

This means, test number 1, 2 and 5, test number 3 and 4, and test number 13 and 14 are the same wave trains, because they have the respective same input parameters.

Those retests were done, to analyze the reproducibility of the wave trains and number of breaking waves accordingly.

Due to the wave period and therefore the phase velocity, record length was limited to max. 100 waves to avoid wave reflection in the testing area.

During each test run, all wave gauges and video cameras were continuously collecting data. The wave gauges have an analog output system (voltage outputs) and the data were sampled by a HBM analog-digital converter in digital form. For data storage, the HBM sampling and control software catmanEasy was used and Mathworks Matlab was used for post-processing.

A waiting time of at least 10-15 min between each test, ensured no remaining oscillations in the flume, thus no interference, from the previous test run.

#### Numerical model tests

As mentioned above, the record length of the physical model tests was limited to max. 100 waves to avoid wave reflections in the testing area. Such a short test run and the necessary waiting time between each test, are a major disadvantage of the physical model tests. Therefore, numerical model tests using the fully nonlinear potential flow theory developed in [2.31] have been conducted to increase the possible test run length. The Fortran code is a Semi-Arbitrary Lagrangian and Eulerian finite element method (SALE-FEM), hereinafter referred to as the numerical wave tank. An important restriction of this numerical wave tank is, that the simulation terminates when the water surface gets discontinuous. This means, the numerical wave tank cannot simulate the breaking process of a wave, but terminates at the breaking onset. It is thus not possible to determine the

frequency of wave-breaking with this numerical wave tank, but to determine the time to breaking onset and the distance to breaking onset. This limitation of the numerical wave tank is accepted here, because the advantages over the physical model tests, namely longer test runs and faster execution of tests, outweigh the disadvantages. Within this final report, solely a small part of the results of the numerical simulations can be presented. More extended work will be part of a future doctoral thesis.

## 4.2.6 Results (FI)

### Plausibility and reproducibility

In a first step, the test runs were analyzed in regard to plausibility (comparison of target value and actual value) and reproducibility (comparison of retests).

The analysis of plausibility shows a mean deviation of 3.5 % for the significant wave height  $H_S$  and a mean deviation of 1.8 % for the peak period  $T_P$ . Please note, that the actual measured significant wave height were determined in frequency domain with Fast Fourier Transform (FFT). The mean deviations are small and the targeted wave parameters are generated.

The analysis of reproducibility shows a mean coefficient of determination of  $R = 0.998$  for test runs 1,2 and 5 and  $R = 0.997$  for test runs 3 and 4.

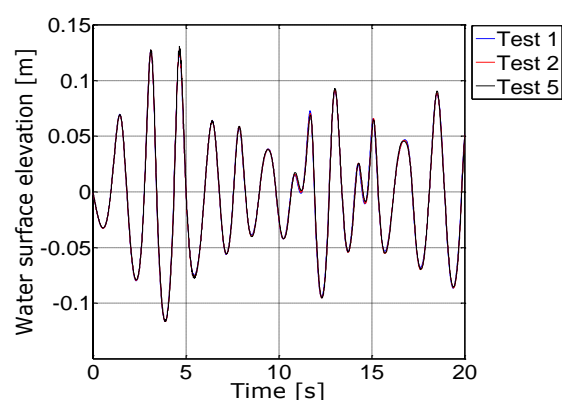


Figure 2.14: Reproducibility of test serie with  $H_S = 0.2$  m,  $T_P = 1.7$  s,  $d = 0.7$  m and phase angle distribution "a"

Figure 2.14 shows exemplary the first 20 sec of the time series with  $H_S = 0.2$  m and phase angle distribution "a".

The analysis shows that the time series can be reproduced very well and therefore the resulting numbers of breaking waves are reliable.

### Influence of wave height and random phase angle distribution

In a second step, the number of breaking waves was determined by re-watching the video camera data. The observed breakers were classified in "spilling breaker" and "whitecapping". In Table 2.5, the results for test number 1 to 10 for the number of breaking waves are compiled with their respective time stamp in relation to the start of the wave maker.

Table 2.5: Comparison of different wave-breaking behavior for tests with different wave height and phase angle distribution

#	$H_S$ [m]	phase angle	Time [s]	breaker type
1	0.200	a	00:47	spilling
			00:52	whitecap.
			00:55	whitecap.
			01:15	spilling
			01:20	whitecap.
7	0.225	a	01:23	whitecap.
			00:47	spilling
			00:52	whitecap.
			01:15	spilling
8	0.250	a	01:19	whitecap.
			01:23	whitecap.
			00:48	spilling
			01:10	whitecap.
3	0.200	b	01:15	spilling
			00:55	whitecap.
			00:59	whitecap.
6	0.200	c	01:03	whitecap.
9	0.200	d	-	no breaker
10	0.200	e	-	no breaker

The results of the retests 2 and 5 are the same as for test 1, as well as the results for the retest 4 is the same as for test 3; the reproducibility is again verified, which is why the results for retests 2, 4 and 5 are not shown in Table 2.5. For direct comparison, the results in Table 2.5 are sorted by phase angle distribution and then significant wave height  $H_s$ . Although, the significant wave height have been increased by 25 % in test number 1 to 8, the number of spilling breakers and their location in time and space did not change; solely an altered number of whitecaps have been observed.

### Influence of wave period and record length

There was no wave-breaking observed in the test area for test number 11 to 15. Thus, a slight variation of the wave period or the sequence of individual waves (change of record length) has a significant influence on the wave-breaking probability.

### Numerical wave tank results

A sensitivity test on the input settings of the numerical wave tank resulted in an optimized setting configuration with a compromise between accuracy and simulation run time. The quality and accuracy of the numerical wave tank have been investigated extensively in [2.31].

The test runs in Table 2.5 have been repeated, and additional simulations with more varying phase angle distributions (thus varying sequences of waves) have been simulated. Results for the time to breaking onset  $t_{br}$  are presented in Figure 2.15 and results for the distance to breaking onset  $x_{br}$  are presented in Figure 2.16.

When considering all simulated test, the mean value for  $t_{br}$  is 15.4 s and for  $x_{br}$  is 25.4 m (distance from the wave maker). When considering only the first five test, which have been also carried out in the physical experiments, the mean value for  $t_{br}$  is 15.1 s and for  $x_{br}$  is 24.3 m; thus slightly lower (approx. 2 % for  $t_{br}$  and

approx. 5 % for  $x_{br}$ ) than for the larger sample size.

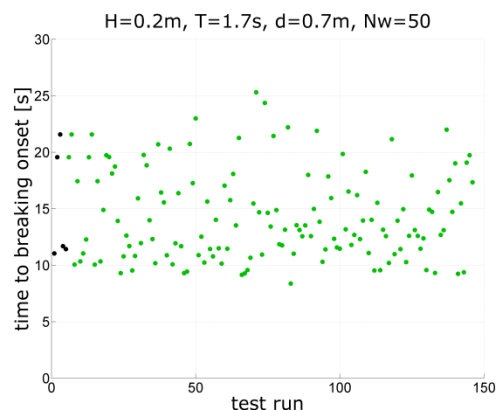


Figure 2.15: Time to breaking onset for different wave train realizations of the same sea spectrum. The first five tests correspond to test number 1, 3, 6, 9 and 10 (black markers)

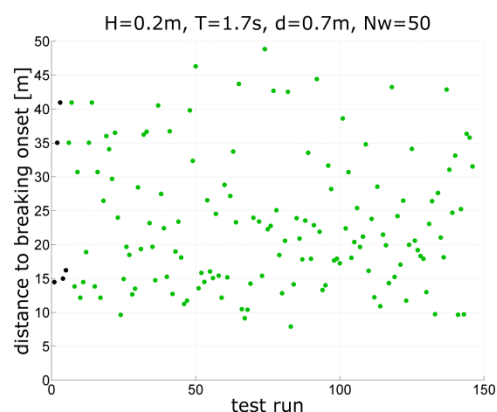


Figure 2.16: Distance to breaking onset for different wave train realizations of the same sea spectrum. The first five tests correspond to test number 1, 3, 6, 9 and 10 (black markers)

The question is: How many test runs have to be considered to determine a confident mean value for  $t_{br}$  and  $x_{br}$ ? To answer this question, the arithmetic mean has been calculated for an gradually increasing number of considered test runs, see Figure 2.17. It can be concluded, that for this investigated sea spectrum, a minimum sample size of approx. 75 test runs (correspond to approx. 3750 single waves) is necessary to determine a confident mean value for  $t_{br}$  and  $x_{br}$ . Further

investigations for varying sea spectra have to be carried out.

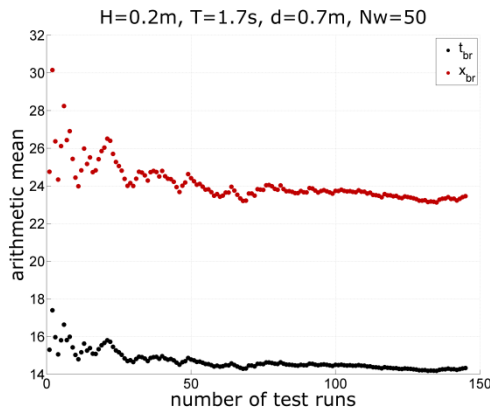


Figure 2.17: Arithmetic mean for  $t_{br}$  and  $x_{br}$  for a gradually increasing number of considered test runs

### Detection of wave-breaking by means of local, nonlinear parameters

In order to detect analytically wave-breaking in a time series, the wave train modulation over time is analyzed by means of local (instantaneous) and geometrical parameters for every wave in the sequence. The selection of parameters is mainly a combination of the parameters used in [2.6], [2.10] and [2.18], see Table 2.6. The definitions of the geometrical wave parameters can be found in Figure 2.18.

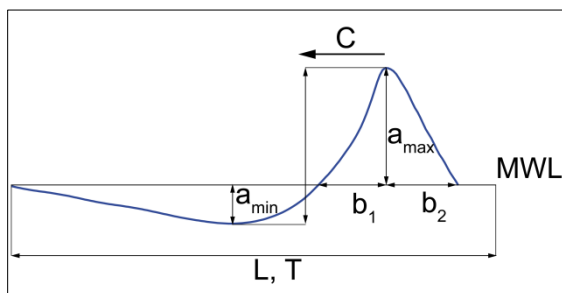


Figure 2.18: Definitions of wave parameter. Wave travels with phase speed  $C$  from right to left

An exemplary time series with a breaking wave and its corresponding local and geometrical parameters is shown in Figure 2.19. A spilling breaker occurs at the wave gauge at approx. 61.5 s. For this

breaker, it can be observed that the frequency, and the crest-front and -rear steepness increases instantly at the moment of wave-breaking and drops afterwards.

Furthermore, the wave gauge measured also the fine ripples of the water surface after a breaker; the instantaneous frequency, which can be defined as the rate of change of the phase of the (analytical) signal, captured these ripples as a high oscillation. Therefore, the time derivation of  $f(t)$  is plotted to illustrate this phenomenon. It is a good attribute to separate the peaks of  $f(t)$  caused by wave-breaking, from the peaks caused by mathematical artefacts due to the calculation method of the Hilbert transform.

Table 2.6: Geometrical and instantaneous parameters

Parameter	Equation
Wave steepness	$\frac{H}{L}$
Crest-front steepness	$\varepsilon = \frac{a_{max}}{b_1}$
Crest-rear steepness	$\delta = \frac{a_{max}}{b_2}$
Frequency of a single wave	$f_0$
Skewness	$S_k = \frac{a_{max}}{a_{min}} - 1$
Asymmetry	$A_s = \frac{b_1}{b_2} - 1$
Instantaneous frequency	$f(t)$
Time derivation of instantaneous frequency	$\dot{f}(t) = \frac{df(t)}{dt}$

The other properties are not conclusive for this one breaker, but an analysis for breakers in other test runs have been shown a good agreement with the observations from Babanin et al., see [2.6].

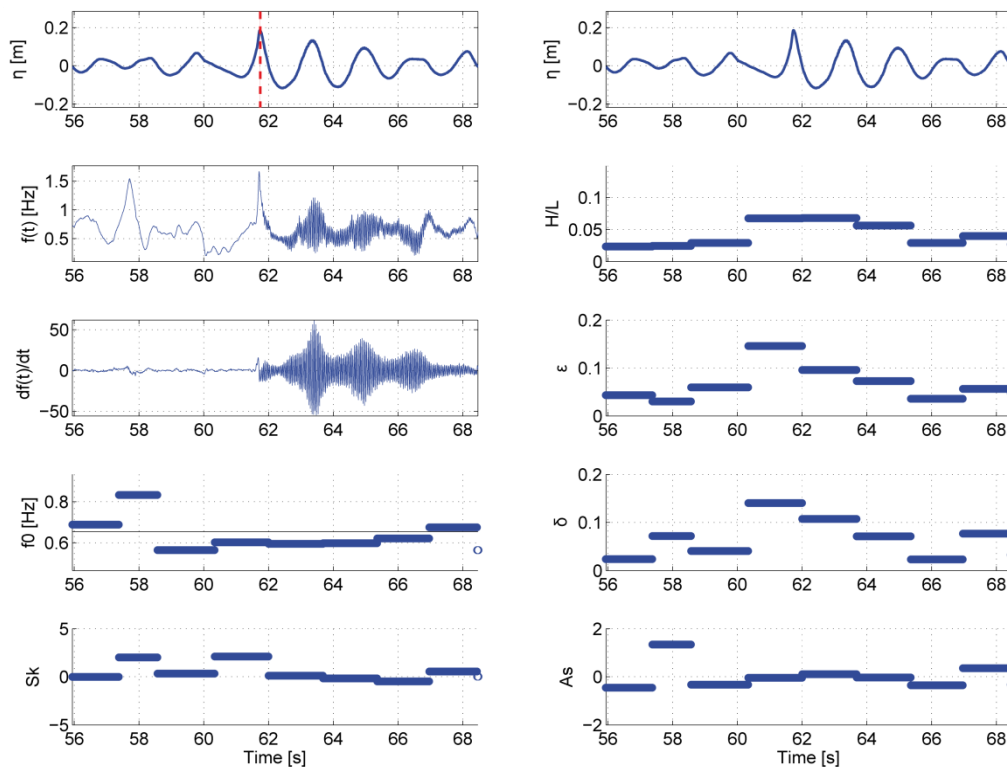


Figure 2.19: Exemplary time series with a breaking wave (dotted red line).  $\eta$ : water surface elevation.  $f(t)$ : instantaneous frequency.  $df(t)/dt$ : time derivation of  $f(t)$ .  $f_0$ : frequency of single waves.  $Sk$ : skewness.  $H/L$ : wave steepness.  $\varepsilon$ : crest-front steepness.  $\delta$ : crest-rear steepness.  $As$ : asymmetry

Special care has to be taken when comparing these results with the work of Babanin et al.: In contrast to a random wave train (JONSWAP spectra), Babanin et al. generated steep monochromatic waves and measured the exact breaking onset. In the test runs here, it was not always possible to measure the exact breaking onset, because the spatial point of breaking varied due to the random nature of the wave trains of the JONSWAP spectra.

#### 4.2.7 Conclusion

The wind speed measurements of the *FINO 1* offshore research platform were analyzed based on the 10-min-mean wind data of the cup anemometers. Aside from low wind speeds, the measured turbulence intensities are lower compared to the values in the IEC standards. In order to yield robust results, the wind shear exponent was determined based on a

nonlinear regression over all cup anemometers at the different heights. The measured mean wind shear exponent is very similar compared to the recommended value in the IEC standards. However, a strong dependency on wind speed was observed in the measured data.

Aeroelastic simulations were performed on the basis of standard and site-specific wind field parameters. The simulations based on the requirements for the design of the support structure and also on the site-specific wind field parameters, yield both significantly lower fatigue and less extreme loads compared to the IEC recommendations for the rotor design during normal power production. The life time probability of failure due to blade root fatigue loads were estimated by means of FORM and MCS. It was shown that the site-specific failure probabilities are significantly lower compared to calcu-

lations based on the IEC standard. Clearly, the requirements in the IEC standard 61400-3 seem to be very conservative for rotor blade design.

The investigations into geometric uncertainties show that variations of the airfoil geometry lead to a significant scatter of the lift and drag coefficients, therefore affecting the rotor blade loads. Contrastingly, the effects on the power and the annual energy production are almost negligible with regard to the assumptions made.

The effect of structural uncertainties in rotor blades (modeled by a spatial random field approach) on the full-system mode shapes and natural frequencies was investigated. The results show a significant scatter of the natural frequencies of the rotor modes and the torsional drivetrain mode, which can lead to an increased risk of resonance with the 3P harmonics of the rotational speed.

In the frame of the hydrodynamic analysis the following conclusions can be drawn from the set of test runs in the experimental and numerical wave tank:

Firstly, the initial steepness of the sea spectrum has a great influence on the number of breaking waves in the time series, whereby the change of the peak period  $T_p$  has a greater influence than the change of the significant wave height  $H_s$ .

Secondly, the randomness of the phase angle distribution, and thereby the

randomness of the wave sequence in the time series, has a significant influence on the number of breaking waves; different realizations of the same energy density spectra in time domain did not produce the same numbers of breaking waves in the experiments. There might be two reasons for that: Either the record length were too short (50 – 100 waves) or an exemplary time series cannot represent all possible time series from one sea spectrum. Therefore, a first set of numerical simulations have been conducted, which resulted in the following conclusion so far: for the investigated sea spectrum, a minimum sample size of approx. 75 test runs (correspond to approx. 3750 single waves) is necessary to determine a stable mean value for the time to breaking onset  $t_{br}$  and the distance to breaking onset  $x_{br}$ . Further investigations for varying sea spectra will be part of a future doctoral thesis. The development of an analytical detection method to find wave-breaking in a time series showed, that not a single parameter, but a combination of parameters are required to detect a wave breaking in a time series. Most promising so far is a combination of minimum surface elevation, instantaneous frequency (and its derivations), and crest-front steepness. The introduction of an enhanced wave-steepness parameter will be part of a future doctoral thesis.

## 4.3 Soil (WP 3)

### Institute for Geotechnical Engineering

Martin Achmus, Kirill Schmoor

#### 4.3.1 Abstract

Within a geotechnical design procedure uncertainties due to environmental impacts and variable soil properties had to be taken into account. Usually this is done by applying partial safety factors for the action and the resistance, where the established safety remains unknown.

By performing reliability based design it is possible to relate the deterministic design in terms of applied partial safety factors to a failure probability or safety, respectively.

In this Work Package first uncertainty sources within a reliability based design were quantified and different approaches to establish a subsoil model were shown. In addition results from reliability based design studies regarding axially and laterally loaded Offshore Wind Turbine (OWT) foundation piles were presented.

#### 4.3.2 Objective

In the near future several offshore wind farms are planned to be installed in the German North Sea.

For moderate water depths (up to 30m) monopile foundations were seen to be suitable to transfer the environmental load into the subsoil. By facing higher water depths Tripod, Tripile or Jacket support structures were used. Thereby the acting load is beared mainly by skin friction of the almost axially loaded foundation piles.

Uncertainties within the design of these foundation piles are usually taken into account by applying partial safety factors for the load and resistance. This procedure is known in the literature as the Load Resistance Factor Design (LRFD). According to the Eurocode 0 [3.5] the LRFD belongs to the Level 1 Reliability Based Design method and should

establish a certain safety level in a system as a function of prescribed damage fault classes.

However, the established safety in terms of a failure probability cannot be proved within the LRFD. Also the magnitude of uncertainty sources is not captured by the LRFD, where this issue strongly affects the safety of a system.

By applying a full reliability design method (or Level 3 Reliability Based Design method) like a Monte Carlo Simulation (MCS) the impact of uncertainties towards the safety and design can be evaluated in a more proper way.

The aim of this work package is to quantify uncertainties and model procedures regarding geotechnical reliability based design as well as to determine the impact on the LRFD for axially and lateral loaded offshore foundation piles.

#### 4.3.3 Approach

##### Quantifying uncertainties

Figure 3.1 elucidates a geotechnical reliability based design procedure. Therein several sources of uncertainties had to be taken into account.

To define a design subsoil, uncertainties regarding the estimation of required soil properties had to be included. These uncertainties which affect the distribution of the resistance are defined as follows:

Spatial Variability: Due to genesis of the soil there is a significant heterogeneity and therefore a spatial variability of soil properties. These uncertainties are specified by the "spatial variability". By modeling a certain soil domain especially the autocorrelation structure has an impact on the soil property distribution.

Measurement Error: Uncertainties which results from in situ measurement errors or from laboratory tests are covered by "measurement errors". These errors mainly arise from measurement equipment or from different operating conditions.

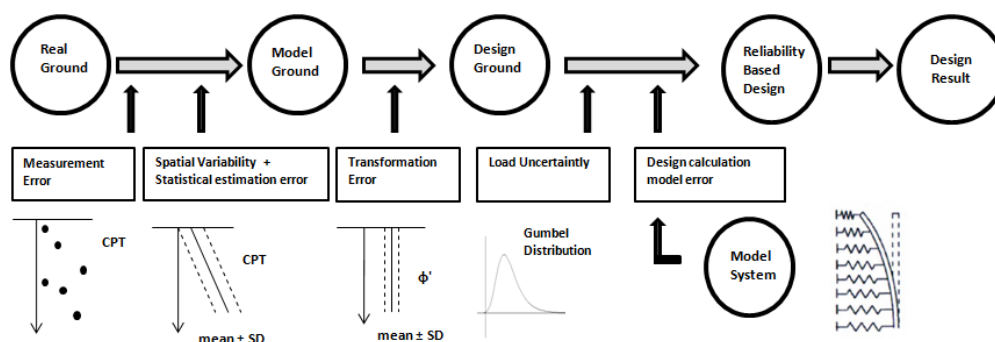


Figure 3.1: Scheme of a geotechnical reliability based design

**Statistical Estimation Error:** Mostly there is only limited information available about the in situ soil properties. By establishing statistical parameters from these data uncertainties result due to approximation errors. However, this error can be decreased with increasing data.

**Transformation Error:** Within the design process it is often necessary to transform one parameter to obtain the required one, like the calculation of the mobilized friction angle ( $\phi'$ ) from the cone penetration test ( $q_c$ ). These uncertainties which result from a transformation process are specified by the “transformation error”.

To proceed a reliability based design also load uncertainties as well as a design calculation model error had to be specified. Both sources have a huge impact on the investigated results.

**Load Uncertainty:** Since OWT are exposed to offshore environmental forces

a large variation in the resulting impact can be expected. Therefore it is important to quantify the loading conditions in a more proper way.

**Design calculation model error:** The calculation of a mechanical system is usually done with an approximated system, since in many cases simplifications due to a lack of knowledge had to be implied. Therefore large divergences comparing to real in situ systems may result. However, this uncertainty can also be reduced by taking into account the corresponding model error for the applied calculation method. A model error can be obtained by comparing calculated to measured results. From several researches it could be identified that the model error has at least as much or even more influence on the results as uncertainties regarding to the subsoil.

Table 3.1 summarizes for different soil

Table 3.1: Range of COV for common soil properties [3.4],[3.5],[3.6]

	Soil Property	Spatial Variability	Measurment	Transformation	Total COV
		COV [%]	Error COV [%]	Error SD [°]	[%]
		$COV_s$	$COV_m$		$COV_t$
Cohesionless soil	$\phi'$	6 – 13	13		10.0 – 17.7
	$\phi'$ (from $q_c$ )	20 – 60	5 – 15	2.8	2.6 – 7.9
	$\gamma'$	10	1 – 2		10.0 – 10.2
	$q_c$	20 – 60	5 – 15		20.6 – 61.8
Cohesive soil	$\phi'$	5 – 14	18 – 26		18.7 – 29.5
	$\phi'$ (from $q_c$ )	20 – 60	5 – 15	2.8	4.9 – 14.8
	$c'$	15 – 60	30		33.5 – 67.1
	$s_u$	20 – 40	20		28.3 – 44.7
	$\gamma'$	10	1 – 2		10.0 – 10.2
	$q_c$	20 – 60	5 – 15		20.6 – 61.8

$\phi'$ , effective friction angle;  $\gamma'$ , effective unit weight;  $q_c$ , CPT tip resistance;  $c'$ , cohesion;  $s_u$ , undrained shear strength

parameters and uncertainty sources the common ranges for the Coefficient of Variation (COV).

More detailed information regarding certain values for soil properties can be found in [3.10], [3.13], [3.14].

### Subsoil model

Certain model approaches exist to establish a stochastic subsoil model. Using only a single random variable to represent a certain subsoil input parameter leads to a rather rough approximation regarding a specified domain. Thereby the output variable is usually stronger affected, which results in a larger variation.

A more detailed approach to take account of random soil properties can be done by applying a random autocorrelated field. Thereby a soil property can be described in a spatial region according to Eq. (3.1):

$$z(x) = t(x) + w(x) \quad (3.1)$$

in which  $z$  is the soil property,  $t$  is a trend function,  $w$  is a fluctuating component and  $x = (x_1, x_2, x_3)$  specifies the spatial position. In most cases  $w(x)$  can be modeled as a stationary (or *homogeneous*) and isotropic random field [3.15]. Due to stationarity the probability density function of a soil property is independent of spatial position, it depends only on the relative position. This implies that the mean and covariance of the random field are constant in space. Isotropic behavior implies that the random field is invariant due to axis rotation. Hence, two points affect each other only by their relative distance between them and not by their relative orientation to each other.

By taking the “measurement error”  $e(x)$  into account the ground model  $z_m(x)$  is described by Eq. (3.2). By applying a transformation function  $T(\cdot, \varepsilon)$  with the “transformation error”  $\varepsilon$  the final design ground model  $z_d(x)$  can be obtained from Eq. (3.3).

$$z_m(x) = z(x) + e(x) \quad (3.2)$$

$$z_d(x) = T(z_m(x), \varepsilon) \quad (3.3)$$

As a result of geological and environmental processes it can be expected that soil properties of two points, which are close together, are more similar comparing to two points which are more separated to each other. This could be covered by modeling the random field as a correlated random field with a specified correlation length  $\theta$ . The determination of the correlation length is in fact complicated. However, it generally arises that the horizontal correlation length is much larger than the vertical one. In Figure 3.2 two typical correlation functions of the distance between two points  $\Delta x$  for a correlation length  $\theta = 1.0 \text{ m}$  are shown. Uncertainty due to variation of the correlation length should also be taken into account for performing reliability analyses.

More detailed information concerning the establishing of a suitable subsoil model is given in the Annual Report 2010 of this research project.

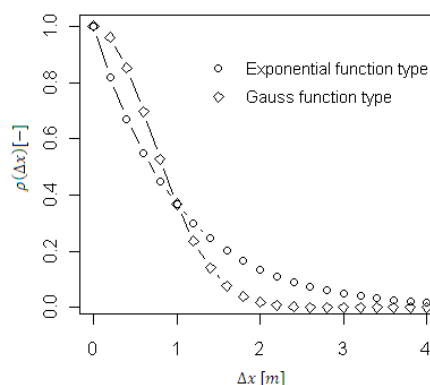


Figure 3.2: Correlation functions

### Simplified soil model

The implementation of an autocorrelated field leads to high computational effort, since a more complex soil structure has to be adopted.

However, regarding the modeling of the bearing capacity for mainly axially loaded offshore foundation piles a simplified approach is presented in the following. Therein the resistance distribution results

from an autocorrelated field, which can be modeled directly as a single random variable for two soil densities ( $D_r = 0.75$  and  $D_r = 0.93$ ) as a function of the deterministic pile properties like the diameter and the embedded pile length. Therefore pile diameters from  $D = 1 - 3\text{ m}$  and embedded pile length from  $L = 20 - 60\text{ m}$  were investigated.

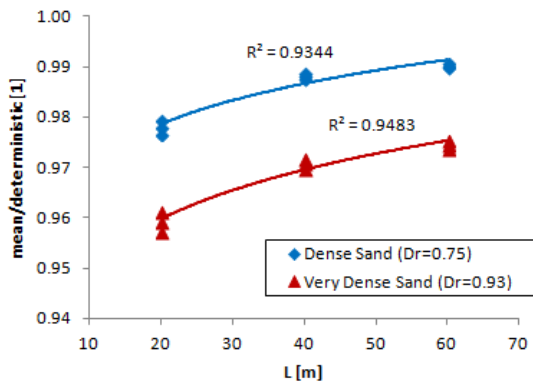


Figure 3.3: Related mean value as function of the embedded pile length for all diameters

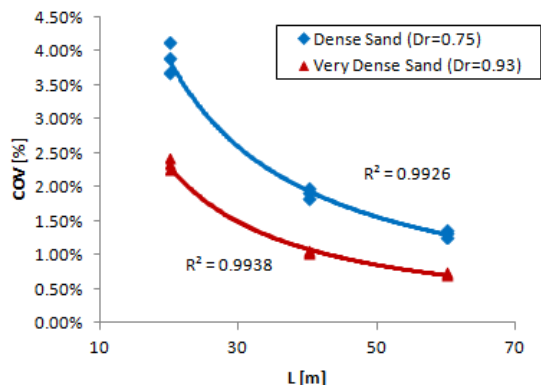


Figure 3.4: COV of the resistance as function of the embedded pile length for all diameters

The applied soil model for the performed study mainly bases on a 1-D auto-correlated field for the cone tip resistance. Therefore a constant inherent variability  $w(qc)$  for a CPT profile was modeled every  $0.5\text{ m}$  with a constant standard deviation of  $6\text{ MN/m}^2$ , where an auto-correlation length of  $\theta = 0.6\text{ m}$  with an exponential autocorrelation function was chosen. In addition the unit weight  $\gamma'$ , the

measurement error for the cone tip resistance  $e(qc)$  and the transformation error for the internal friction angle  $te(\varphi')$  were modelled as uncorrelated and normal distributed random fields with typical values for the mean and standard deviation.

Figure 3.3 elucidates the mean values of the resulting distributions in comparison to the deterministic computed ones by assuming no variability. As it can be seen a small dependency with the embedded pile length can be noticed. Also the COVs for the pile resistances show a correlation to the embedded pile length as can be noticed from Figure 3.4. With increasing pile length the variation in the resistance is decreasing.

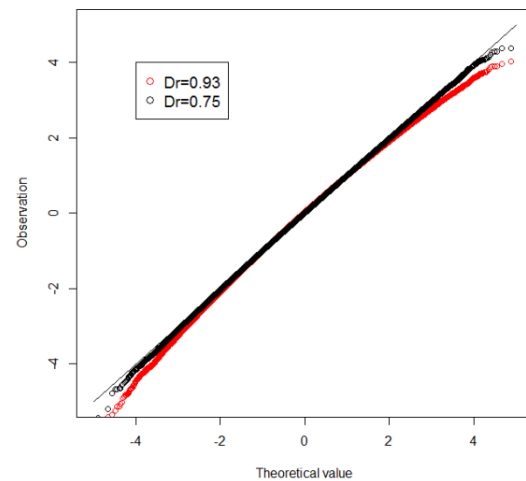


Figure 3.5: Standard normal Q-Q plot of the pile resistances with  $L = 40\text{ m}$  and  $D = 2\text{ m}$

By comparing the quintile values of a normal distribution with the obtained ones (Q-Q plot), it could be determined that for dense soil conditions a Gaussian distribution for the pile resistance can be assumed, since the observed values almost corresponds to the theoretical ones. For very dense soil conditions it could be recognized that the resistance more probably does not follow a normal distribution. However, a normal distributed resistance also for very dense sand seems to be the best estimate distribution type.

More detailed information regarding the proposed model approach is given in the Annual Report 2012.

### 4.3.4 Results

#### Laterally loaded offshore foundation piles

Monopile foundations are primary laterally loaded and transfer their acting load via bedding into the subsoil. Typical distributions of the horizontal stresses due to a loading event can be seen in Figure 3.6.

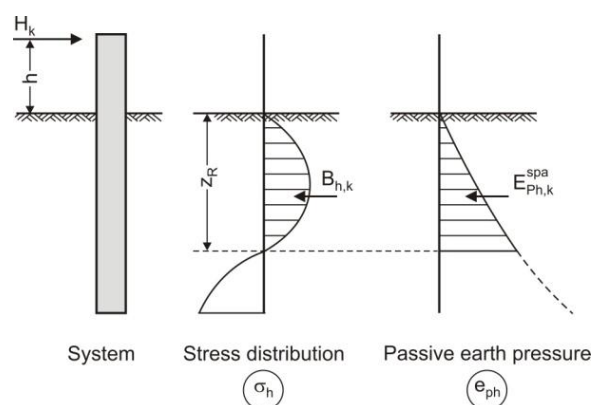


Figure 3.6: Elucidation of effect and resistance forces

Therefore the Ultimate Limit State (ULS) is defined acc. EC 7 [3.6] and DIN 1054 [3.4] in combination with the “EA-Pfähle” [3.3] in terms of the ratio of the resulting horizontal force and the spatial ground resistance as shown in Eq. (3.4).

$$\mu_{ULS} = B_{h,d}/E_{ph,d}^{spa} = \gamma_Q B_{h,k} / \frac{E_{ph,k}^{spa}}{\gamma_{R,e}} \quad (3.4)$$

Where:

- $\gamma_Q$  Partial safety factor for loading
- $\gamma_{R,e}$  Partial safety factor for resistances
- $B_{h,k}$  Resultant horizontal force (characteristic)
- $E_{ph,k}^{spa}$  Spatial ground resistance (characteristic)

As a first indicating study the failure probability of a deterministic proofed monopile system was investigated within a

reliability based design regarding the ULS acc. to Eq. (3.4).

Thereby typical North Sea soil conditions in terms of a non cohesive homogeneous dense sand layer were assumed. Hence, a friction angle of  $\varphi' = 36^\circ$  and a buoyant unit weight of  $\gamma' = 10 \text{ kN/m}^3$  were applied. Also typical loading conditions with a horizontal force of  $H = 13 \text{ MN}$  in combination with a moment arm of approximately  $h = 38.5 \text{ m}$  were considered.

Regarding to the defined soil properties and loading conditions, first a pile design had to be specified which closely fulfils the ULS design proof. For the calculation of the monopile system and the resulting horizontal force  $B_{h,k}$  the well known p-y method acc. to [3.2] was used, respectively. Therein non linear p-y springs substitute the lateral bedding reaction of the subsoil along the embedded pile. The spatial ground resistance  $E_{ph,k}^{spa}$  was calculated acc. to DIN 4085.

By choosing a pile length of  $L = 40 \text{ m}$ , a diameter of  $D = 5 \text{ m}$  and a pile wall thickness of  $t = 70 \text{ mm}$ , a valid pile design was obtained.

Regarding the probabilistic design, these pile properties were applied as deterministic variables. The friction angle and the buoyant unit weight were modelled as single random variables, where the friction angle was assumed as lognormal distributed with a varying COV of 0.11 – 0.18 and the buyout unit weight as normal distributed with a constant COV of 0.10. The horizontal load was modelled acc. to the recommendation of [3.8]. Thereby, a gumbel distribution with a COV of 0.15 – 0.35 was applied.

The failure probability was calculated by performing a plain MCS with  $n = 1E6$  realisations. By assuming a target reliability index  $\beta_T = 3.3$  with the corresponding failure probability of  $pf_T = 4.83E-4$  the accuracy of the

Table 3. 2: Estimated reliability index for the deterministic pile design for ULS

	$COV_{\varphi'} = 0.11$	$COV_{\varphi'} = 0.14$	$COV_{\varphi'} = 0.18$
$COV_{H,M} = 0.15$	$\beta = \infty (n_{pf} = 0)$	$\beta = \infty (n_{pf} = 0)$	$\beta = 4.47 (n_{pf} = 4)$
$COV_{H,M} = 0.25$	$\beta = 4.75 (n_{pf} = 1)$	$\beta = 4.42 (n_{pf} = 5)$	$\beta = 3.98 (n_{pf} = 35)$
$COV_{H,M} = 0.35$	$\beta = 4.47 (n_{pf} = 4)$	$\beta = 4.12 (n_{pf} = 19)$	$\beta = 3.67 (n_{pf} = 119)$

estimated reliability can be specified to  $COV_{pf} = 0.05$ .

The resulting distributions for  $B_{h,k}$  and  $E_{ph,k}^{spa}$  are shown in Figure 3.7 as a function of the applied COV for the load.

The calculated reliability index for the ULS is shown in Table 3. 2, where  $n_{pf}$  specify the number of failed systems. Usually the failure probability or target safety is declared in terms of the reliability index acc. to Eq. (3.5), respectively.

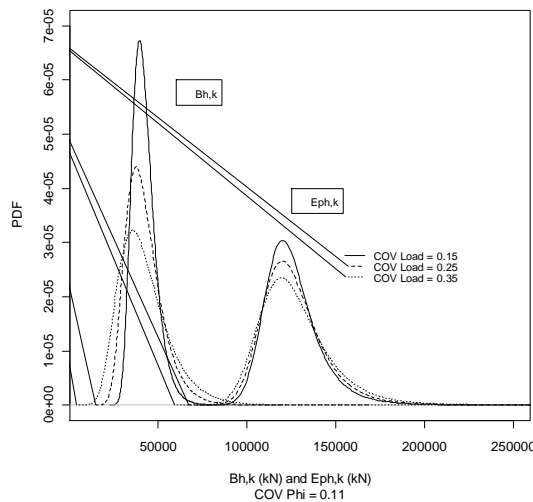


Figure 3.7: Empirical response distributions of  $B_h$  and  $E_{ph}^{spa}$  with  $COV_{\varphi'} = 0.11$

Regarding to the annex in the EC 0, a target reliability index of  $\beta = 3.8$  should be established in a system which was design acc. to the LRFD with prescribed partial safety factors.

Evidently a higher reliability index except for the highest COV of the internal friction angle and load was obtained. Keeping in mind that a conservative model approach was used and that for OWT also a target reliability of  $\beta = 3.3$  is suitable, it can be concluded that in this case the design leads to very safe conditions.

$$\beta = \Theta^{-1}(1 - pf) \quad (3.5)$$

Where:

- $\Theta$  Cumulative standard distribution
- $pf$  Failure probability

In addition to the calculated safety also sensitivity values were obtained. Sensitivity values or  $\alpha$ -values indicate how an output variable is influenced by an input variable.  $\alpha^2$ -values just emphasize the more important input variables in comparison to each other.

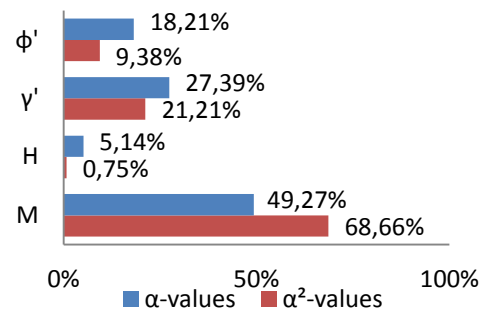


Figure 3.8: Sensitivity values for the safety with  $COV_{\varphi'} = 0.14$  and  $COV_{H,M} = 0.25$

Figure 3.8 elucidates the outcome for the ULS design proof. Hence, it can be noticed that the resistance parameters ( $\varphi'$  and  $\gamma'$ ) have almost the same impact on the ULS as the action variables (H and M), where the pile head moment M appears to have the most dominant impact. Thus also more effort should be investigated in quantifying loading variability.

More detailed information concerning the performed study is given in the annual report 2011.

Regarding a complete design of monopiles also the Serviceability Limit State (SLS) had to be fulfilled. Often the SLS is design driving compared to the ULS. Thereby the

SLS can be ensured if the accumulated plastic (or permanent) pile head rotation  $\theta_{pl}(N)$  does not exceed a certain specified value  $\theta_{lim}$  acc. to Eq. (3.6). Therein the cyclic increase in the pile head rotation had to be taken into account by a cyclic increase factor. Further the elastic portion of the total rotation had to be subtracted. However, several pile designs are possible which fulfill the defined limit state in Eq. (3.6). Hence, a study towards an optimized pile design in terms of pile properties like the embedded pile length and diameter was conducted, where an optimization regarding to the minimum pile mass was aspired.

$$\theta_{pl}(N) \leq \theta_{lim} \quad (3.6)$$

Where:

- $\theta_{pl}(N) = \theta(N_1)\xi_{cyc} - \theta_{el}(N_1)$   
Accumulated plastic head rotation
- $\theta(N_1)$  Head rotation due to 1 cycle
- $\xi_{cyc}$  Cyclic increase factor
- $\theta_{el}(N_1)$  Elastic head rotation due to 1 cycle

The cyclic increase factor was derived from the Stiffness Degradation Method introduced by Kuo (2005) [3.12], which mainly based on numerical calculations.

$$\xi_{cyc} = e^{(A-1.208)\ln\left(\frac{H(h+L)}{\gamma'DL^3}\right)+B-0.588} \geq 1 \quad (3.7)$$

Where:

- $L$  Pile embedded length (in m)
- $H$  Horizontal load (in kN)
- $h$  Moment arm (in m)
- $D$  Pile diameter (in m)
- $\gamma' \approx 10kN/m^3$  Buoyant effective unit weight
- $A, B$  Parameters from Table 3.3

Table 3.3: Regression parameters acc. to Kuo (2008) [3.12]

Number of cycles N	A	B
100	1.361	1.331
1000	1.427	1.639
10000	1.505	1.981

For the investigated study also the loading conditions had to be adapted within the

optimization process, since changes in pile properties like the pile diameter almost lead to variation in the current considered action. In this study a horizontal load of  $H = 5 MN$  was applied to a diameter of  $D = 3 m$ . In addition also an increase of  $2 MN$  was considered with an increase of  $1 m$  in the diameter.

Figure 3.9 shows the obtained slenderness ratios as function of a dimensionless coefficient, which was introduced to achieve a suitable regression as a function of the specified limit pile head rotation  $\theta_{lim}$ , horizontal load  $H$ , moment arm  $h$ , pile diameter  $D$  and embedded pile length  $L$ .

As it can be seen slenderness ratios were obtained in a range of approximately  $L/D = 7 - 8$ .

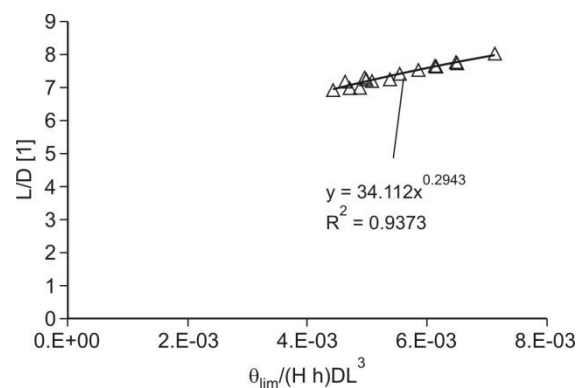


Figure 3.9: Optimized slenderness ratios as function of dimensionless coefficient

### Axially loaded offshore foundation piles

By facing water depths higher than approximately 30 m, Tripod, Tripile or Jacket support structures were seen as more suitable to install an OWT. Thereby foundation piles were used to transfer the acting load mainly via shaft friction and in case of compression also via the tip resistance into the ground.

A comprehensive study was performed to validate the prescribed partial safety factors for mainly axially loaded foundation piles. Therefore a reliability based design for two common soil profiles corresponding to typical North Sea conditions and two design methods, the API-method

and the ICP-method, was conducted. Thereby a calibration of partial safety factors was carried out to match the safety requirements of the EC 0 more specifically.

Generally it can be observed that in almost all design cases the tension limit state is the controlling one with regard to the required pile length. Hence, only the ULS tensile capacity is considered, where the limit state function is presented as follows.

$$V_k \gamma_L \leq R_k / \gamma_R \quad (3.8)$$

Where:

- $V_k$  Characteristic load
- $\gamma_L$  Partial safety factor for the loading
- $R_k$  Characteristic resistance
- $\gamma_R$  Partial safety factor for the resistance

The calculation of the resistance was done by applying the API-method as well as the simplified ICP-method acc. to [3.1], [3.11]. Basically the resistance acc. to the API-method strongly depends on the assumed density profile, where the resistance of the ICP-method is more influenced by the Cone Penetration Test (CPT) measurements.

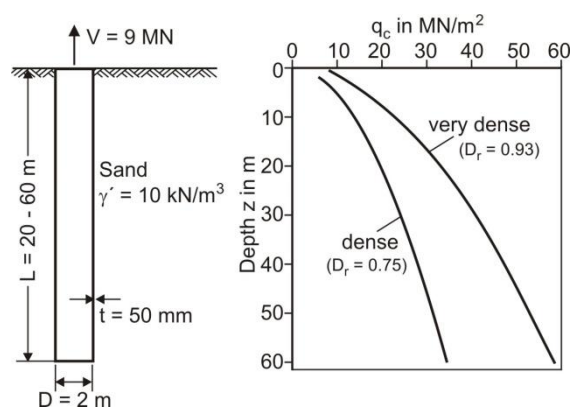


Figure 3.10: Considered pile system

Figure 3.10 shows the considered system. Therefore a pile design with a diameter of  $D = 2 \text{ m}$ , a pile wall thickness of  $t = 50 \text{ mm}$  and a various pile length of  $L = 20 - 60 \text{ m}$  was considered. Regarding the soil conditions, two CTP profiles with constant densities, namely dense ( $Dr = 0.75$ ) and

very dense ( $Dr = 0.93$ ) in combination with a buoyant unit weight of  $\gamma' = 10 \text{ kN/m}^3$  were applied. A characteristic load of  $V_k = 9 \text{ MN}$  was assumed, which corresponds to a water depth of  $30 \text{ m}$ . The distribution of the axial pile resistance was basically obtained by simulating and evaluating various CPT profiles. Thereby each CPT profile was modeled as an autocorrelated field, where the two assumed CPT profiles were used as trend functions.

A normal distributed constant standard deviation of  $6 \text{ MN/m}^2$  was applied as inherent variability. In addition the auto-correlation structure was established by assuming an exponential function with an autocorrelation length of  $\theta = 0.6 \text{ m}$ . A normal distributed measurement error with a COV of 0.15 was added as well. The axial load was applied as gumbel distributed with a COV of 0.35 acc. to Holicky et al. (2007) [3.9].

As already mentioned above a model error has a significant influence on the outcome result. Hence, a model error can be determined by comparing measured properties with calculated ones. Achmus & Müller (2010) [3.7] compared measured with calculated results for the API and the ICP-method only with pile tests which are closely related to the boundary conditions in the North Sea. Therefore the following pile tests were considered: Open-ended piles, tension test, steel piles, dense to very dense soil state and slenderness ratios between 10 and 40. By taking into account only pile tests within a range of 95% confidence interval, only 6 pile test for the ICP-method and only 4 pile tests for the API-method could be evaluated. The mean and standard deviations for these related tests are summarized in Table 3.4 and should be seen as rough approximations of the real values. Since only a few pile tests exist it is difficult to define a distribution type. Nevertheless, a normal distribution was assumed for the model error.

Table 3.4: Model error ( $R_m / R_c$ ) for the ICP-method and API-method

	Method	Mean [-]	SD [-]	COV [-]
Achmus & Müller (2010) [1]	ICP-method, only related tests	1.16	0.19	0.16
	API-method, only related tests	1.26	0.14	0.11

The determination of the failure probability was done by applying a plain MCS with  $n = 6E6$  simulations.

Figure 3.11 elucidates for both investigated methods the resulting safety in terms of the reliability index as function of the embedded pile length. Thereby also the required depths from the deterministic

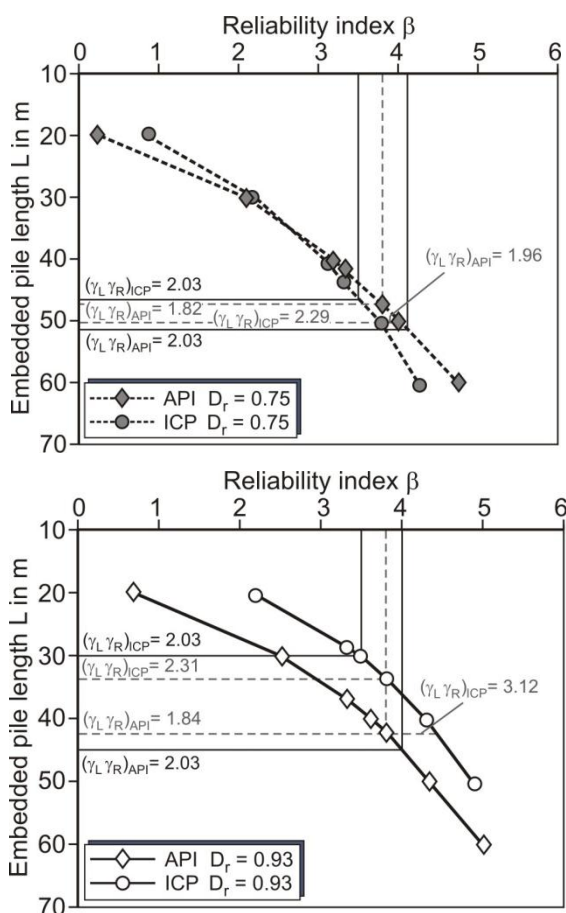


Figure 3.11: Evaluated safety with increasing pile length

Table 3.5: Comparison of the separation of required pile lengths for different designs

	$\Delta L$ ( $D_r = 0.75$ )	$\Delta L$ ( $D_r = 0.93$ )
For deterministic design	5.94	14.95
For reliability $\beta = 3.8$	3.12	8.77

design with the corresponding product of the partial safety factors ( $\gamma_L \gamma_R = 2.03$ ) is added. In addition also the corresponding product of partial safety factors for the desired target reliability index of  $\beta = 3.8$  is shown.

By performing reliability based design the same safety can be aspired as also more information, like a model error, can be taken into account within the design process. This leads to a more robust

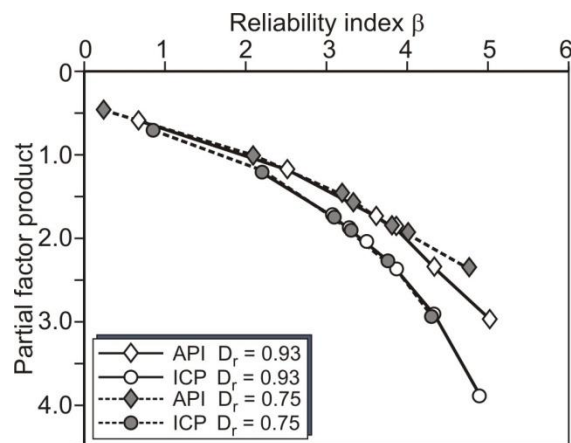


Figure 3.12: Evaluated safety vs. the product of partial safety factors

determination of the required pile length. Therefore Table 3.5 summarizes the separation for different design procedures. As it can be seen the gap between the obtained pile lengths via reliability based design is decreased about 47 % for dense and 41 % for very dense soil conditions.

Also a link between the deterministic design and reliability based design can be obtained. Figure 3.12 shows the product of partial safety factors ( $\gamma_L \gamma_R$ ) versus the established safety within the design for both methods as well as both densities. It should be emphasized that only the product of partial safety factors affects the failure probability. Therefore each partial safety factor may vary a lot while the

product of both stays constant. As it also can be noticed the deterministic result is almost independent of the density. Therefore approximately a product of partial safety factors  $\gamma_L\gamma_R = 2.30$  for the ICP-method and  $\gamma_L\gamma_R = 1.83$  for the API-

method should be used within a deterministic design to reach the target reliability index acc. to EC 0 of  $\beta = 3.8$ . More detailed information regarding the performed study is given in the annual report 2013.

## 4.4 Foundation and Support Structure (WP 4)

### Institute for Steel Construction

Peter Schaumann, Sebastian Kelma

### Institute of Structural Analysis

Raimund Rolfes, Jan Goretzka

### Institute of Concrete Construction

Boso Schmidt, Michael Hansen

### 4.4.1 Abstract

Within work package 4, advanced design and optimization of support structures for offshore wind turbines are evaluated with respect to the probabilistic safety concept. Therefore, design relevant limit states are identified. Uncertainties as well as scattering of action effects and resistances are considered by applying probabilistic methods.

Measurement-based offshore data are analysed in order to estimate relevant design parameters for offshore wind turbines. For the probabilistic design, models of offshore wind turbines are set up in finite-element software. Probabilistic design of the ultimate axial-load bearing capacity for foundation piles is carried out in cooperation with work package 3 "Soil". The dynamic behaviour of an offshore wind turbine with monopile substructure is examined, taking probabilistic influences of various model input parameters into account. Probabilistic fatigue design is applied on joints of a jacket substructure.

### 4.4.2 Objectives

Within work package 4 (WP 4), relevant failure types are identified and analysed for different support structures of offshore wind turbines (OWTs). Therefore, the exceeding of the underlying limit state for both semi-probabilistic as well as probabilistic safety concept was considered. Limit states of the semi-probabilistic safety concept as stated in standards for OWTs (e.g. [4.2], [4.9], [4.7]) are to be adapted for the probabilistic design.

For the probabilistic design, stochastic descriptions of both action effects and resistances are required. Based on offshore data obtained from the measurement platform *FINO 1*, design parameters are to be identified. Models of support structures are set up in finite-elements software to calculate and evaluate the dynamic response of OWTs. Probabilistic modelling of soil properties is carried out in accordance with WP 3 "Soil". Considering fatigue design, fatigue loads are determined and scattering of fatigue resistance is evaluated.

Probabilities of failure are determined within the probabilistic reliability assessment of OWTs. For this purpose, suitable methods such as the Monte-Carlo simulation are applied.

Applying the methods described in this report for the probabilistic safety concept, economic optimization of the structural design of OWTs can be performed.

Investigations are carried out on OWTs with monopile and jacket substructures, (cf. Figure 4.1). These types of substructures are the most used and most relevant substructures installed in the German Exclusive Economic Zone [4.36].

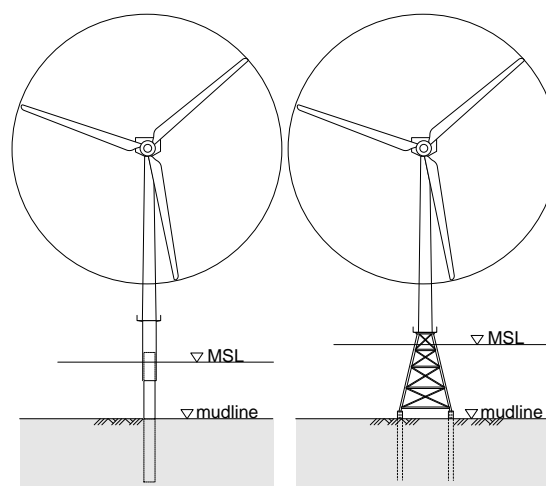


Figure 4.1: OWT with monopile substructure (left) and jacket substructure (right)

### 4.4.3 Approach

#### Introduction / Probabilistic approach

The approval process of OWTs within the German Exclusive Economic Zone is regulated within the standard "Design of Offshore Wind Turbines" [4.2], published by the Federal Maritime and Hydrographic Agency (BSH). Here, regulations for all phases of the life time such as design, transportation, installation etc. are stated. For the structural design of OWTs, the standard refers to different national and international guidelines for both action effects and resistance.

These standards are based on the semi-probabilistic safety concept. Here, characteristic values for effects  $E_k$  and resistance  $R_k$  are determined for specific design load cases (DLCs) as stated in standards. For OWTs, the DLCs are given in e.g. [4.9]. In order to cover uncertainties and scatter of these characteristic values, design values are calculated by multiplying the characteristic values with partial safety factors  $\gamma$ . The values of the partial safety factors are also stated in the adequate standards. For structural approval of the components, the design values of action effects of actions must not exceed the design values of resistance. The design values are set such that the probability of failure is as great as allowed by the adequate consequence classes.

$$\begin{aligned} E_k \cdot \gamma_E &\leq \frac{R_k}{\gamma_R} \\ E_d &\leq R_d \end{aligned} \quad (4.1)$$

Scattering of action effects and resistance as well as the corresponding characteristic and design values for action effects and resistance are shown in Figure 4.2.

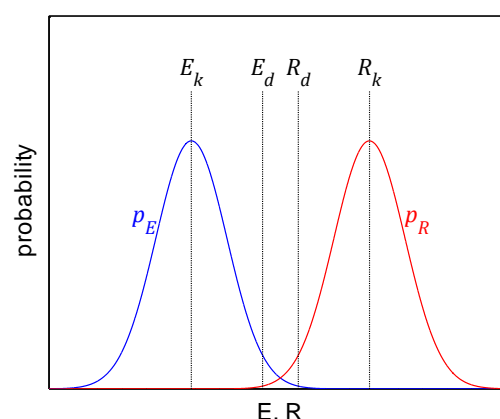


Figure 4.2: Probabilities of effects and resistances as well as the associated characteristic and design values

When using the probabilistic safety concept, scattering of action effects and resistance are taken into account by their probability density function  $p_E$  and  $p_R$ . To fulfil the proof of safety, the probability that the effect  $E$  is greater than the resistance  $R$  must not exceed a predefined value for the probability of failure  $P_F$ ,

$$P_F \geq \int \int p(R - E < 0) \cdot dEdR \quad (4.2)$$

where  $p$  is the probability density function of the limit state  $R - E < 0$ . In general, the values for probability of failure  $P_F$  lie between  $10^{-4}$  and  $10^{-3}$  for OWTs. The standard DNV-OS-J101 [4.4] recommends a value of  $10^{-4}$ . However, recent research results suggest a value of about  $2.0 \cdot 10^{-4}$  to  $1.0 \cdot 10^{-3}$  [4.38].

In comparison to the structural design based on the semi-probabilistic safety concept, no DLCs are not used within the probabilistic design of OWTs. Instead of DLCs, all possible environmental and operational states are to be considered. Certain scenarios might be eliminated for the further design.

Also, sufficient accuracy of the underlying distribution functions for both action effects and resistance has to be ensured. In case that this is not possible, the scattering of possible errors due to e.g. modelling shall be considered as well.

### Effects and actions

Environmental conditions of OWT influence significantly the results of probabilistic calculations because they are subject to large variations. Wind and wave loads have great uncertainties. In order to assure correct input parameters for the probabilistic design, the applied statistical parameters of these loads are determined with their measured natural scatter.

Therefore, available measurement data in particular from the *FINO 1* measurement platform were analysed. In order to obtain reliable statistical data and to capture seasonal fluctuations, data of *FINO 1* within the period 2004/01/01 – 2011/01/01 were analysed.

Extreme events were investigated like they are listed for example in load case DLC 6.1c [4.9]. In this context, the wind speed and wave height at the *FINO 1* measurement platform were evaluated. A general description of the measuring device of the *FINO 1* platform can be found in [4.27]. For the mentioned period, 10-min averages of wind speed exist for eight different heights starting at 33 m up to 100 m. In the extreme value analysis different reference periods were considered. Within the investigations 6-hour up to 4-week extreme values were used and the resulting quantiles were compared. The most reliable results have been achieved using extreme values with large reference periods, provided a sufficient number of measurements. About 90 4-week extreme values were determined for each of these measuring heights.

The distribution functions and statistical parameters were determined for the 10 min mean values and extreme values. Hereby, different reference periods of wind speed are used.

Parameters of the statistical distribution of 4-week extreme values were determined for each of the eight measurement heights. Due to the long measurement period and height resolution an analysis of

the extreme wind profile is possible. In guidelines such as [4.9] [4.7] [4.4], the reference wind speed is an important input parameter for the determination of the wind profile and wind loads in general. The GL [4.7] defines the reference wind speed as an extreme wind speed at hub height with a return period of 50 years. This wind speed is equivalent to the 98 %-quantile for a period of one year, cf. eq. (4.3).

$$1 - \frac{1}{50 \text{ years}} = 0.98 \quad (4.3)$$

Within these investigations, the distribution function  $F_u(x)$  was determined for a Gumbel distribution (extreme-value distribution type 1 for maximum values), see eq. (4.4).

$$F_u(x) = \exp\{-\exp[-a \cdot (x - u)]\} \quad (4.4)$$

The parameters of the distribution are:

$$a = \frac{\pi}{\sqrt{6} \cdot \sigma_{Ext}} \quad (4.5)$$

$$u = m - \frac{0.577216}{a} \quad (4.6)$$

with mean value  $m$  and standard deviation  $\sigma_{Ext}$  of the chosen distribution.

For the Gumbel distribution  $F_{Extr}$  of a parameter  $x$ , the shape of the distribution function is independent of the reference period because the standard deviation is constant also for different periods. A modified reference period leads to a parallel shift of the distribution function  $F_{Extr,N}$ , cf. eq. (4.7) – (4.9). Every year  $N = 13$  4-week extreme-values are available.

$$\begin{aligned} F_{Extr,N}(x_N) &= [F_{Extr,1}(x_{4-week})]^N \\ &= \exp\{-\exp[-a \cdot (x_{4-week} - u_{4-weeks}) + \ln(N)]\} \quad (4.7) \end{aligned}$$

$$\begin{aligned} &= \exp\{-\exp[-a \cdot (x_N - u_N)]\} \\ u_N &= u_{4-weeks} + \frac{\ln(N)}{a} \quad (4.8) \end{aligned}$$

$$= u_{4-weeks} + \ln(N) \frac{\sqrt{6}}{\pi} \cdot \sigma$$

$$m_N = m_{4-weeks} + \frac{\ln(N)}{a} \quad (4.9)$$

where  $u$  and  $a$  are the location parameter and the scale parameter of the Gumbel distribution, respectively. The characteristic value for a return period of 50 years can be calculated using eq. (4.7) with  $F_{Extr,N}(x) = 0.98$ . Alternatively, the determination of quantiles can be performed by using linear regression analysis. The results of both procedures agree very well.

Similar to the evaluation of wind speeds, also significant and extreme wave heights at the site of *FINO 1* measurement platform were investigated. For the observation period mentioned above, 30-min values of significant wave heights are available. 30-min values of extreme wave height are available for the period from January 2004 until mid-February 2006.

The analysis of wave data has shown that even 1-week extreme values of wave height can be described by a Gumbel distribution. 1-week extreme values were chosen to ensure a sufficient number of extreme values. According to the extrapolation of extreme values mentioned before, the characteristic wave height with a return period of 50 years was determined, see section 4.1.4.

Wave-induced loads depend on various parameters. Therefore, some assumptions have been made for the load simulations. First of all, static analyses were carried out. Therein increasing loads due to dynamic system response were not considered. Due to the stiffness of the jacket and its transparency to waves this approach is acceptable, cf. [4.37]. The connection between significant wave height  $H_S$  and maximum wave height  $H_{max}$  was assumed to eq. (4.10) according to valid guidelines, cf. [4.9] [4.7] [4.4]. The significant wave height is defined as four times the standard deviation of the

underlying wave spectrum, cf. e.g. [4.7]. This is roughly the mean value of the 1/3 highest waves.

$$H_{max} = 1.86 \cdot H_S \quad (4.10)$$

In addition to the wave height, the wave period  $T$  affects the wave load. In guidelines such as [4.9] [4.7] [4.4] a period range  $T$  depending on significant wave height  $H_S$  is proposed according to eq. (4.11),

$$11.1\sqrt{H_S/g} \leq T \leq 14.3\sqrt{H_S/g} \quad (4.11)$$

with gravitational acceleration  $g$ . Within this research project, the holistic investigation of the whole construction leads to some assumptions: For example, only the minimum wave period is considered. In case of static analysis, maximum loads are usually obtained with the minimum wave period as the lower bound of eq. (4.11). The simulations are to be performed with a stream function 11<sup>th</sup> order [4.17] whereby all wave heights and periods were covered, cf. [4.9] Figure C.1. The measured data from the *FINO 1* platform are only valid for this site with a local water depth of 28 m. For different water depth they have to be adapted. Thus, within performed probabilistic calculations at OC4 jacket for a planned water depth of 50 m these parameters were modified.

An procedure to adapt the significant wave height is given in the Shore Protection Manual [4.16]. Equations given there are used to predict sea conditions depending on wind speed, fetch length and wind duration. So-called fetch diagrams illustrate these parameters for deep- and shallow water. Deep- and shallow water are defined by the ratio of water depth  $d$  and wave length  $L$ :

$$\text{Deep water: } \frac{d}{L} \geq 0.5 \quad (4.12)$$

$$\text{Shallow water: } \frac{d}{L} < 0.5 \quad (4.13)$$

The prediction method for shallow water was considered because the adaption was carried out in the context of extreme-value considerations with wave length of more than 200 m, cf. eq. (4.14) – (4.16).

$$\frac{g \cdot H_{m0}}{U_A^2} = 0.283 \cdot \tanh \left[ 0.530 \cdot \left( \frac{g \cdot d}{U_A^2} \right)^{3/4} \right] \cdot \tanh \left\{ \frac{0.00565 \cdot \left( \frac{g \cdot F}{U_A^2} \right)}{\tanh \left[ 0.530 \cdot \left( \frac{g \cdot d}{U_A^2} \right) \right]} \right\} \quad (4.14)$$

$$\frac{g \cdot T_p}{U_A} = 7.540 \cdot \tanh \left[ 0.833 \cdot \left( \frac{g \cdot d}{U_A^2} \right)^{3/8} \right] \cdot \tanh \left\{ \frac{0.0379 \cdot \left( \frac{g \cdot F}{U_A^2} \right)^{1/3}}{\tanh \left[ 0.833 \cdot \left( \frac{g \cdot d}{U_A^2} \right)^{3/8} \right]} \right\} \quad (4.15)$$

$$\frac{g \cdot t}{U_A} = 5.370 \cdot 10^2 \cdot \left( \frac{g \cdot T_p}{U_A} \right)^{7/3} \quad (4.16)$$

with

- $H_{m0}$ : corresponds to  $H_S$ , cf. [4.16]
- $U_A$ : mean wind speed in the period  $t$  at 10 m height
- $F$ : fetch length
- $T_p$ : peak period
- $t$ : wind duration

The influence of water depth can be estimated assuming constant wind conditions, i.e. same wind speed and fetch length.

The extreme wind speed  $U_A$  of duration  $t$  is determined from *FINO 1* measurement data. The fetch length for the site of the *FINO 1* measurement platform lies in the range of 50 km up to 850 km [4.25] depending on wind direction. The variation of significant wave height for increasing water depth is shown in the following section “Results”.

To verify this very rough and location-independent estimation, significant wave heights in different water depths were evaluated at three sites in the German Bight. In addition to the measured values at *FINO 1*, data of *FINO 3* and *North-Sea-Buoy II (NSB 2)* were evaluated.

*FINO 3* was built 2009 in a water depth of 22 m about 80 km north-west of Sylt. *NSB 2* is located 150 km west of Sylt in 42 m water depth. The locations of the measurement sites are shown in Figure 4.3. The evaluation of *FINO 1* and *NSB 2* measurement data are based on a seven-year measurement period. For the evaluation of *FINO 3* data, only a measurement period of four years could be used. Therefore, these results are less reliable. The approximation of  $H_S$  in deeper water based on measurements analyzed at different sites is listed in section 4.1.4.

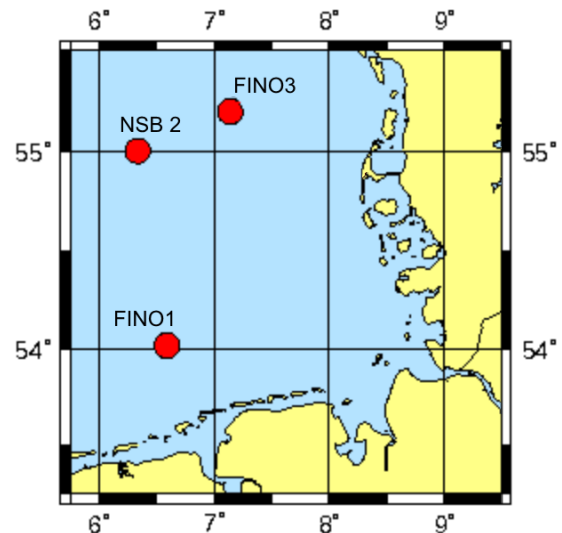


Figure 4.3: Locations of measurement platforms *FINO 1* and *FINO 3* and of the measurement buoy *NSB 2* (image adapted, [www.bsh.de](http://www.bsh.de))

In addition to scattering loads, the correlation between load parameters significantly influences the reliability of the OWT. For fatigue load simulations and structural analysis of various operating states conditional input parameter are taken from so-called scatter diagrams, cf. [4.13]. Though, the correlation of different

environmental parameters for frequently occurring events is considered.

Due to measurement periods of up to 10 years, there is a lack of measurement data for extreme events with return periods of 50 or 100 years. According to common regulations such as [4.7], these extreme single events shall be modeled conservatively unless a joint probability distribution does exist. In the past, there was often a lack of adequate data to determine joint probability distributions.

With the measurement data at the location of *FINO 1*, synchronously measured series of wind speed, wind direction, wave heights, wave periods and wave directions for a long measurement time are available. Based on a temporal assignment of these data, first investigations of simultaneously occurring extreme wind speed and significant wave heights have been carried out.

### **Resistance**

Until today, support structures of OWTs mostly consist of steel components. The tower is always designed as a steel tubular tower. Contrary to OWTs, onshore wind turbines can also be realized as e.g. pre-stressed concrete tower.

For OWTs with piled foundations, the substructures are almost exclusively steel structures. The piles are made of steel as well. Until today, the only solution for substructures made of concrete is the gravity-based foundation. Due to the great dead load and the great foot print, these substructures are stable without applying piles.

For the design, characteristic values of material properties are defined as a certain quantile of the underlying probability distribution. Compliance of these values has to be ensured by the manufacturers.

#### *Steel*

Main steel components of OWTs are the tower, the tubes used for the transition piece, and the foundation piles, which are either drilled or driven into the seabed. Depending on the importance of structural

member, type of load and stress level, it is differentiated between three component categories: secondary, primary, and special structural members. According to [4.7], secondary structural members are components of marginal importance to the support structure, such as stairs and mountings for cables. Whereas, primary and special structural members are of significant importance to operational safety and overall integrity of the structure. Special components are exposed to extraordinary conditions such as stress concentrations or multi-axial stresses due to the geometrical shape.

Beside the component definitions, the steel strength can be separated into normal steel strength with yield stress up to 285 N/mm<sup>2</sup>, higher strength steel with yield strength over 285 N/mm<sup>2</sup> up to 380 N/mm<sup>2</sup>, and high strength steels with a yield strength over 380 N/mm<sup>2</sup>. Due to fatigue resistance the yield strength should not exceed 355 N/mm<sup>2</sup>. Further information on appropriate steel materials concerning structural components are given in [4.7]. The type of distribution for yield strength and Young's modulus of steel is lognormal as recently stated in [4.39]. The values of stochastic parameters such as mean value and standard deviation depend on the chosen steel strength.

Usually, scattering of the fatigue resistance of steel can be described by a lognormal distribution [4.10]. For the semi-probabilistic fatigue design, the characteristic value of fatigue resistance is chosen on basis of the underlying probability distribution. For example, the characteristic value is defined as the 2.3%-quantile according to [4.5]. However, the characteristic value is defined differently in other standards.

#### *Concrete*

The scattering of the concrete compressive strength was determined in [4.33] with an almost constant standard deviation of about 5.0 N/mm<sup>2</sup>, which is approximately independent of the mean

compressive strength. However, because of more high-grade materials and manufacturing methods, today's results can be different from the previous knowledge. A distinction is made for different concrete strength classes in consideration of different production types. Statistic parameters for concrete elements out of job-mixed concrete at the building site, concrete from precast-concrete factories as well as precast-concrete units are given in e.g. [4.10].

Also, the distribution which is used in probabilistic analyses has to be described accurately. In literature, the Gaussian distribution is indicated as the best description of measurements for a parent population of concrete compressive cube strength. This distribution has to be converted into a lognormal distribution to avoid negative strength values.

#### *Soil*

Appropriate modeling of the soil properties is required for the embedding of piles in the soil. Within the work of WP 4, the results achieved in WP 3 "Soil" are used.

#### **Modelling**

The response of OWTs effected by loads due to wind, sea state and operation are calculated with numerical models. The probabilistic behavior of the action effects and resistances is evaluated on basis of the simulations.

#### *Modelling of support structures and soil*

Data of dimensions of OWTs, which are publicly available, are used to set up the models. The wind turbine as well as the tower is the NREL 5-MW turbine [4.20] which was used in the OC3 project [4.22] [4.21]. Within WP 4, monopile substructures and jacket substructures are investigated. The models for the substructures investigated are described in the following. Also, modeling of soil is important for an accurate estimation of the loads and resistances. The forces and moments acting on the OWT are transferred into the seabed by the

foundation piles. The load capacity of and the nonlinear properties of the soil layers as well as the induced loads are dependent on each other. In order to catch the scattering of both soil properties and of loads acting on the soil, the soil shall be modeled numerically.

#### *Modeling of loads*

In order to determine the loads acting on OWTs, the model of the OWT is set-up in suitable software. The FE software Poseidon [4.15] is used for the calculation of loads caused by sea states. Poseidon can be coupled with the software WaveLoads [4.26], which includes wave models to describe the kinematics of water particles. WaveLoads includes especially nonlinear wave models that consider the nonlinearity of Bernoulli's principle for modeling of kinematics of water particles, cf. [4.19]. Poseidon can also be coupled with Flex5, a widely-used software in wind industry. By applying the software Flex5, the loads induced by the operation of the wind turbine as well as the wind-induced loads acting on the RNA of the wind turbine are calculated.

#### **Modal and robustness analyses of the vibration behavior of an OWT with monopile substructure**

One investigation within work package 4 combined modal and robustness analyses of the vibration behavior of an OWT with monopile substructure. The monopile substructure is still the most common type of foundation for OWTs in the industrial sector, and was the first support structure investigated within WP 4 (cf. [4.29]-[4.31]). Modal and robustness analyses were carried out in order to predict the influence of various input parameters on the vibration behavior of the OWT. Considered input parameters are material properties, geometry of the structure and the composition of the soil layer. Soil-pile interactions were also implemented within the numerical models and presented at the 8th PhD Seminar on Wind Energy in Europe [4.18].

### Modeling

The numerical model of the OWT with monopile substructure consists of a tower with a two-split top mass of 240,000 kg for the rotor-nacelle assembly (RNA) and 110,000 kg for the rotor, as well as a monopile substructure including a soil-dependent foundation (see Figure 4.4). Within the modeling scope, a valid design basis was defined [4.29] and implemented in the finite-element software ANSYS® [4.11]. Geometrical data for the investigated wind turbine was taken from the NREL 5-MW Turbine definition [4.20]. The hub height above mean sea level (MSL) is 90.55 m, the water depth is modified to 28 m in order to fulfill the environmental conditions of the German North Sea at the location of the *FINO 1* measuring platform.

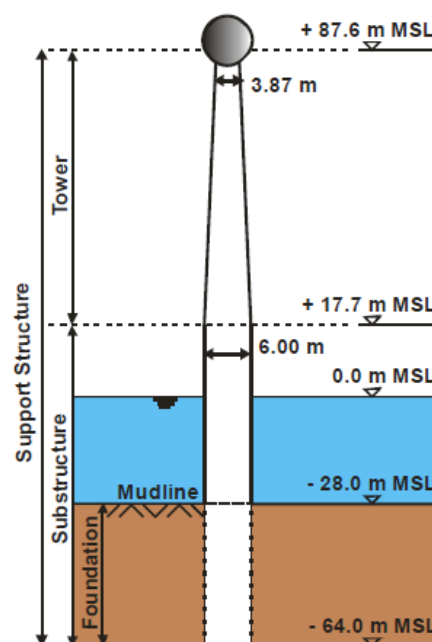


Figure 4.4: Investigated support structure of the OWT with monopile substructure [4.18]

Table 4.1: Statistical values of input parameters within robustness analysis for the vibration behaviour of the OWT with monopile substructure

Input Parameter	Symbol	Mean Value	Coefficient of Variation	Distribution Type
1a water depth Type 1	$L_{water}$	28 m	0.1	TruncNormal 24.0 – 32.0
1b water depth Type 2	$L_{water}$	28 m	0.04	Normal
1c water depth Type 3	$L_{water}$	28 m	0.08	Uniform 24.0 – 32.0
2 wall thickness tower top	$th_{TowTop}$	0.019 m	0.1	TruncNormal 0.0182 – 0.0198
3 wall thickness tower bottom	$th_{TowBot}$	0.027 m	0.1	TruncNormal 0.0269 – 0.0271
4 wall thickness monopile	$th_{Pile}$	0.060 m	0.1	TruncNormal 0.0587 – 0.0613
5 Young's modulus	$Mat_{Emod}$	$2.1 \cdot 10^{11}$ N/m <sup>2</sup>	0.02	LogNormal
6 Poisson's ratio	$Mat_{nu}$	0.3	0.03	LogNormal
7 specific density of steel	$Mat_{dens}$	8500 kg/m <sup>3</sup>	0.01	Normal
8 internal friction angle	$Soil_{phi}$	38°	0.15	LogNormal
9 relative density of sand	$Soil_{Dr}$	0.8	0.125	Normal
10 effective unit weigh	$Soil_{gamma}$	10 kN/m	0.1	Normal

Robustness analysis was used to predict the influence that each of the scattering input parameters has on the natural bending frequencies of the support structure of the OWT. Relevant geometry parameters and material properties were also taken into account with their statistical values as displayed in Table 4.1. The dataset for the material properties is taken from international reports dealing with probabilistic design of wind turbines and other steel constructions [4.39] [4.32]. The statistical data for the geometrical input variables like wall thickness and water depth are based on national standards [4.8] [4.3]. The statistical dependencies between these input parameters and the natural bending frequencies of the support structure (as output quantities) are carried out using the optimizing structural language optiSLang® [4.28]. The data for this robustness analysis are obtained from Latin hypercube sampling generating  $N = 1000$  samples.

Soil-pile interactions of the foundation were modelled with spring and damper elements. The spring stiffness depending on the soil layer is calculated with a software tool developed at the Institute for Geotechnical Engineering (Leibniz Universität Hannover). Therein,  $p$ - $y$  curves for sand under cyclic loading conditions are implemented as defined by the American Petroleum Institute [4.1]. The soil is modelled as displayed in Figure 4.4, consisting of a single sand layer for the whole embedment depth. The determination of the linear initial stiffness within the  $p$ - $y$  model is based on the effective unit weight  $\gamma'$ , the angle of internal friction  $\varphi'$  and the relative density  $D_r$  of the sand, as well as on the diameter of the monopile and the local soil depth. The dataset for the soil parameters, shown in Table 4.1, was attuned with WP 3.

The first and second natural bending frequencies (in side-to-side as well as in fore-and-aft mode) of the support structure are shown in Table 4.2. In

contrast to the investigations within the OC3 project [4.21], a water depth of 28 m is set (instead of 20 m within the OC3 project). Also, the foundation is slightly different; only one instead of three different soil layers is considered.

*Table 4.2: Natural bending frequencies of the support structure (in Hz) compared to the results in [4.21]*

mode	PSB-OWEA	OC 3 [4.21]
1 <sup>st</sup> fore-and-aft	0.24	0.25
1 <sup>st</sup> side-to-side	0.24	0.25
2 <sup>nd</sup> fore-and-aft	1.42	1.58
2 <sup>nd</sup> side-to-side	1.39	1.65

#### *Probabilistic approach*

In stochastic analysis, the sample sizes as well as the statistical values of the input parameters have to be chosen very carefully. To explicate this, three analyses are carried out with different types of distributions for the water depth ( $L_{water}$ ) in the numerical model of the OWT with monopile substructure (see Table 4.1 a-c). In the first investigation (a), the values of  $L_{water}$  are generated by a truncated normal distribution with a mean value of 28 m (water depth at *FINO 1*) and a coefficient of variation (COV) of 0.1, whereby only values in the interval of 24.0 m to 32.0 m below mean sea level are set, see Figure 4.5. The displayed bars in this plot are fitted by a partial density function (PDF).

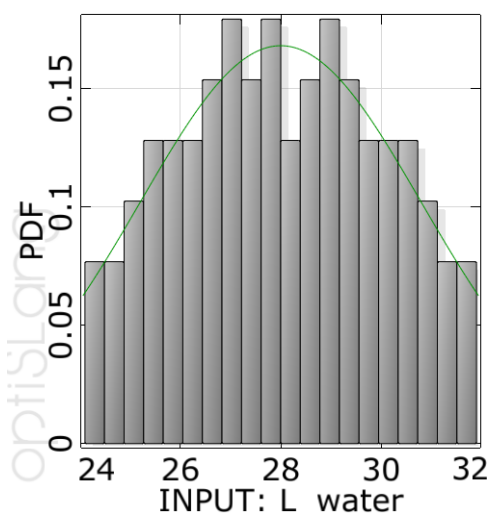


Figure 4.5: Histogram of input variable water depth (1a,  $L\_water$ ), modelled as truncated normal distribution with COV of 0.1

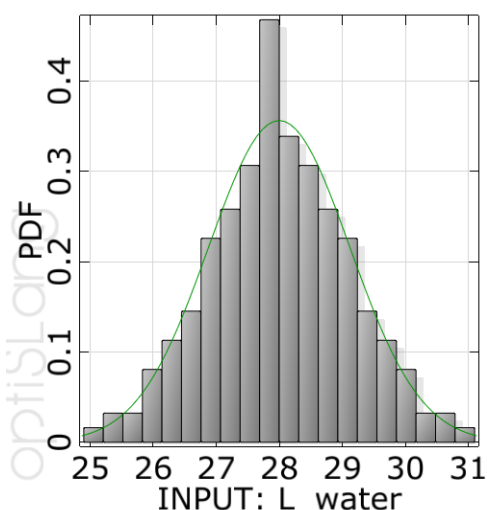


Figure 4.6: Histogram of input variable water depth (1b,  $L\_water$ ), modelled as a simple normal distribution with COV of 0.04

In a second analysis (b), a simple normal distribution with a COV of 0.04 is set to obtain the values of input parameter  $L\_water$  (see Table 4.1, parameter 1b). In such a way, at least over 99.8% of the random values of  $L\_water$  within the robustness analysis are in the interval of 24.0 m to 32.0 m below mean see level, see Figure 4.6. To illustrate the dependence of the chosen distribution type for the scattering input parameters with respect to the changes to the outcomes, a third analysis is carried out, in which the values for the water depth

are generated by a uniform distribution with realizations between 24.0 m and 32.0 m (see Table 4.1, input parameter 1c).

In order to predict the intensity of influence which each input parameter  $X_i$  has on the natural bending frequencies of the support structure (output variables  $Y_j$ ), various tools of multivariate statistics are used. Possible sensitivities between the quantities can be indicated with the linear correlation coefficient  $\rho_{X_i Y_j}$  (also called Pearson correlation coefficient, short PCC),

$$\rho_{X_i Y_j} = \frac{\sum_{k=1}^N (x_{ik} - \mu_{X_i})(y_{jk} - \mu_{Y_j})}{\sigma_{X_i} \sigma_{Y_j}} \quad (4.17)$$

Therein,  $x_{ik}$  stands for the  $N$  realizations of input variable  $X_i$ ,  $1 \leq k \leq N$  with sample size  $N$ ,  $\mu_{X_i}$  is the mean value and  $\sigma_{X_i}$  the standard deviation. The quantities of the output variables  $Y_j$  are denoted analogously. The PCC  $\rho_{X_i Y_j}$  measures the strength of a linear relationship between  $X_i$  and  $Y_j$ . A value for  $\rho_{X_i Y_j}$  near  $\pm 1$  indicates a strong positive or negative linear correlation. A value close to zero does not permit any statement about linear relations; random correlations of higher order between two variables or even no correlations at all might be possible. The coefficients according to eq. (4.17) could be collected in a matrix scheme, which delivers a comprehensive overview of all linear correlations within the numerical model, see Figure 4.7. Here, significant linear dependencies of input variable 1 (water depth) or 8 (internal friction angle) on the four output variables 11-14 (natural bending frequencies, c.f. Table 4.2) are detected, as can be seen by the blue and yellow squares in the matrix.

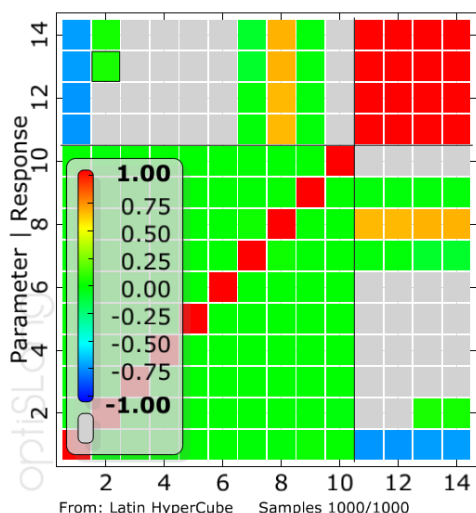


Figure 4.7: Linear correlation matrix including the input variables 1-10 of Table 4.1a and the four output variables 11-14 according to Table 4.3

The percentage of variability due to the influence of a model parameter is indicated with the coefficient of determination (COD),

$$R_{Y_j}^2 = 1 - \frac{\sum_{k=1}^N (y_{jk} - \hat{y}_{jk})^2}{\sum_{k=1}^N (y_{jk} - \mu_{Y_j})^2} \quad (4.18)$$

Therein,  $\hat{y}_{jk} = \hat{y}_j(x_{ik})$  are fitted values of a linear regression towards the realizations  $y_{jk}$ , e.g. described by minimal residuals of a least squares problem [4.18] [4.28]. So, the COD characterizes how much of the variability in the fitted value  $\hat{y}_{jk} = \hat{y}_j(x_{ik})$  can be explained by a linear relation to the input parameters  $x_{ik}$ . A value of  $R^2$  near one indicates a high linear relation, i.e. the linear regression  $\hat{y}_{jk}$  fits the data of realizations  $y_{jk}$  better than in comparison to the simple average  $\mu_{Y_j}$ .

**Ultimate limit state (ULS): axial load bearing capacity of foundation piles**

The axial load bearing capacity of the piles is one design driver for foundation piles subjected to predominant axial loads, as they are found for lattice structures, such as jackets and tripods.

In cooperation with WP 3 "Soil", the probabilistic design of foundation piles

regarding the axial load bearing capacity is carried out. Results are already published in [4.24].

The design of the ultimate limit state (ULS) is carried out for a storm event. For the semi-probabilistic design, a storm event with a recurrence period of 50 years (the so-called 50-years storm) is defined in DLC 6.1 [4.9]. Here, it is assumed that the 50-years sea state and the 50-years wind conditions occur simultaneously. The characteristic values to describe the environmental conditions with a recurrence period of 50 years are given as the 98 %-quantile of the corresponding probability distribution with a recurrence period of one year, see eq. (4.3). A rough description of the DLCs 6.1 for wind and wave is listed in Table 4.4.

Table 4.3: Input parameters for wind and sea state within DLC 6.1 [4.9]

DLC	wind model	wave model
6.1a	50-years wind, turbulent	50-years sea state
6.1b	50-years wind, stationary	reduced 50-years design wave
6.1c	reduced 50-years wind, stationary	50-years design wave

DLC 6.1a covers a transient fully-coupled simulation of the OWT during a 50-years storm. The OWT is effected by a sea state and a turbulent wind field, which are generated numerically. The time series of actions can be assumed to be stochastically distributed. Due to the fact that the numerical simulation of the sea state does not cover the nonlinearity of Bernoulli's principle [4.19], the effect of this nonlinearity has to be considered for the further evaluation. Suitable methods are indicated in e.g. [4.9] [4.37].

Even though DLCs 6.1b and 6.1c are known to be more conservative compared to the fully-coupled simulation of a 50-years as required by DLC 6.1a, those load cases are highly suitable to underline the general methods of probabilistic design in

ULS. Within DLCs 6.1b and 6.1c, different load combinations of a single wave and a steady wind field are considered for quasi-static simulations. The dynamic amplification due to wind turbulence and sea state has to be considered for the further evaluation of the quasi-static numerical solution by applying appropriate methods. The studies concerning the ULS concentrate mainly on the DLCs 6.1b and 6.1c.

#### Modeling

The jacket substructure, which is shown in Figure 4.8 and is considered within WP 4, was defined within the OC4 project [4.41]. This jacket is designed for a site at the North Sea with a local water depth of 50 m. Compared to jacket substructures already built, the foot print of 12x12 m is comparatively small. It is connected to the seabed by foundation piles, whose dimensions are also given in [4.41].

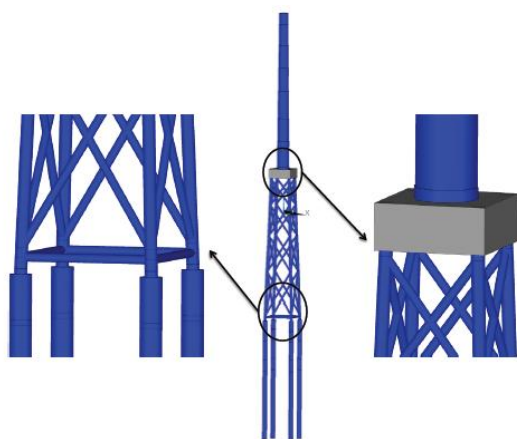


Figure 4.8: OC4 jacket (middle), foundation piles (left) and transition piece (right) [4.41]

For predominant axially-loaded foundation piles, simplified models of the embedded piles are used. Here, two possibilities of embedment are considered. On one hand, the piles are modeled to be hinged as shown in Figure 4.9 (b). Using this approach, loadings on the structure do not result in moments (by bending and torsion). Subsequently, axial forces acting on the piles are overestimated. On the other hand, the embedded piles are mod-

eled as clamped (Figure 4.9 (c)). This approach, which describes embedded piles more realistically, eventually results in underestimated forces acting on the pile.

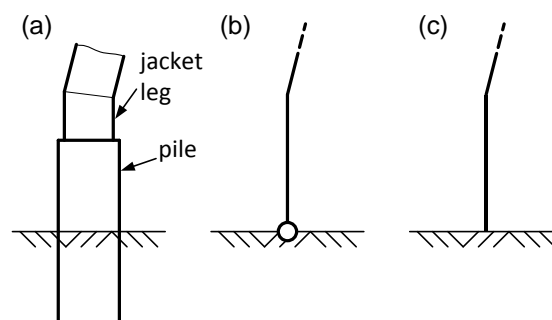


Figure 4.9: (a) Foundation in soil, (b) modeled as hinged bearing, (c) modeled as clamped bearing

The realistic values for the axial forces at the pile's head lie within the range of the values which are determined by using clamped and hinged bearings.

#### Probabilistic approach

In order to determine the probability that the axial load capacity of the foundation piles is exceeded by the acting axial forces, eq. (4.2) has to be solved. Therefore, the underlying distribution functions of action effects and resistance have to be determined.

The probabilistic distribution of the action effects is given on basis of the underlying extreme-value distributions for the environmental conditions during a 1-year storm. Only the parameters of wind speed and significant wave height are considered, since they are most dominant for the design. For each possible value of these scattering parameters, the resulting axial forces acting on the foundation piles are calculated with numerical simulations. On basis of the distributions describing the 1-year storm and the associated values of axial forces, the probabilistic distributions of the action effects can be found.

Probabilistic models to describe the soil resistance that are developed in WP 3 "Soil" are applied.

### Probabilistic fatigue design exemplified on tubular joints of jackets

For branched components in offshore substructures such as jackets and tripods, fatigue has to be considered. Due to their complex geometry, the joints are highly stressed by fatigue loads caused by wind, operation and sea state during the life time.

The probabilistic fatigue design for the tubular joints of tripod substructures are already carried out in [4.40]. Here, the focal point is set on the modeling fatigue resistance and its scatter.

Within the semi-probabilistic design according to [4.9], a limited number of simulations with a duration of 10 minutes has to be carried out for each wind-speed occurring during life time combined with the associated sea state. The resulting time series of stresses occurring at specified locations are transferred to stress ranges  $\Delta\sigma$ , which are put in bin classes. Based on the achieved histogram, the fatigue damage is calculated by applying the Palmgren-Miner rule,

$$D = \sum_i \frac{n_i}{N_i} \quad (4.19)$$

where  $n_i$  is the number of cycles associated with the stress range  $\Delta\sigma_i$  and  $N_i$  is the endurance (in cycles) for a stress range  $\Delta\sigma_i$ , where  $n = \sum n_i$  is the number of all stress ranges considered.

For the probabilistic design, the stress ranges are not put in bin classes  $\Delta\sigma_i$ , but the probabilistic distribution of the stress ranges  $p(\Delta\sigma)$  is taken into account,

$$D = \int \frac{n \cdot p(\Delta\sigma)}{N(\Delta\sigma)} d\Delta\sigma \quad (4.20)$$

The dynamic response of an OWT with jacket substructure is simulated numerically. The distribution of the stress ranges is given by stochastic analysis of the determined stress ranges  $\Delta\sigma$  within the simulated time series. The stochastic description of the very high stresses,

which occur with a very low percentage, is quite complicated, since usually only few of these values exist. However, the stochastic description is important since it is assumed that especially very high stresses are decisive for the fatigue design. For example, the peak-over-threshold method can be applied to describe the distribution of the very high stress ranges.

In order to estimate the distribution of the fatigue loads and especially of the very high stress ranges appropriately and accurately, at least 50 time series with a minimum duration of 30 minutes for each wind speed are required. Compared to the semi-probabilistic design, high numerical effort is necessary for the probabilistic fatigue design.

Detailed results on the probabilistic fatigue design of joints in jacket structures are to be published in [4.23].

## 4.4.4 Results

### Wind loads

The 10-min averages of wind speed are well described by a Rayleigh distribution, cf. [4.7] and Figure 4.10.

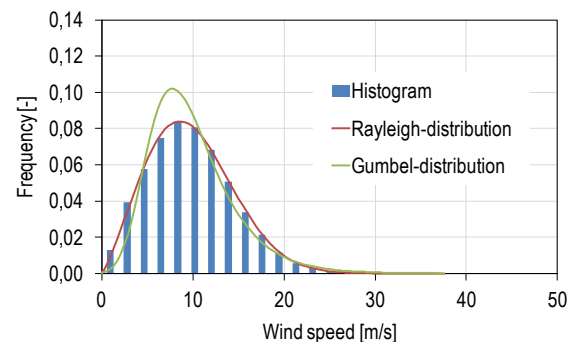


Figure 4.10: Histogram and different distribution functions of 10-min mean values for the wind speed in 100 m above sea level

The extreme wind speed better could be approximated by a Gumbel distribution, cf. Figure 4.11. In addition to adapt the chosen distribution by visual assessment of fitting, this result is confirmed by the Chi-squared test and the Kolmogorov-Smirnov test.

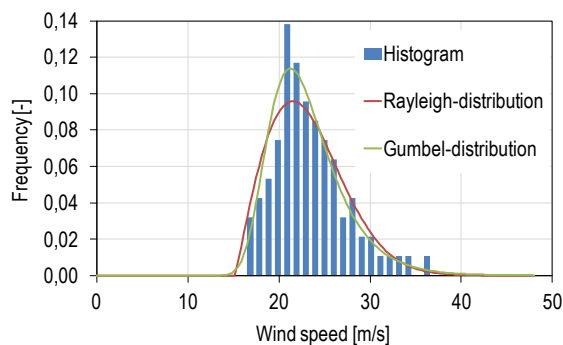


Figure 4.11: Histogram and different distribution functions of 4-week extreme values for the wind speed in 100 m above sea level

Based on *FINO 1* data within the period 2004/01/01 – 2011/01/01 and eq. (4.5) – (4.8), the statistical values of the annual extreme-value distribution of wind speed in different measurement heights were determined, cf. Table 4.5 and [4.12].

Table 4.4: Statistical values (mean  $m_{Ext}$  and standard deviation  $\sigma_{Ext}$ ) of the one-year extreme-value distribution of wind speed in different measurement heights at the site of *FINO 1*

Measurement height	$m_{Ext}$ [m/s]	$\sigma_{Ext}$ [m/s]	a [s/m]	u [m/s]
33 m	28.140	3.869	0.332	26.398
40 m	28.384	3.845	0.334	26.654
50 m	29.026	3.971	0.323	27.238
60 m	29.824	4.070	0.315	27.992
70 m	30.343	4.137	0.310	28.481
80 m	30.630	4.164	0.308	28.756
90 m	30.937	4.169	0.308	29.061
100 m	31.368	4.123	0.311	29.513

Therein, 4-week extreme values were considered. The 98 %-quantile for a period of one year corresponds to the characteristic value for a return period of 50 years, cf. eq. (4.3). The resulting values of the 50-years wind speed  $V_{50}$  are listed in Table 4.5.

Table 4.5: Extreme wind speed  $V_{50}$  in different heights at the site of *FINO 1*

Measurement height	$F_u^{-1}(0, 98)$ [m/s]
33 m	38.17
40 m	38.35
50 m	39.32
60 m	40.37
70 m	41.07
80 m	41.42
90 m	41.74
100 m	42.06

The statistical values were determined using the method of moments. With the method of linear regression, the same ingoing data were analyzed, too. These results of both evaluation methods agree very well [4.12].

The profile of wind speed with a return period of 50 years is depicted in Figure 4.12. By comparison of the measured wind profile with the approach of [4.7], an underestimation of wind speeds for the *FINO 1* measurement platform could be recognized. For the reference speed at hub height (in this case 100 m) the reference speed extrapolated from the measurement data was used.

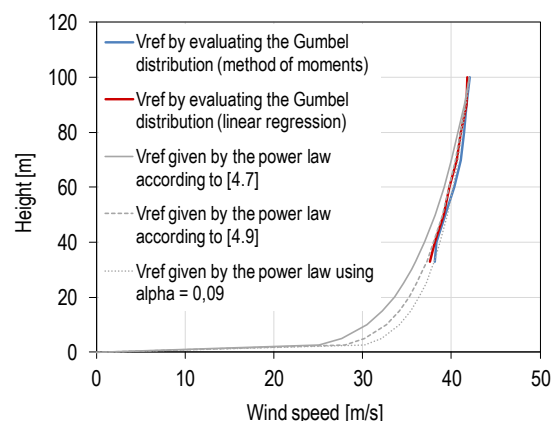
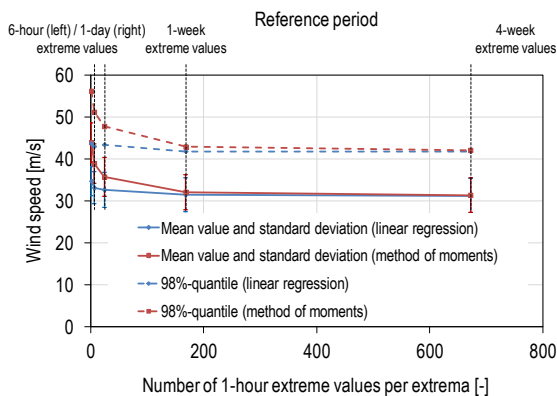


Figure 4.12: Profile of the 50-years wind speed  $V_{ref}$  from measurements compared to the approach of [4.9] and [4.7] (method for determining the distribution parameters in brackets)

In Figure 4.11, an example of the exponential function according to [4.7] with a lower exponent is shown, too. This approach represents the analyzed wind speeds for 33 m to 100 m height much better. This nearly vertical run of the evaluated curves describes wind speeds within the heights between 33 m and 100 m and is comparable to approaches in the standards. For wind speeds below 33 m and above 100 m, measurement data are not available. Further investigations of wind conditions at the site of *FINO 1* are listed in WP 2 and [4.12].

For the statistical analysis of extreme values in particular areas far away from the mean value like the tails of an analyzed distribution are important. The type of distribution depends on the kind of population and often differs from extreme values of the same population, cf. Figure 4.10 and Figure 4.11. Extreme values of a longer reference period (here: 4-week extreme values) are more suitable for extrapolation to an annual extreme-value distribution, see Figure 4.13.



**Figure 4.13: Mean values, standard deviations and 98 %-quantiles of the annual extreme-value distribution based on 6-hour up to 4-week extreme values (method for determining the distribution parameters in brackets)**

For longer reference periods the mean values and the quantiles both run asymptotically to a limit value. As well the results determined by linear regression and method of moments agree very well if

the reference period is sufficiently long. This result confirms the assumption that extreme values of a short reference period are less suitable as extrapolation basis for annual extreme-value distributions. Using 1-week or 4-week extreme values as extrapolation basis leads to almost identical results.

**Wave loads**

The significant wave height is an important input parameter for wave simulations. Common guidelines propose the Rayleigh distribution or Weibull distribution to approximate the distribution of significant wave height.

An even higher goodness of fit has been achieved by a Gumbel distribution at the observed measurement site of *FINO 1*, cf. Figure 4.14.

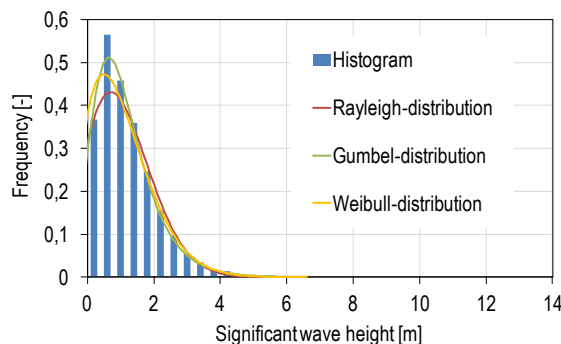


**Figure 4.14: Histogram and different distribution functions of 3-hour average values for the significant wave height**

The extreme values of significant wave height are also well described by a *Gumbel* distribution, cf. Figure 4.15. In addition to a visual assessment of the goodness of fit, this result is confirmed by the Chi-square test and Kolmogorov-Smirnov goodness of fit test.

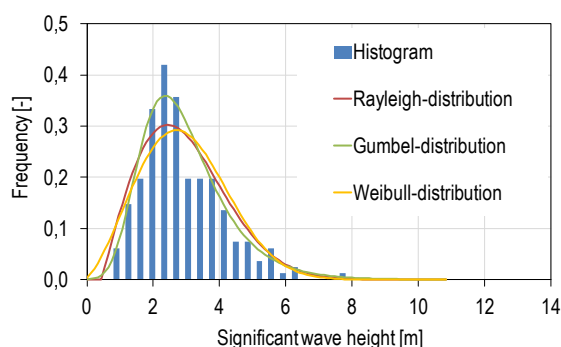


Figure 4.15: Histogram of 1-week extreme values of the significant wave height and different distribution functions

Therefore, the *Gumbel* distribution was used for extreme values of significant wave heights, too. Using the methods listed in the previous subsection "Wind loads", the annual extreme-value distribution of significant wave height was determined based on 6-hour up to 4-week extreme values, cf. Table 4.6.

Table 4.6: Statistical values (mean  $m_{Ext}$  and standard deviation  $\sigma_{Ext}$ ) of the one-year extreme-value distribution of significant wave height at the site of FINO 1

Extrema	$m_{Ext}$ [m]	$\sigma_{Ext}$ [m]	$a$ [m <sup>-1</sup> ]	$u$ [m]
6-hour	7.044	0.969	1.324	6.608
1-day	7.052	1.115	1.150	6.550
1-week	7.091	1.311	0.979	6.501
4-week	7.056	1.361	0.942	6.443

The resulting significant wave height  $H_{s50}$ , based on different extrema, is listed in Table 4.7.

Table 4.7: Extreme significant wave height  $H_{s50}$  extrapolated on the basis of annual extreme-value distribution

Extrema	$F_u^{-1}(0, 98)$ [m]
6-hour	9.56
1-day	9.94
1-week	10.49
4-week	10.58

The statistical values were determined using the method of moments and linear regression. The results of both evaluation methods agree very well [4.14].

The results apply to a water depth of 28 m. Using the eq. (4.14) – (4.16), significant wave heights depending on the water depth and the fetch length were estimated. The resulting significant wave height (here:  $H_{m0}$ ) for an increase of water depth from 28 m to 50 m depending on fetch length is pictured in Figure 4.16.

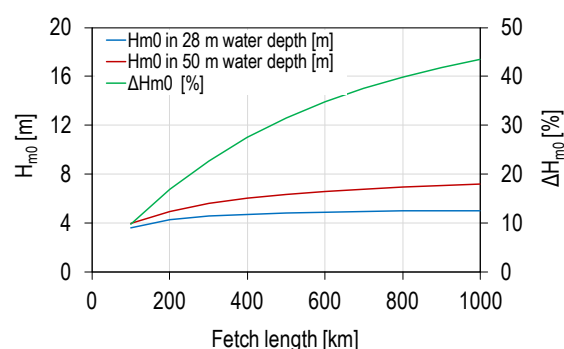


Figure 4.16: Significant wave height  $H_{m0}$  and percentage change of  $H_{m0}$  for the increase of water depth from 28 m to 50 m depending on fetch length

A clear influence of fetch length on the significant wave height was determined. For larger fetch length the wave height barely changes. This decreasing variation of the wave height is also observed for a water depth of 50 m. Compared with the significant wave height  $H_{m0}$  in 28 m water depth the almost constant significant wave height  $H_{m0}$  in a depth of 50 m only occurs with greater fetch length. Consequently, the percentage change of wave heights from 28 m to 50 m water depth increases with the growth of fetch length, until a limit-value is reached for great fetch lengths. If this critical fetch length has been achieved, a constant increase of the significant wave height is expected at the pictured change of the water depth. The reason for the limited increase in wave height  $H_{m0}$  is the wave height limit due to the water depth. By using Figure 4.16, the mean value of significant wave height at the site of FINO

1 can be adapted to a site with 50 m water depth. To verify this very coarse and location-independent estimation, significant wave heights in different water depths were evaluated at three sites in the German Bight. In addition to the measured values at *FINO1*, data of *FINO 3* and *North-Sea-Buoy II (NSB 2)* were evaluated. The methods for data analysis have already been discussed. Actually, the results are focused.

The probability density functions obtained for each site of 1-week extreme values of  $H_S$  are shown in Figure 4.17.

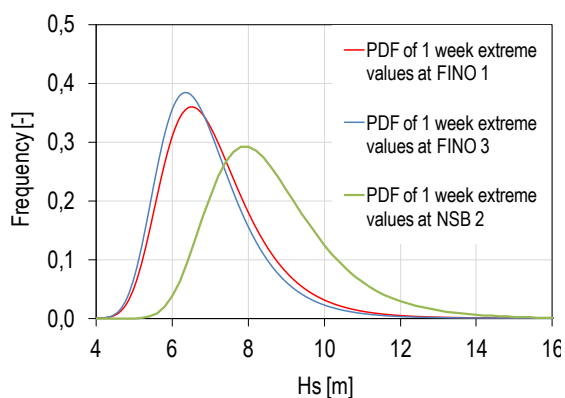


Figure 4.17: Probability density function of 1-week extreme values at three different measurement sites in the German bight

The extreme values of each measurement site can be well approximated by Gumbel distribution. Mean values as well as standard deviations of the significant wave height  $H_S$  increases with deeper water. The comparison of the statistical values is shown in Table 4.8.

Table 4.8: Statistical values (mean  $m_{Ext}$  and standard deviation  $\sigma_{Ext}$ ) of the one-year extreme-value distribution of  $H_S$  at the site of *FINO 1*, *FINO 3* and *NSB 2*

	water dept h	parameter	distribution	$m_{Ext}$ [m]	$\sigma_{Ext}$ [m]
<i>FINO3</i>	22	$H_S$	Gumbel	6.893	1.227
<i>FINO1</i>	28	$H_S$	Gumbel	7.091	1.311
<i>NSB 2</i>	42	$H_S$	Gumbel	8.633	1.611

Based on these data the statistical values of the significant wave height  $H_S$  in 50 m water depth were approximated. It should be noted for the following analyses that an extrapolation based on three values is very uncertain. Assuming a linear relationship, a mean value of the significant wave height of 9.22 m can be expected in 50 m water depth. Thus, with an increase of water depth from 28 m to 50 m the significant wave height rises about 30 %. The standard deviation of the significant wave height increases by almost the same factor as the mean value, meaning the coefficient of variation is nearly constant over the water depth, c.f. Figure 4.18.

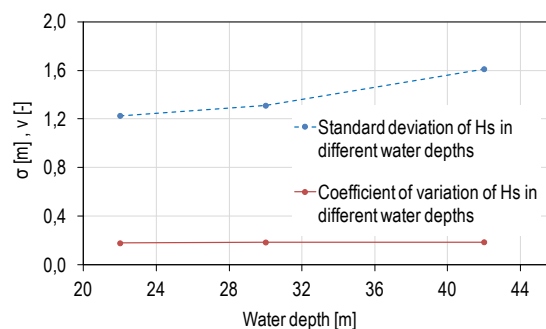


Figure 4.18: Standard deviation and coefficient of variation of  $H_S$  in different water depths

Furthermore, the maximum wave height was investigated, too. Current regulations propose the Rayleigh or Weibull distribution for the modeling of extreme wave heights, cf. [4.7] [4.6]. For the evaluated data on the location of the measurement platform *FINO 1*, the Gumbel distribution fits measurement data much better. Figure 4.19 shows the histogram of the 1-week extreme values of  $H_{max}$  and different extreme-value distributions.

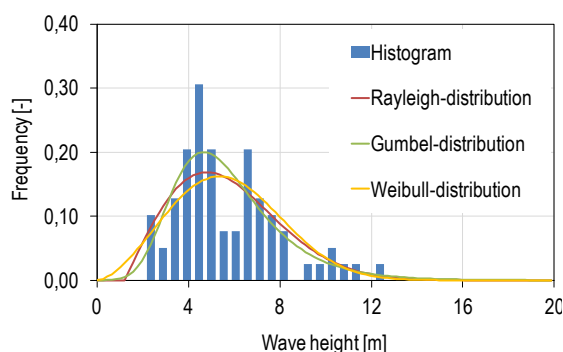


Figure 4.19: Histogram of 1-week extreme values of the maximum wave height and different distribution functions

Due to the small number of measurement values, a visual assessment of a suitable distribution function became more difficult. The goodness of fit is confirmed by the Chi-square test and Kolmogorov-Smirnov test, too. The annual extreme-value distribution of maximum wave height was determined based on 6-hour up to 4-week extreme values, cf. Table 4.9. The resulting maximum wave height  $H_{50}$  based on different extrema is listed in Table 4.10.

Table 4.9: Statistical values (mean  $m_{Ext}$  and standard deviation  $\sigma_{Ext}$ ) of the one-year extreme-value distribution of maximum wave height at the site of FINO 1

Extrema	$m_{Ext}$ [m]	$\sigma_{Ext}$ [m]	$a$ [m <sup>-1</sup> ]	$u$ [m]
6-hour	12.622	1.726	0.743	11.846
1-day	12.734	2.007	0.639	11.830
1-week	12.940	2.341	0.548	11.886
4-week	12.989	2.465	0.520	11.880

Table 4.10: Maximum wave height  $H_{50}$  extrapolated on the basis of annual extreme-value distribution

Extrema	$F_u^{-1}(0,98)$ [m]
6-hour	17.10
1-day	17.94
1-week	19.01
4-week	19.38

The statistical values were determined using the method of moments and linear regression. The results of both methods agree very well [4.13].

The determined significant and maximum wave height with a return period of 50 years confirmed the formal relation in [4.7] for the estimation of the design wave height  $H_D$  within a sea state defined by inter alia the significant wave height. In [4.7], the design wave height  $H_D$  can be estimated as being the expected value of the highest wave during a 3-hour storm ( $T_{ref} = 10\,800\text{ s}$ ), cf eq. (4.21).

$$H_D = H_{50} = H_{s50} \cdot \sqrt{0.5 \cdot \ln(T_{ref}/T_D)} \quad (4.21)$$

According to [4.7] the design wave period  $T_D$  may be estimated by eq. (4.22).

$$11.1\sqrt{H_{s50}/g} \leq T_D \leq 14.3\sqrt{H_{s50}/g} \quad (4.22)$$

According to [4.7], the smaller value of the period  $T_D$  should be chosen because a larger wave height  $H_D$  results. Using the significant wave height  $H_{s50} = 10.6\text{ m}$ , cf. Table 4.7, the design wave height according to eq. (4.21) and (4.22) can be calculated to  $H_D = 19.2\text{ m}$ . This result agrees well with the maximum wave height  $H_{50}$ , extrapolated on the basis of the annual extreme-value distribution, cf. Table 4.10.

Contrary to the measurement time series of significant wave height and wind speed, the measurement time series of extreme wave height only from 2004 to February 2006. In this short measurement period, only 18 4-week extreme values are available for determining the density function. The determination of a density function based on such a small amount of data is very unreliable and may lead to significant differences in particular for the 98 %-quantiles, see Figure 4.20.

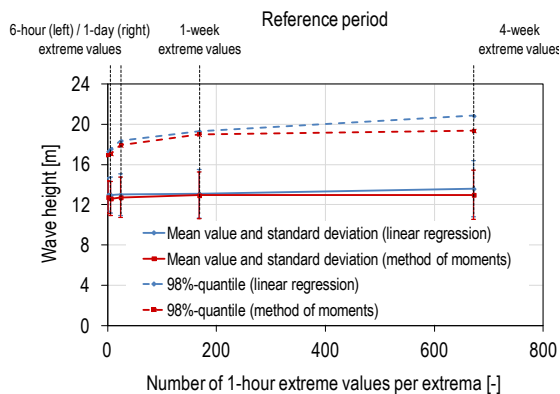


**Figure 4.20: Mean values, standard deviation and 98 % -quantiles of the annual extreme-value distribution based on 6-hour up to 4-week extreme values, cf. [4.35] (method for determining the distribution parameters in brackets)**

In case of these less quantity of data, the results based on the 1-week extreme-value distribution are more reliable. These data were the basis for the analysis of extreme wave height, too. On one hand, there is the demand for a long reference period as extrapolation basis. On the other hand, there is a limited number of measurement data. If a Gumbel distribution will be used, it is suggested to use at least 50 measurement values. Taking this minimum number of measurement values into account, extreme values of a long reference period is more suitable for extrapolation basis.

With the measurements at the location of *FINO 1*, synchronously measured series of wind speed, wind direction, wave heights, wave periods and wave directions for a long measurement time are available. Based on a temporal assignment of these data, first investigations of simultaneously occurring extreme wind speed and significant wave heights have been carried out. The investigations show that extreme wind events do not coincide with the extreme sea conditions. For extreme wind speed as well as significant wave height direction dependencies could be detected, cf. Figure 4.21 and Figure 4.22.

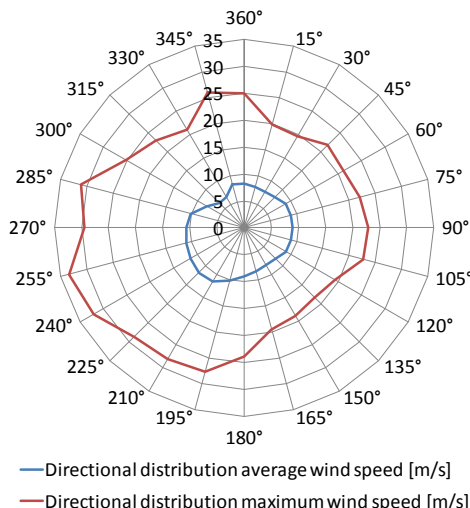


**Figure 4.21: Directional distribution of average and maximum wind speed at the FINO 1 platform**

The highest average and maximum wind speed is expected from the direction west-south-west.

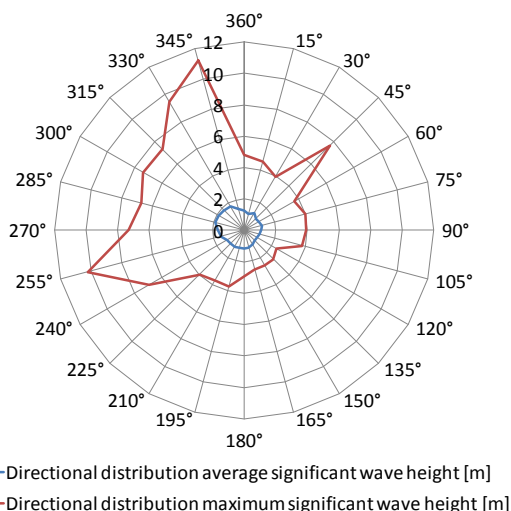


**Figure 4.22: Directional distribution of average and maximum significant wave height at the FINO 1 platform**

The direction of the maximum significant wave height has an offset to this direction of almost 90°. The maximum significant wave height is expected from north-north-west. A simultaneous occurrence of extreme wind speeds and significant wave heights with a direction offset of 90° could be excluded by the measurement data. These preliminary studies demonstrate that a simple superposition of rectified

extreme wind speeds and sea states is unrealistic and leads to inefficient design results.

A comprehensive safety assessment of OWTs needs further investigations of the correlation and directional dependency of extreme load parameters.

### Modal and robustness analyses of the vibration behavior of an OWT with monopile substructure

For the investigated support structure as shown in Figure 4.4, robustness analyses were carried out in order to predict the fluctuation in the eigenfrequencies under scattering model input parameters. As can be seen from the top line of Figure 4.23, the linear COD of the first natural bending frequency in side-to-side mode ( $fr1\_side$ ) with respect to all input parameters amounts to  $R^2 = 0.90$ . So, 90 % of the total fluctuation in this frequency can be explained by a linear relation between the input parameters. The remaining 10 % of the total variation in this frequency remain unexplained by a linear regression within this model. The bars in Figure 4.23 show pairwise linear correlations between the output parameter ( $fr1\_side$ ) and each of the input parameters  $X_i$ . Thereby, the influence of the water depth ( $L\_water$ ) seems to be most dominant. Also, the internal friction angle of the soil layer ( $Soil\_phi$ ) has a significant impact.

The fluctuation in the first natural bending frequency in side-to-side mode ( $fr1\_side$ ) within this robustness analysis as shown

in Figure 4.24. As can be seen by the fitted PDF, the variation in this frequency is characterized by a normal distribution with a mean value of 0.235 Hz and a COV of 0.025. The results of the other natural bending frequencies of the investigated support structure are quite similar. Table 4.2 summarizes the statistical values of the calculated frequencies. For example, Figure 4.25 shows the CODs of the input parameters  $X_i$  towards the second natural bending frequency in fore-and-aft mode ( $fr2\_for$ ). Figure 4.26 displays the variation in this frequency. Again, the dataset is fitted by a normal distributed PDF with a mean value of 1.38 Hz and a COV of 0.046.

To illustrate the high importance of a well known statistical dataset for the use of robustness analysis, two further investigations are carried out as described before. In a second robustness analysis, the statistical properties of water depth ( $L\_water$ ) are adapted to a normal distribution as shown in Figure 4.6 with values as listed in Table 4.1 (input parameter 1b). Again,  $N=1000$  designs are created by Latin Hypercube Sampling. The results for the first natural bending frequency in side-to-side mode and the second one in fore-and-aft mode are shown in Figure 4.27 – Figure 4.30. Again, the only two significant input parameters within the numerical model of the investigated support structure are the internal friction angle  $\varphi'$  of the soil layer and the water depth  $L\_water$ . In

Table 4.11: Statistical values of first and second natural bending frequencies of the support structure (shown in Figure 4a) as outcomes of robustness analysis with  $N=1000$  designs

	Output Parameter	Symbol	Fitted Distribution Type	Mean Value	Coefficient of Variation
11	1 <sup>st</sup> side-to-side mode	$fr1\_side$	Normal	0.235	0.026
12	1 <sup>st</sup> fore-and-aft mode	$fr1\_for$	Normal	0.236	0.026
13	2 <sup>nd</sup> side-to-side mode	$fr2\_side$	Normal	1.348	0.044
14	2 <sup>nd</sup> fore-and-aft mode	$fr2\_for$	Normal	1.380	0.046

comparison to the previous analysis, the influence of the soil parameter  $\varphi'$  is significant higher than the water depth, as can be seen in Figure 4.27 and Figure 4.29.

The two histograms in Figure 4.28 and Figure 4.30, displaying the variation in the first and second natural bending frequencies of the support structure, are once again fitted with normal distributed PDFs. It is seen that these fits are not as good as in the case of the previous analysis (cf. Figure 4.24 and Figure 4.26), where the realizations for the input parameter  $L_{water}$  are generated by a truncated normal distribution. This illustrates the high influence of the underlying distributions in the stated input variables. Beholding the histograms of the two different settings of input variable  $L_{water}$  (Figure 4.5 and Figure 4.6), it becomes clear that the influence of the water depth is lower in case of normal distributed realizations, since more values closer to the mean are generated than in the case of a truncated normal distribution. Nevertheless, comparing the differences in the outcoming CODs caused by this alternation, the calculation seem to be very sensitive, i.e. the statistical dataset has to be chosen carefully (see Figure 4.23, Figure 4.25, Figure 4.27, Figure 4.29).

A third robustness analysis is carried out, wherein the input parameter  $1c$  (see Table 4.1) is set to generate uniform distributed realizations for the water depth. The results are shown in Figure 4.31–Figure 4.34. Since less values are generated near the mean value than in the previous two analyses (i.e. more extreme values at the sides of the interval from 24 m to 32 m are generated for the water depth), the variations in the out coming

frequencies are slightly increased as can be read from the coefficient of variations (see Figure 4.32 and Figure 4.34). Thus, the water depth is more significant and has a stronger impact on the results compared the two previous analyses. This can be seen by the CODs in Figure 4.31 and Figure 4.33, wherein the water depth (input parameter  $L_{water}$ ) influences the results proportionally over 50 %, whereas the internal friction angle takes part with only 35 %. In comparison, if  $L_{water}$  is normal distributed, the CODs to the outcomes were only at about 20 % (see Figure 4.27 and Figure 4.29), whereas the internal friction angle (this input parameter was not adapted at all) is the most dominant one with CODs to the outcomes at about 60 %. So, the alternations in the CODs seem to be high and not robust against small changes in the model input variables.

In contrast, the variability in the outcoming frequencies seems to be more robust. Evaluating the results shown in Figure 4.24, Figure 4.28 and Figure 4.32, a comparison of the results for the first natural bending frequency (in side-to-side mode) shows largely corresponding results. In all investigations the mean value is at 0.235 Hz, the COVs are at 0.025, 0.021 and 0.028. The results for the second natural bending frequency (in fore-and-aft mode) are similar, see Figure 4.22, Figure 4.30, Figure 4.34 (mean value at 1.38 Hz, COVs at 0.046, 0.038, 0.048).

In summary, the CODs in robustness analyses seem to be very sensitive against small changes in the statistical dataset, whereas the outcoming natural bending frequencies of the support structure show only small changes in its determined statistical data.

Coefficient of Determination (linear)  
full model: adjusted  $R^2 = 90\%$

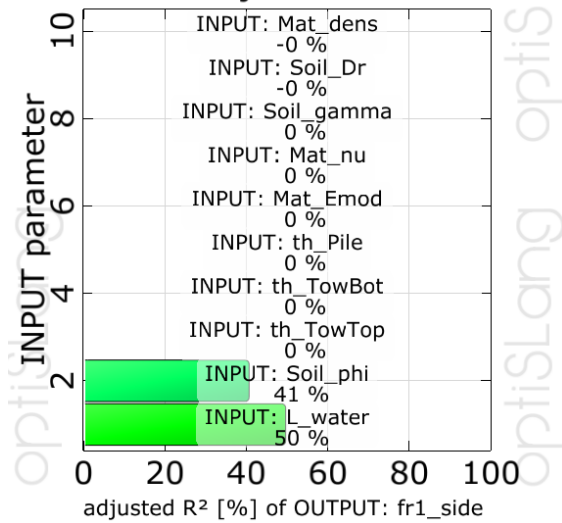


Figure 4.23: Linear Coefficients of Determination of the first natural bending frequency in side-to-side mode ( $fr1\_side$ ) with respect to the input parameters according to Table 4.1a, truncated normal distributed water depth,  $N=1000$

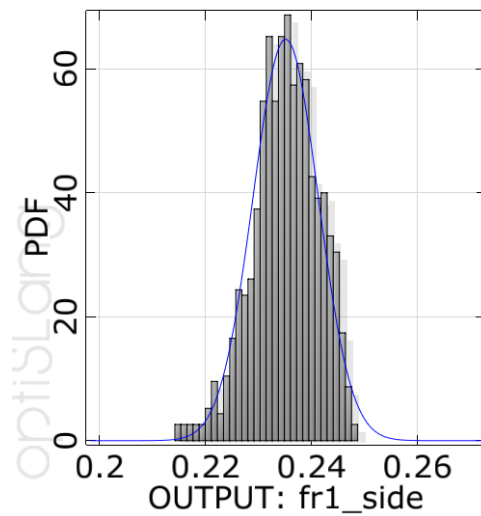


Figure 4.24: Histogram of the first natural bending frequency in side-to-side mode ( $fr1\_side$ ) with fitted PDF (Normal distribution, mean=0.235, COV=0.025),  $N=1000$

Coefficient of Determination (linear)  
full model: adjusted  $R^2 = 90\%$

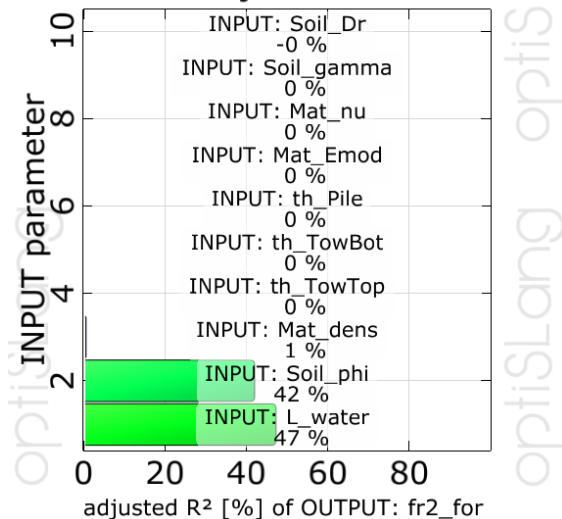


Figure 4.25: Linear Coefficients of Determination of the second natural bending frequency in fore-and-aft mode ( $fr2\_for$ ) with respect to the input parameters according to Table 4.1a, truncated normal distributed water depth,  $N=1000$

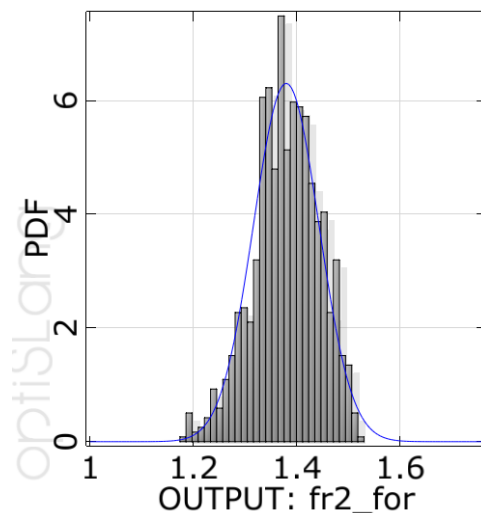


Figure 4.26: Histogram of the second natural bending frequency in fore-and-aft mode ( $fr2\_for$ ) with fitted PDF (Normal distribution, mean=1.38, COV=0.046),  $N=1000$

Coefficient of Determination (linear)  
full model: adjusted  $R^2 = 84\%$

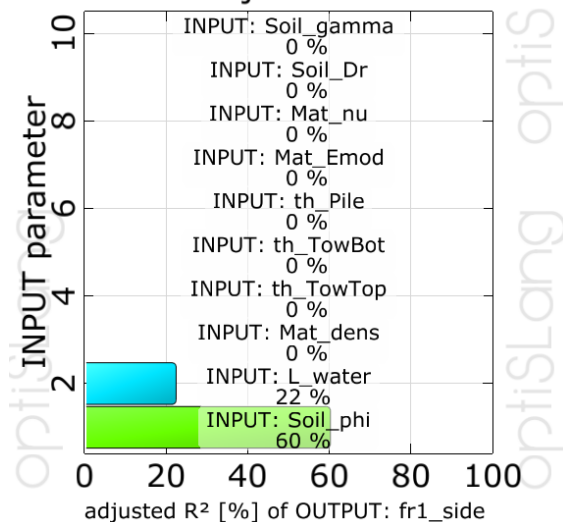


Figure 4.27: Linear Coefficients of Determination of the first natural bending frequency in side-to-side mode ( $fr1\_side$ ) with respect to the input parameters according to Table 4.1b, normal distributed water depth,  $N=1000$

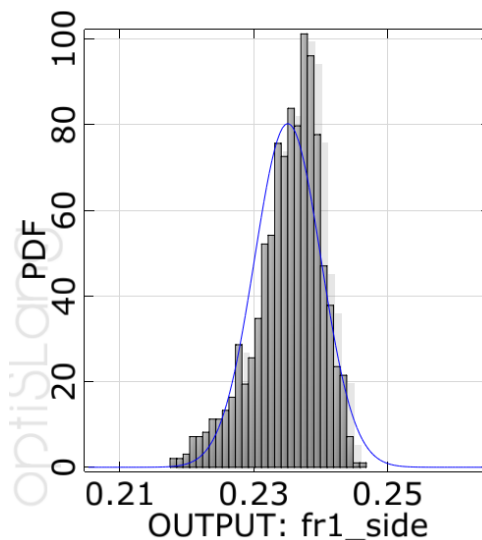


Figure 4.28: Histogram of the first natural bending frequency in side-to-side mode ( $fr1\_side$ ) with fitted PDF (Normal distribution, mean=0.235, COV=0.021),  $N=1000$

Coefficient of Determination (linear)  
full model: adjusted  $R^2 = 85\%$

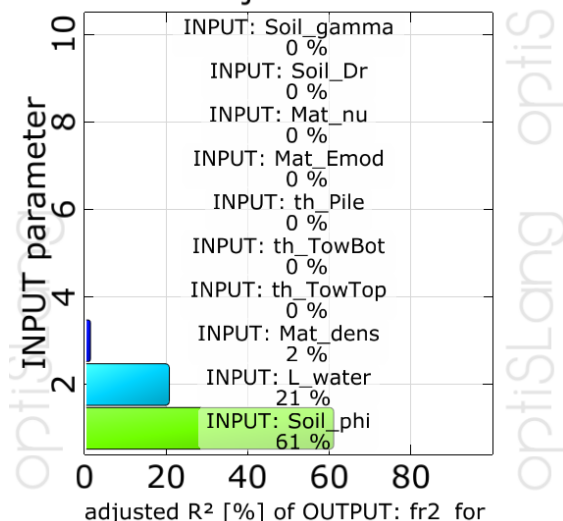


Figure 4.29: Linear Coefficients of Determination of the second natural bending frequency in fore-and-aft mode ( $fr2\_for$ ) with respect to the input parameters according to Table 4.1b, normal distributed water depth,  $N=1000$

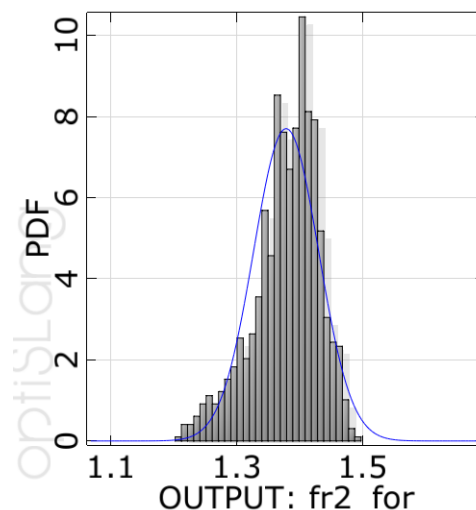


Figure 4.30: Histogram of the second natural bending frequency in fore-and-aft mode ( $fr2\_for$ ) with fitted PDF (Normal distribution, mean=1.38, COV=0.038,  $N=1000$ )

Coefficient of Determination (linear)  
full model: adjusted  $R^2 = 91\%$

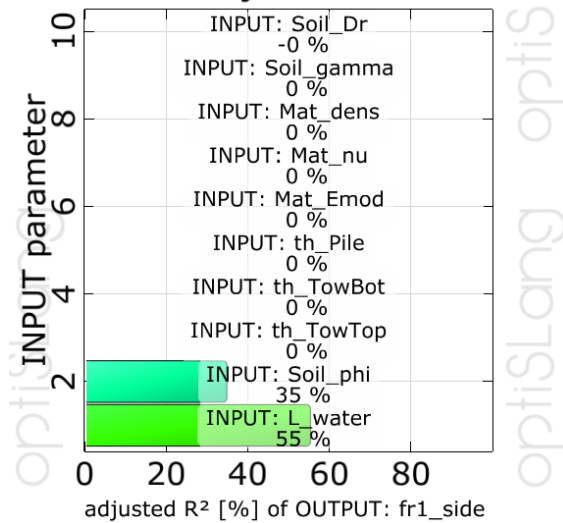


Figure 4.31: Linear Coefficients of Determination of the first natural bending frequency in side-to-side mode ( $fr1\_side$ ) with respect to the input parameters according to Table 4.1c, uniform distributed water depth,  $N=1000$

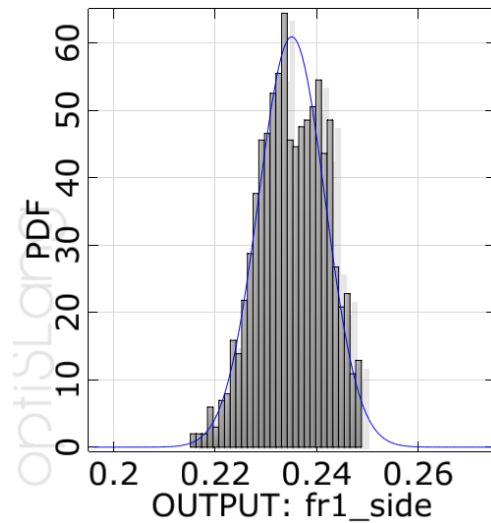


Figure 4.32: Histogram of the first natural bending frequency in side-to-side mode ( $fr1\_side$ ) with fitted PDF (Normal distribution, mean=0.235, COV=0.028),  $N=1000$

Coefficient of Determination (linear)  
full model: adjusted  $R^2 = 90\%$

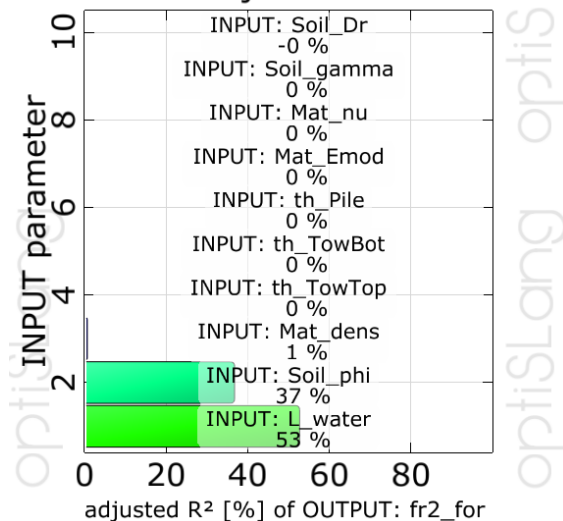


Figure 4.33: Linear Coefficients of Determination of the second natural bending frequency in fore-and-aft mode ( $fr2\_for$ ) with respect to the input parameters according to Table 4.1c, uniform distributed water depth,  $N=1000$

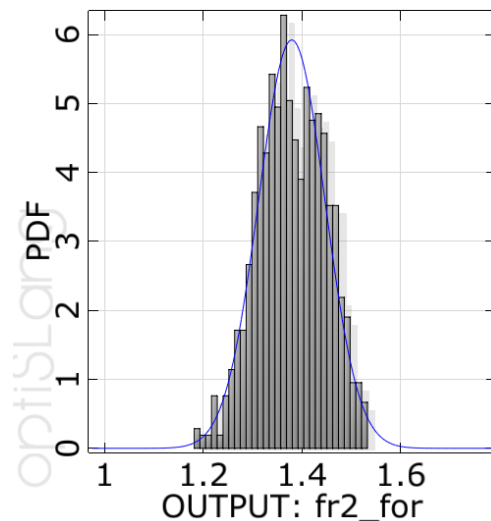


Figure 4.34: Histogram of the second natural bending frequency in fore-and-aft mode ( $fr2\_for$ ) with fitted PDF (Normal distribution, mean=1.38, COV=0.048,  $N=1000$ )

### Ultimate limit state (ULS): axial load bearing capacity of foundation piles

When applying the probabilistic design of foundation piles instead of the semi-probabilistic design, the annual probability of failure  $P_f$  of the considered component has to be calculated. Therefore, the probabilistic distributions of the relevant environmental conditions with a recurrence period of one year are to be determined. As stated previously, the underlying parent distributions of both speed  $v$  and the significant wave height  $H_s$  during the extreme event can be approximated by Gumbel distributions. The corresponding parameters of the Gumbel distributions are listed in Table 4.8. The data for the site of the measurement platform *FINO 1* are used.

#### Modeling and load distributions

The model of the OWT consists of the NREL 5-MW turbine [4.20] and of the OC4 jacket substructure [4.41]. For the embedment of the foundation pile in the soil, hinged and clamped bearings are applied in the numerical set-up, which eventually result in different values of the axial forces acting on the pile head. If the soil with its scattering properties and embedded piles is modeled for each case considered during the Monte-Carlo simulation, an unreasonable high computational effort is required. As stated above, the real values of the axial forces acting on the foundation piles lie within the range defined by the two types of bearing.

The axial load bearing capacity of the foundation piles depends on the piles' geometry as well as on the soil structure. The soil properties are scattering, resulting in varying values for the axial load bearing capacity, which has to be considered within the probabilistic design. Therefore, the soil with scattering properties is modeled in accordance to [4.1]. The modeled axial load bearing capacities can be described by a Gaussian distribution [4.31]. A dense soil with relative density

$D_r = 0.75$  as well as a very dense soil with  $D_r = 0.93$  is considered for the evaluation. Further information on modeling of the soil as well as on the assumptions for scattering of soil parameters can be found in the section "Soil (WP 3)" as well as in [4.24].

#### Probability distributions of wind- and wave-induced loads

The axial loads acting on the foundation piles are determined for a direction of the incoming wind and sea state parallel to the diagonal of the jacket's foot print. This most unfavorable configuration results in the greatest axial pile loads. The steady wind-induced loads as required for DLCs 6.1b and 6.1c are determined using the software Flex5 coupled to Poseidon. The wave-induced loads are calculated with the FE software Poseidon [4.15] coupled with WaveLoads [4.26]. The kinematics of the water particles required for the load calculated with Morison's equation are determined by applying the wave model "stream function wave theory" of 11th order according to [4.17]. For wind speeds in the range of  $25 \text{ ms}^{-1}$  to  $60 \text{ ms}^{-1}$  with steps of  $1 \text{ ms}^{-1}$  (covering 98.3 % of the associated distribution of the 1-year wind speed), the corresponding wind-induced loads are determined. They can be described by polynomial functions, as shown in Figure 4.35 for both types of bearing.

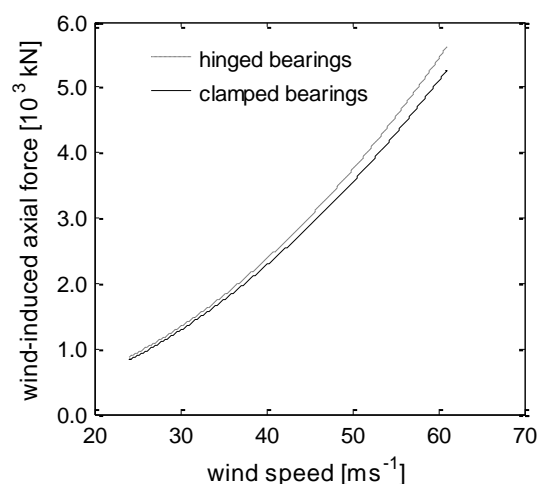


Figure 4.35: Axial forces acting on foundation piles over 10-minutes mean wind speed

Analogously, a polynomial function is found for significant wave heights in the range of 2 m to 12 m with steps of 1 m (covering 99.3 % of the associated extreme-value distribution). More details on the polynomial functions are given in [4.24] [4.31]. On basis of the distributions describing the 1-year storm and the associated polynomial functions of axial forces, the distributions of the loads are determined, as shown in Figure 4.36 for both types of bearings.

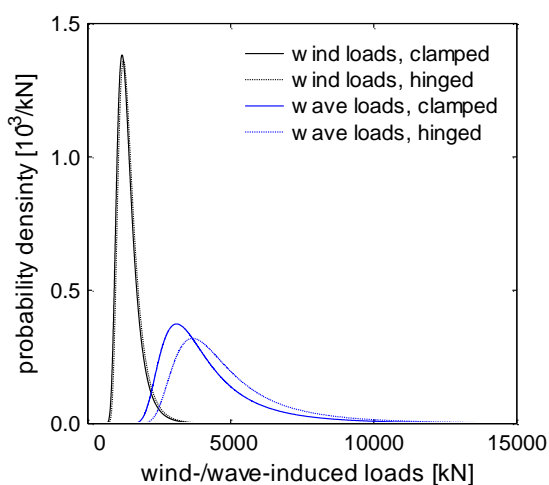


Figure 4.36: Probability density functions of the wind-induced and wave-induced axial forces on the foundation piles

Assuming that wind speed and significant wave height are uncorrelated during storms, the probability distribution of the combined extreme axial force during an 1-year storm can be determined. The probability density functions for both types of bearings are plotted in Figure 4.37 (blue lines). Additionally, the probability density function of the axial pile capacity in very dense soil (red line) as well as characteristic and design values, as required for the semi-probabilistic design, is shown.

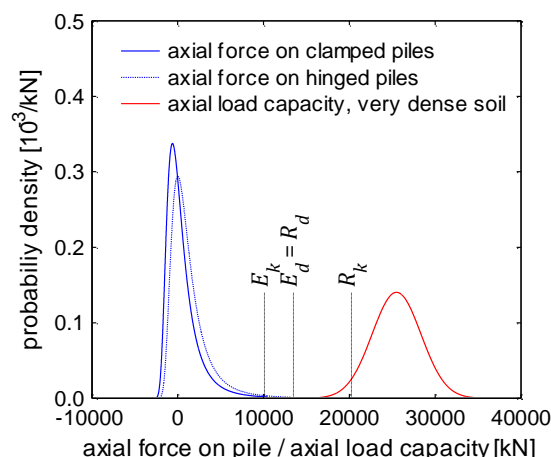


Figure 4.37: Probability density functions of the annual extreme axial loads acting on the pile and of the axial load bearing capacity of the pile

#### Probabilistic design of foundation piles

In order to determine the annual probability that the axial load capacity of the foundation piles is exceeded by the acting axial forces, eq. (4.2) has to be solved. Here, the Monte-Carlo simulation is applied to solve the integral in eq. (4.2), which is a common procedure in reliability analysis: the limit state  $R - E < 0$  is evaluated for a very high number of values for effect and resistance, which are randomly chosen in accordance to the underlying probability distributions. For the considered soil profiles and types of bearings, the resulting probabilities over the embedded pile length of failure are shown in Figure 4.38.

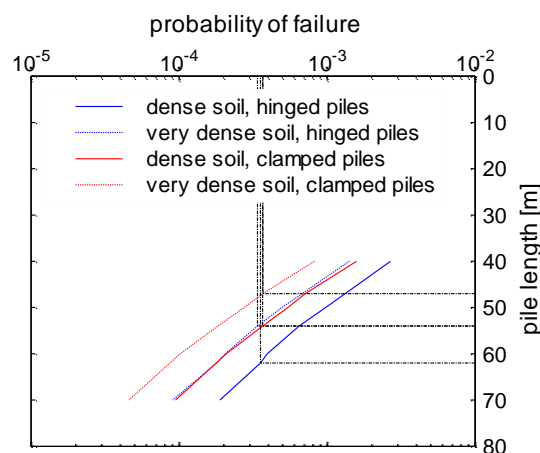


Figure 4.38: Probability of failure over the embedded pile length

In addition, the probabilities of failure for the pile lengths determined with the semi-probabilistic safety concept are emphasized (black dashed lines). The corresponding probabilities of failure lie in the range of  $2.96 \cdot 10^{-4}$  to  $3.14 \cdot 10^{-4}$ . These values lie within the range recommended by [4.38], but they are greater than the probability of failure as required by [4.4].

However, the value of the probability of failure is very sensitive to the chosen probability distributions. This is exemplarily shown for a different probability distribution of the significant wave height: the extrapolated data for a site with a local water depth of 50 m (c.f. Table 4.8, Figure 4.18) is used instead of the data from the site of *FINO 1* with a local water depth of about 28 m, as carried out in [4.24]. First, the pile lengths are calculated with the semi-probabilistic safety concept. Using the previously stated method to calculate, the values of the associated probabilities of failure lie within the range of  $6.50 \cdot 10^{-3}$  to  $8.09 \cdot 10^{-3}$ . The reason for the increased values (by a factor of  $\sim 30$ ) is the increased scattering of the wave-induced loads due to a greater standard deviation of the underlying probability distribution of the 1-year significant wave height.

#### *ULS in accordance to DLC 6.1a*

Similar to the requirements of DLC 6.1a [4.9], fully-coupled simulations of OWTs are used for a more realistic numerical simulation. Here, turbulence of wind fields and the irregular sea state are included, resulting in scattering of dynamic response. Scattering of the effects acting on OWTs can be described stochastically. Hence, extreme-value distributions are found for the greatest loads occurring during a time series with an appropriate duration. A stochastic investigation of extreme wind-induced loads acting on foundation piles was carried out in [4.37], but only for the characteristic wind speed during a 50-

years storm. A probabilistic density function  $p(F|v)$  of the extreme loads  $F$  can be found in dependence of each wind speed  $v$  that might occur during an 1-year storm. Combining this distribution  $p(F|v)$  with the distribution of the extreme wind speed  $p(v)$  occurring during an 1-year storm, a joint distribution  $p(v, F)$  is given,

$$p(v, F) = \int \int p(F|v) \cdot p(v) \cdot dFdv \quad (4.23)$$

Due to the high numerical effort, it is not reasonable to determine the distribution  $p(F|v)$  of extreme wind-induced loads for each wind speed to be considered, since at least 50 fully-coupled simulations with a duration of one hour are required for each wind speed in order to estimate the extreme-value distribution accurately. Therefore, a method to reduce the number of required simulations was proposed. First, the extreme-value distribution of wind-induced loads is found for one wind speed, as carried out in [4.37]. In the following step, the parameters describing this distribution are normalized by mean value and standard deviation of the associated time series. These values are almost constant for each time series with constant wind speed. On basis of these normalized parameters, the extreme-value distributions of wind-induced loads can be found for other wind speeds in dependence of the associated stochastic values. The resulting joint distribution of 1-year wind speed and extreme axial loads acting on the foundation piles is plotted in Figure 4.39.

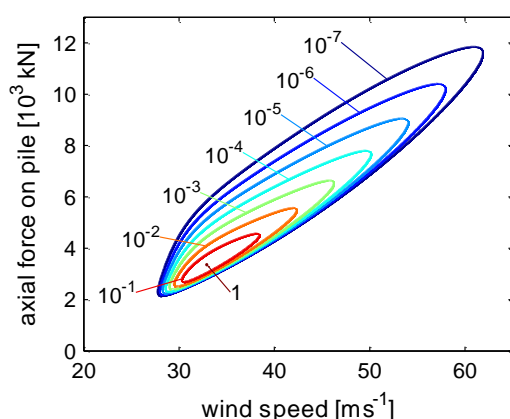


Figure 4.39: Joint distribution of extreme wind speed and extreme wind-induced loads, normalized by its maximum value

More details on this procedure are found in [4.34]. An adaption for other parameters having an impact on the load distribution is also possible.

#### 4.4.5 Conclusions

Within work package 4, advanced design and optimization of support structures for offshore wind turbines are evaluated with respect to the probabilistic safety concept. Therefore, design driving limit states critical for the design are identified. Uncertainties as well as scattering of effects and resistance are considered by applying probabilistic methods.

In case that the probabilistic design is applied instead of the semi-probabilistic design, the probability of failure of the considered components for a period of one year has to be calculated by evaluating the probabilistic distributions of both effects and resistance. Especially for OWTs which are effected by heavily scattering loads during their life time, advanced structural design and optimization can be found on basis of the probabilistic safety concept.

#### Estimation of relevant design values

Measurement series of design relevant wind and wave parameters over a period of several years at the site of *FINO 1* have been analyzed. These works result in

important input parameters for the probabilistic calculations and recommendations for distribution types and statistical values. Additionally, the following findings were obtained for the analyzed measurement site:

- Compared to GL-guideline [4.7], the power law in IEC 61400-3 [4.9] represents the measurement based wind speed profile much better.
- The extreme-value distributions of wind speed, significant and maximum wave height are well approximated at the site of *FINO 1* by *Gumbel* distribution (extreme-value distribution type I) for maximum values.
- Extreme values of a long reference period (here: 1-week or 4-weeks) are much more suitable (in comparison to 6-hour and 1-day extreme values) for the extrapolation of annual extreme values. Of course, a sufficient number of measurement values have to be available to determine an adequate and reliable density distribution.
- At least 50 data points are recommend for the using of *Gumbel* distributions.
- The relation according to GL-guideline [4.7] to determine the design wave from a sea state was confirmed by the investigations carried out in this project.

#### Modal and robustness analysis

Robustness analyses were carried out in order to estimate the influence of various model input parameters against the first and second natural bending frequencies of a support structure of an offshore wind turbine with monopile-substructure. Therefore, material properties, geometrical data as well as soil conditions for the foundation were taken into account as scattering statistical parameters. In all investigations, the only remaining significant parameters were the internal

friction angle of the soil and the water depth, which reflects the embedment depth. Linear correlations and coefficients of determination (COD) were used to quantify the influence of the model parameters. It was shown that small changes in just one single input parameter affects the resulting CODs significantly. Therefore, no statement can be made on which parameter is the most dominate one. But it could be detected, which parameters are responsible for the variation in the outcomes and which parameters are negligible. Nevertheless, the fluctuations in the natural bending frequencies of the investigated support structure are low at all.

#### **Probabilistic design**

Probabilistic design of different components of a jacket substructure was carried out. The ultimate bearing capacity of the

foundation piles during a 1-year storm was assessed. Also, the probabilistic fatigue design was carried out for the tubular joints in jacket substructures.

Since the probabilistic design is very sensitive to the underlying probability distributions, the accuracy of the underlying probabilistic distributions has to be ensured by precise analyses of data. Otherwise under- or overestimation of the probability of failure is possible, which results in a low level of safety and increased economic risks of unnecessary costs during the design, respectively.

Simplifications within structural modeling might be required due to otherwise unreasonably high computational effort. The effect of the simplification on the probability of failure has to be quantified and has to be considered within the design process.

## 4.5 In Situ Assembly (WP 5)

Institute of Building Materials Science  
Ludger Lohaus, Michael Werner

### 4.5.1 Abstract

Grouted Joints are tube-in-tube connections with the gap between pile and sleeve filled with grout. The grout material could be concrete, mortar or cement paste. High-performance mortars are normally used for the grouted joints of offshore wind turbines in Germany [5.1].

Grouted joints connect the piles, which are driven into the seabed, with the upper part of the supporting structure. Accordingly, this kind of connection is a key part to ensure the stability and durability of the supporting structure [5.16]. Previous wind farms have shown that the design and the completion of grouted joints are challenging and also cost-intensive if failures occur [5.13].

Contrary to the preassembled and well-controlled parts of the supporting structure, grouted joints have to be assembled under harsh offshore conditions. Thereby, the quality control of the in situ assembly is greatly complicated by the design and the exposure of the connection. The connection represents a black box [5.8] and the in situ material properties of the grout are only assumptions with high safety factors.

Risk factors of the in situ assembly and a deeper knowledge of the in situ material properties are needed for the optimization of grouted joints.

### 4.5.2 Objective

The Objective of this work package “supporting structure production in situ” focused on the determination of risk factors during the assembly process of grouted joints and on the in situ material behavior of grout materials. Furthermore, concepts used to minimize possible defects before and during the execution will be developed.

### 4.5.3 Approach

The work package is divided into six parts:

- analysis of boundary conditions;
- analysis of common supporting structures and types of grouted joints;
- preliminary hazard analysis (PHA) of the *in situ* assembly;
- fault tree analysis;
- development of the laboratory test facility; and
- experimental investigations.

Firstly, the boundary conditions will be analyzed, and secondly, the different kinds of supporting structures and their different types of grouted joints will be analyzed.

Based on these findings, a PHA will be conducted to develop concepts to minimize possible defects, ensure quality control and devise management solutions. Fault trees will be designed to get a basic idea about the probability of possible failure modes.

A special formwork for the simulation of the filling process will be developed to evaluate the influence of identified failure modes on the material behavior of grout. A transparent front panel in the formwork will be used to observe the phenomena that occur during and after grouting. This laboratory testing facility will be used to simulate exemplary failure modes to obtain basic knowledge of the possible effect of these failures.

### 4.5.4 Results

#### Boundary conditions

A staff member of the research institute received special offshore safety and emergency training (basic offshore safety induction and emergency training, BOSIET) to enable them to analyze the offshore conditions and possible risk factors of the in situ assembly. Thus, two offshore operations in 2011 allowed the institute’s trained staff member to take a deeper look behind the scenes and to gain valuable practical knowledge.

The findings could be separated into three main groups: material properties, the application method, including the grouting procedure, and offshore conditions

*Grout material*

The fresh grout properties are relevant to the application process. The fresh grout has to be pumped over long distances and has to be self-leveling inside the gap between the pile and the sleeve [5.8]. The grout also has to be stable regarding sedimentation and segregation and has to harden rapidly after filling to avoid complications due to early-age movements of the structure [5.6] [5.7]. After hardening, the grout has to bear the load of the turbine over a period of a minimum of 20 years, therefore, the fatigue resistance is important, especially under submerged conditions [5.4]. Because of the harsh offshore conditions, the material has to be robust in terms of different temperatures and weather conditions. Detailed information is given in [5.8].

*Application Method*

Figure 5.1 shows a functional flow diagram of a typical grouting procedure. This flow diagram starts with the storage of the grout material. The grout mixers are supplied with dry premixed grout by crane or silo. High-performance grouts need high shear forces to reach their material properties and long mixing times. After mixing, the material is delivered to the grout pump. Different mixers and grout pumps could influence the quality of the grout [5.2]. The pump delivers the fresh grout via grout lines and grout hoses to the supporting structure until the annular gap is reached and the grout material fills the grouted joint completely. The material of the grout line, the length of the line and the diameter must be taken into account [5.3]. Moreover, the duration of the grouting process could have an influence on the grout homogeneity.

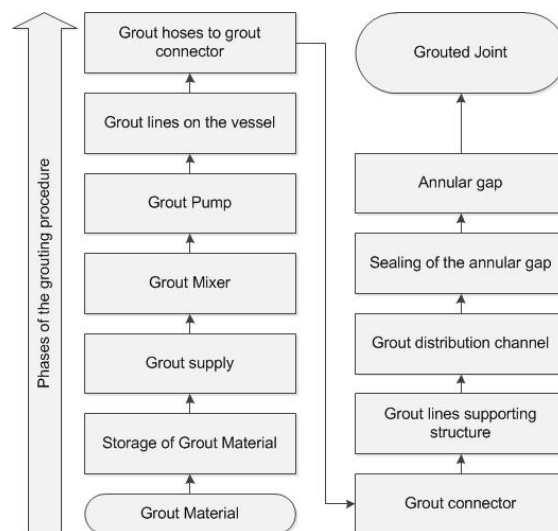


Figure 5.1: Functional flow diagram of a grouting procedure [5.10]

*Offshore Conditions*

Offshore conditions have a significant influence on the quality of grouted joints. The harsh offshore conditions influence the grout material, the technical equipment and the on-site staff responsible. The main factors are the ambient conditions, such as wind, waves and the temperature of the air and water. The on-site staff responsible, who face harsh offshore working conditions, are a key factor in the estimated quality of the offshore construction. Furthermore, the standards of health and safety are very complex and reduce the workability of the crew. An example of the proper protective clothing is given in Figure 5.2. Detailed information is given in [5.9] and [5.5].



Figure 5.2: Immersion suit as work wear [5.9]

## Supporting structure

The design of the supporting structures depends on the depth of the water. At a low water depth up to 30 m, monopiles are mainly used. At deeper water depths, it is more common to use tripods or jackets as the supporting structure. Figure 5.2 shows some different types of supporting structure.

The chosen design results in different boundary conditions and constructions of grouted joints.

Depending on the design, the width of the gap between pile and sleeve and the shear key geometry differ. The length of the connection and possible imperfections between pile and sleeve are also different. Moreover, the distribution channel for the fresh grout changes from wind farm to wind farm. More detailed information is given in [5.5].

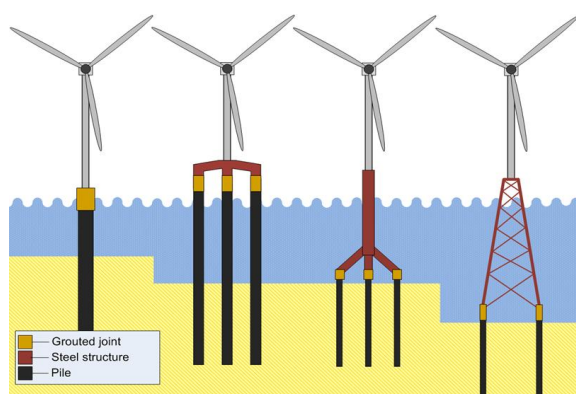


Figure 5.2: Supporting structures [5.7]

## Preliminary Hazard Analysis

The PHA can be divided into five parts, which are shown in Figure 5.3. The first step is to find the undesirable system states, and the second is to identify the failure modes and their effects, evaluate the possible failures and recommend corrective actions.

### System Design Analysis

The function of the grouted joint is to bear the loads of a turbine and the upper part of the supporting structure. These loads are mainly axial loads and vertical loads for jackets and tripods. For monopiles and

tripiles, the grouted joints are additionally stressed by bending moments [5.5]. Critical conditions exist when the load from sleeve to pile is not securely transferred. According to experiences in offshore constructions, the following items are supposed to be critical:

- partially filled or unfilled gap between pile and sleeve
- faults in the material in the gap, e.g. voids, insufficient material properties and
- an insufficient bond between the grout and shear keys.

Components which could be prone to failure are:

- sealing of the annular gap;
- the distribution channel;
- grout lines which supply the distribution channel;
- the grout connection of the supporting structure; and
- the annular gap.

These parts are prefabricated and a proper quality control is possible, but a further quality control after the upper part of the supporting structure is placed onto the sea-bed is much more difficult.

The maintenance and testing of the parts for the filling process on the ships are more easily possible, but these parts are also exposed to the offshore conditions on the deck of the ship and are prone to failure.

### Critical conditions

Incidents which could lead to critical conditions are leakage of the grout seal and irregularities in the grout material, especially influence on the fresh grout properties. Furthermore, longer filling processes and higher pump pressures could also be critical.

The main specific reasons for these incidents could be:

- damage to the grout seal because of the pile-driving process or the

setting process of the upper part of the support structure;

- a fluctuating water demand of the grout material;
- impurities in rubber hoses and grout lines connected to the supporting structure;
- unfavorable running of the grout lines on the ship; and
- extended time for supplying raw materials by crane because of wind and waves.

#### *Failures*

The following are incidents which could lead to failures:

- massive loss of grout material in the annular gap because of damage to the annular grout seal;
- permanently blocked grout lines;
- grouting procedure outside the working time of the grout; and
- early-age cycling [5.14][5.6][5.7].

#### *Causes of the incidents which could lead to failures*

The grout seal could be destroyed due to the pile-driving process (post-pilled), the placing of the support structure on the piles (pre-pilled) or by placing a transition piece on the pile. The loss of material could not only occur during the grouting process, but also at the end of the grouting if the seal is not able to take the loads of the fresh mortar.

The running of the lines influences the blocking tendency of the grout in the lines. However, the fresh concrete properties are also important. If the consistency is too stiff, the pump pressure may exceed the maximum, or if the consistency is too soft, sedimentation of the material in the lines could occur. The breakdowns of a pump, a mixer or a crane during raw material supply are also a possible reason for blockages.

Early-age cycling may occur because of an unsatisfactory fastening of pile and sleeve, and also because of elastic deformations of the pile and the sleeve because of higher waves than expected.

#### *Effects of the failure modes*

Consequences of these failures could be as follows:

- the grouted joint is not filled with grout or only partly filled; this could be caused by destruction of the annulus seal or permanently blocked grout lines;
- flaws in the grout or layers with unknown material properties; this could be caused by changing material properties over time and a too early setting time of the grout;
- planned material properties are not reached because of failures of the mixing proportions, mixing process, storage, or ambivalent temperatures; or
- sedimentation, segregation and damage to the grout matrix because of early-age cycling movements [5.6][5.7].

#### *Examples of failure mitigation*

The following examples of possible measures for the minimization of failure are reasonable:

- redundant design of the annulus seal [5.8];
- a redundant grout line system [5.8];
- emergency schedules for possible failures;
- strong fixing of the pile and sleeve to avoid effects from the early-age cycling;
- preliminary material tests and mock-up test;
- quality management system for the grouting process; and
- conformity tests of the grout prior to its offshore use.

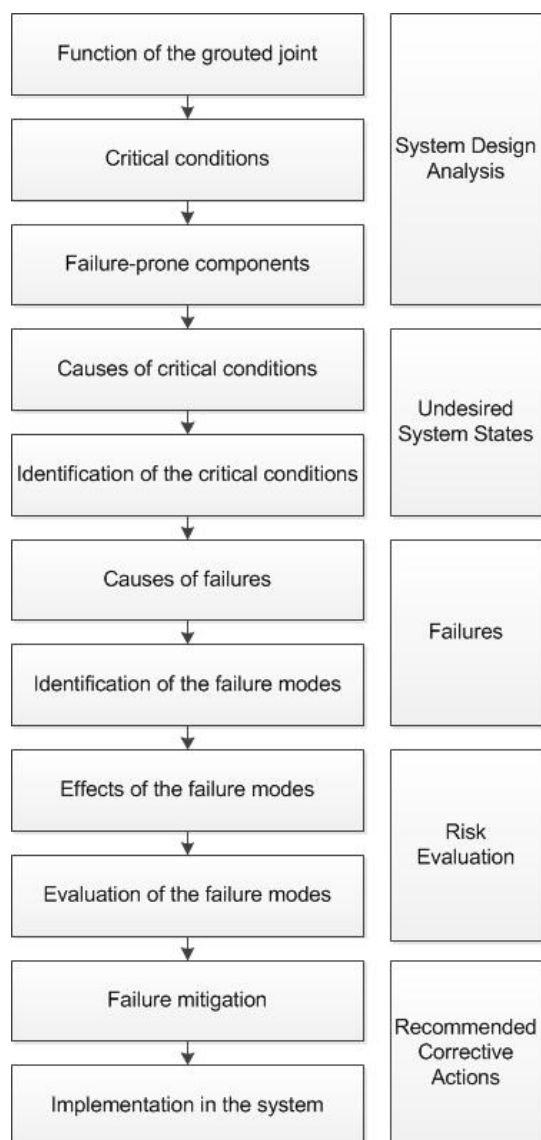


Figure 5.3: PHA Process for the in situ assembly [5.10]

#### Exemplarily implementation of the examples in the system

A laboratory test of the grout material and mixing and pumping tests could be carried out in the early design stage of the supporting structure.

A large-scale pumping test could be carried out before the design stage is finished, for example, in test facilities presented in [5.15], [5.16] and [5.12].

An external survey could be implemented and external material testing [5.2] for each production batch of the grout material.

An annulus seal test and leakage tests of the lines and rubber hoses prior to grouting operations could be carried out [5.8].

Equipment tests could be carried out prior to grouting.

Documentation of the overflow to check if the annulus seal is leaking and if the grouted joint is completely filled. Detailed information is given in [5.10] and [5.15].

#### Fault Tree Analysis

Two fault trees were designed to assume the probability of failure of two top events which are exemplarily chosen. Furthermore, the important basic events could be found.

The first top event is a minor failure during the filling process. In this case, the grouted joint is completely filled, but a minor failure occurs during the filling process which leads to a nonconformity report (NCR). Consequently, an influence on the load-bearing capacity or an influence on the fatigue behaviour is possible and has to be evaluated case by case.

Table 5.1: probabilities of failure of the basic events

Primary event	Probability of failure
Pump: temp. breakdown	0.05
Mixer: temp. breakdown	0.025
Crane: temp. breakdown	0.025
Grout hoses: defective	0.01
Lubrication mix: not used	0.01
Grout hoses: poor running	0.05
Material consistency: not pumpable	0.025
Grout hoses: impurities	0.05
Grout material consistency	0.05

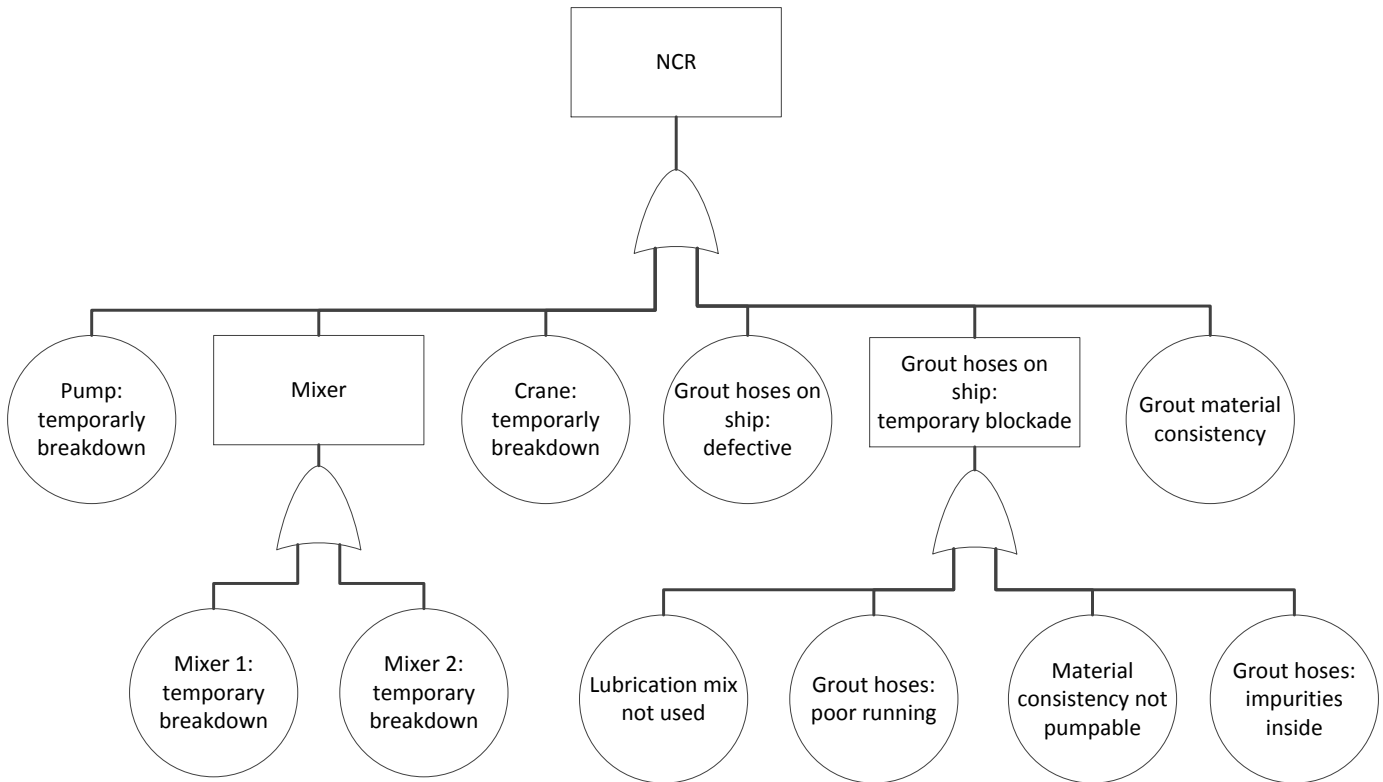


Figure 5.4: Fault tree with top event NCR

Figure 5.4 shows the fault tree. The assumptions for the probabilities of failure for primary events are presented in Table 5.1.

The basic events are a temporary breakdown of one of two mixers, temporary breakdown of the grout pump, temporary breakdown of the crane, a defect in a grout hose, or a temporary blockage of grout hoses. Temporary blockages of grout hoses are possible because of the poor running of the grout hoses, impurities in the grout hoses, consistencies of the material which are not pumpable, wrong consistency of the grout material and when a lubrication mix is not used.

The fault tree was simulated by using the software OpenFTA. The probability of failure was 26 % for the assumed parameters. The dominant primary events were a temporary breakdown of the pump, impurities in the grout hoses, poor running of the grout hoses, and a wrong consistency of the grout material. The

second case represents a major failure during the filling process: the grouted joint is partially filled or not filled with grout. In this case, the grouted joint has to be repaired, for example, with a “stinger operation”.

The basic events could be a permanent breakdown of two (or all) mixers, permanent breakdown of the primary and spare pumps, permanently blocked fixed grout lines, defective grout seals, or collision with a ship or jack-up barge.

Table 5.2: Probabilities of failure for basic events

Primary event	Probability of failure
Pump: perm. breakdown	0.02
Mixer: perm. breakdown	0.01
Crane: perm. breakdown	0.01
Grout lines: blockage	0.05
Grout seal: defective	0.10
Ship collision	0.05

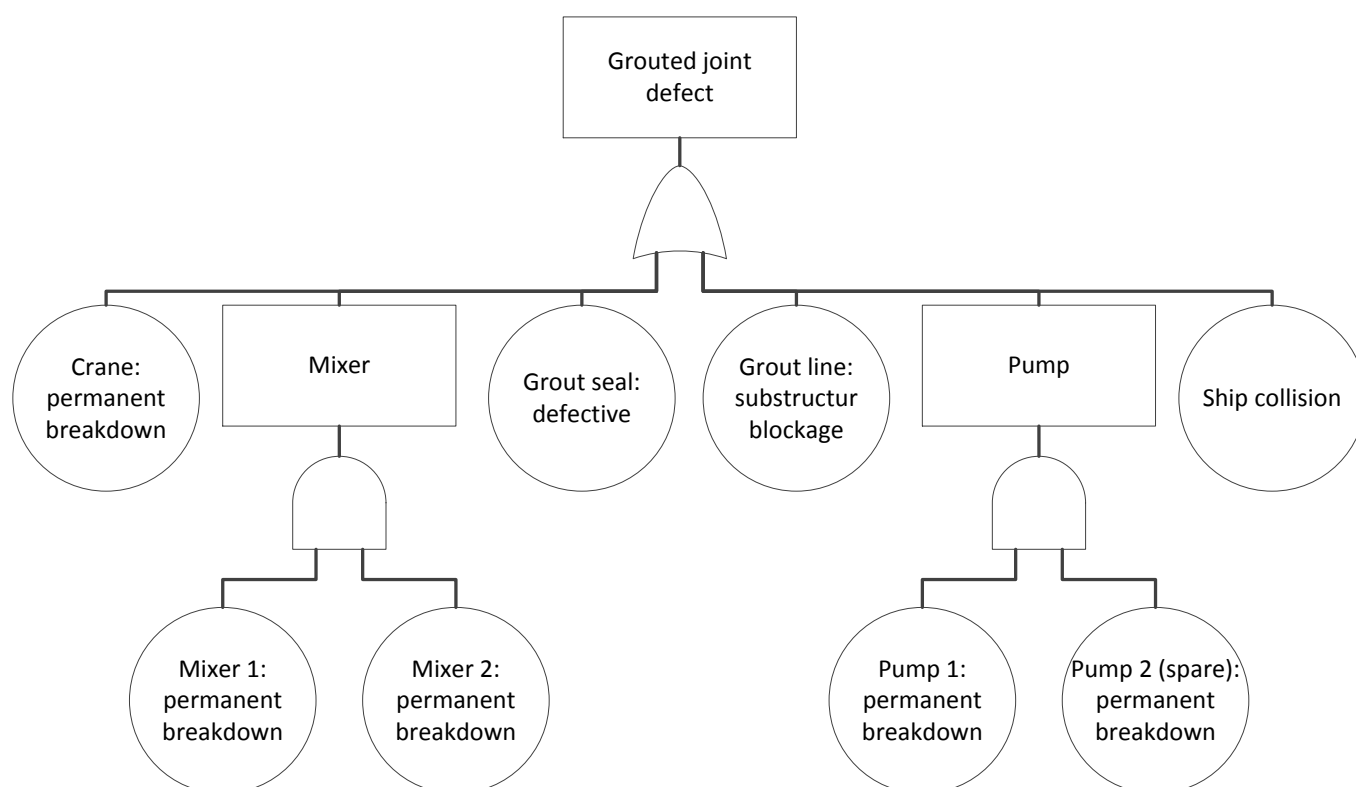


Figure 5.5: Fault tree with the top event grouted joint defect

The fault tree is shown in Figure 5.5 and the assumed probabilities of failure for the basic events are presented in Table 5.2.

In this case, the probability of failure for the top event was 22 %. Dominant primary events are a defective grout seal, a blocked grout line on the substructure and a collision with a ship.

The probability of failure is for example for the top event about 18 % using 5 % for the probability of failure for the basic event “grout seal: defective”. Furthermore by using additionally 2.5 % for the basic event “grout lines: blockage” the probability of failure is reduced to 15 % for the top event.

With the knowledge of the dominant basic events, it is possible to prevent these events in order to minimise the probability of failure of the top event.

### Laboratory Testing Facility

Experimental simulations of failure modes are essential to evaluate the influence on the material behaviour. However, firstly, the in situ material behaviour of the grout

of undisturbed filling processes has to be evaluated.

Therefore, a laboratory scaled test facility was developed. The laboratory test facility is based on a grouted joint with a pile diameter of 3 m (Figure 5.6). The grout length of the connection is 6 m high, and the grouted joint is supplied with grout via four inlets.

Because of the assumption that the gap is filled by four inlets, we adopted a segment of  $\frac{1}{4}$  of the whole arc length for the testing facility. The segment was downscaled by 1:4 to get a test facility which is easy to handle in the laboratory and also suitable for parametric studies.

A transparent front panel was used to observe the filling process. The formwork will be filled by a grout pump with a 1 inch hose and inlet, as shown in Figure 5.7. The width of the gap is flexible from 1 cm up to 20 cm.

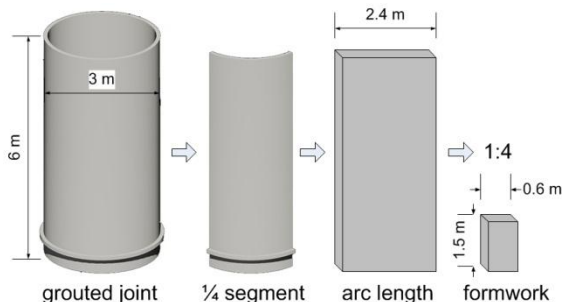


Figure 5.6: Basic principle of the laboratory testing formwork [5.10]

The laboratory testing formwork will be filled with two batches of grout. Cement slurry is used for the lubrication of the grout hose. Firstly, the filling process will be observed optically. After one day of hardening, the formwork will be dismantled and prismatic samples will be generated from the wall for compressive strength tests. These test samples will be compared with a set of standard test specimens.

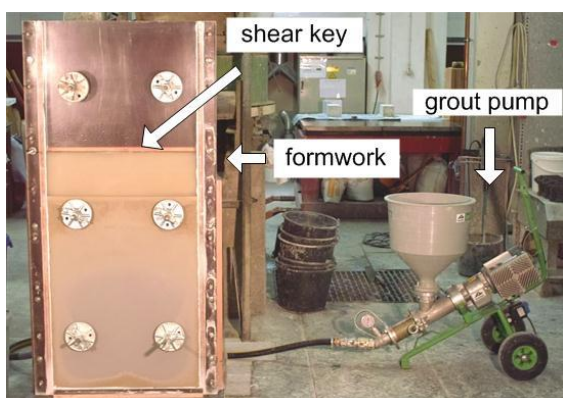


Figure 5.7: Laboratory testing facility [5.10]

### Experimental Investigations

A standard grout material for offshore purposes was used for the experimental investigation. Firstly, an undisturbed filling process was simulated without water inside the gap of the formwork.

The results showed a minor negative effect of the filling process on the compressive strength. However, a negative effect of water inside the gap was observed mainly in the upper and lower part of the test wall. An “overflow” of the

grout material out of the gap is recommended to reduce this effect [5.15]. Two failure modes, which represent one basic event of each developed fault tree, were exemplarily simulated.

The experimental simulation of the first failure mode represents a temporary stop of the filling process, which led to an NCR. Twenty centimetres of the formwork was filled with water, and a lubrication mix was used prior to grouting. Half of the testing formwork was filled with grout. After a stop of approximately 3.5 hours, the formwork was filled up to the top. A small amount of material was lost due to the overflow.

Figure 5.8 shows the results of the compressive strength in percent in relation to standard test specimens. The picture on the left shows the surfaces of the test wall, and on the right, an interpolated map of the relative compressive strength. The values on this map were used for the interpolation.

This failure mode shows an almost general reduction of the compressive strength up to 39 %. However, the mean value was higher at 90 %.

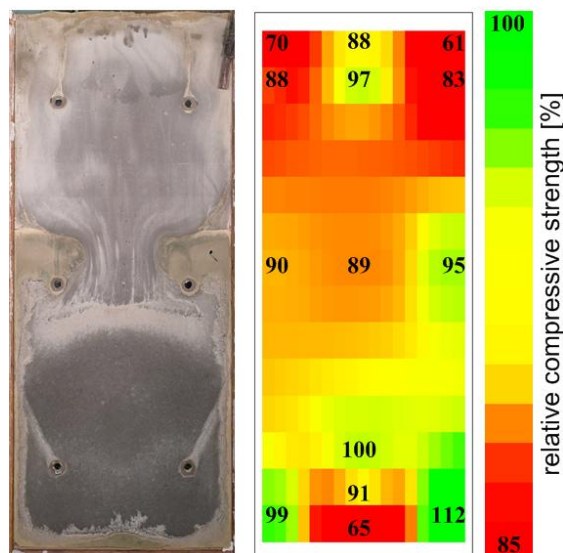


Figure 5.8: Failure mode 1: blocked line for 3.5 h, lubrication mix, 20 cm water [5.11]

The simulation of the second failure mode represents a permanently blocked grout line after filling half of the grouted joint. The grouted joint was completely filled

after a break of 2.5 hours with the contractor method from the top by using a “stinger” as a repair action. The time should represent the time to carry out the modification for the “stinger operation” and insert the “stinger” into the grouted joint. This method is well-known as “grouting with a stinger” in the offshore oil and gas industry [5.14]. The gap in the formwork was filled with water up to 20 cm prior to grouting and a small volume of material as overflow was accepted.

Figure 5.9 shows the results of the simulation of the second failure mode according to Figure 5.8.

A reduction of the compressive strength up to 59 % was observed in the upper and the lower parts of the test wall. Equal values for the compressive strength were found in the lower middle part of the wall. Here, the mean value is 83 %.

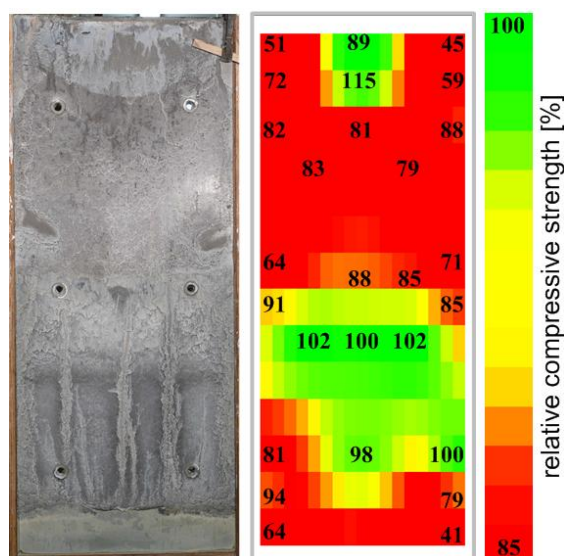


Figure 5.9: Half-filled grouted joint, stinger operation, lubrication mix, 20 cm water [5.11]

The failure modes presented show that an influence on the load-bearing capacity of grouted joints is possible and has to be taken into account.

Failure mode 1 shows a minor reduction of the compressive strength in the middle area of the test wall. Fewer reductions of the compressive strength should be

expected by using a large volume of grout material for the overflow.

Failure mode 2 shows greater reductions in larger areas of the test wall. However, high values for the compressive strength are also present in the areas where the repair action took place.

Detailed information and more simulated failure modes are presented in [5.11].

#### 4.5.5 Conclusions

Important influences of offshore conditions on the material properties of grout and on the in situ assembly were found. The influencing factors were analysed and separated into four groups: grout material, application method, offshore conditions, and the type of construction. Manifold influences on the in situ assembly were found which vary from case to case.

Main influences are the diverse temperature conditions, wind, and waves. Furthermore long grout hoses length and the length and size of grout lines, the exposition of the grouted joint and the size of the gap between pile and sleeve are important variables.

With this knowledge, a basic PHA was carried out. The analysis included a system design analysis, undesirable system states carried out, failures, evaluation of the risks, and recommended corrective actions for the in situ assembly.

Top and basic events were found for fault tree analysis (FTA) within the PHA. Two fault trees were designed; firstly, a minor failure, e.g. extended filling times, and secondly, a major failure, e.g. an incompletely filled grouted joint. The probability of failure was determined for both events using the software OpenFTA.

A probability of failure about 26 % was determined for the top event “NCR” (extended filling time).

The second fault tree with the top event “defect grouted joint” has a probability of failure about 22 %. Here the grout seal was the most important basic event. The probability of failure for “defect grouted

joint” could be reduced by improving the grout seal (from 0.1 to 0.05) to 18 % and by improving additionally the grout lines (from 0.05 to 0.025) to 15 %.

The laboratory testing facility was developed for the evaluation of the influence of different failure modes on the material behaviour of the grout. Exemplarily failure modes were simulated and analysed e.g. a temporary blocked grout line and a

“stinger operation” as repair action for a defect grouted joint. The experimental simulation of the temporary blocked grout line show a reduction of the mean value to 10 % and partly up to 39 % of the compared compressive strength. A reduction of the mean value of the compressive strength for the repair action “stinger operation” was determined to 17 % and partly up to 59 %.

## 4.6 Monitoring of mechanical Components (WP 6)

Institute for Machine Design and Tribology (IMKT)

Gerhard Poll, Roman Böttcher

### 4.6.1 Abstract

Technical systems are subjected to damage mechanisms with a stochastic distribution of failure probability. Therefore, the exact time of failure of mechanical components in the drivetrain of offshore wind turbines e.g. due to rolling fatigue of bearings in the gearbox cannot be predicted. The use of condition and load monitoring systems together with the basic understanding of damage mechanisms allows the early detection of damages in mechanical components and as a result their timely repair to prevent expensive secondary damages and downtimes.

Work package 6 therefore deals with the development and evaluation of analyzing methods of vibration based condition monitoring systems, the evaluation of experimental vibration pickups as well as the examination of force sensors for screw connections suitable to monitor the forces on bearings and structural components.

### 4.6.2 Objective

The number of installed wind turbines grows dramatically as well as the power of newly developed turbines in light of the turnaround in energy politics towards renewable energies. In addition, there are an increasing number of wind turbines installed or planned to be installed in near and far offshore conditions. Offshore wind turbines (OWT) are more difficult to access which results in a longer downtime in case of a failure that has to be repaired.

Damages in the mechanical drive train of wind turbines e.g. on rolling element bearings, cannot be determined and excluded in advance sufficiently. The aim of work package 6 therefore is the development and optimization of monitoring and diagnosis systems that should be

applicable to OWT to provide reliable operation and efficient maintenance through early detection of damages and force monitoring. It also helps to achieve basic knowledge during experimental studies on single components of the OWT drive train.

### 4.6.3 Approach

The approach of work package 6 is divided into two parts. One part focuses on condition monitoring systems (CMS) for large size bearings, the other part deals with methods for the measurement of forces on components attached with screw connections.

#### Condition Monitoring of large Size Bearings of Wind Turbines

Fatigue damages of rolling element bearings as a result of repetitive overrolling occur even under ideal lubrication conditions and are typically distributed stochastically. For the dimensioning of bearings, a failure probability can be calculated in regard to rolling fatigue. Dynamic loads can be approached by histograms with a finite number of simplified static values. Thereby, short time events with high loads, e.g. wind gusts on the wind side or short circuits on the electric side of a wind turbine cannot be taken into account as well as the sequence of the load distribution when calculating over an estimated life time of a turbine of 20 years. Non-stationary loads and interactions of the lubricant and the bearing material induce additionally particular effects, such as slip of rolling elements with subsequent smearing damages or white etching cracks (WEC) that can reduce the lifetime of bearings in wind turbines dramatically, see [6.9], [6.6] (selection). The risk of slip increases with growing bearing dimensions on account of an increasing mass-inertia of the rolling elements. Many damage mechanisms of bearings are not yet investigated sufficiently and are therefore not even implemented in their lifetime prediction.

Damages in the raceways of rolling element bearings produce a shock pulse repetition when rolled over repeatedly. The frequency of the pulse repetition depends on the geometry of the bearing, damage location (inner ring, outer ring, cage or rolling element) and the rotational speed.

To detect pulse shocks of damages in the best possible way, acceleration sensors have to be mounted in load direction and as close as possible to the specific bearing and its loaded zone. Every interruption in the propagation of the pulse shock through the elements carrying the bearing such as close or loose fits acts as a damping of the signal.

However, several bearings can be monitored by only one sensor in practice by taking advantage of transmission properties of structural components. The particular mounting position of vibration pick-ups has to be selected carefully with regard to transmission behavior at all desired frequencies. The certification guideline of Germanischer Lloyd for CMS in wind turbines demands at least six acceleration sensors on main shaft, gearbox and generator, [6.1]. Figure 6.1 shows an actual approach with seven sensors, which are mounted both radially and axially, at different parts of the drive train of a wind turbine.

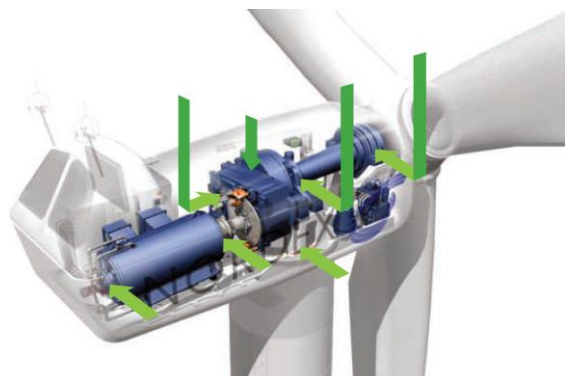


Figure 6.1: Minimum number of sensors  
[6.3]

The vibrational signal measured by means of acceleration sensors cannot be analyzed directly because of an amplitude modulation with other vibrations of higher

frequencies which result e.g. from structural vibrations, tooth meshing frequencies or additional components for operation. Current condition-monitoring-devices use low-pass-filters to separate an envelope curve with the interesting part of the signal from the overall signal. Cut-off frequency, filter type and order of the filter have to be adapted for different rotational speeds and every gearbox. This approach requires that the modulated vibrations and the transmission behavior of the structural components do not vary during operation and life time of the wind turbine. The envelope curve produced by filtering can be distorted due to transient response or overshoots.

The envelope curve has to be transferred to a frequency spectrum by help of FFT, where amplitudes of characteristic overrolling frequencies can be evaluated to detect damages. Depending on the movement of the bearing parts, harmonics show up in the frequency spectrum, too. While operating with variable speed, the original vibration signal can be frequency modulated additionally. This influence can be removed by use of an order tracking analysis instead of frequency spectrums.

The design of drive trains in wind turbines changes with increasing size and power. In partly integrated designs as shown in Figure 6.1, one bearing of the rotor is integrated into the gearbox. To reduce the tower head mass further, integrated drive trains were developed, where rotor and gear box as well as gear box and generator are connected directly without the use of intermediate shafts. Therefore, more rotating parts emit vibration signals in the housing of the gearbox, making it less easy to separate certain pulse shocks of bearing damages in signals measured with acceleration sensors.

Further space savings and the utilization of medium speed generators or higher gear ratios for slower rotating rotors could be achieved by the substitution of spur gears with planetary gears. Due to the compact design, planetary gear levels

have a high material damping on vibration signals e.g. from overrolled failures in bearings. The shock pulses of damages in planetary bearings have to be transmitted resp. modulated by the tooth meshing of the planetary stage before it could be measured by acceleration sensors on the outside of the gearbox housing. The tooth meshing frequency of the planetary stage is very low due to the low rotational speed of the rotor. The planet wheels rotate around themselves and also rotate with their carrier. Pulse shocks emitted by damages in the planetary bearings therefore change direction and position in regard to stationary acceleration sensors on the gearbox. Damages in planetary bearings are therefore difficult to detect with conventional CMS-analysis-methods, especially when the damages are in an initial stage and emit only minute shock pulses.

It was intended to evaluate the performance of a new analyzing procedure for a condition monitoring system that was developed at IMKT, see [6.7], by help of a large size bearing test rig. The analysis method was already tested on small cylindrical roller bearings (CRB) with constant load and high speed, see [6.8]. It

uses a Hilbert transformation to get an envelope curve without the use of filters. Small shock pulses can be remodulated reliably from the overall vibration signal. It is therefore ideal for the application at planetary gears or otherwise challenging drive train components of wind turbines respectively their gear boxes and bearings under dynamic operation conditions.

The large size bearing test rig that is operated by IMKT was designed for experimental investigations with large size bearings under various conditions, especially those that may cause unexpected bearing damages or failures in practical applications. The test rig consists of a single test bearing and also two cylindrical roller bearings and one radially relieved four point bearing as support bearings. The axial and radial load as well as tilting can be applied by means of hydraulic cylinders both in tension as well as in compression. In addition the test bearing can be operated optionally with a rotating inner or a rotating outer ring.

Figure 6.2 shows all accessible positions on which acceleration sensors were mounted on the large size bearing test rig to cover as many loaded zones of each bearing as possible.

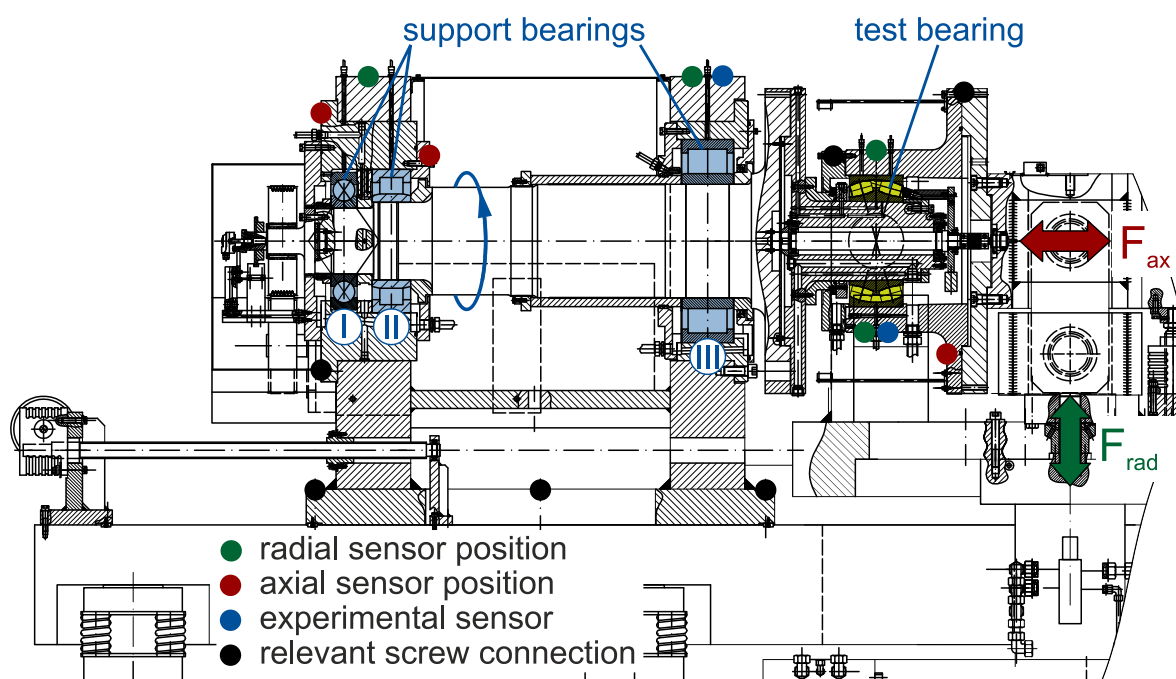


Figure 6.2: Drive train layout wind turbine for CMS-test

In addition to commercial acceleration transducers that utilize shear of a piezo-ceramic by a seismic mass to measure vibration signals, experimental sensors were bonded to the test rig in direct vicinity to proven sensors, see Figure 6.3.

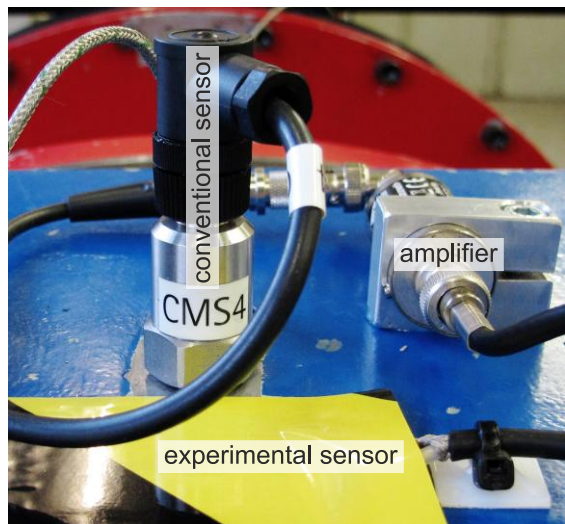


Figure 6.3: Amplifier and experimental vibration pick-up

These sensors use the lateral piezoelectric effect and require less space and are lighter than their traditional counter parts. While the latter have integrated electronic components to convert a charge, generated by a deformation of the piezo-

ceramic, to an output voltage, a detached amplifier has to be used to operate experimental sensors.

Furthermore to an utilization on the test rig, basic examinations regarding the sensitivity on elongation, temperature behavior and electromagnetic compatibility (EMC) were performed with experimental sensors in individual test set ups. Thereby, defined shock pulses were generated by help of a modal hammer.

Since it isn't supposed to perform life time tests on the large size bearing test rig, it is difficult to determine the frequency-weighted level of acceleration of real fatigue damages during scheduled tests. Therefore, a separate test bearing for the large size bearing test rig was acquired, that is kept available for tests with an aimed damage by scratching or the application of small welding seams.

In the meantime, an opportunity arose to perform measurements on a real wind turbine. The installation of sensors and a data acquisition system was given priority to experiments in the test lab. The particular wind turbine was built in woodland with a hub height of 100 m and 1,5 MW of power. It has a partial integrated drive train, where main bearing,

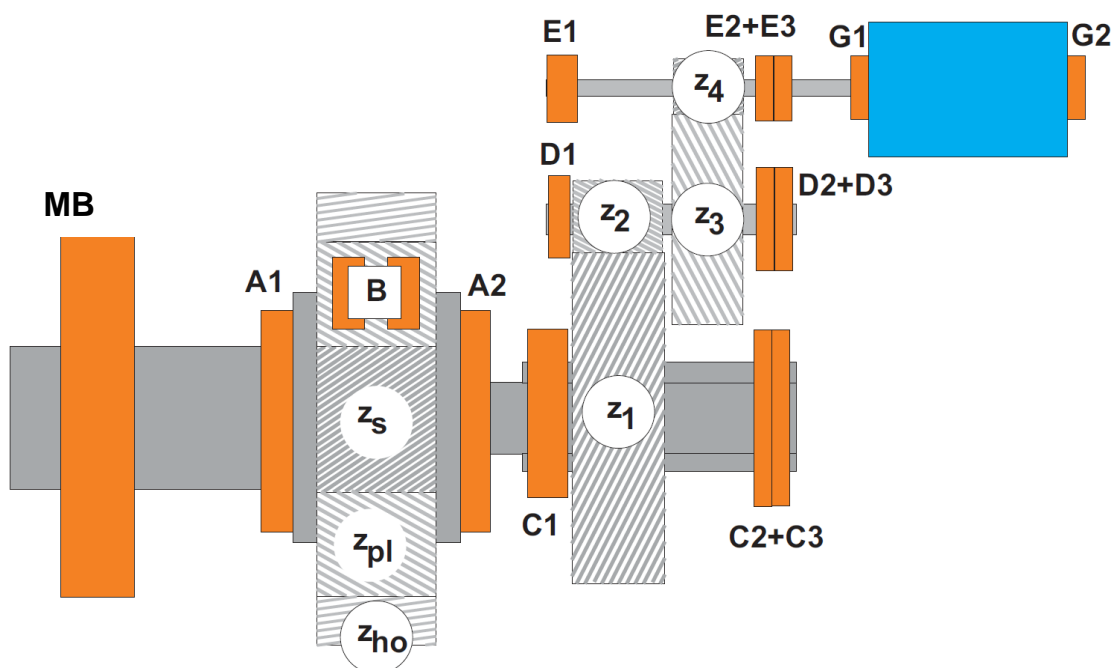
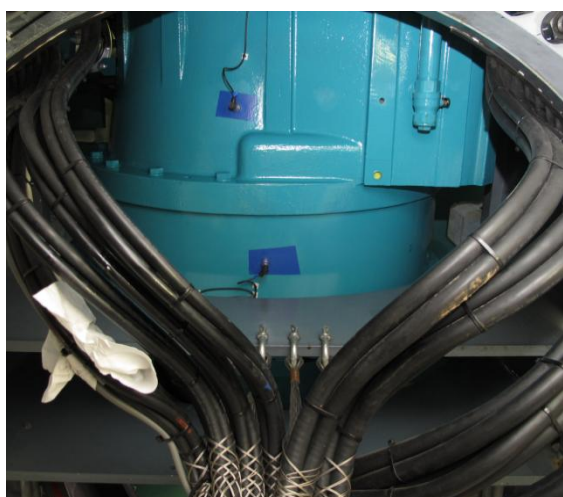


Figure 6.4: Drive train layout wind turbine for CMS-test

gearbox and generator are fixed separately on the nacelle, see Figure 6.1. In a partial integrated drive train, the gearbox is used as the second bearing for the rotor shaft instead of a separate second rotor bearing.

Figure 6.4 shows a scheme of the drive train. The rotor shaft is supported by one main bearing (MB, spherical roller bearing) and the input shaft of the gearbox. The gearbox contains one planetary stage and two spur wheel levels. The planetary gear is supported by two cylindrical roller bearings (A1 & A2), each of the three planets contains two double-row CRBs (B). Each shaft of the spur gears (C, D and E) is supported by two CRBs for radial and one four point contact bearing for axial loads. The generator contains two deep groove ball bearings (G1 & G2).



*Figure 6.5: Acceleration sensors (radial position) underneath the gearbox*

To measure the vibrations generated by the overrolling of the bearing parts and possible failures on their surfaces, two acceleration sensors were mounted radially on the generator, one for each generator bearing. Another four sensors were mounted radially on the gearbox. A seventh accelerometer is located axially on the generator side of the gearbox, where the four point contact bearings emit shock pulses in axial direction in case of damage. To attach the acceleration sensors, mounting pads were bonded to the

outside of the drive train components. The accelerometers were threaded on them, see Figure 6.5. The sensor positions were chosen in regard to the load direction of the bearings to detect the shock pulses in their direction of propagation if possible.

The eighth analog input channel of the data acquisition device is allocated to a laser distance sensor measuring the axial position of the gearbox that varies due to rotor thrust. It is supposed to use the eighth input channel for another acceleration sensor on the main bearing later as well.

While utilizing a condition monitoring system in serial application, system data such as wind speed, power and rotary speed of the generator can be received directly from the control system of the wind turbine. For our experimental setup and to be autonomous, own rotational speed sensors were installed using inductive and optical proximity switches and appropriate marks on the output shaft of the gearbox. With known transmission ratios of the gearbox, the rotational speed of each bearing can be calculated and utilized for an evaluation of the measured frequency spectrum regarding particular overrolling frequencies.



*Figure 6.6: Wired data acquisition device*

The data acquisition device shown in Figure 6.6 is operated stand-alone without the use of further computers on the wind turbine. Data measured periodically are saved on an internal storage and can be downloaded by help of a wireless data

connection regularly. Evaluation routines were programmed to analyze the vibrations signals in the order spectrum depending on different sensor positions and the particular bearing type and size.

### Preload of Screw Connections

Since most of the bearings in gearboxes of wind turbines are carried by housing parts that are bolted together, actual forces on bearings could be examined by measuring of preload forces on their screw connections. Different sensorized washers that enable the measurement of preload forces can be already purchased. These sensors use either strain gages or piezoceramics. However, both measurement principles as well as the determination of preload forces by ultrasonic measurement have characteristics that are not compatible with one of the following requirements for this particular application in OWT:

- measurement of both static and dynamic loads
- retrofitable
- durable
- simple design
- no influence on the stiffness of screw connections



Figure 6.7: Schematic configuration of a piezoresistive sensor

To match all requirements listed above, new sensors are developed by Fraunhofer IST from Braunschweig, see [6.4], and DLR in Cologne. These sensors consist of microstructured layers on a steel substrate, as shown in Figure 6.7, to take advantage of the piezoresistive effect as described first in [6.10]. The sensor layer based on diamond-like-carbon (DLC) allows to measure forces by means of a change of resistance

without significant deformations in contrast to strain gauges. It was intended to evaluate characteristics of these novel sensors, e.g. transmission behavior, influence of temperature and drift with static basic tests as well as in an application to measure static forces in a lifetime test rig for smaller bearings. The test rig was redesigned to test the sensors under static conditions during a student research project. The relevant sensor should match in screw size and measurement range to applications of screw connections for large size bearings and OWT. After basic investigations with static loads, the sensor ought to be applied to the large size bearing test rig to measure forces under dynamic conditions similar to those in OWT. Relevant screw connections on the large size bearing test rig are indicated in Figure 6.2. Some of them lay in direct flux of the rigs test force while the change of screw preload forces due to test forces is also affected by friction between components on other screw connections.

Unfortunately, despite lengthy efforts it was not possible to satisfactorily obtain sensors for a relevant screw size with an integrated conduction layer by Fraunhofer IST, where connection cables could be soldered directly, see Figure 6.8. Instead, coated washers were provided as an alternative solution by DLR in the end, where the electrical connection should be established by electrodes getting in touch with the coating. Figure 6.9 shows the utilized sensor arrangement with two coated washers and two electrodes. In addition, the behavior of existing experimental sensors for smaller screw connections (M8) as shown in Figure 6.8 was investigated at first.

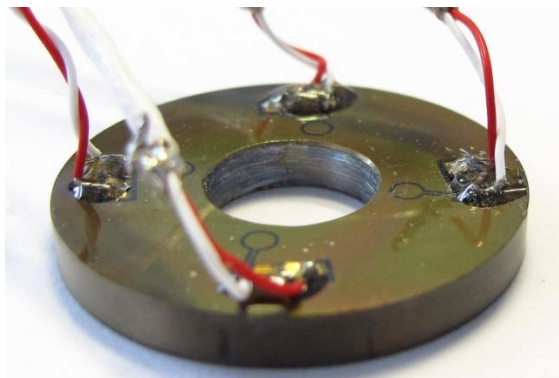


Figure 6.8: Piezoresistive sensor-washer for smaller screw sizes (M8) with directly connected cables

The change of electrical resistance of the piezoresistive sensor layer respectively the resulting voltage drop when exposed to load was measured by help of a quarter bridge. The bridge circuit was balanced before the test force was applied. To protect the junctions, where the connection cables are soldered to a conduction layer on the sensor for M8 screws, the load was induced in the active micro-structured sensor areas by help of an appropriately shaped shim.



Figure 6.9: Sensor washer for M16 screw: sensor system (left), coated washer (right)

#### 4.6.4 Results

##### Condition Monitoring of large Size Bearings of Wind Turbines

Before it was decided to perform measurements on a wind turbine, first measurements could be completed on the large size bearing test rig during scheduled tests with a spherical roller bearing (SRB). The plotted curves in Figure 6.10 represent

added up amplitudes of the characteristic overrolling frequencies and their harmonics of both inner and outer ring of the test bearing. The related vibration signal was recorded during non-continues investigations over several weeks with different operation conditions by an accelerometer on the housing of the large CRB, marked as III in Figure 6.4.

The magnitude of the pulse shock measured as acceleration signal depends on the particular operation condition. An increase in the characteristic value of the acceleration can be observed in Figure 6.10. This can be partly attributed to an increasing of speed and radial force with every test step after week two. However, the last tests were performed with identical operation conditions, so that the increase in the characteristic value of the inner ring can be assigned to a change in the raceway surface leading to more distinct pulse shocks. Another indicator for modifications of the inner ring raceway could be observed, too. The distinct pattern in the frequency order spectrum will be described when showing the measurements from the wind turbine.

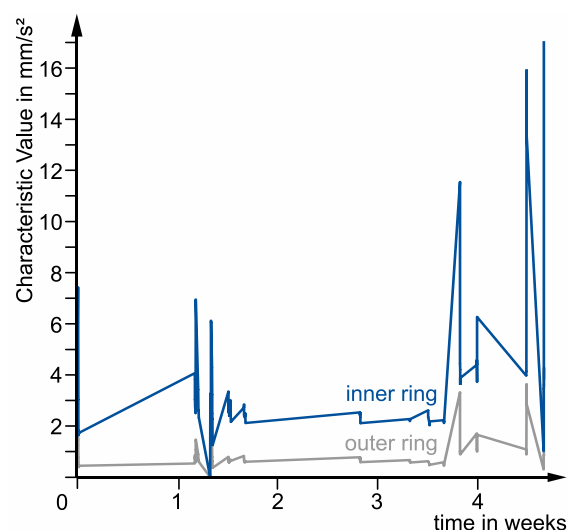


Figure 6.10: Envelope curve trend of a test bearing at the large size bearing rig

After dismounting, the test bearing showed no fatigue failures but small indentations due to particles in the raceways of the inner ring. Thus, by help of the condition

monitoring system, even small damages in the bearing raceway could be detected even before the functionality of the bearing was influenced.

Figure 6.11 shows the response on a single mechanical impulse of both conventional and experimental vibration pickup mounted respectively bonded on the large size bearing test rig as pictured in Figure 6.3. The plotted signal of the experimental pickup with an external amplifier shows a better transmission behavior with less damping due to a more direct coupling to the component. The fade out of the structural vibration as a result of the mechanical impulse applied on the housing of support bearing III, see Figure 6.2, can be observed longer and more clearly.

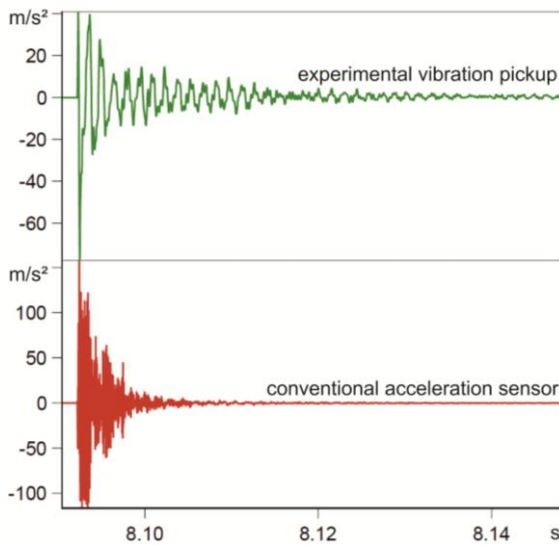


Figure 6.11: Impulse response in time domain of both conventional and experimental vibration pickup

During basic investigations, a distinct dependency of the transmission behavior as well as the signal-to-noise characteristic from the temperature could be observed. The cause of this effect could be the pyroelectric effect that describes a charge displacement due to temperature gradients in the piezoceramic. Conventional sensors using the shear effect of the piezoceramic are less sensible to this effect. With rising temperature, the meas-

ured amplitude of the vibration signal sank and the noise level rose.

The experimental pickup has no conductive housing in contrast to a conventional acceleration sensor. However, the observed effect of defined electromagnetic interferences on the measured signal was less pronounced. The interference was applied by help of an air-core coil close to both sensors and with selected frequencies. Instead of the test frequencies, the grid frequency affects the signal measured while using the experimental pickup distinctly. This interference cannot be assigned to the experimental sensor only, since the whole measurement chain can be affected.

Dynamic loads have an effect on the output signal of the experimental sensor since they deform the piezoceramic just like mechanical vibration in the object they are applied to. Static loads cannot be monitored with piezoelectric sensors. The small charge within the sensor generated by the charge separation as a result of the deformation of the piezoceramic is discharged continuously through the internal resistance of the charge amplifier or connected measuring instruments. The effect of dynamic loads could be observed by help of experimental pickups bonded to a structure together with strain gages. The structure was loaded resp. relieved rapidly to achieve a dynamic change of load on the experimental sensors.

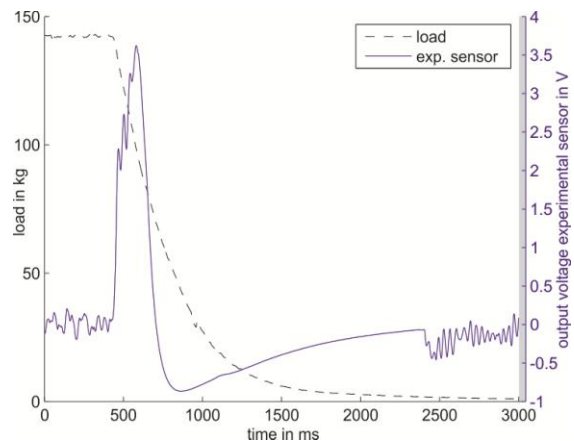


Figure 6.12: Measured load and output voltage of an experimental sensor while relieving a test load

The output voltage of one experimental sensor and its response to a relief of a test load is shown in Figure 6.12. The output signal rises with a change of load, overshoots in negative direction and approaches zero level. It can be observed, that the signal is smoothed in some parts of the signal. Since this behavior couldn't be noticed while measuring the output of the sensor directly, a characteristic of the charge amplifier has to be responsible. It seems to filter superimposed vibrations and therefore affects the recording of vibration signals negatively.

Additional investigations will be performed subsequent to this project e.g. regarding the performance of different charge amplifiers and the interaction of sensor and adhesive with oil and its components. The installation and operation of a condition monitoring system in a wind turbine gave knowledge not only about vibration analyzing in real application but also about requirements to the hardware of the CMS. The installation and use of a mobile network router for a transfer of measured data was necessary since the data infrastructure in the wind park was not sufficient and reliable enough at first. However, it also turned out, that stationary mobile network connections carry their own risks. To bypass power failures or

power cuts and overvoltage that occur occasionally, an uninterruptible power supply was installed, too.

The first measurement step was performed during a start-up of the wind turbine to detect natural frequencies of the gear box elements. Figure 6.13 shows Campbell diagrams of this start-up for two different sensor positions. The system's response as a frequency spectrum is displayed versus the rotational speed of the high speed shaft of the gear box. The color indicates the amplitude of the vibration level with blue for low and red for high levels. Lines parallel to the ordinate of the plot indicate speed independent eigenfrequencies while diagonal lines through the origin of the plot indicates speed dependant resonant frequencies resp. the rotational speed of the system. Both Campbell diagrams show different responses although the excitation of the system was identical. Vibration signals measured on the planetary gear level are exposed to more damping due to the effects already described. Signals with higher frequencies suitable to transmit pulse shock signals from bearings by a modulation are missing for the measuring position on the outside of the rotor gear, see Figure 6.13 on the right side.

As already mentioned before, the over rolling frequencies of single bearing parts

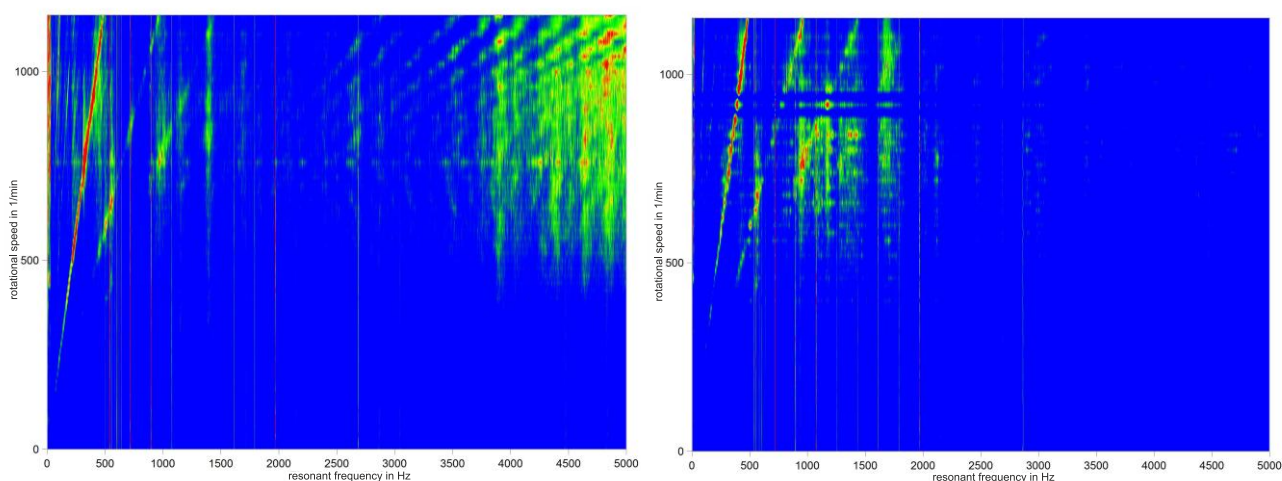


Figure 6.13: Campbell diagram of a start-up measured with an acceleration sensor near a spur wheel stage (left) and on the planetary stage (right)

depend on their geometry and the rotational speed of the bearing. Since the bearing sizes in a wind gear box decrease from rotor to generator with decreasing torques while the rotational speed increases, the over rolling frequencies of the single bearings and their related elements differ and can be therefore identified in a frequency or order spectrum of the vibration signal.

While operating with variable speed, the original vibration signal can be frequency modulated. By using an order tracking analysis instead of a frequency spectrum, the problems induced by a frequency modulation can be avoided. For this purpose, the actual rotational speed has to be measured as well. An order spectrum

contains a distribution of accelerations over multiples of the rotational speed instead of frequencies in Hz. Figure 6.14 shows two order spectra of datasets recorded with the same radial sensor on two different days of operation with similar rotational speed.

The measured signal of both measurements transferred to an order spectrum by the analysis procedure as described in [6.7] is plotted in blue. The characteristic order of the outer ring and three of its related harmonic orders are marked magenta. The areas framed in green contain the rotational speed and two harmonics (order one, two and three) as well as the characteristic order of the inner ring (order 10,85), its harmonic order

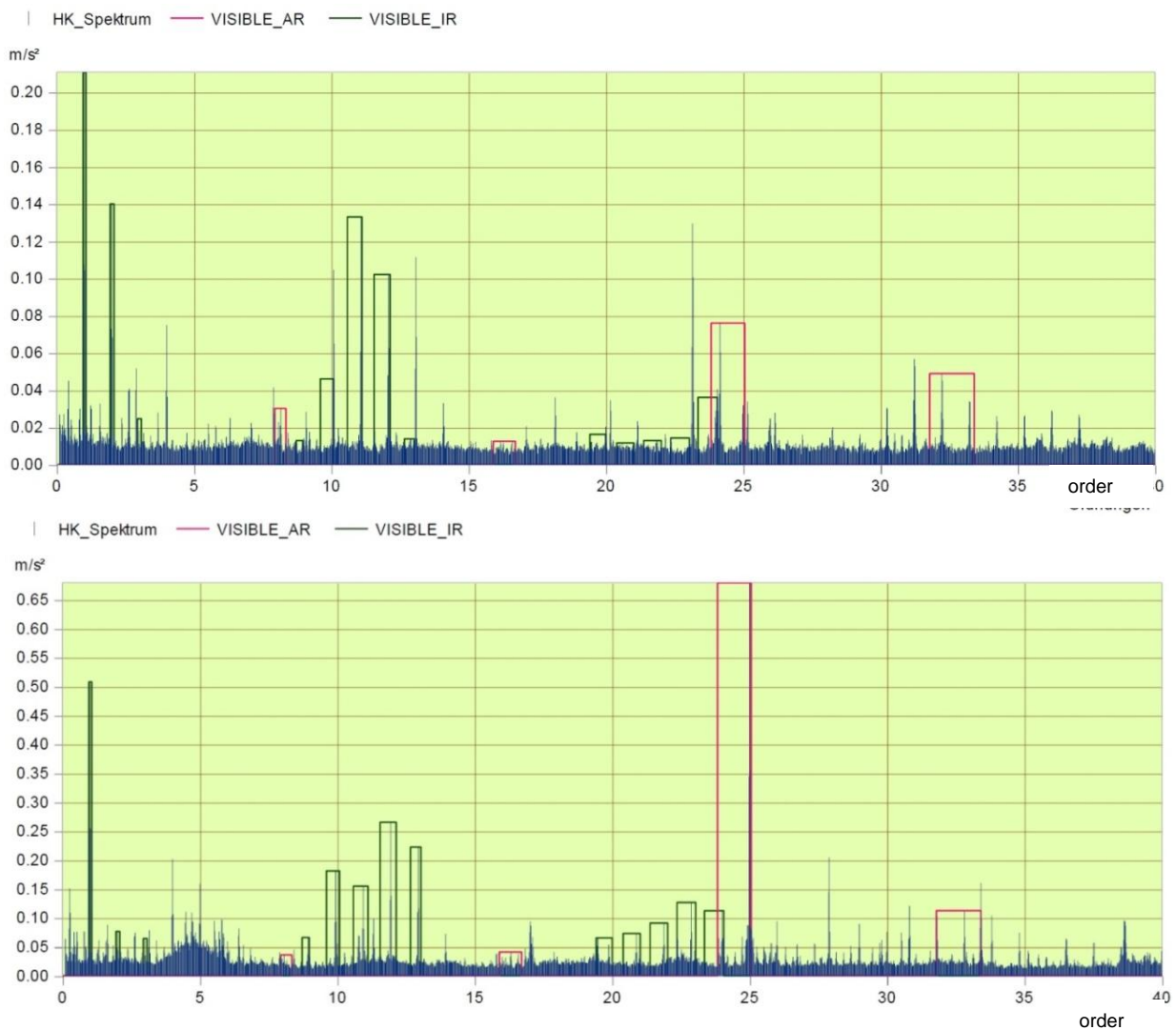


Figure 6.14: Order spectra based on measurements with acceleration sensor 1 on different days of operation: 18.07.2013 (top) and 28.10.2013 (bottom)

(order 21,7) and four sidebands (distance +/- one and +/- two orders from the inner ring frequency resp. the harmonics) for each of them. The over rolling frequencies belong to a cylindrical roller bearing on the high speed shaft.

An increase in the level of the signal components at the over rolling frequencies of the inner and outer ring can be identified. This variation also shows up in other datasets of the same period of time and sensor position. However, It could not be found in the characteristic spectrum of other bearings in the particular gear box.

Considering the experience made with smaller bearings and the experimental validation on the large size bearing test rig, the vibration levels don't seem to be high. Nevertheless, the pronounced appearance of the characteristic inner ring order with its harmonic orders and sidebands can already indicate a beginning modification of the bearing surface on the inner ring as experienced in earlier investigations with CMS. Unfortunately, from the point of view of

research, stagnation was observed after a growth of the inner ring specific signal level in the beginning of the measurements. Figure 6.15 shows the order spectrum of the same bearing for a multitude of measurement series recorded over seven months after the growth of the inner ring specific signals. The plot contains measurements at different rotational speeds of the drive train. It can be seen that the higher amplitudes - measured at nominal speed - of the characteristic over rolling frequencies resp. their harmonics of the inner ring (marked IR1 to IR7) and its sidebands as well as the frequencies of the outer ring (AR1 to AR6) are nearly constant over the recording time. The inner ring related over rolling frequency with its characteristic sidebands can be tracked to its seventh harmonic order easily. The rotary frequency and its harmonics occur in the region of the order spectrum marked with n. The measurements on the wind turbine will be continued after completion of this project. An acceleration sensor on the main

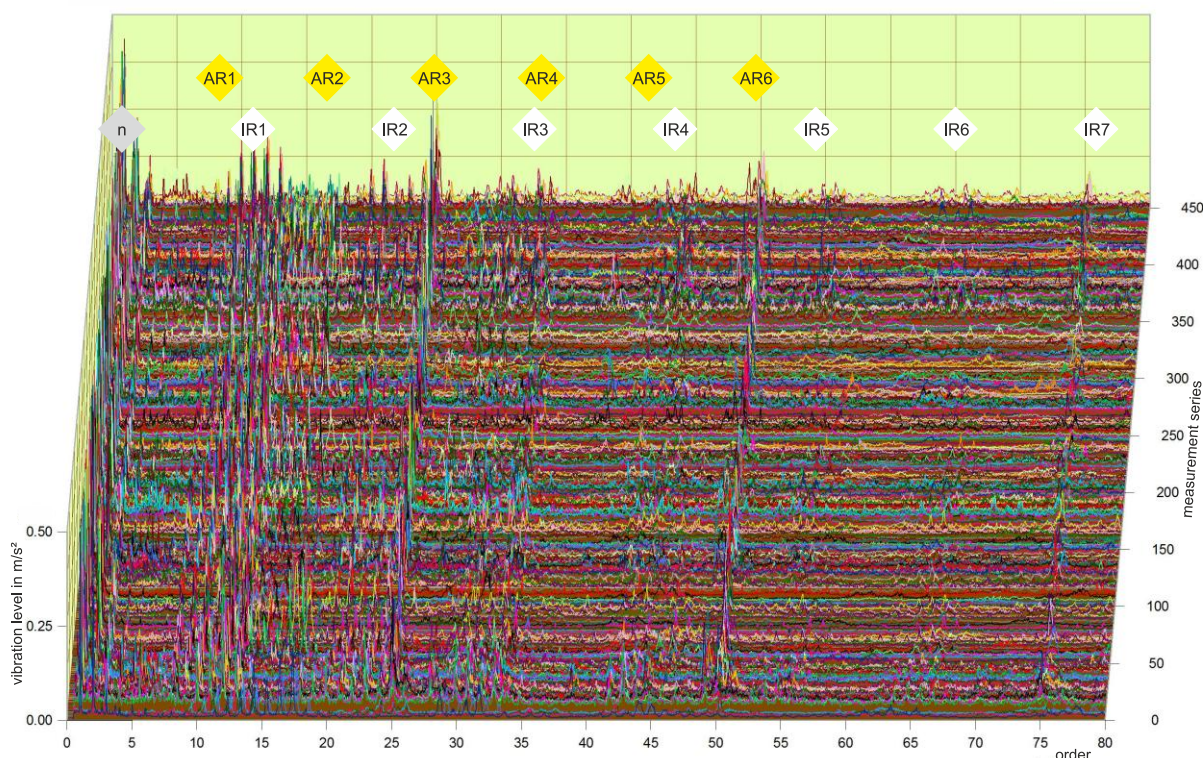


Figure 6.15: Waterfall display of measurement series with acceleration sensor 1 over a period of seven month

bearing of the wind turbine will be retrofitted in addition to a new attempt of using the local network of the wind park for data transfer. If a signal level of an over rolling frequency rises, the particular bearing will be inspected with a borescop to gain knowledge about the extent of the damage.

**Preload of Screw Connections**

While loading the preload force sensor for a M8-screw-connection with a static force by help of different weights, it was observed, that the measured bridge voltage approaches delayed to an end value. Therefore, the measurement was recorded in defined time steps after loading. The load was increased stepwise. The sensor washer was fully relieved after the highest load was reached and before the load and measuring procedure was repeated.

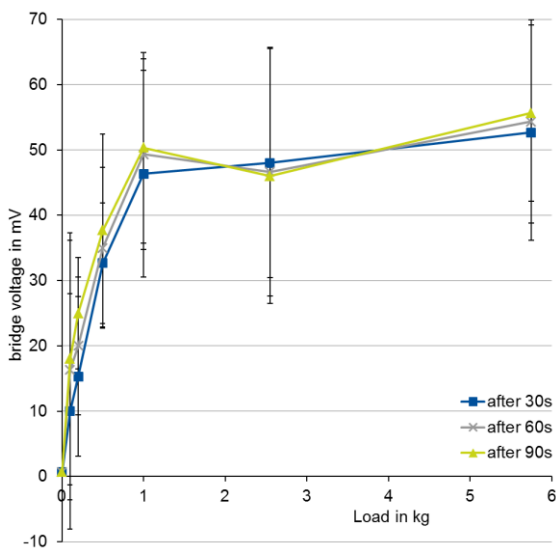


Figure 6.16: Measured bridge voltage on a piezoresistive force washer for M8-screw-connections for different loads

The bridge voltage measured for different loads and time steps is shown in Figure 6.16 as a mean value of several repetitions of each parameter combination with related error bars. It can be observed that the transmission behavior of the sensor is not linear. The sensitivity decreases with increasing load. The

measured bridge voltage varies further after the first time step. The statistic deviation of each measuring point is similar. Since the sensitivity decreases with increasing load, the accuracy is reduced with rising load. The loads examined for the small force sensor were low, since the loading capacity resp. the permissible surface pressure of the sensor layer was unknown. Since the contact shim is only supported on the microstructured areas as shown in Figure 6.8, the contact area is small.

The sensors for M16-screw-connections had to be conducted by additional washers appearing as electrodes. To preserve the stiffness of the screw connection, steel electrodes were used at first. Since the repeat accuracy of this sensor setup wasn't satisfactory enough, copper electrodes were used for further experimental investigations. Applying microstructured elements and conduction layers on the force washers for bigger screw connection was not pursued due to cost reasons.

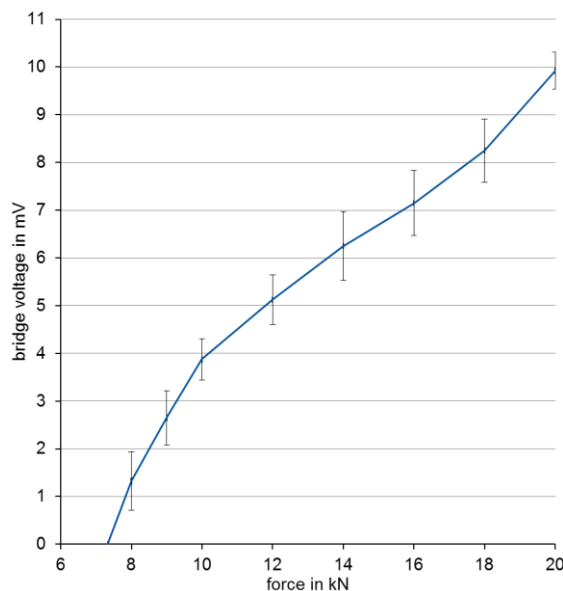


Figure 6.17: Measured bridge voltage (mean value) on a piezoresistive force washer for M16-screw-connections for different loads

The M16 sensor was loaded by help of a hydraulic press. A load cell was used in

the path of force in order to measure the applied loads. The sensor showed no delay in its response characteristic. Figure 6.17 contains the mean value of recorded bridge voltages from different measurements. The sensor was relieved between each measurement. The transmission behavior is nonlinear, too, but is not overly degressive. The statistic deviation pictured as error bar is smaller in relation to the slope of the plotted curve compared to the M8-force-sensor as long as the parts of the sensor setup were not moved against each other when relieving the force. Lacks of accuracy when changing the mounting position e.g. due to a rotation of sensor parts against each other can be observed on commercial donut load cells, too, see [6.2]. A calibration before the sensor is mounted in the particular application is therefore only possible with limitations to accuracy.

Irrespective of the statistic deviation, the changes in the bridge value due to a loading are small and therefore difficult to measure when the sensor is operated in the real application with convenient measuring equipment and interferences. The electrical bridge was operated with a bridge supply voltage of 30 V. A higher supply voltage, e.g. of 300 V, would result in a higher bridge voltage. This variation of the setup was nevertheless declined due to the effort necessary to ensure the security of the user.

Due to the unexpected delay until the sensor washers could be obtained, further examinations regarding influences on the output signal could not be performed within this project. Nevertheless, the investigations will be continued.

#### 4.6.5 Conclusions

A condition monitoring system based on the evaluation of vibration signals and a more precise and therefore more reliable analysis method could be tested successfully on a large size bearing test rig and on a real wind turbine. This method was developed in the research center and was

already used for an identification of bearing damages on a life time test rig for smaller bearings successfully. Measuring systems were installed and optimized regarding the particular demands of large size bearing test rig and wind turbine. This includes the installation of acceleration sensors, speed sensors and equipment for data transfer. By using the analysis method, modifications of the bearing surface due to particles could be detected on a test bearing of the large size bearing test rig. A peculiar pattern in the order spectrum of one of the 16 bearings of the gear box installed in the wind turbine has been found that could be an indication for an upcoming damage.

The condition monitoring system on the test rig will be utilized further to identify damages on the rigs components especially on those bearings that aren't supposed to be exchanged regularly. The measurements on the wind turbine will be continued and even extended to gain knowledge about the bearing behavior respectively their vibration signals in case of damages as well as the long time performance of the measuring systems.

Experimental vibration pickups were tested in an application on the large size bearing test rig in direct comparison to conventional acceleration sensors as well as in basic investigation aimed to identify disturbance variables. Due to a more direct coupling to the structural components housing the examined bearing, the experimental vibration sensor showed a better transmission behavior with less damping effects. However, the experimental sensor also had a higher sensitivity towards disturbance variables when compared to a commercial acceleration sensor. Some identified influences on the signal of the experimental vibration sensor can be assigned to its operating principle, other on the measurement chain. Further investigations will be performed regarding alternative charge amplifiers, the quantification of disturbance values and

their possible utilization as useful signal. The long term goal is to utilize an experimental acceleration sensor inside a wind gear box as close as possible to a bearing to achieve an even more early recognition of damages on bearings that are difficult to monitor by help of sensors on the gear box housing.

The examination with coated sensor washers for M16 screws showed satisfactory results regarding transfer curve and statistic deviation in the laboratory. However, further developments have to be considered to ensure an operation in practical application. Both sensors examined in this project did not have a

galvanic isolation protecting against electrical influences through the applied objects. Adjustments of the characteristic curve towards higher changes of resistance resp. higher bridge voltages could reduce the effect of influences on the measuring chain. An approach to utilize piezoresistive washers with a contactless data transmission based on RFID and specially developed software is shown in [6.5].

Further investigations will be performed to characterize the sensitivity of the measuring method regarding influences like temperature and electromagnetic compatibility (EMC).

## 4.7 Diagnostic Systems for Electronic Systems (WP 7)

### Institute of Drive Systems and Power Electronics

Meike Wehner

#### 4.7.1 Abstract

WP7 deals with early fault detection in wind turbine generators. The important types of faults and damages in electrical machines directly lead to characteristic changes in the electromagnetic air-gap field, whose dependency on position and time was investigated in previous works at IAL-AS. Using sensors such as search coil systems, the spatial dependence acts as a filter supporting the detection of a fault or defect with high distance between the signal in normal operation and in case of a fault, as well as the identification of the type of fault by signal frequency.

#### 4.7.2 Objective

In theory, the sensor signals are assumed to be zero in faultless wind turbines. In real applications, the signal fluctuation as well as the reachable ratio of the signal at fault and the value of faultless generators has to be evaluated. In addition, the influence of the generator type and the power electronic components concerning reliability has to be researched. The influence of the generator type (doubly fed induction generator, permanent magnet synchronous generator, etc.) as well as the influence of power electronic components concerning reliability of failure diagnosis has to be examined, too. For this reason, two diagnostic systems are being dimensioned, the data are evaluated, and based in this, appropriate design criteria are elaborated for this kind of diagnostic systems.

#### 4.7.3 Approach

Due to the increasing use of renewable energies, early fault detection in wind turbine generators becomes more and

more important. Especially in units with restricted accessibility like offshore wind turbines (OWT), an early detection of faults is necessary to avoid subsequent damages and long downtimes. WP7 focuses in the online fault detection in electrical machines using search coil systems. In recent years, a lot of methods for condition monitoring have been described, mostly focusing on turn-to-turn faults in stator or rotor windings, air-gap eccentricities or asymmetries. A review of the most established methods is given in [7.5] [7.3] [7.4]. Most of them use sensors coupled with algorithms and architectures, like neural networks, fuzzy logic, state-space observers measuring spectral components of voltage, current and power. All important types of faults and damages in electrical machines, such as interturn faults, short-circuit faults or rotor eccentricities, result in characteristic changes of the magnetic air-gap field. These changes can be used to detect a fault by search coils placed in the stator slots based on the voltage induced in them to identify the type of fault from the induced frequency. Search coil systems are especially suitable for the detection of interturn faults and eccentricities, since these faults have no or little influence on the quantities at the terminals of a machine and are therefore not easy to be detected from outside. [7.6] uses rotor-mounted search coils as reference and as a more sensitive alternative compared to field current based monitoring, however without detailed examination of the search coil system. Small residual eccentricities and other asymmetries can be caused by manufacturing inaccuracies or during assembly, while large eccentricities are generally due to damages during operation (e.g. bearing damages). Eccentricities cause an unbalanced magnetic pull, resulting in an even larger eccentricity which finally leads to rubbing of rotor against the stator bore. Among the faults occurring in stator windings, interturn shorts are the most difficult ones to be

detected. Interturn faults lead to high circular currents within one coil of the winding only, without significantly influencing the behavior at the terminals of the machine. Thus, they cannot be detected based on the terminal voltage or current. The thermal influence of the short-circuit current has the potential to deteriorate or destroy a machine's winding within minutes.

First of all, the magnetic air-gap field of an electrical machine during normal operation is described, as well as the field components which occur in case of an interturn fault or an eccentricity. In the following, the search coil system to be placed in the stator slots is presented and additional design criteria for the special case of high-pole machines are explained. Afterwards, the conclusions drawn from the stator-fixed system are transferred to a rotor-fixed search coil system. The results of the simulation are presented subsequently.

For the application in wind energy plants, three generator types are in common use. Besides doubly fed induction machines and salient pole synchronous machines, permanent magnet synchronous machines have been used more and more during the last years.

### Air-gap field

The flux density of the magnetic air-gap field of an electrical machine during normal operation results from the magnetic voltage at the air gap  $v(x, t)$  and the magnetic permeance of the air gap  $\lambda(x, t)$

$$b(x, t) = v(x, t)\lambda(x, t) = \sum_v B_v \cdot \cos(vx - 2\pi f_v t + \varphi_v) \quad (7.1)$$

with the fundamental wave of the number of pole pairs  $p$  and an infinite number of spatial harmonic fields, the number of pole pairs complying with

$$v = p \left( 1 + \frac{2m}{n} g \right) + g_2 2p \quad \forall g, g_2 \in Z \quad (7.2)$$

$B_v$  is the amplitude and  $\varphi_v$  the phase angle of a spatial harmonic of flux density,  $f_v$  is the frequency referred to the number of pole pairs  $v$ .  $m$  is the number of phases. For fault detection, it is necessary that no voltage is induced in the search coils during normal operation and that a fault can clearly be identified in case of a fault.

In case of a fault in the stator winding, all spatial harmonics of the flux density of the number of pole pairs

$$v = g \quad \forall g \in Z \quad (7.3)$$

are generated. Due to eccentric shifting of the rotor, additional permeance waves are produced by modulation of all spatial harmonics of the magnetic field during normal operation with the permeance waves due to eccentricity. According to [7.1], permeance waves with the order numbers

$$v = \tilde{v} \pm 1 \quad (7.4)$$

have the largest amplitude,  $\tilde{v}$  characterizing the order numbers during normal operation. In case of large eccentricities, the order numbers  $\tilde{v} \pm 2$  and  $\tilde{v} \pm 3$  are of importance. The frequency

$$f_v = f_{\tilde{v}} \pm f_{\epsilon} \quad (7.5)$$

depends on the type of shifting with

$$f_{\epsilon, se} = 0 \quad (7.6)$$

$$f_{\epsilon, de} = n \quad (7.7)$$

for static eccentricities with index  $\epsilon_{se}$  and for dynamic eccentricities with index  $\epsilon_{de}$ .  $n$  is the speed of the rotor. In case of a static eccentricity, the position of the smallest air-gap remains at the same spot on the circumference, as shown in Figure 7.1a. In case of a dynamic eccentricity, the position of the air gap rotates with angular velocity of the rotor (Figure 7.1b).

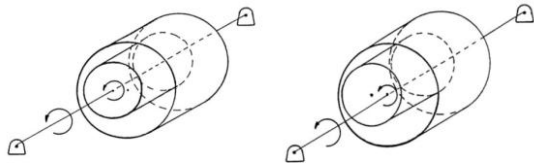


Figure 7.1a: Static eccentricity    Figure 7.1b: Dynamic eccentricity

### Stator-fixed search coil system

Fault detection using search coils is achieved based on the inductive effect of spatial harmonics of the so-called reference number of pole pairs  $\nu_R$  which does not exist when the machine operates normally, but which is caused by all faults to be detected. Based on the aforementioned correlations, the reference number of pole pairs  $\nu_R = p \pm 1$  seems suitable.

The parasitic spatial harmonics generated by the faults are detected by means of search coils placed in the slots of the stator core. The search coil system is designed in such a way that the reference number of pole pairs  $\nu_R$ , by which the respective fault shall be detected, induces with maximum amplitude, whereas the spatial harmonics in the air-gap field of the machine during normal operation do not induce any voltage in the search coil system. This is especially valid for the machine's fundamental field of the number of pole pairs  $p$ .

The complete calculation of the spatial harmonics in the air-gap field during normal operation and in case of a fault and the resulting design criteria for a stator fixed search-coil system are explained in detail for doubly fed induction machines in [7.7][7.2] as well as for electrical excited synchronous machines in [7.8]. In the following, only the basics are presented which are of importance due to the special case of search coil system design for high-pole machines as well as for the further development of rotor mounted search coil systems.

The voltage induced in the search coils depends on the number of conductors  $z_w$  and the position of forward and return

conductor  $\varphi_{hi}$  and  $\varphi_{ri}$  in the stator slots; according to [7.8], it is summed up for all numbers of pole pairs  $\nu$  to

$$\underline{U}_i = \sum_{f_\nu=\text{konst}} \underline{U}_{i\nu} \cdot e^{j\varphi_\nu} \quad (7.8)$$

with

$$U_{i\nu} = \sqrt{2} \cdot \pi \cdot f_\nu \cdot l \cdot R \cdot \xi_{\text{schr}_{k\nu}} \left| \underline{\zeta}_\nu \right| \cdot \frac{1}{\nu} \cdot B_\nu \quad (7.9)$$

$$\varphi_{u_\nu} = \pi - \varphi_\nu - \arg\{\underline{\zeta}_\nu\} \quad (7.10)$$

$$\underline{\zeta}_\nu = \sum_{i=1}^{z_w} e^{j\nu\varphi_{hi}} - e^{j\nu\varphi_{ri}} \quad (7.11)$$

$B_\nu$  is the amplitude and  $\varphi_\nu$  the phase angle of a spatial harmonic of flux density,  $f_\nu$  is the frequency,  $\xi_{\text{schr}_{k\nu}}$  is the skew angle of the search coil and  $\zeta_\nu$  is the effective number of conductors of one search coil referred to the number of pole pairs  $\nu$ ,  $l$  is the ideal length of the machine and  $R$  the radius of the bore. The induced voltage according to eq. (7.8) depends strongly on the fault position, i.e. on the position of the shorted turn or the narrowing of the air gap respectively, relative to the position of the search coil. To reduce this dependency, two identical search coils are used, and the resulting induced voltage  $U_{res}$  is split up by the use of the symmetrical components, the so-called positive and negative sequence components  $U_m$  and  $U_g$ . With the voltages  $U_{ia}$  and  $U_{ib}$  induced in the search coils  $a$  and  $b$ , splitting is made according to the relation

$$\underline{U}_m = \frac{1}{2} \cdot (\underline{U}_{ia} + j\underline{U}_{ib}) \quad (7.12)$$

$$\underline{U}_g = \frac{1}{2} \cdot (\underline{U}_{ia} - j\underline{U}_{ib}) \quad (7.13)$$

In recent years, the application of direct driven permanent magnet synchronous generators with large number of poles has increased. The design of search coil

systems for these high-pole machines thus bears a special challenge. Among the design criteria explained by [7.8], one important design condition is, that the stator slot number is a multiple of

$$\tilde{N}_1 = 2 v_R \quad (7.14)$$

For machines with 80 pole pairs, fundamental fields of the number of pole pairs of  $v_R = p \pm 1 = 79$  or 81 are excited in case of a fault, according to equation (7.14) leading to a minimum number of slots of the search coil  $\tilde{N}_1 = 2 v_R = 158$  or 162. The investigated permanent magnet synchronous generator has a number of stator slots of  $N_1 = 480$ , so that there is no common divisor of  $N_1$  and  $\tilde{N}_1$  to match with the slot number condition according to equation (7.14). For machines with high pole pair/slot number combinations, specific measures must be taken when designing search coil systems.

The selection of the reference number of pole pairs depends on the faults which shall be detected. According to equation (7.3) and (7.4) a reference number of pole pairs of  $v_R = p - 1 = 79$  is selected.

In case of an interturn fault, the appearing distortion of the air-gap field is locally restricted. For this reason, a search coil is required detecting the whole air-gap field along the bore, in order to detect an interturn fault independent of its position with a minimum of conductors.

The selectivity of a search coil can be characterized by the winding factor. The aim of the design is to reach a winding factor near 1 for the reference number of pole pairs  $v_R$ , while spatial harmonics during normal operation lead to a winding factor of zero, above all the fundamental field of the number of pole pairs  $p$ . The complex winding factor referred to the number of pole pairs is given by

$$\xi_v = \frac{1}{2z_w} \zeta_v \quad (7.15)$$

with the effective number of conductors

$$\zeta_v = \sum_{i=1}^{z_w} e^{jv\varphi_{hi}} - e^{jv\varphi_{ri}} \quad (7.16)$$

It depends on the number of conductors  $z_w$  and the position of forward and return conductor  $\varphi_{hi}$  and  $\varphi_{ri}$  in the stator slots. As can be seen from equations (7.15) and (7.16), the winding factor is maximum at distances between forward and return conductors (called coil pitch  $W$  below) of

$$W = \left(\frac{1}{2} + g\right) \frac{N_1}{v_R} \quad \forall g \in Z \quad (7.17a)$$

and minimum for

$$W = g \cdot \frac{N_1}{v_R} \quad \forall g \in Z \quad (7.17b)$$

Since the search coils are placed into the slot openings of the stator winding, the coil pitch must be an integer multiple of one stator slot pitch. For the investigated generator and the selected reference number of pole pairs, this leads to an optimum coil pitch of  $W = 240$  slots. For this slot pitch, the condition of equation (7.17b) is fulfilled for the fundamental number of pole pairs  $p$ , so that the fundamental field does not induce in the search coil.

According to [7.8], the two identical search coils, splitting the resulting induced voltage into positive and negative-sequence component, are ideally shifted according to

$$\varphi_M = \frac{\pi}{2v_R} \quad (7.18)$$

by half of the pole pitch of the reference field. In this case, the forward conductor of the second system is below the maximum of the reference field's excitation curve. As shown in [7.9], it is unproblematic to use multiples of this shifting. Even for high-pole machines, shifting is thus possible as an integer multiple of one slot pitch. For the investigated generator, the first

maximum of the field excitation reaching an integer slot position is  $\varphi_M = g \cdot \frac{\pi}{2\nu_R} = 120$  slots. Figure 7.2 shows the conductors as they are distributed in the search coil system based on the above made considerations. The search coil system consists of two identical search coils with  $z_w = 2$  turns each, a coil pitch of  $W = 240$  slots, circumferentially shifted against each other by  $\varphi_M = 120$  slots.

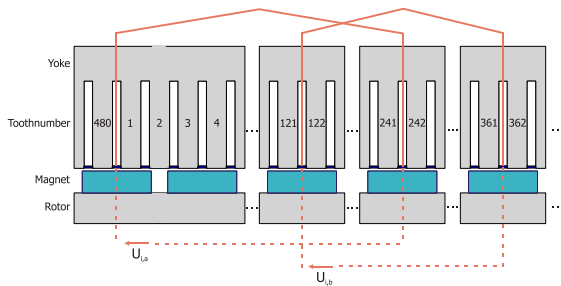


Figure 7.2: Distribution of conductors in the search coil system

### Rotor-fixed search coil system

The need for two identical search coil systems and the resulting duplication of conductors required arises from the dependency of the induced voltage on the fault position as well as on the characteristic component induced with the same reference frequency for different faults. To avoid these disadvantages, to minimize the complexity of the search coil system as well as to improve unambiguous fault detection in synchronous machines, a rotor-mounted search coil system was designed. Since the coil rotates together with the rotor, it is not necessary that the search coil surrounds the machine's complete circumference. Moreover, no second search coil system is necessary. The considerations about the optimum coil pitch remain valid. The term for the value of the induced voltage proposed in equation (7.9) can be enhanced for the rotor-fixed search coil as follows

$$U_{iv} = \sqrt{2} \cdot \pi \cdot f_{2\nu} \cdot l \cdot R_{rot} \cdot \xi_{schrk_v} \left| \underline{z}_v \right| \cdot \frac{1}{\nu} \cdot B_{vR} \quad (7.19)$$

With

$$B_{vR} = B_v \frac{2 \cdot \left( \frac{R}{R_{rot}} \right)^{|\nu|+1}}{\left( \frac{R}{R_{rot}} \right)^{2|\nu|} + 1} \quad (7.20)$$

The frequency converted into rotor-fixed values is given by

$$f_{2,\nu} = f_v - n \cdot \nu \quad (7.21)$$

with the rotational speed  $n$ . An example for the distribution of the conductors in the rotor-fixed search coil system is shown in Figure 7.3.

### Signal-to-noise-ratio

For an adequate condition monitoring system it is essential, that the measured variable in case of a fault changes considerably compared to normal operation in order to avoid a false activation of the system. In theory, it is presumed for normal operation that no voltage is induced in the search

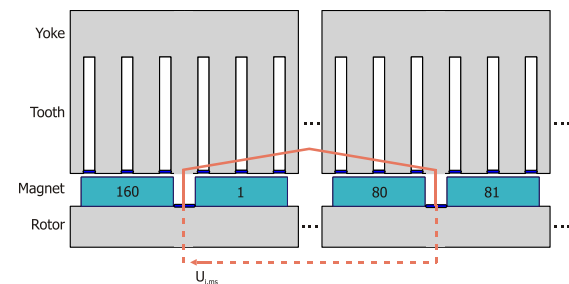


Figure 7.3: Distribution of conductors in the rotor-fixed search coil system

coil system. In reality, residual eccentricities due to manufacturing and mounting tolerances cannot be avoided. So voltages are induced in the search coils. For this reason, it is investigated by means of interturn faults, in how far existing residual eccentricities have an effect on the fault detection and how large is the signal to noise ratio of the sensor signal, when the fault occurs, to the value in faultless mode. In order to determine the signal to noise ratio (SN) the voltage induced at interturn fault with static

eccentricity  $U_{ieff}$  are compared to the voltage induced  $U_{ieff,sta}$  at residual eccentricity only.

$$U_{ieff,SN} = \frac{U_{ieff}}{U_{ieff,sta}} \quad (7.22)$$

#### 4.7.4 Results

In the following, the design criteria of search coil systems described before are incremented for two different types of generators. First a search coil system is designed for a 900 kW doubly fed induction machine with two pole pairs and 72 stator slots. Afterwards, the conclusions drawn from search coils systems for multi pole permanent magnet synchronous machines are examined with a 3 MVA permanent magnet synchronous generator having 80 pole pairs on the rotor and 480 stator slots. The fault simulation and the evaluation of the voltage induced in the search coil systems are realized based on the analytical program ALFRED developed at the institute for drive systems and power electronics.

##### Doubly-fed induction generator

For the doubly-fed induction generator the examined search coil system is designed, based in the aforementioned correlations, for a reference number of pole pairs  $v_r = p - 1$ . As a compromise between the number of conductors and the selectivity a two slot winding is selected whereby the coils are shifted by 12 slots against each other. The coil pitch is selected to be  $W = 36$ . The distribution of the search coils in the stator slots is shown in Figure 7.4. The frequency analysis of the voltage induced for a static eccentricity of 30 % of the air-gap width leads to frequency components with uneven multiples of line frequency, the amplitude being largest at line frequency

(Figure 7.5). For the relevant line frequency, the separation of the induced voltage in its symmetrical components shows a purely positive-sequence component.

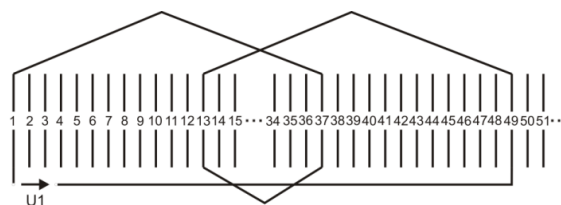


Figure 7.4: Distribution of the search coils in the stator slots

It is thus a good indicator for a static eccentricity. Figure 7.6 shows the voltage induced in the search coils for static eccentricities of 10% to 40% of the air gap width. The amplitude of the voltage increases proportionally to the eccentricity. Figure 7.7 shows the frequency spectrum of the voltage induced in the search coils at dynamic eccentricity  $\epsilon_{dyn} = 30\%$ . Based on the component with 25 Hz at  $s=0$  which is dominating in the voltage spectrum, a dynamic eccentricity can clearly be detected. The voltage induced increases proportionally to the dynamic eccentricity, so that here too, clear conclusions can be drawn about the degree of eccentricity (Figure 7.8). By using a 2-phase search coil arrangement, the voltage induced is independent of the fault location for static as well as for dynamic eccentricities. An interturn fault was simulated with a fault current of  $I_{fe} = 1000$  A. As it can be seen in Figure 7.9, only significant voltages with line frequency are induced. The negative-sequence component of the induced voltage serves as indicator of an interturn fault, because the positive-sequence component can also be observed by static eccentricities.

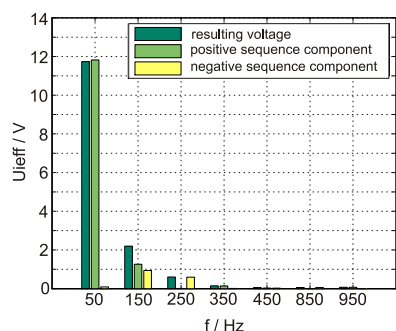


Figure 7.5: Frequency analysis of the voltage induced for a static eccentricity

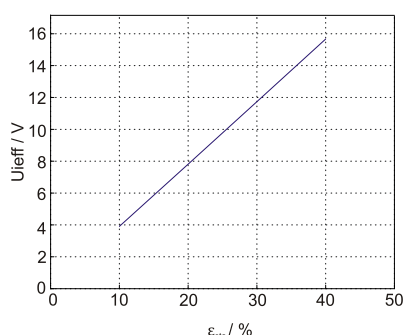


Figure 7.6: Induced Voltage for different static eccentricities at line frequency

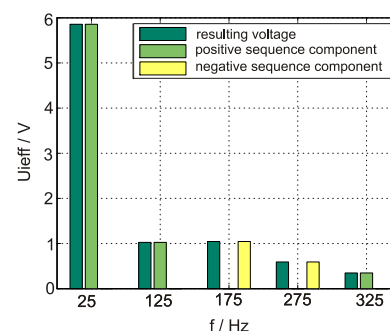


Figure 7.7: Frequency analysis of the voltage induced for a dynamic eccentricity

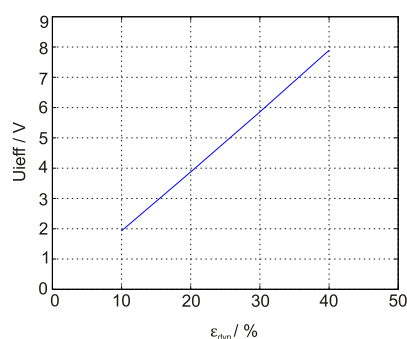


Figure 7.8: Induced Voltage for different dynamic eccentricities,  $f = 25$  Hz

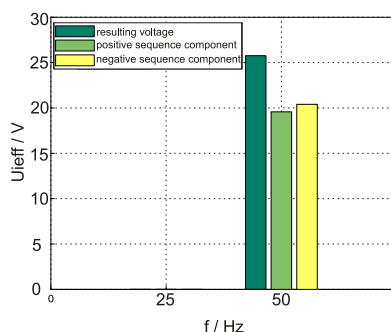


Figure 7.9: Frequency analysis of induced voltage for an interturn fault

### Signal-to-noise ratio DGASM

In order to evaluate the influence of residual eccentricities on the fault detection of interturn faults and to determine the signal to noise ratio, an interturn fault is superimposed by a low eccentricity. First, the effect of a residual static eccentricity was examined. The short-circuit current assumed is  $I_{fe} = 1000$  A at line frequency, the residual static eccentricity was assumed with  $\epsilon_{sta} = 20$  % and fault location  $\varphi_{sta} = 30^\circ$ . For both failures, the characteristic frequency of the induced voltage is the line frequency. In case of a static eccentricity however, the induced voltage has negligible negative-sequence component at line frequency, which hereby is a good indicator for the detecting of interturn faults with high signal-to-noise ratio, as shown in Figure 7.10. Next, the effect of an existing dynamic eccentricity on the voltage

induced in the search coils in case of an occurring interturn fault was examined. The dynamic eccentricity was assumed with  $\epsilon_{dyn} = 20$  % and a fault location of  $\varphi_{dyn} = 30$  %, the short-circuit current with  $I_{fe} = 1000$ A. The indicator for a dynamic eccentricity is an induced frequency of

$$f = f_1 \left\{ 1 - \frac{1}{p} (1 - s) \right\} \quad (7.23)$$

which results in a characteristic frequency of 25 Hz for the simulated generator. There is no effect on the detection of an occurring interturn fault. Figure 7.11 shows the frequency for an interturn fault with existing dynamic eccentricity. The difference between the characteristic frequencies also simplifies the detection of an occurring dynamic eccentricity and vice versa. As seen in Figure 7.5 a static eccentricity results in

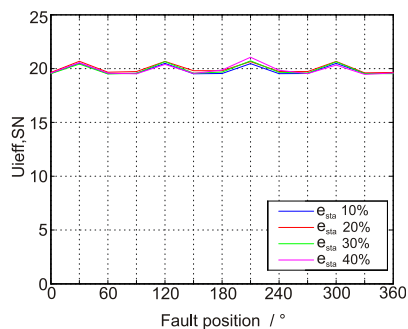


Figure 7.10: Signal-to-noise ratio of negative-sequence component of induced voltage for an interturn fault with static eccentricity

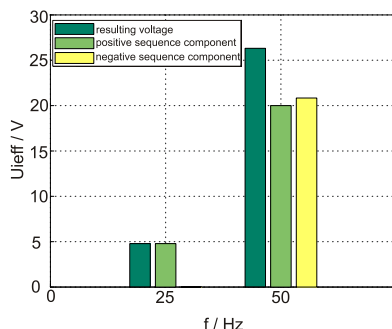


Figure 7.11: Frequency analysis of induced voltage for an interturn fault and dynamic eccentricity

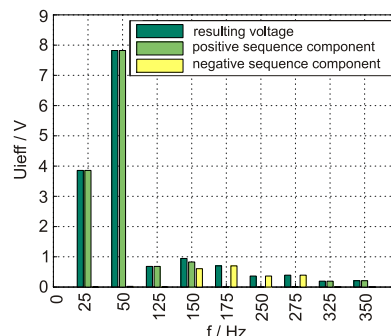


Figure 7.12: Frequency analysis of induced voltage for a dynamic eccentricity and an existing static eccentricity

frequencies of induced voltage with line frequency. Hence the measuring-relevant frequencies of both kinds of eccentricities are not influenced by each other and both failures can be detected with high signal-to-noise ratio. The frequency analysis of combined static and dynamic eccentricity is shown in Figure 7.12.

### Permanent magnet synchronous generator

The design of the search coil system for the investigated high-pole permanent magnet synchronous generator is related to eq. (7.15) to (7.18), resulting in the selected reference number of pole pairs  $\nu_R = p - 1 = 79$ , the optimal coil pitch  $W = 240$  slots and the shift of  $\varphi_M = 120$  slots between two identical search coils. Figure 7.13 shows the voltage induced in the stator fixed search coil system for a shorted turn for different fault positions distributed along the circumference of the machine (given in slots). According to equation (7.15), the largest component of the induced voltage is induced by the spatial harmonic of flux density of the order number  $\nu = 1$  with the frequency  $f_\nu = f_1$ . It can be seen that the induced voltage depends on the fault position. If the fault position is directly above the forward or return conductor of a search coil, the resulting voltage is zero. Considering the positive- or negative sequence system, dips can also be observed at these positions, but the

induced voltage at each position is large enough to ensure unambiguous fault detection. Besides the type of fault, it is also desirable to evaluate the magnitude of the fault. As can be seen in Figure 7.14, the induced voltage directly depends on the level of short-circuit current, but is also influenced by the dependency of the fault position. In case of a static eccentricity (index  $st$ ) along the circumference of the machine, according to equation (7.16), the largest components of the induced voltage are induced into the search coil system with the number of pole pairs  $\nu_R = 79$  and the frequencies  $f_\nu = f_1 \pm f_\epsilon$  with  $f_{\epsilon, st} = 0$ . Similar to an interturn fault, the resulting voltage strongly depends on the fault position. As shown in Figure 7.15, the positive sequence component is on the contrary nearly constant and can thus be used for fault detection. According to Figure 7.16, the level of the induced voltage is a measure to evaluate the level of static eccentricity. As both interturn faults and eccentricities results in the characteristic frequency  $f_\nu = f_1$ , unambiguous fault detection is problematic. To avoid this problem in [7.10] the use of two separate search coil systems is proposed. Since the separate search coil systems are quite complex however, a rotor-fixed system is proposed in the following.

To minimize the complexity of the search coil system as well as to improve fault

detection, a rotor-mounted search coil system was designed. In case of an interturn fault in the stator winding, the largest value of the voltage induced in the search coil system is according to equation (7.15) induced for small order numbers  $\nu$ . With respect to (19) the stator fixed frequency  $f_\nu = f_1$  leads in the rotor to the characteristic frequencies

$$f_{2,WS} = 11,85 \text{ 1/s for } \nu = 1$$

$$f_{2,WS} = 12,15 \text{ 1/s for } \nu = -1.$$

According to Figure 7.17, the value of the induced voltage is an ambiguous measure for the fault current level. Compared to a stator-fixed search coil system, the induced voltage does not depend on the fault position. In contrast to stator-mounted

search coil system, no search coil is required which surrounds the machine's complete circumference. It is sufficient when it covers just part of it, because the coil rotates together with the rotor. In case of static eccentricities, the interesting numbers of pole pairs for a rotor mounted search coil system are

$$\nu = -5p \pm 1 \text{ and } \nu = -11p \pm 1$$

with the corresponding frequencies

$$f_{(\nu = -5p+1 = -399)} = 71,85 \text{ Hz}$$

$$f_{(\nu = -5p-1 = -401)} = 72,15 \text{ Hz}$$

$$f_{(\nu = -11p+1 = -879)} = 143,85 \text{ Hz}$$

$$f_{(\nu = -11p-1 = -881)} = 144,15 \text{ Hz}.$$

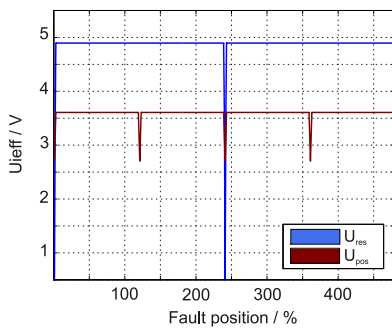


Figure 7.13: Voltage induced in the search coil system in case of an interturn fault for different fault positions

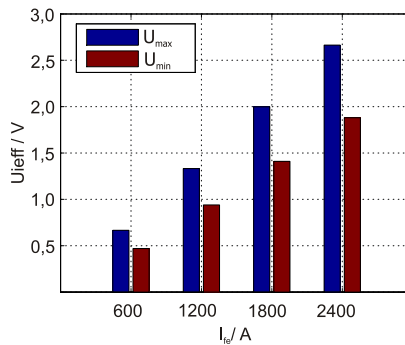


Figure 7.14: Minimum and maximum positive-sequence component of the induced voltage for different fault currents

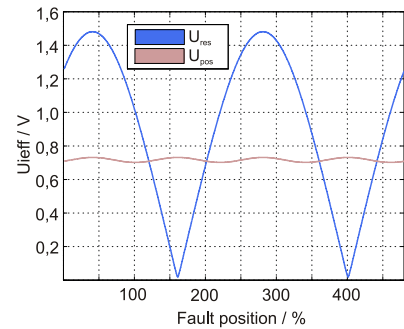


Figure 7.15: Induced Voltage in case of a static eccentricity of 30 %

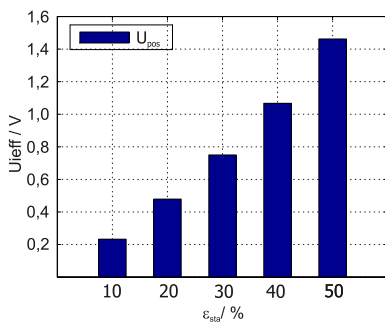


Figure 7.16: Positive-sequence component of the induced voltage for different levels of eccentricity

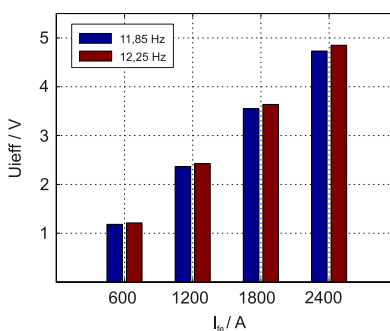


Figure 7.17: Induced voltage in case of an interturn fault and different fault currents for main frequency components

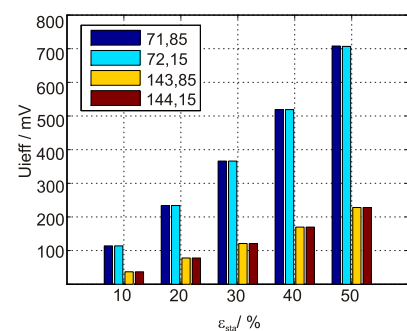


Figure 7.18: Induced voltage for different levels of eccentricity for main frequency components

According to Figure 7.18, the value of the induced voltage is a measure for the level of eccentricity. Similar to an interturn fault, no dependency of the induced voltage on the fault position can be observed. For rotor-mounted search-coil systems, different faults thus lead to different characteristic frequencies. In this way, different faults can unambiguously be identified without the use of a second search coil system to observe the positive- and negative sequence system.

### Signal-to-noise ratio PMSM

To evaluate the influence of residual eccentricities on fault detection of the investigated PMSM the interturn fault is superimposed by a low residual eccentricity. Figure 7.19 shows in comparison the frequency analysis of the voltage induced in the search coil system for a pure interturn fault (a), a pure static eccentricity (b) as well as to an interturn fault combined with an existing residual eccentricity (c). It can be seen that residual eccentricities have no effect on interturn fault detection.

## 4.7.5 Conclusions

Within WP7 early fault detection of wind turbine generators by using search coil systems are analyzed.

First of all, a search coil system was designed for a doubly fed induction generator

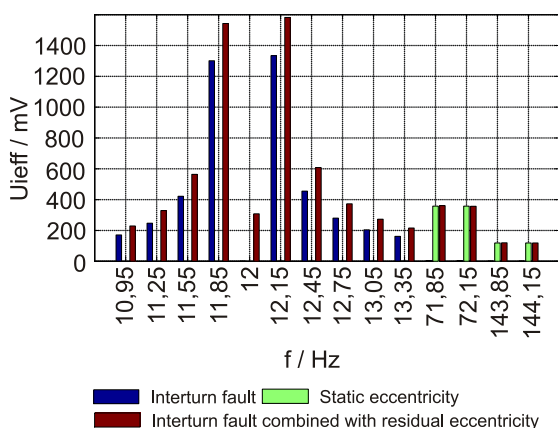


Figure 7.19: Frequency analysis of induced voltage

and the ability of detecting interturn faults, even turn-to-turn faults and eccentricities was shown. Considering the frequency analysis of the voltage induced in the search coil system, static eccentricities can be detected by the positive sequence component at rated frequency. Whereas a dynamic eccentricity is indicated by frequencies respectively to the mentioned equation, which leads to half of rated frequency at the considered generator. In addition to that the negative sequence component of rated frequency of the voltage induced in the search coil system points to a fault of the stator winding. To evaluate the signal to noise ratio, it was determined, in how far the detection of faults will be influenced by existing static or dynamic eccentricities. In case of a static eccentricity, interturn faults can be detected by evaluation of the negative-sequence component of rated frequency. As dynamic eccentricities result in a different characteristic frequency than interturn faults and static eccentricities, the detection of these faults is not effected by an existing dynamic eccentricity.

In recent years, the application of direct driven permanent magnet synchronous generators with large number of poles increases. Based on previous research of search coil systems for synchronous machines, the special challenges of the design of search coil systems for permanent magnet synchronous machines with high pole pair/slot number combinations are determined. In case of a shorted turn in the stator winding the largest component of the search coil voltage is induced with rated frequency. Considering the positive- and negative sequence component the induced voltage directly depends on the level of short-circuit current, but is also influenced by the dependency of the fault position. For the detection of static eccentricities, the positive sequence component of the induced voltage is an indicator, independent of the fault position.

To minimize the complexity of the search coil system as well as to improve fault detection, a rotor-mounted search coil system was designed. For rotor-mounted search-coil systems, different faults thus lead to different characteristic frequencies. In this way, different faults can unambiguously be identified without the use of a second search coil system to observe the positive- and negative sequence system. In order to evaluate the

influence of residual eccentricities on the fault detection and to determine the signal to noise ratio, an interturn fault is superimposed by a low eccentricity. As the characteristic components respectively the frequency component of the induced voltage are different for the examined faults, unambiguous fault detection is ensured, even if residual eccentricities are taken into account.

## 4.8 Reliability of the Grid Connection (WP 8)

Institute for Drive Systems and Power Electronics (IAL)

Felix Fuchs

Institute of Electric Power Systems  
Division of Power Supply (IEE)

Stefan Brenner

### 4.8.1 Abstract (IAL)

Regarding the reliability of offshore wind turbines, the electrical system and the grid connection is also an important part to analyse. Together with work package 6 and 7, the mechanical and electrical topics are covered.

The work package 8 is a collaboration between the Institute for Drive Systems and Power Electronics and the Institute of Electric Power Systems. The overall aim is to evaluate different grid connection topologies from the probabilistic point of view concerning the reliability. The two mentioned institutes are on the one hand specialized in the generator and its frequency converter and on the other hand in the grid connection. The probabilistic reliability model of the whole electrical system is implemented by the Institute of Power Systems, while the Institute for Drive Systems and Power Electronics analyses reliability models for power electronics within the grid connection.

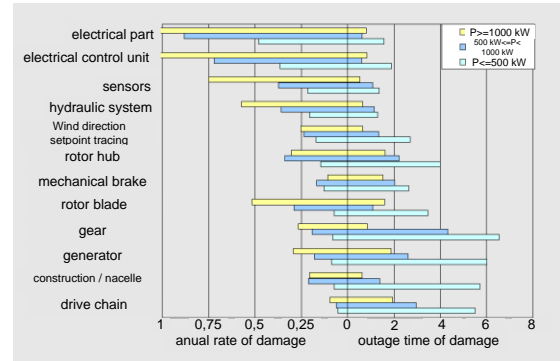


Figure 8.1: Frequency of damage and corresponding outage time of wind power plants sorted by components for different output power [8, 10]

### 4.8.2 Objective (IAL)

In the field of electrical power supply the reliability of the system plays an important role. For the investor the breakdown of a wind turbine always means losses by reason of costs of repair and loss of (financial) compensation for energy fed into the grid. Especially in the field of offshore wind parks a breakdown leads inevitably to long down times, because repair times are longer due to limited accessibility. In Figure 8.1 it can be seen, that the higher the power of the wind turbines is, the more often the electrical part of the system fails. It is thus most important to investigate the reliability of the electrical system of large (offshore) wind turbines and their grid connection.

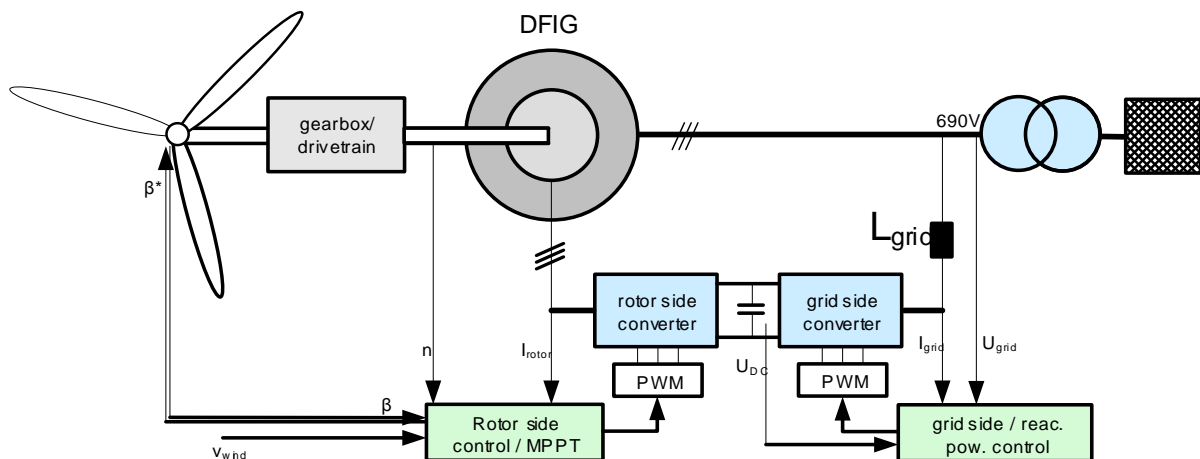


Figure 8.2: Top: DFIG wind turbine system

The wind as a stochastic factor is an important input factor that determines load cycles and stress of the wind turbine. This gives also a motivation to examine the system from a probabilistic point of view.

### 4.8.3 Approach (IAL)

At the Institute for Drive Systems and Power Electronics the focus of the project is on the converter of offshore turbine.

Weak elements of the power transmission chain in a wind turbine are the power semiconductor modules of the frequency converter [8.2]. Due to this fact, the first aim is to set up a reliability model for the failure of the power semiconductors of the converter. In offshore wind turbines, mainly two topologies of generator-converter systems exist: The doubly-fed induction generator (DFIG) and the permanent magnet synchronous generator (PMSG). In this project, the focus lies on the DFIG system (Figure 8.2). The influence of operating points on the lifetime of power semiconductor modules is investigated first. The most important factor influencing their lifetime is the varying junction temperature [8.2].

#### Doubly-fed induction generator

The junction temperature is dependent on the voltage and current setpoints and switching frequency of the converter. As software Matlab/Simulink/PLECS is applied. With this software, it is possible to simulate current and voltage operating points and their corresponding junction

temperature variation of the power semi-conductors. To receive the link to the lifetime, the following procedure is pursued (Figure 8.3):

First, the junction temperature swings of the module (power semiconductors) via the wind speed are computed in steady state operation. In the next step the wind speed data (*FINO* station [8.16]) is included. From this data, the operating time in 2009 for each wind speed is calculated. The number of cycles is divided in temperature swing frequency and mean temperature. This is fed into a "cycles-to-failure-statistic" for the power semiconductor modules (taken from the LESIT project [8.8] or given by the manufacturer). For every wind speed (discretized at 0,1 m/s) the consumed percentaged lifetime is computed. This is summed up linearly to a yearly consumed lifetime.

A simulation model of the converter is extended with the thermal equivalent circuit of a standard low voltage module taken from its data sheet. A standard cooling system with the ambient temperature set to 40 degree is chosen. As input of this circuit, the absorption power  $P_v$  of the power semiconductors must be computed.

It is composed of temperature dependent turn off, turn on and conducting losses specified in the data sheet. A wind turbine model of a 2 MW DFIG is taken (for system parameters see Tab. 1). The control system always tracks the maximum

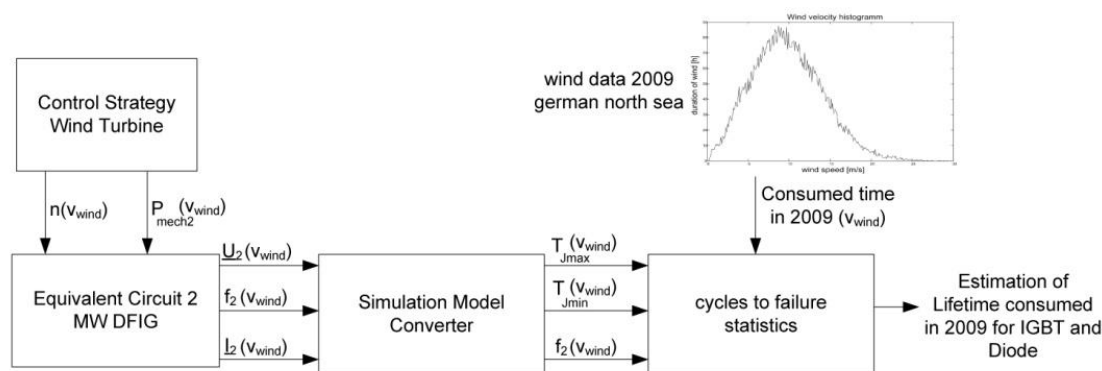


Figure 8.3: Procedure for lifetime estimation of the power module.

of the  $c_p$ -characteristic of the wind turbine assumed (fixed pitch angle [8.15]). An example junction temperature swing of the machine side converter is shown in Figure 8.4 for a wind speed  $v_{wind} = 7.8$  m/s.

Table 8.1: System Data.

Symbol	Quantity	Value
$P$	Rated Power	2 MW
$U_L$	Line voltage (phase-to-phase, rms)	690 V
$\omega$	Grid frequency	$2\pi 50$ Hz
$p$	Pole Pairs	2
$f_{s,machine}$	Switching frequency machine side converter	3 kHz
$n$	Gearbox ratio	1:72,65
$R$	Turbine radius	37 m
$v_{min}$	Cut-in wind speed	3.5 m/s
$v_{rated}$	Rated wind speed	12 m/s

It can be seen that in steady state the temperature oscillates with the frequency of the rotor current. The junction temperature of the IGBT and diode of one phase leg is taken and mean, minimum and maximum values are extracted. Two power modules were taken.

One module is dimensioned to the simulated operating points and another is oversized by a factor of two. The results are provided in the next chapter.

### Dynamic Model of a DFIG wind turbine

A dynamic model of a DFIG wind turbine is realized to get the dynamic thermal load of the power semiconductors in the converter. This will be described in the following. The first aim is to find a suitable power characteristic ( $c_p$ -characteristic). Several characteristics are found in literature.

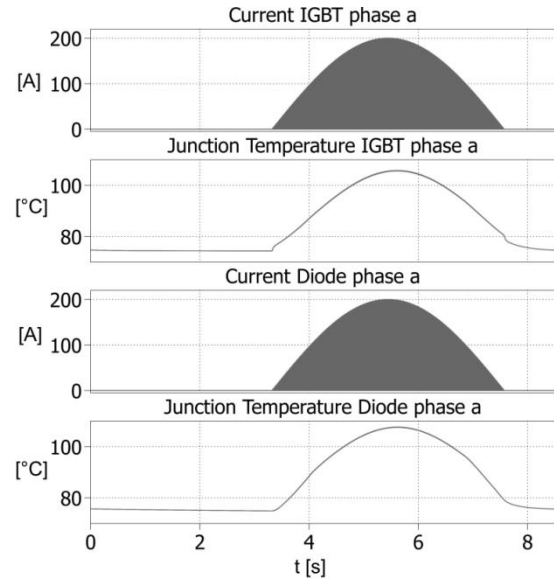


Figure 8.4: Example: Currents and junction temperatures at steady state with  $v_{Wind} = 7.8$  m/s

They are described by the following equations:

$$c_p(\lambda, \beta) = c_1 \left( \frac{c_2}{\lambda_i} - c_3 \beta - c_4 \beta^{c_5} - c_6 \right) e^{-\frac{c_7}{\lambda_i}} \quad (8.1)$$

$$\frac{1}{\lambda_i} = \frac{1}{\lambda + c_8 \beta} - \frac{c_9}{\beta^3 + 1} \quad (8.2)$$

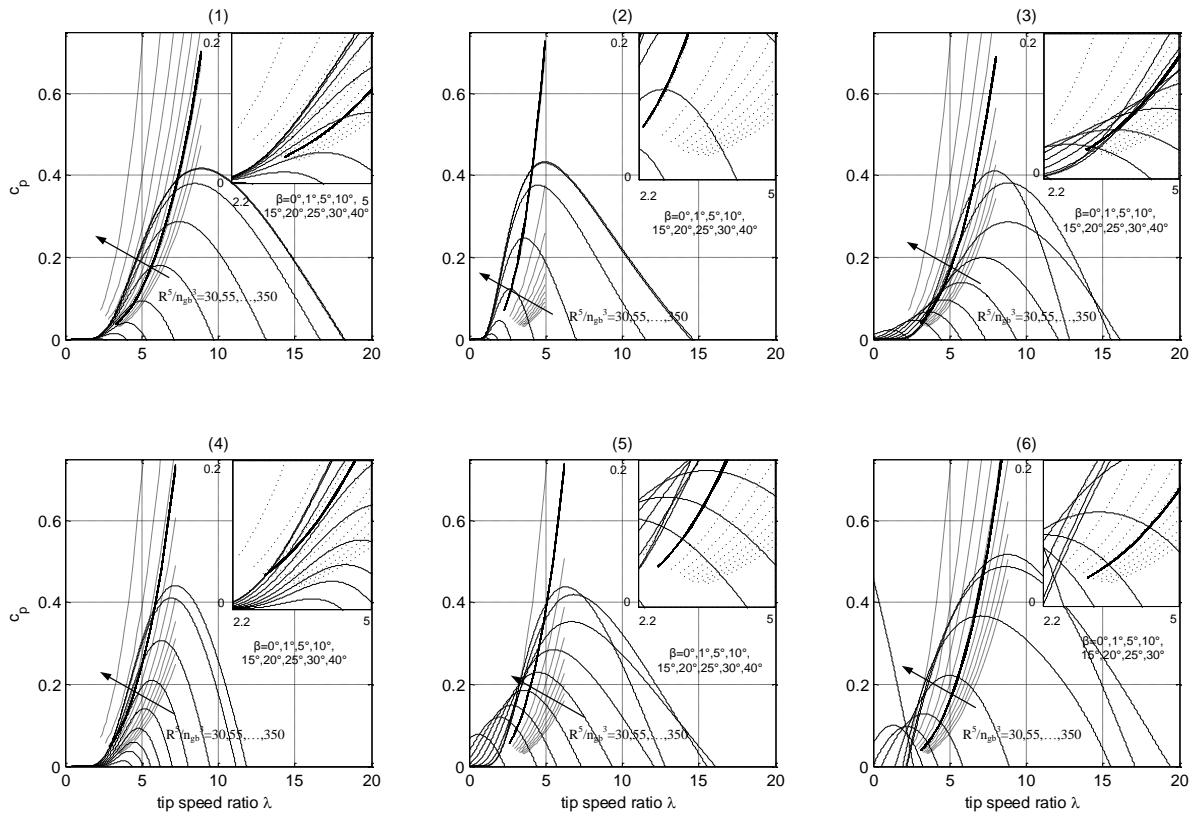
Here,  $\lambda$  is the tip speed ratio and  $\beta$  is the pitch angle. The coefficients  $c_i$  are given in Figure 8.5. For configuration 6, the following equation holds:

$$c_{p,GE}(\lambda, \beta) = \sum_{i=0}^4 \sum_{j=0}^4 \alpha_{i,j} \beta^i \lambda^j \quad (8.3)$$

The characteristics are plotted versus the tip speed ratio  $\lambda$  in Figure 8.5. Table 8.2 gives characteristic values.

Table 8.2: Characteristics of  $c_p$  curves

Config.	$\lambda_{opt}$	$c_{pmax}$	$c_p$ drop 0° to 5°
(1)	8.9	0.4176	~91%
(2)	4.95	0.4332	~87%
(3)	8	0.4109	~69%
(4)	7.2	0.438	~69%
(5)	6.2	0.44	~80%
(6)	8.8	0.52	~71%



	Ref.	c <sub>1</sub>	c <sub>2</sub>	c <sub>3</sub>	c <sub>4</sub>	c <sub>5</sub>	c <sub>6</sub>	c <sub>7</sub>	c <sub>8</sub>	c <sub>9</sub>	Comment	R [m]
1	[12]	0.5	$\frac{R\lambda_i}{\lambda}$	0	0.022	2	5.6	$\frac{0.17R\lambda_i}{\lambda}$	-	-	,MOD-2' turbine, 2.5 MW, 1981	45.72
2	[13]	0.5	$\frac{Rc_f\lambda_i}{\lambda}$	0	0.022	2	2	$\frac{0.255Rc_f\lambda_i}{\lambda}$	-	-	c <sub>f</sub> =1.9547, 250 kW, 1993	15
3	[15]	0.5	116	0.4	0	0	5	21	0.08	0.035	-	-
4	[7]	0.73	151	0.58	0.002	2.14	13.2	18.4	-0.02	-0.003	Variable speed turbine	-
5	[16]	0.22	116	0.4	0	0	5	12.5	0.08	0.035	2 MW, 2001	37.5
6	[11]	-	-	-	-	-	-	-	-	-	1.5, 1.6, 3.6 MW, GE	-

Figure 8.5: Different  $c_p$  characteristics from literature and corresponding parameters

Concerning the speed control, only configuration 1 was found to be suitable for the 2 MW wind turbine [8.4]. The corresponding pitch angle reference for full load is shown in Figure 8.6. In the next step a rotor inertia was estimated. In [8.4], the results from a literature research can be found. Due to limited space, it is not shown here. Finally, the rotor inertia was set to 700 kgm<sup>2</sup>.

The generator inertia was computed with a CAD program and the given model of the rotor of a 2 MW DFIG. It is 85.66 kgm<sup>2</sup>. These results were published in [8.4].

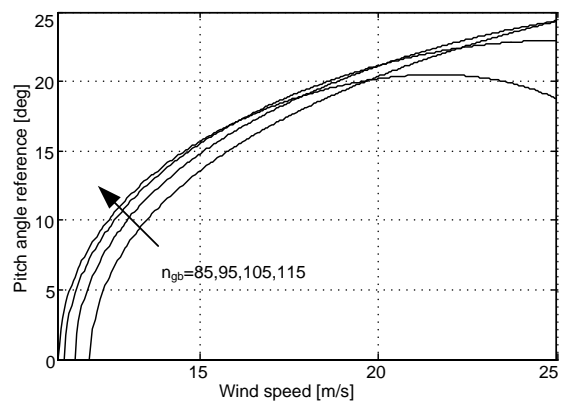


Figure 8.6: Resulting pitch angle reference in full load for different gearbox ratios

### 4.8.4 Results (IAL)

#### Steady State Model

Figure 8.7 shows the results for the low rated module (left column) and the high rated module (right column). It should be mentioned that for both systems the same liquid cooling system with a temperature of 40 degree is chosen. The high rated module is not heating up as much as the low rated module. The tendencies are equal in both modules: with increasing power the mean temperature of the modules increases until the rated operating point is reached where it has its maximum. With both modules, the temperature swing increases at the synchronous operating point. As expected in both modules - due to the fact that they include a standard diode - the diode has higher mean temperatures than the IGBT in the over-synchronous operating area. The number of used temperature cycles in 2009 can be derived (assuming that the

wind turbine only operates in steady state): The duration for a specific wind speed has to be divided by the electrical rotor period. In this way a rough lifetime estimation can be done, also revealing which operating point takes most of the lifetime. The results can be seen in Figure 8.8 for the low rated module (left column) and the high rated module (right column). The consumed lifetime per 0.1m/s is plotted. In line with the results of the ZULES project [8.3] it can be stated, that the main lifetime consuming operation point is the rated wind speed of 12 m/s. The synchronous operating point is not critical. Several cycles-to-failure statistics have been applied. The curve with the lowest lifetime, respectively the top trace in all plots corresponds to the LESIT results. The LESIT tests have been established in the end of the 1990ies. Until today the power cycling capability of modules was enhanced.

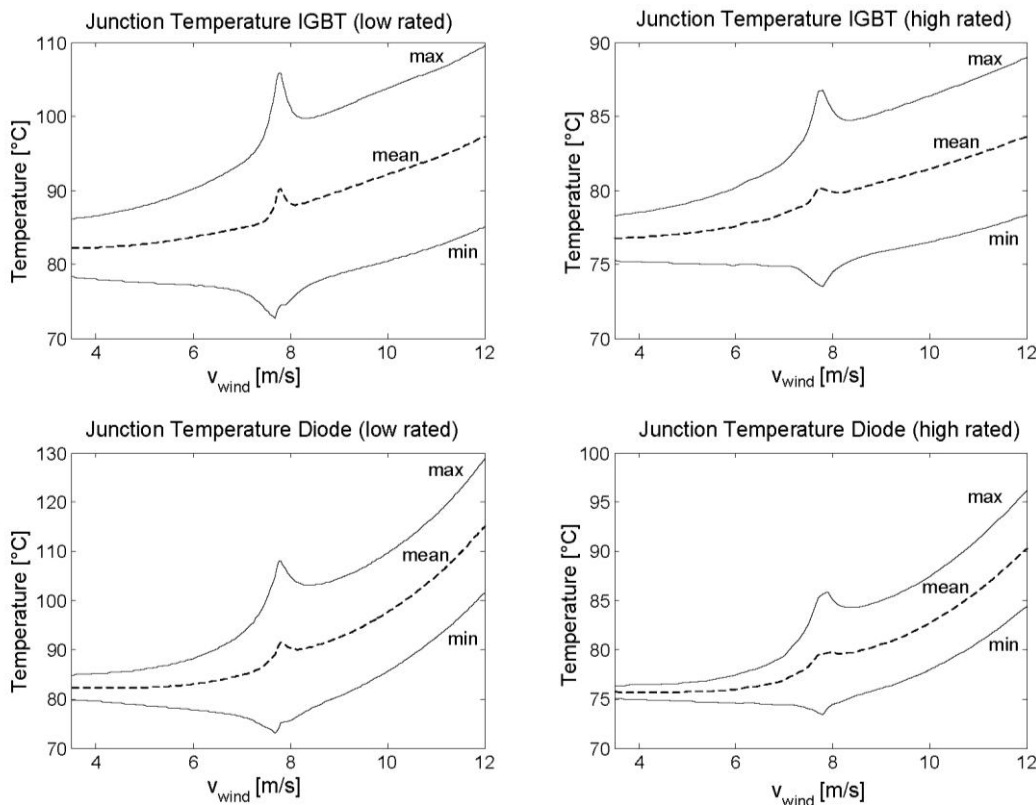


Figure 8.7: Junction temperature over wind speed of IGBT (top) and diode (bottom) with low rated module (left) and high rated module (right)

So, for comparison, the cycles-to-failure statistics provided by the manufacturer are taken into consideration, too. The lowest curve is the one for the newest IGBT module, the one in the middle is for standard modules. The totally consumed lifetime can be seen in Table 8.3. It can be said that the low rated module has a life expectancy of less than 0.25 years with an actual IGBT module. This is not enough regarding the intentioned lifetime of 20 years. With the high rated (actual) module a very acceptable lifetime of approx. 50 years can be reached. It is interesting to note that the diodes are the limiting factor concerning expected lifetime.

In a next step, the work is focused on consideration of the dynamic operation of DFIG.

### Dynamic Model

The dynamic model of the DFIG wind turbine has been equipped with a wind speed profile which originates from the measuring point *FINO* in the german north sea [8.16].

Table 8.3: Consumed Lifetime for low rated and high rated module in 2009 in %

Cycles-to-failure statistic	IGBT, lr	Dio-de,lr	IGBT, hr	Dio-de,hr
<i>LESIT</i>	1542	7333	10	23
<i>Industrial standard</i>	736	2833	5.8	12
<i>Actual</i>	118	430	0.9	1.9

Simulation results are presented for the real wind speed step shown in Figure 8.9. In Figure 8.10, an example plot of the wind speed measured in 80 m height of the *FINO* station can be seen.

The complete turbine simulation model cannot be run for a simulation time of one year due to the fact, that the simulation takes too much time. It is not possible to reduce the model so that it would be possible to simulate the desired one year operation. This is the reason why other approaches must be found to analyze the lifetime consumption of the turbine

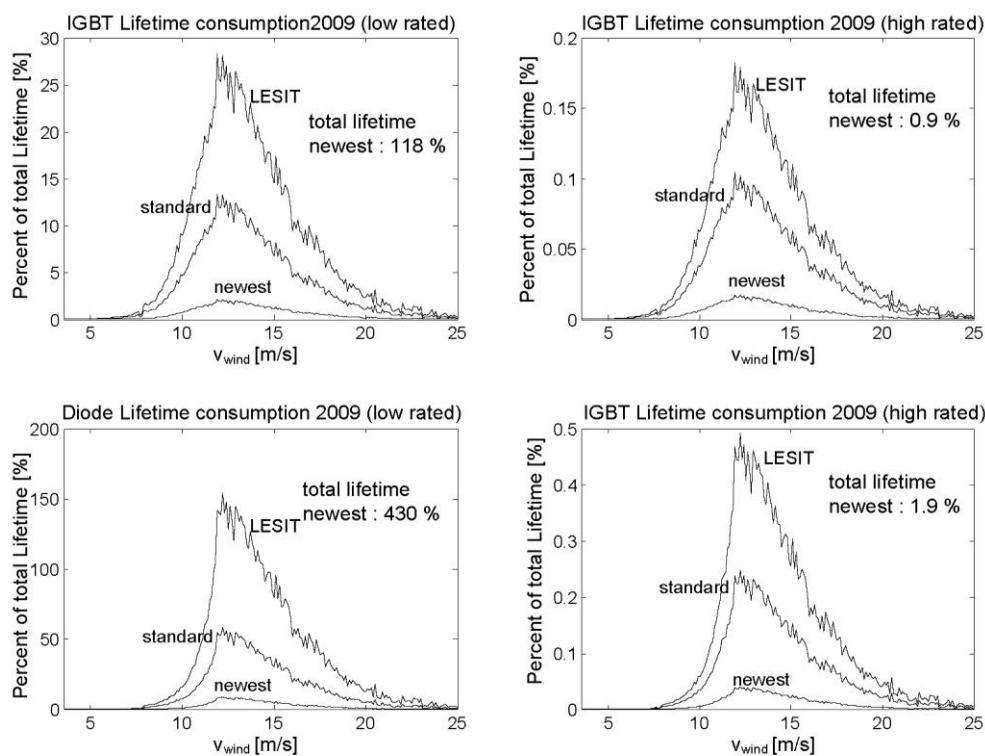


Figure 8.8: Lifetime consumption of IGBT (top) and diode (bottom) with low rated module (left) and high rated module (right) (different cycles to failure statistics)

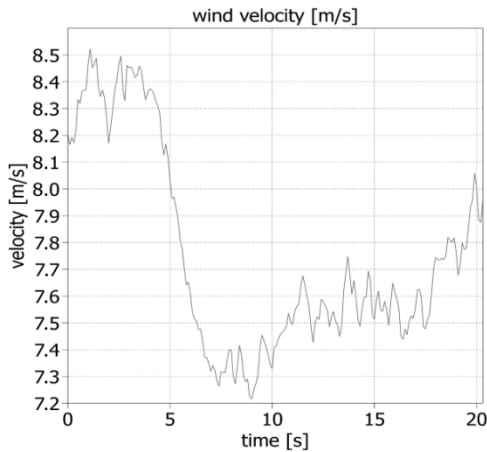


Figure 8.9: Wind speed step for crossing the synchronous operating point

converter in dynamic operation. Here, a splitting of thermal cycles in different durations, e.g. in long term, medium term and short term intervals [8.4] and adequate reducing of the model complexity results in a shorter and more realistic simulation time. This is also the aim of this work. Therefore first simulations are done with the example wind speed step shown in Figure 8.1. This real speed step is interesting to analyze, because here, the DFIG turbine rotational speed reference crosses the synchronous operating point. The simulation model is built in Matlab/Simulink/Plecs. The controllers for speed and current control are appropriately

tuned. The  $c_p$ -characteristic [8.8] of the turbine is included in the model. Also the speed control strategy based on the actual wind speed is integrated. Current and voltage limitations of the converter are respected. The simulation results are shown in Figure 8.11. It can be seen that the synchronous operating point is crossed when the electrical frequency is near zero (at  $t=6s$ ). Consequently, the junction temperature has higher  $\Delta T$ . When the wind speed drops to approx. 7.5 m/s at  $t=7s$ , the electrical frequency increases again and so the  $\Delta T$  of the IGBT decreases. Near  $t=20s$ , the wind speed increases again to about 8 m/s and the turbine is again approaching the synchronous operating point.

#### 4.8.5 Conclusions (IAL)

Within this project, an analysis concerning the lifetime of the converter of a wind turbine equipped with doubly fed induction generator (DFIG) is done. This is done for steady state operation as a first step.

Afterwards, a dynamic model of the wind turbine is developed for dynamic lifetime analysis. The results and models of this research project are the starting points for a further research project at the IAL (see Follow-up projects).

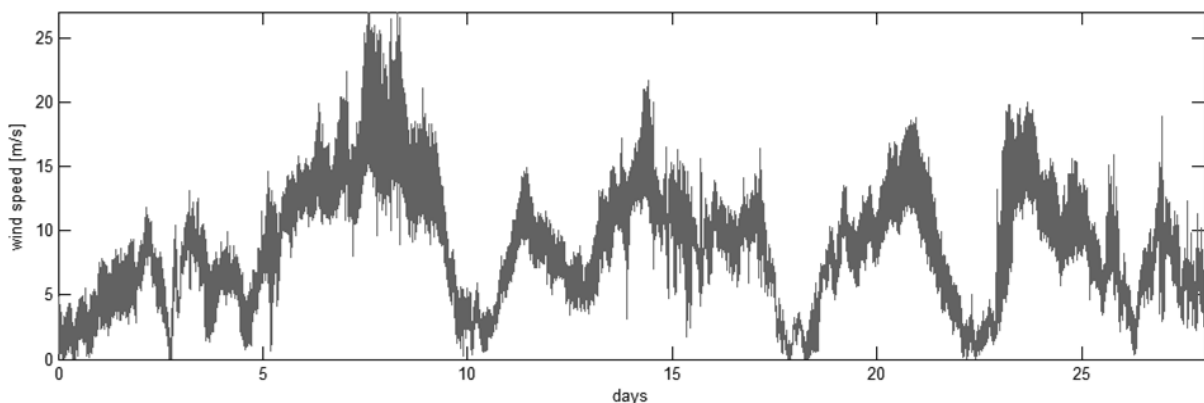


Figure 8.10: Wind speed at a height of 80 m at FINO 1 station in february 2006; time interval; one month

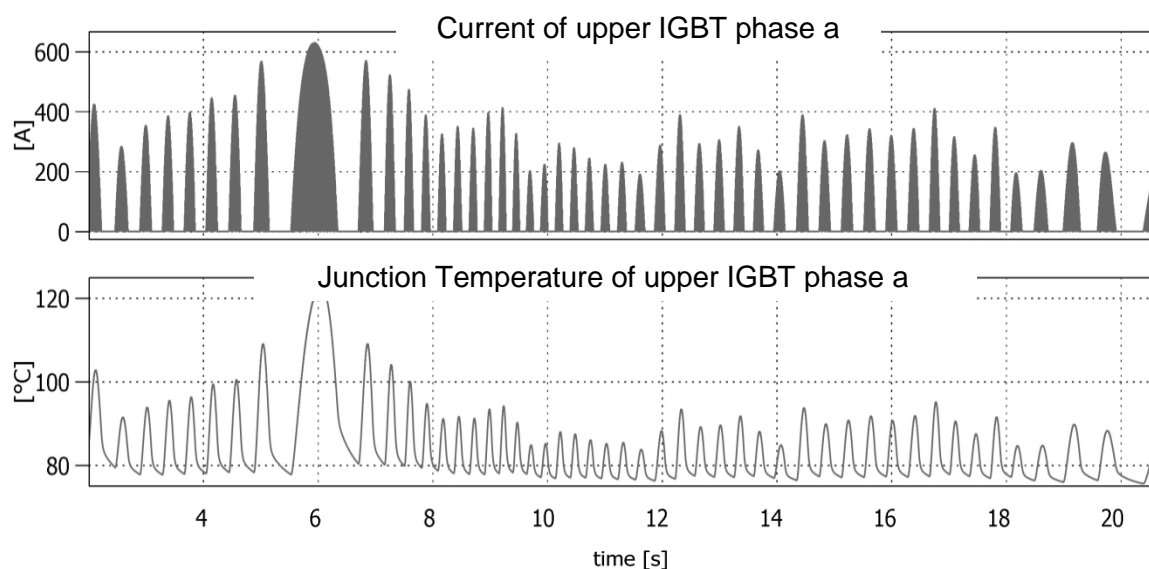


Figure 8.11: Current of IGBT and corresponding junction temperature for the wind speed step shown in Figure 8.1

#### 4.8.6 Abstract (IEE)

The operation and grid connection of large offshore wind farms (OWF) in Germany is particularly challenging due to long distances of OWF to the nearest point of common coupling as a result of protection of coastal areas and of the Wadden Sea. Long distances have to be bridged with submarine cables from the offshore substation to substation on land. In German North Sea, this is done usually as high voltage direct current transmission (HVDC).

Due to specific concepts a fault-free condition of OWF grids is already an n-0 operation and counts thus as an endangered operation, considered with grid security standards of supply grids [8.7]. Due to the very poor accessibility of equipment, which is also strongly affected by weather, any possible damage, failure and its consequences must be considered in the project planning.

#### 4.8.7 Objective (IEE)

In order to consider the effects of the stochastically arising or time-variant environment effects such as wind, weather and aging of the equipment, reliability investigations with stochastic models must be developed. These must consider the

influences of these parameters sufficiently exactly, in order to supply a possibility for the estimation of the probable failure behavior which can be expected with a desired dependability. For this problem various reliability analysis methods and methods for condition assessment are suitable. Depending on the objective both analytical and simulative methods are of choice.

#### 4.8.8 Approach (IEE)

Differential equation systems and their calculations can become very complex in the analytical procedures. The reason for this is that systems with large number of components and with increasing interaction of equipment among themselves become very complex. These methods provide very accurate results, but they also require a high modeling expenditure of the overall system.

Hence, simulation methods are often applied. These methods let a variety of freely distributed input parameters and provide a detailed analysis of the results, at this using a stochastic model [8.7]. In the simulation presented in this work based on a Monte-Carlo procedure a stochastic model (see Figure 8.12) is used. With this model both the time of a failure and the duration during the outage

can be considered. Also modeled load curves of various input parameters can be taken into account.

For the reliability of a system, not only the stochastic or deterministic outage occurrences are significant, but also the effects of aging or mechanical stress.

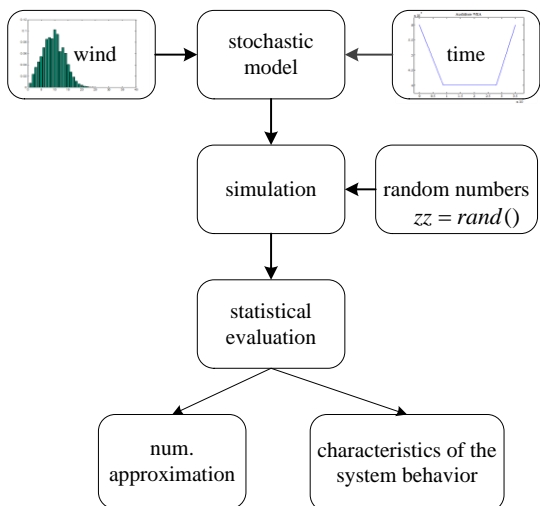


Figure 8.12: Principle of Monte-Carlo Simulation

For the failure distribution stochastic processes such as wind supply and aging in an OWF are taking into account. For this, the Monte-Carlo procedure is very well suitable.

**Stochastic modeling**

The reliability investigation of expanded systems, like an OWF, needs a concept for a stochastic modulation as shown in Figure 8.13 to be able to represent the technical conditions primarily on the respective failure behavior and so to provide an easy handling [8.9].

Thus, various characteristics and interference can be converted on the central reliability data like the failure rate  $\lambda$  and the repair rate  $\mu$ .

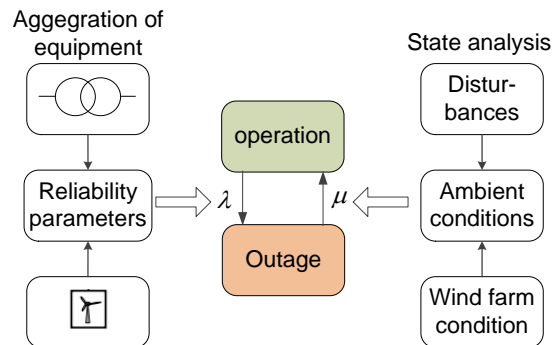


Figure 8.13: Stochastic model

On account of few values of experience and through a bulk of different concepts of OWF which are worldwide planned and also in operation, generally valid reliability characteristic data of the equipment are hardly available.

Hence in Table 8.1 a database for the evaluation of the dependability characteristics was carried out on the basis of different investigations. These values represent a purely qualitative estimate of the expected reliability parameters for one of some possible scenarios. In further scenarios sensitivity analysis can be done in case studies in order to advance several reliability values. For other values averaging or large detail investigations are necessary due to the very improbable sizes or further reasons. (compare e.g. [8.7])

**Wind speed**

The wind speed is important not only when considering the economic efficiency and production capacity of wind parks, but it was also chosen in the sequence and in the structure of the simulation as a key state variable. The probability distribution of the wind corresponds to a Weibull-Distribution (see Figure 8.14a)) [8.19], [8.14]. Nevertheless, every wind park is defeated by an individual accumulation of wind loads which can be returned by the form factor and the scale factor.

Table 8.4: failure rates and repair times

Equipment	Failure rate $\lambda$ in 1/a	Repair times in days
<b>Wind turbine (WT)</b>		
6 MW WT	2,5	7
6 MW WT	1	7
<b>HVDC</b>		
Single pole error ( $P_{50\%}$ )	0,7	3
Single pole error ( $P_{50\%}$ )	9,79	3
<b>Bus bars</b>		
33 kV busbar	0,2	5
155 kV busbar	0,2	5
<b>155/33 kV transformer</b>		
Three-winding transformer	0,02	30
<b>Cable</b>		
33 kV cable (~0.8 km)	0,0177 1/km	20
155 kV cable (~4 km)	0,0177 1/km	20

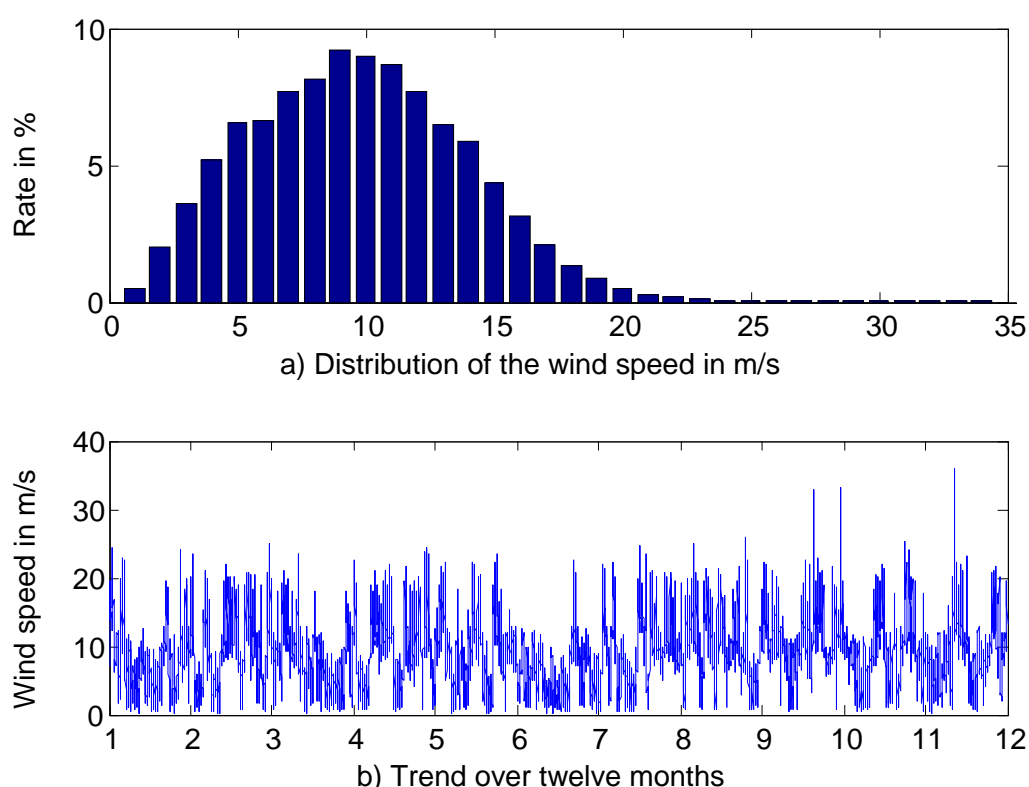


Figure 8.14: Weibull-Distribution and b) Distribution of wind speed over a year

Since in reality the stress, imposed by the different wind speeds within a day or even year, steadily changes (see Figure 8.14b). Also the failure frequency and the achievement feed of the wind turbines (WT) vary also.

To adequately emulate this stochastic behavior in a simulation, a modeling is necessary with most realistic models of stress and time schedules. In particular with a huge number of simulations, varying time series are

necessary, which represents however on the average a comparable wind load.

**Wind model**

The modeling of wind time series is based on a Markov chain [8.5]. From a measuring row, in this case of the measuring station *FINO 1* with the number of values, the wind speeds are discretized in 14 wind areas.

Using this discretization state durations of every wind range during the overall time period can be calculated initially.

Subsequently, transfer rates of individual state transfers between every wind range can be calculated [8.19].

**Maintenance**

An exact analysis of respective availability of the maintenance crews and individual location-dependent risk estimate of the weather conditions is badly feasible in a simulation. Due to the many different factors influence these variables. Therefore, a scattering of repair times is realized according to the maintenance model in Figure 8.15 by a direct coupling to the wind distribution. This returns the bad accessibility of the offshore OWFs (sometimes not more than 60 % of the year [8.5]), due to the weather conditions.

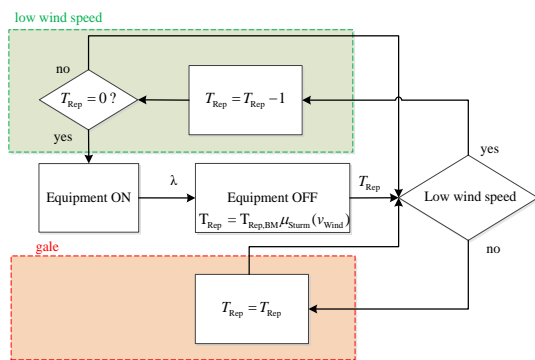


Figure 8.15: Model of the repair times in dependence of the wind velocity

The maintenance model, developed in this work puts the repair time  $T_{rep}$  of the failed equipment into a counting vector. The repair time determined in advance in case of failure and first applies a normal case. In each interval step (corresponding to 15

minutes) with low wind this repair or maintenance time is decremented 'Equipment is being repaired'. In case of a gale, where the wind speed is exceeds the specified limit of wind speed, the registered time to repair is not processed "Equipment will not be repaired, due to gale". Thus, the repair may be significantly extended during gale times. Thus the stochastically occurring serious failures, as well as the long-lasting repair and maintenance durations witch are relevant in practice can be simulated depends on the wind speed.

**Gale model**

High wind speeds produce strong mechanical and in particular high electrical stress for the WT [8.11]. Therefore, the blades of WT propeller will be feathered to stop the rotor during too high wind speeds (pitch-control) or the airflow through the blades will be changed by turning the blades (storm-control). A failure at high wind speeds is not only more probable due to the high stress, but if an error occurs the damage is more significantly. In this case longer repair times are to be taken into consideration and, hence, a partition in light and heavy damage categories is sensible.

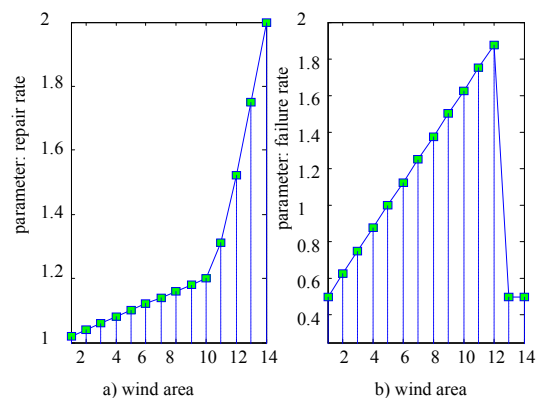


Figure 8.16: gale modeling for increased a) repair and b) failure rate

Hence, two models were developed (see Figure 8.16). These models describe defined parameters depending on the wind speed at any time. The described parameters are, for example, the duration

of an outage (see Figure 8.16a)) or factors for use in the maintenance model (see Figure 8.15). This permits a very exact distinction of the damage classes. The simultaneous conditioned increase of the failure probability became by a linear increase Figure 8.16b) with consideration of the turn-off speeds with very high wind stresses depending on the wind energy plants. The single unities of the wind energy plants show very different failure dependence with increasing wind speeds [8.12]. Therefore, the model includes an averaging of the various correlations between the wind and the damage frequency of every asset component.

### Inherited errors and aging

The reliability of equipment involved in OWF changes both at the beginning and in the end the period of operation, due to the constantly progressing time Figure 8.17. Especially with new technologies, there are often problems with prototypes in the first years of production and occasional assembly or design errors in the construction phase. Therefore, the so-called “technical teething troubles” [8.18] must be considered, which are to be expected especially at the wind turbines.

Since, explicitly offshore a lot of new product series are used and about this product series only few reliability data are available.

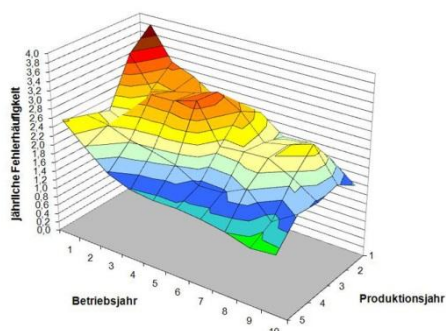


Figure 8.17: Age-related failure rates [8.12]

The manufacturers often specify that their resources have very high availability (over

98 %), however, longitudinal studies lack this information. Additionally, the failure probability of equipment arises with increasing age of this equipment. Even with sequential maintenance and exchange of susceptible components a high vulnerability in the end of the operation duration is to be expected due to wear of the components (corrosion, fatigue) (compare also [8.21], [8.11], [8.1]).

Only during the main operation duration after the initial problems low and constant failure rates for a longer period can be assumed [8.6]. Therefore, two different ageing profiles included in the modulation on the one hand the bathtub curve Figure 8.18a), and on the other hand a curve which describes the rising ageing Figure 8.18b).

This function generally represents a good model for all technical resources. To emphasize the expectable early failures of wind turbines the bathtub curves-model was used only for this type of equipment. These assets in an offshore OWF are clearly most vulnerable to errors at the beginning compared with other resources and considering the high number of pieces errors in assembling and production processes must be expected.

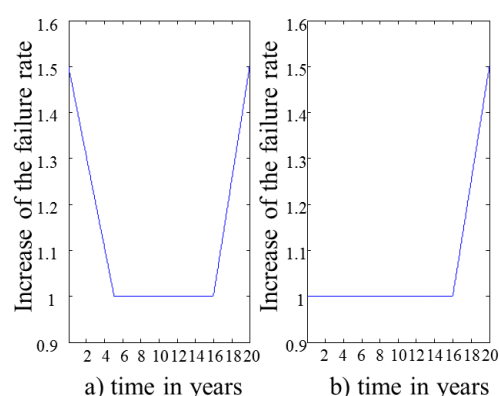


Figure 8.18: Aging models for equipment

The modeling of the curve was simplified for better control function by a linear distribution of the function in the three areas of operation „Early failures“, „Random failures“ and „Wear failures“ [8.20] with

$$f(t) = \begin{cases} c_0 - c_1 t + \lambda & , \text{for } 0 < t \leq \frac{c_0}{c_1} \\ \lambda & , \text{for } \frac{c_0}{c_1} < t \leq t_0 \\ c_2(t - t_0) + \lambda & , \text{for } t_0 < t \end{cases} \quad (8.4)$$

where

$$\begin{aligned} c_0 &= 0,5 \\ c_1 &= \frac{c_0}{0,25t_{\text{tot}}} \\ c_2 &= \frac{c_0}{0,2t_{\text{tot}}} \\ t_0 &= 0,8t_{\text{tot}} \end{aligned} \quad (8.5)$$

### Stochastic failures

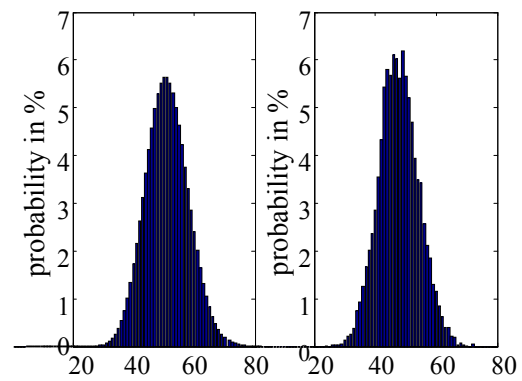
After calculating the effects of wind speed and the aging model presented before, a vector of temporary failure rates  $\lambda_{\text{temp}}$  of all equipment assets is calculated. Stochastic failure will be simulated using a vector  $zz$  of the same size  $[EQ,1]$  with random numbers in the range  $[0,1]$  under the condition  $zz_i \leq \lambda_i$

$$zz = \begin{bmatrix} 0,13 \\ 0,01 \\ \vdots \\ 0,42 \\ 0,98 \end{bmatrix} \leq \lambda_{\text{temp}} = \lambda_{\text{EQ}} \lambda_{\text{gale}} \lambda_{\text{aging}} = \begin{bmatrix} \lambda_{\text{temp},1} \\ \lambda_{\text{temp},2} \\ \vdots \\ \lambda_{\text{temp},EQ-1} \\ \lambda_{\text{temp},EQ} \end{bmatrix} \rightarrow \begin{bmatrix} 0 \\ 1 \\ \vdots \\ 0 \\ 0 \end{bmatrix} \quad (8.6)$$

These failures are entered into the state matrix, and the associated repair times in the list of repairs. The next step  $i+1$  is done by modeling the investigation of the effects of the failed equipment to other components, e.g. as an interruption. Whether this assumption actually reflects the expected distribution of failures, can be verify by comparing the probability distribution versus number of failures  $k$  of every equipment asset with the consideration of the Poisson-Distribution. As the comparison in Figure 8.19 shows, the Poisson-Distribution Figure 8.19a)

and the static Monte-Carlo simulation Figure 8.19b) (600 runs in a single wind turbine over 20 years without consideration of grid errors, wind and time models) have very similar failure distribution results for  $\lambda_{\text{WT}} = \frac{2,5}{a}$ . With a

larger number of runs, the individual probability distribution of the Monte-Carlo simulation approximates more and more clearly to the Poisson-Distribution. Thus, the validity of the model developed in this work which calculates stochastic failures, through drawing random numbers according to Eq. (8.6) is occupied.



a) number of failures k (Poisson) b) number of failure: k (Monte-Carlo)

Figure 8.19: Comparison of the a) Poisson distribution with b) results from Monte-Carlo simulation

### 4.8.9 Results (IEE)

According to the image of used modeling concepts and the various procedures in the following an OWF in several scenarios is examined.

Thus, the impact of model changes and assumptions should be clarified. The functioning of the simulation will be shown in addition. For all studies, an OWF shown in Figure 8.20 was examined by modifying in various case studies.

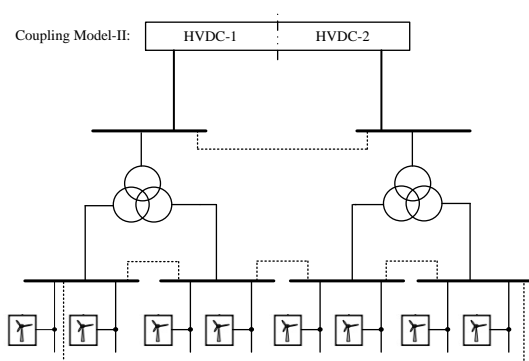


Figure 8.20: Topology wind farm model-I and model-II

### OWF model-I

As comparison model for the more detailed investigations a simple OWF with 80 wind energy plants in 8 strands is modeled. The data from the presented concept are used and as an initial case there are no switching options or topological optimizations e.g. some couplings of bus bars inserted in the model-I.

Thus, changes in equipment or configuration of the OWF can be compared with the values of this simulation in further investigations and their optimization potential can be estimated.

Because the approaches of all investigations after the simulation-procedure pursue the same expiry, the result investigation of comparative model investigation should be explained in the following with the target of closer understanding. A total of 178 resources

were tested on reliability and performance with the parameters from Table 8.5.

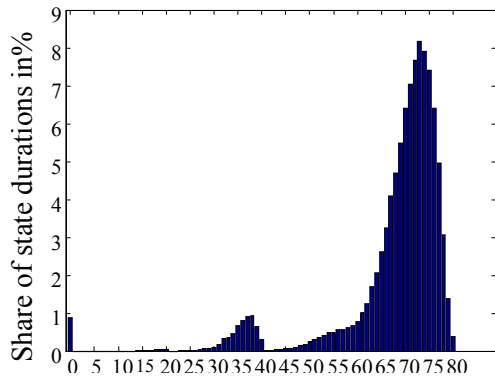
The equipment was switched according to the topology in Figure 8.20 and was examined with Monte-Carlo simulation on the basis of the *FINO 1* wind data. The HVDC was divided in two parts to simulate both common mode errors and single pole failures.

### OWF model-I, state durations

The most important results of the proposed reliability analysis are the state duration's calculation of the operational wind turbines which also form the frequencies by the always same interval lengths. All failures, grid failures, gale effects or repair delays have an impact on this distribution and can be analyzed with this. The state durations shown in Figure 8.21 are averages of 20 simulations over 20 years. At each interval time  $i$  the number of feedable WTs was counted and divided by the total number the number of conditions, in order to receive the proportional distribution. It will be appreciated that for larger OWF system an error-free state is very unlikely (here below 1%). This is due to the high probability of failure and the repair and maintenance periods of the plants. While Figure 8.21 represents only the aggregated duration of states, the Figure 8.22 shows in addition the dependence of the single interval states on the wind speed.

Table 8.5: case study I – data of equipment

Equipment	Quantity	Failure rate $\lambda$ in 1/year	Repair duration in days
Wind turbines	80	2,5	7
Cable 33 kV I	80	0,8 km·0,0177	20
Cable 33 kV III	4	2,0 km·0,0177	20
Cable 155 kV I	2	3,0 km·0,0177	20
Cable 155 kV II	2	5,0 km·0,0177	20
Bus Bar 33 kV	4	0,2	5
Transformer 33 kV / 155 kV	2	0,02	30
Bus Bar 155 kV	2	0,01	5
HVDC	2	0,7	3



wind turbines in operation

Figure 8.21: OWF model-I state distribution (WT in operation)

It can be seen that most of the state durations can be found in the lower wind speeds up to the nominal speed with a small number of individual errors.

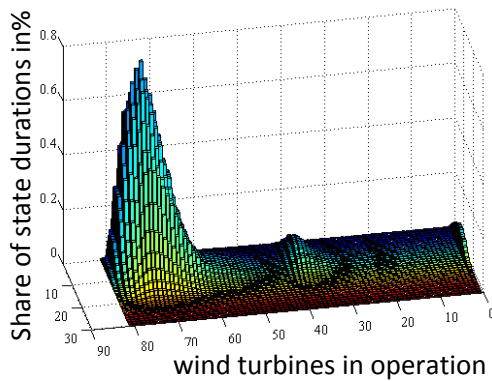


Figure 8.22: OWF model-I state distribution vs WT in operation with wind ranges as additional parameter

It's easy to recognize that the state distribution within the wind speeds is very similar to the Weibull distribution. Remarkable are the maxima at 32 and 0 feeding plants with this topology. This is a result of mistakes in the main transference means which show no redundancy in the easy consideration and lead, hence, with a failure to long mistake times.

**OWF model I – assessment of electrical power**

For each time point the number of plants in operation is multiplied with the power curve of the plants and calculated the total energy produced.

$$P_{gen} = \sum_i^n NumWTs_{operation}(i)P(v_{wind}(i)) \quad (8.7)$$

The not transmitted or not used energy results from the equivalent in which the number of non-operating wind power plants (where  $Time(WEAs, i) = 0$ ) is calculated.

Since with Monte-Carlo simulation always several runs take place, the calculated values are afterwards averaged. So, for the OWF model-I the following power values were:

$$\bar{P}_{gen,WF-I} = 1592,1 \text{ GWh/a} \quad (8.8)$$

$$\bar{P}_{loss,WF-I} = 308,5726 \text{ GWh/a} \quad (8.9)$$

From the ratio of these values the efficiency of OWFs results as:

$$\eta_{WF-I} = 1 - \frac{P_{loss,WF-I}}{P_{loss,WF-I} + P_{gen,WF-I}} = 83,77 \% \quad (8.10)$$

and the full-load hours of generated energy in relation to the nominal power

$$T_{FullLoad,WF-I} = \frac{P_{gen,WF-I}}{P_N} = \frac{P_{gen,WF-I}}{64 \cdot 6,15 \text{ MW}} = 3236 \text{ h} \quad (8.11)$$

Simulation shows 3226 full load hours. This is in principle a good extent of utilization for the enterprise of wind energy plants, however for the location with 3616 h possible full load hours a moderate result. This is due to the high failure time which result in 308,5 GWh electrical loses, while the electrical transmission losses are not even included in these values.

These would impair the efficiency and the economy of the OWF further negatively, which should be considered in future investigations.

**OWF model-II, Redundant couplings**

The calculations for the model in have been carried out without any couplings of the transmission equipment. How the high

loss achievement and the indicate, this topology would be unsafe as well as uneconomical, because it can come at long down-times of several arrangements at the same time. In order to work against these losses, couplings between all bus bars are introduced, so that in the loss of a transmission means in the backbone network path an alternative grid connection can be determined.

The circuits were made thereby according to Figure 8.20. The bus bars and couplings are designed in such a manner that each main component (transformer, transmission cables) can transmit 100 % power and each other some 50 % rated to nominal power, in order to ensure full redundancy for the case study.

#### OWF model-II, state distribution

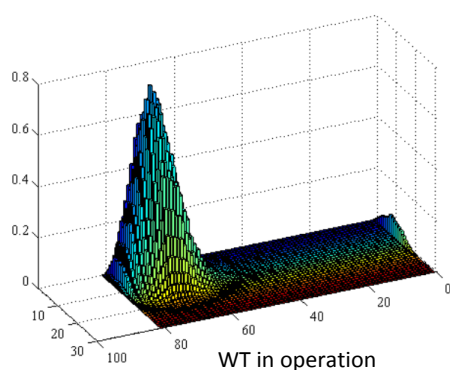


Figure 8.23: OWF model-II state distribution

In the comparison to the simple OWF model-I a clear increase of the availability can be recognized here.

The most severe error could be compensated by switching on the coupling except the common-mode error of HVDC or occurring minimal cut.

#### OWF model-II, assessment of electrical power

The generated power and the power lost due to interruptions or failures were calculated according to. Then, a surplus compared to the simple model was determined and showed in Table 8.6. The additional yield is considerably with 65,9 GWh, which is already recognized by

the state distributions. The difference to the higher yield in the losses is due to the fluctuations of the wind speed, which balance only at very high cycle numbers. This increment and the availability of the OWF reached by the circuits in model-II are very worthwhile results.

However, these could be reached only on account of high investments in the partly 100 % redundancy of the transference means. For commercial operation, this means high losses in the economy so that more far-reaching investment calculations are required.

#### Comparison with MCMC analysis

The two case studies were also evaluated with the Markov Chain Monte-Carlo simulation. According to determination of the system matrix consisting of the reliability parameters, Table 8.7 shows in the following some estimations for the model-I and the model-II. It is clearly visible that the MCMC method produces inaccuracies in case of topology with the biggest outage differences due to transmission failures, since these are difficult to describe.

In the model II, which is determined mainly by cable and system errors, the results are too optimistic, since the influence of the disturbances has not been taken into account.

#### Case studies of further quantities of influence

##### Failure rate of wind turbines

To determine the impact of the high failure rate of the wind turbines, a case study of the OWF model I with a reliable 6 MW plant was implemented with.

$$\lambda_{WT}^* = \frac{1}{a} \quad (8.12)$$

The results showed again a high vulnerability to interruptions of the OWF; however states with high number of wind turbines in operation were significantly more likely than in the reference model, as Table 8.8 shows.

Table 8.6: OWF model-II assessment of electrical power

Description	Value 1/a	Acquired surplus compared to model I
generated power	1658 GWh	65,9 GWh
lost power	248,1 GWh	-60,5 GWh
full-load hours	3370 h	134
efficiency factor	86,98 %	3,21 %

Table 8.7: MCMC analysis of OWF models

description	MCMC	Monte-Carlo
<b>OWF model-I</b>		
generated power	1198,3 GWh	1592,1 GWh
lost power	308,4 GWh	308,57 GWh
full-load hours	2435,6	3226 h
efficiency factor	79,53 %	83,77 %
<b>OWF model-II</b>		
generated power	1904 GWh	1658 GWh
lost power	124 GWh	248,1 GWh
full-load hours	3871 h	3370 h
efficiency factor	93,89 %	86,98 %

As could be expected, and the Table 8.9 shows, a significantly higher yield by improving wind turbines, in addition to the topological optimization in can be achieved. Therefore, in investment calculations both optimistic calculations, such as the lower failure rates as well as worst-case scenarios for the reference model should be made to identify a range of potential future returns.

#### *High failure rate of the high voltage transmission system*

In addition to demonstrate the effects of low grid security, a case study of the OWF model-II with an unreliable HVDC system was examined with

$$\lambda_{\text{HVDC}}^* = \frac{9,79}{a} \quad (8.13)$$

Here, the value of the 92% availability of a HVDC was calculated from [8.17]. The HVDC transformer platform was divided into two equal parts, therefore significant outages can be expected. The results showed a high number of operating points at 0 and 40 plants in operation, as the

Table 8.9 shows. This case study highlights the high dependency level of the OWF efficiency from the grid connection. Since this is not generally redundant and during the first years of operation of the hitherto less proven HVDC stations increased failures are quite expected, this factor should be taken into account in the further design.

#### **4.8.10 Conclusions (IEE)**

In this work package (WP) a simulative method based on analytical considerations and a Monte-Carlo simulation was developed to analyze all input parameters and status values. Furthermore the efficiency of OWF and the accessibility of them for repair and maintenance work are strongly depends on the prevailing wind speed. This dependence of reliability from wind speed distribution requires a modeling approach, which is provided by a wind time series model. This can then take influence on the reliability parameters and state variables of the equipment by various methods

Table 8.8: Comparison of the results for a change of wind turbine failure rate

Description	$\lambda_{WT}^*$	Reference
<b>WT in operation</b>	$P(Z^*)$	$P(Z)$
80	5,149 %	0,37 %
79	10,95 %	1,51 %
78	13,48 %	3,1 %
77	12,25 %	4,99 %
<b>OWF model-II</b>		
generated power	1709,3 GWh	1592,1 GWh
lost power	200,27 GWh	308,57 GWh
full-load hours	3474,2 h	3226 h

Table 8.9: Comparison of the results for a change of the HVDC failure rate

Description	$\lambda_{hvdc}^*$	Model-II
<b>WT in operation</b>	$P(Z^*)$	$P(Z)$
0	2,838 %	0,096 %
40	1,064 %	0,011 %
39	2,773 %	0,013 %
38	3,888 %	0,012 %
<b>OWF model-II</b>		
generated power	1381,5 GWh	1658 GWh
lost power	516,06 GWh	248,1 GWh
full-load hours	2808 h	3370 h

## 5 Exploitation of results

The findings of the work package In Situ Assembly (WP 5) could be used to analyse the specific boundary conditions for wind farm projects more easily. The basic PHA could find hidden failures and carry out corrective actions in the design phase and also in running projects. The failure modes detected could be analysed by using the FTA. Herewith, the probability of failure could be determined to evaluate if changes in the design are needed, or to compare failure probabilities between different constructions. A trend for the influence of the failure mode on the material properties could be determined by simulating the failure modes in the laboratory testing facility. However, a large-scale test is worthwhile for the verification of the results.

A large-scale testing facility was developed within the research project GROWup based on the findings of the work package In Situ Assembly (WP 5). The height of the transparent and waterproof formwork is 3.75 m and the length is 3.3 m. The width of the gap is flexible up to 20 cm. The test facility is equipped with temperature sensors, and pressure gauges inside the formwork and inside the grout hoses.

Furthermore, an underwater test facility is under development for nearly realistic filling tests for grouted joints. The steel formwork of the test facility is completely submerged. The maximum height is 8.1 m and the maximum length is 7.2 m.

Failure modes of the in situ assembly will be investigated, amongst others, within this project.

Furthermore, the PHA of the in situ assembly will be investigated in more depth and more detailed fault trees will be designed.

### 5.1 Follow-up projects

**GIGAWIND life (2013 – 2016)**, funded by the Federal Ministry for the Environment,

Nature Conservation, Building and Nuclear Safety (BMUB):

Goal of the comprehensive project GIGAWIND *life* is the enhancement of the economic dimensioning concept for offshore wind turbine support structures, that has been developed in GIGAWIND *alpha ventus*, by consideration of long-time operation. There are both degradation mechanisms on the resistance side of the environmental surrounded support structure (damages of structure and welds, fatigue, damages of corrosion protection systems, scour, degradation of pile support behavior) and the determination of acting loads from waves and marine growth, which interact with the support structure. Data of damage and stress at the interfaces will be obtained over a longer timeframe from measurements in the offshore test site *alpha ventus* by usage of the hitherto developed monitoring methods. This is the requirement to get a scientific perception from the previous investments and to make validated methods and structural models based on world-wide unique long-time measurements for single studies as well as for holistic offshore support structure design concepts available.

**GROWup (2011 – 2016)**, funded by the Federal Ministry for the Environment, Nature Conservation, Building and Nuclear Safety (BMUB), Ref. No. 0325290:

The research project GROWup focuses on the installation and the design of grouted joints of support structures for offshore wind turbines. A more detailed knowledge of the in situ material properties of the grout material used for grouted joints is needed for the optimisation of substructures. Therefore, a nearly realistic filling test will be conducted to simulate the in situ assembly of grouted joint at a scale of ~ 1:1 under submerged conditions. Undisturbed filling processes will be simulated as well as disturbed filling processes and failure modes. Furthermore, the fatigue behaviour of large-scale tube-to-tube connections with

large grout thicknesses as well as the influences of different grout materials and water will be investigated. The combination of all aspects will lead to a holistic design and will be implemented in future guidelines.

**HyConCast (2014 – 2016)**, funded by the Federal Ministry for Economic Affairs and Energy (BMWi):

The research project "HyConCast - Hybrid substructure of high strength concrete and ductile iron castings for offshore wind turbines" deals with the development of a novel, hybrid substructure for offshore wind turbines. The innovative concept is based on the combination of large-sized, thin-walled ductile iron casting knots with high-strength, lightweight precast concrete pipes customized for the environmental conditions and conditions of use. Several institutes of the Leibniz University of Hannover, commercial companies and engineering consultings are involved in this research project.

The overall objective of this project is to assess the feasibility and applicability as well as to investigate the necessary foundations for planning, design and construction of a hybrid substructure. For the substructure transport and installation concepts will be developed, the risk of scour on the seabed will be analyzed and the structural behavior of the installed components and connections will be investigated using numerical and physical models in different levels of detail.

**INNWIND.eu (2012 – 2017)**, co-financed by the European Union under the Seventh Framework Programme:

The project is an ambitious successor for the UpWind project, where the vision of a 20MW wind turbine was put forth with specific technology advances that are required to make it happen. This project builds on the results from the UpWind project and will further utilize various national projects in different European countries to accelerate the development of

innovations that help realize the 20MW wind turbine.

The Institute for Steel Construction is involved in Work Package 4 focussing on Offshore Foundations and Support Structures. Objectives of WP4 are to achieve significant cost reductions and to enable mass-production of for jacket-type structures in the 10MW class by applying innovation on the component level. Furthermore, to assess risks and possibilities and to preliminary design an innovative 20 MW substructure and finally to accelerate the time-to-market for floating concepts, as here structural designs and design methods are still not finalized and validated.

Besides the Institute for Steel Construction also the Institute of Building Materials Science (Prof. Lohaus) and the Institute of Structural Dynamics (Prof. Rolfes) are involved as the core research group of the ForWind-Hannover.

**IRPWIND (2014 – 2018)**, co-financed by the European Union under the Seventh Framework Programme:

IRPWIND is an integrated research programme that combines strategic research projects and support activities within the field of Wind Energy, with the aim of leveraging the long term European research potential. IRPWIND gathers together 24 leading research institutions and will directly contribute to promoting joint collaborative projects and overall reinforcement of research excellence across Europe, as well as optimising networking benefits from joint use of European facilities.

**Large-Sized Bolts 2 (2013 – 2015)**, funded by the Federal Ministry for Economic Affairs and Energy (BMWi) and the German Federation of Industrial Research Associations (AiF):

For the connection of different segments of wind turbine support structures bolts with large diameters M36 to M64 are used. Protection against corrosion of the bolts is commonly achieved by coating the steel

surface with zinc. Until now, the affect of zinc coating on the bolts fatigue strength has not been quantified. The aim of the research project " Large-Sized Bolts 2 - Experimental and analytical assessment of the fatigue strength of bolts with large dimensions under consideration of boundary layer effects" is to develop a secured assessment method for the fatigue strength of large size bolts which considers the influence of the zinc boundary layer.

**MaRINET (2011 - 2015)**, funded by the European Union Seventh Framework Programme (FP7) under grant agreement no. 262552:

MaRINET (Marine Renewables Infrastructure Network for Emerging Energy Technologies) is an EC-funded consortium of 29 partners bringing together a network of 42 specialist marine renewable energy testing facilities. The network also conducts co-ordinated research to improve testing capabilities, implements common testing standards and provides training and networking opportunities to enhance expertise in the industry. The aim of the MaRINET initiative is to accelerate the development of renewable marine energy technology. The Institute of Building Materials Science participates in research on the design and accuracy of sensor and Structural-Health-Monitoring systems. The focus of the research is on local monitoring of the support structure, because it has particular advantages to screen out parts of the structure that are affected by structural changes that ultimately lead to changes in the deformation or stiffness behaviour. In combination with global monitoring, the specific evaluation of local measuring points can be used for the quantification of the structural state, such as damage propagation. The grouted joint is a suitable structural component in OWEC in order to conduct local monitoring.

**Optical In-Field Measurements of Rotor Blade Deformations (2011-2014)**, funded by the Ministry of Science and Culture of Lower Saxony, Germany:

Within the framework of this project a new measurement system, based on Digital Image Correlation (DIC) was developed and effectively applied to a full-scale 3.2 MW wind turbine. So far, the optical measurement system can provide data for absolute and relative out-of-plane and in-plane deformations of the rotor blades at arbitrary positions along the blade's span and relative torsion of the blades.

**OWEA Loads (2013 – 2015)**, funded by the Federal Ministry for the Environment, Nature Conservation, Building and Nuclear Safety (BMUB):

Research in the framework of the OWEA Loads project deals with the systematic analysis of load relevant events and model properties of offshore wind turbines (OWT). Investigations are based on real scale measurements of actions and system response of OWTs. Consequential demands on load simulation models of OWTs shall be derived. The ultimate goal is to determine the impact of relevant support structure properties, enabling enhanced predictions of OWT loads in future.

**Smart Blades (2013-2016)**: Development and Construction of Intelligent Rotor Blades, funded by the Federal Ministry for the Environment, Nature Conservation, Building and Nuclear Safety (BMUB):

The design of modern wind turbines tend to an increasing blade length which causes higher loads, especially in the blade root region. In order to reduce the loads new innovative blade technologies, e.g. blade twist coupling or morphing trailing edges, are investigated in collaboration with ForWind Oldenburg, DLR, Fraunhofer IWES.

**WindBucket (2012 – 2014)**, funded by the Federal Ministry for the Environment, Nature Conservation, Building and Nuclear Safety (BMUB):

Many offshore structures are fixed to the seabed by driven piles, which can seriously harm the marine fauna due to the high noise pollution from the installation. Even though well established in oil and gas industry, suction buckets for OWTs are still topic of research in Germany and Europe. This innovative foundation concept uses under-pressure to install the bucket into the seabed without mentionable noise emission. Within the research project WindBucket, the suction bucket solution is adopted to the needs of offshore wind. The feasibility application as well as the limits of application are assessed. Basics of planning, design and installation of suction buckets made of steel or reinforced concrete are developed, considering ecological and economical aspects.

**Zuverlässige Leistungselektronik (2014 – 2017)**, Fraunhofer - Innovationscluster Leistungselektronik für Regenerative Energieversorgung is funded by the Ministry of Science and Culture of Lower Saxony, Germany and the Fraunhofer-Gesellschaft zur Förderung der angewandten Forschung e.V.: Available: <http://www.power4re.de/de/zuverlaessige-leistungselektronik.html>. [Accessed: 03-Nov-2014].

## 5.2 Publication List

### 5.2.1 Journal Paper

Ernst, B; Seume, J.R.:  
Investigation of Site-Specific Wind Field Parameters and Their Effect on Loads of Offshore Wind Turbines.  
*Energies* 2012, 5, 3835-3855,  
DOI: 10.3390/en5103850

Gatzen, M./ Poll, G.:  
Polymerzusätze in Wälzlagerfetten.  
*Tribologie und Schmierungstechnik*,  
58(2011)2, S. 42-46

Gatzen, M.M.; Pape, F.; Bruening, C.;  
Gatzen, H.H.; Arlinghaus, H.F.; Poll, G.:

Correlation between performance and boundary layers in highspeed bearings lubricated with polymer-enhanced greases.  
*Tribology International* 43 (2010) 5-6, S. 981-989, ISSN: 0301-679X (reviewed)

Gunst, U.; Zabel, W.-R.; Valle, N.; Migeon, H.-N.; Poll, G.; Arlinghaus, H.F.:  
Investigation of laminated fabric cages used in rolling bearings by ToF-SIMS.  
*Tribology International* 43 (2010) 5-6, S. 1005-1011, ISSN: 0301-679X (reviewed)

Hansen, M.; Schmidt, B.:  
Sicherheit von Offshore Windenergieanlagen.  
*Bautechnik* 91 (2014), Heft 8, S. 525-532  
DOI: 10.1002/bate.201400048

Kelma, S.; Schmoor, K.A.; Goretzka, J.; Hansen, M.:  
Sicherheitsaspekte der Tragstruktur von Offshore-Windenergieanlagen.  
*Bautechnik* (91), issue 8, Ernst&Sohn, Berlin, pp. 543-553.  
DOI: 10.1002/bate.201400035

Lohaus, L.; Lindschulte, N.; Scholle, N.; Werner, M.:  
Betontechnik für Grouted Joints – Baustoffliche und bauausführungstechnische Anforderungen.  
*Stahlbau* 81(2012), Heft 9, pp. 689 - 694 (reviewed)

Mertens, A.; Fuchs, F.; Baruschka, L.:  
Wandler im Meerespuls.  
*Erneuerbare Energien*, 07/2012

Poll, G. / Wang, D. (2012):  
Fluid rheology, traction/creep relationships and friction in machine elements with rolling contacts.  
*Proceedings of the Institution of Mechanical Engineers, Part J: Journal of Engineering Tribology*, 226 (2012) 6, S. 481-500,ISSN 1350-6501 (reviewed)

Poll, G.; Baly, H.:  
Lubricant film formation and friction of

grease lubricated ball bearings.

6. Arnold-Tross-Kolloquium der HAW Hamburg, Shaker Verlag, Aachen (2010), S. 271-310, ISBN 978-3-8322-9599-8 (reviewed)

Schmidt, B., Ernst, B., Wilms, M., Hildebrandt, A., Hansen, M.:

Messdatenbasierte Empfehlungen von Wind- und Wellenparametern für die Auslegung von Offshore-Windenergieanlagen.

Bautechnik 91 (2014), Heft 8, S. 533-542, DOI: 10.1002/bate.201400033

Schmidt, B.:

Wissenschaftlich betrachtet - Windenergie in schwerer See.

neue energie 06/2014

Schmidt, B.; Göthel, O.; Göhlmann, J.; Grünberg, J.; Marx, S.:

Wellenbeanspruchung auf hydrodynamisch kompakte Betonstrukturen für Offshore-Windenergieanlagen.

Beton- und Stahlbetonbau 109 (2014), Heft 4, S. 265-274

Schmoor, K. A.; Achmus, M.:

Optimum geometry of monopiles with respect to the geotechnical design.

Journal of Ocean and Wind Energy (submitted October 2014)

Werner, M.; Lohaus, L.:

Ausführungstechnische Einflüsse auf Aspekte der Tragsicherheit von Grouted Joints.

Bautechnik 91 (2014), Heft 8, August 2014, pp. 554 – 560 (reviewed)

## 5.2.2 Books and essays

Lohaus, L.; Werner, M.:

Probabilistic aspects of Offshore Wind Turbines: Influence of in situ assembly of grouted Joints.

In: Life-Cycle and Sustainability of Civil Infrastructure Systems, CRC Press/Balkema, Leiden, 2013, pp. 2209-2213 (reviewed)

Scholle, N.; Weicken, H.; Werner, M.:

Windenergieforschung am Institut für Baustoffe.

In: Festschrift Ludger Lohaus zur Vollendung des sechzigsten Lebensjahres (Berichte aus dem Institut für Baustoffe, Heft 12), Hannover, 2014, pp. 31-40 (reviewed)

## 5.2.3 Conference proceedings

Denkena, B.; Poll, G.; Maiß, O.; Neubauer, T.:

Affecting the Life Time of Roller Bearings by an Optimal Surface Integrity Design After Hard Turning and Deep Rolling.

Advanced Material Research: Proceedings of 6th International Conference on Tribology in Manufacturing - Processes & Joining by Plastic Deformation. Vol. 967, S. 425-434, TransTech Publications, Switzerland (2014), ISBN 978-3-03835-127-6

Ernst, B.; Schmitt, H., Seume, J.R.:

Effect of Geometric Uncertainties on the Aerodynamic Characteristic of Offshore Wind Turbine Blades.

Presentation: The Science of Making Torque from Wind, October 9-12, 2012, Oldenburg, Germany

Fuchs, F., Mertens, A.:

Aspects of Wind Turbine Converter related Research at IAL.

University of Hannover, Germany International Wind Engineering Conference (IWEC) 2014, Hannover (presentation, reviewed)

Fuchs, F., Mertens, A.:

Steady State Lifetime Assessment of (Power) Semiconductors in DFIG Wind Turbines.

EPE Joint Wind Energy and T&D Chapters Seminar, 2012, Trondheim, Norway (presentation, reviewed)

Fuchs, F.; Mertens, A.:

Dynamic modeling of a 2 MW wind turbine for converter issues: part 1.

Power Electronics and Motion Control (EPE PEMC 2011 ECCE Europe), Proceedings of the 2012-15th International Conference and Exposition on Novi Sad, Serbia (reviewed)

Fuchs, F.; Mertens, A.:  
Steady State Lifetime Estimation of the Power Semiconductors in the Rotor Side Converter of a 2 MW DFIG Wind Turbine via Power Cycling Capability Analysis. 14th European Conference on Power Electronics and Applications 2011, EPE 2011, September 2011, Birmingham, United Kingdom (reviewed)

Garske, S.; Brenner, S.; Hofmann L.:  
Zuverlässigkeitsbetrachtung und Zustandsanalyse der Netzanbindung von Offshore Windparks. Institut für Energieversorgung und Hochspannungstechnik, Fachgebiet Elektrische Energieversorgung, IEH, Dresdener Kreis, Leipzig, 2012

Gatzen, M.; Poll, G.:  
Polymerzusätze in Wälzlagerfetten. 51. GfT-Tribologie-Fachtagung „Reibung, Schmierung und Verschleiß“, 27.-29.9.2010, Göttingen

Goretzka, J.; Rolfes, R.:  
Modal and Robustness Analysis of the Support Structure of an Offshore Wind Turbine with Scattered Soil Parameters. Proceedings of 8th PhD Seminar on Wind Energy in Europe, ETH Zürich, 2012

Hacke, B.; Poll, G.:  
Early Detection of Bearing Damages in Wind Energy Plants. DEWEK 2010 - 10th German Wind Energy Conference 17.-18.11.2010, Bremen

Hacke, B.; Poll, G.:  
Fehlerfrüherkennung von Wälzlagerschäden in drehzahlvariablen Windgetriebeagern.

VDI-Tagung „Schwingungen von Windenergieanlagen 2010“ 3.-4.2.2010, Hannover

Lohaus, L.; Cotardo, D.; Werner, M.:  
A test system to simulate the influence of early age cycling on the properties of grout materials. Proceedings of the 24th International Ocean and Polar Engineering Conference, Busan, June 2014, pp. 234 – 239 (reviewed)

Lohaus, L.; Cotardo, D.; Werner, M.:  
The Early Age Cycling and its Influence on the Properties of hardened Grout Material. Proceedings of the International Wind Engineering Conference, Hanover, September 2014 (reviewed)

Lohaus, L.; Werner, M.; Cotardo, D.:  
Experimental Test Procedures to Simulate the In Situ Assembly of Grouted Joints. Proceedings of the International Wind Engineering Conference, Hanover, September 2014 (reviewed)

Marx, S.; Göhlmann, J.; Gröthel, O.; Schmidt, B.:  
Concepts for gravity base foundations. RAVE International Conference 2012, 08.-10. Mai 2012, Bremerhaven

Neubauer, T.:  
Wälzlager und Betriebsfestigkeit. FVA-Seminar „Betriebsfestigkeit in der Antriebstechnik“ der Forschungsvereinigung Antriebstechnik e. V. 3.-4.12.2013, Mannheim

Neubauer, T.; Poll, G.; Denkena, B.; Maiß, O.:  
Fatigue Life Extension of Rolling Element Bearings by Residual Stresses Induced Through Surface Machining. 5th World Tribology Congress 2013 8.-13.9.2013, Turin (I)

Poll, G.:  
Fluid Rheology, Traction/Creep Relationships and Friction in Machine Elements with Rolling Contacts.

38. Leeds-Lyon Symposium on Tribology  
6.-9.9.2011 Lyon (Fr)

Poll, G.:  
Polymerzusätze in Wälzlagerfetten.  
GETLUB - FVA Tribologie und Schmierstoffkongress, 15.-16.12.2010, Würzburg

Poll, G.:  
Rheologie von Schmierstoffen in konzentrierten Wälzkontakten.  
7. Arnold-Tross-Kolloquium 17.06.2011, Hamburg

Poll, G.; Baly, H.; Kuhlmann, J.; Gatzen, M.:  
Schmierfilmbildung und Reibung in fettgeschmierten Wälzlagern.  
VDI-Conference „Gleit und Wälzlagerungen“ 9.-10.6.2009, Wiesloch/Heidelberg

Poll, G.; Hacke, B.:  
Berücksichtigung von Betriebszuständen, Sonderereignissen und Überlasten bei der Berechnung der Wälzlager-Lebensdauer in Windenergieanlagen und Großgetrieben.  
Informationstagung 2010 der Forschungsvereinigung Antriebstechnik e. V., 23.-24.11.2010, Würzburg

Poll, G.; Meyer, C.; Neubauer, T.; Wittek, E.; Wang, G.:  
Untersuchungen zur Rheologie von Schmierstoffen in Wälzkontakten.  
52. GfT-Tribologie-Fachtagung „Reibung, Schmierung und Verschleiß“ 26.-28.9.2011, Göttingen

Schaumann, P.; Kelma, S.:  
Probabilistic Design of Extreme Loads Acting on the Foundations Piles of a Jacket during an 1-Year Storm.

Proceedings of 9th PhD Seminar on Wind Energy in Europe, Uppsala University Campus Gotland (Sweden), 2013

Schmidt, B.:  
Probabilistische Sicherheitsbewertung von Offshore-Windenergieanlagen.  
Doktorandensymposium des DAfStb 2010, 11.-12. November 2010, Kaiserslautern

Schmidt, B.; Hansen, M.:  
Analyse mehrjähriger Messzeitreihen zur Ermittlung designrelevanter Lastparameter für Offshore-Windenergieanlagen.  
DVW-Seminar "Zeitabhängige Messgrößen", 26. - 27. Februar 2014, Hannover

Schmidt, B.; Marx, S.; Hansen, M.:  
Measurement based investigations of design load parameters for offshore wind turbines.  
International Wind Engineering Conference (IWEC) 2014, Hannover

Schmoor, K. A., Achmus, M.:  
On the validation of reliability and partial safety factors for axially loaded piles in dense sand.  
4th International Symposium on Geotechnical Safety and Risk (4th ISGSR), 4-6 December 2013, Hong Kong, (reviewed)

Schmoor, K. A.; Achmus, M.:  
On the influence of the variability of soil parameters on the behaviour of laterally loaded piles in sand.  
Proceedings of the 9th International Probabilistic Workshop, 17.11. – 18.11.2011, Braunschweig (reviewed)

Stammler, M.; Poll, G. :  
Schadensmechanismen in Rotorblattlagern.  
GfT-Tribologie-Fachtagung „Reibung, Schmierung und Verschleiß“ 22.9.-24.9.2014, Göttingen

Tischmacher, H.; Gattermann, S.; Kriese, M.; Wittek, E. C.; Ponick, B.; Poll, G.:

Lagerströme bei umrichter-gespeisten Elektromotoren.

VDI-Tagung „Gleit und Wälzlagerungen“  
24.-25.05.2011, Schweinfurt

Wang, D.; Neubauer, T.; Poll, G.:  
Anwendung rheologischer Modelle zur Berechnung des Schlupfes in Wälzlagern.  
53. GfT-Tribologie-Fachtagung „Reibung, Schmierung und Verschleiß“ 24.-26.9.2012, Göttingen

Wang, D.; Poll, G.:  
Prediction of Traction in EHL Contacts.  
5th World Tribology Congress 2013 8.-13.9.2013, Turin (I)

Wehner, M.; Ponick, B.:  
Search coil systems for early fault detection in wind turbine generators.  
International Symposium on Power Electronics, Electrical Drives, Automation And Motion (SPEEDAM), Ischia, Italien, 2014, reviewed

Werner, M.:  
Grouted Joints in Offshore-Windenergieanlagen - Materialverhalten hochfester Vergussmörtel bei unplanmäßigen Ereignissen während des Verfüllvorgangs.  
Tagungsband zur 1. DfStb Jahrestagung 2013, Bochum, November 2013, pp. 347 - 354 (reviewed)

Wilms, M.; Hildebrandt, A.; Schlurmann, T.:  
A laboratory study on wave-breaking probability of two-dimensional wave trains depending on their input parameters.  
Proceedings of the 7th Chinese-German Joint Symposium on Hydraulic and Ocean Engineering, Leibniz Universität Hannover, Hannover, Germany, September 07.-12., 2014

Wilms, M.; Schlurmann, T.:  
Investigation on wave-breaking probability in deep water.  
Proceedings of the 6th Chinese-German Joint Symposium on Hydraulic and Ocean Engineering, National Taiwan Ocean

University, Keelung, Taiwan, September 23.-29., 2012

Wittek, E.; Poll, G.:  
Wälzlagerermüdung bei Mischreibung in Abhängigkeit vom Schmierstoff.  
Informationstagung 2009 der Forschungsvereinigung Antriebstechnik e. V., 1.-2.12.2009 Würzburg 2009

Wittek, E. C.; Smirnov, A.:  
Wälzlagerermüdung bei Mischreibung in Abhängigkeit vom Schmierstoff.  
Informationstagung 2013 der Forschungsvereinigung Antriebstechnik e. V. 26-27.11.2013, Würzburg

Wittek, E.; Kriese, M.; Gattermann, S.; Tischmacher, H.; Ponick, B.; Poll, G.:  
Capacitance of Bearings for Electric Motors at Variable Mechanical Loads.  
20th International Conference on Electrical Machines ICEM 2012 02.-05.09.2012, Marseille (Fr)

Wittek, E.; Kriese, M.; Tischmacher, H.; Gattermann, S.; Ponick, B.; Poll, G.:  
Capacitances and lubricant film thicknesses of motor bearings under different operating conditions.  
Proceedings of the XIX International Conference on Electrical Machines ICEM 2010, 6.-8.9.2010, Rom (I) ISBN 978-1-4244-4175-4 (reviewed)

Wittek, E.C.; Bader, N.; Poll, G.:  
Tribological Properties of Fuel Economy Gearbox Oils.  
69th Annual Meeting and Exhibition, Society of Tribologists and Lubrication Engineers (STLE), 18.5.-22.5.2014 Lake Buena Vista, Florida (USA)

## 5.3 Academical Theses

### 5.3.1 Habilitation and Doctoral Theses

Gatzen, M.:  
Wälzlagerschmierung mit polymerhaltigen Fetten.

Doctoral Thesis  
Leibniz Universität Hannover 2010

Hacke, B.:  
Früherkennung von Wälzlagerschäden in drehzahlvariablen Windgetrieben.

Doctoral Thesis  
Leibniz Universität Hannover 2011

Hansen, M.:  
Monitoringgestützte Risikobewertung bestehender Massivbauwerke

Habilitation Thesis  
Leibniz Universität Hannover 2014

Hildebrandt, A.:  
Hydrodynamics of Breaking Waves on Offshore Wind Turbine Structures.

Doctoral Thesis  
FI April 2013

Keßler, A.:  
Schiefstellung und Axialschubverhalten von Zylinderrollenlagern.

Doctoral Thesis  
Leibniz Universität Hannover 2010

Kuhlmann, J.:  
Tribologische Eigenschaften von Wälzlagerschmierfetten bei dauerhaft niedrigen Betriebstemperaturen.

Doctoral Thesis  
Leibniz Universität Hannover 2009

Meyer, C.:  
Reibung in hoch belasteten EHD-Wälzkontakten.

Doctoral Thesis  
Leibniz Universität Hannover 2010

### 5.3.2 Diploma / Master Theses

Bank, S.:  
Experimentelle Simulation typischer bei der Bauausführung von Grouted Joints auftretender Risiken.

Diploma Thesis  
IfB April 2013

Bode, M.:  
Korrelation von Wind- und Seegangsbedingungen am Standort *FINO 1*.

Diploma Thesis  
IfMa December 2012

Bojnourdi, A.:  
Validierung von Teilsicherheitsbeiwerten für axial belastete Offshore-Gründungspfähle.

Master Thesis  
IGtH December 2012

Diederley, J.:  
Numerische Schädigungsuntersuchung an Spannbetontürmen für Windenergieanlagen infolge Ermüdung.

Diploma Thesis  
IfMa June 2013

Frerichs, G.:  
Konzeptionierung eines Blattlagerprüfstandes.

Diploma Thesis  
IMKT 2014

Garske, S.:  
Zuverlässigkeitsbetrachtung und Zustandsanalyse der Netzanbindung von Offshore Windparks.

IEE 2012

Ghassen, C.:  
Modellierung und Modalanalyse einer Offshore- Windenergieanlage vom Typ REpower.

Master Thesis  
ISD May 2010

Heseding, J.:  
Modellierung, Regelung und Simulation eines HGÜ-angebundenen Offshore Windparknetzes.

Master Thesis  
IAL-LE March 2013

Hoheisel, K.:  
Einsatz von Schwingungsdämpfern zur  
Reduktion von Lasten auf Monopile-  
Tragstrukturen  
Diploma Thesis  
IMKT 2014

Jamarani, M. E.:  
Investigation of the Thermal Load of  
Power Semiconductors Used in Wind  
Turbines with Doubly Fed Induction  
Generator.  
Master Thesis  
IAL-LE May 2011

Kerßen, J.:  
Statische und konstruktive Bearbeitung  
einer Suction-Bucket Gründung aus Beton  
für Offshore-Windenergieanlagen.  
Master Thesis  
IfMa August 2013

Knöfel, S.:  
Strukturdynamische Analyse einer Jacket-  
Tragstruktur mittels Finite-Elemente- und  
Mehrkörpersimulation zur Verifikation  
eines Gesamtsimulationspakets für  
Offshore-Windenergieanlagen.  
Master Thesis  
ISD December 2010

Koch, M.:  
Analyse von Netzfehlern bei Windenergie-  
anlagen mit permanent-erregter Synchron-  
maschine und NPC-Mittelspannungs-  
umrichter in der Simulation.  
Master Thesis  
IAL-LE May 2011

Kusserow, K.:  
Stromharmonischenregelung eines netz-  
seitigen dreiphasigen Wechselrichters mit  
dSPACE.  
Diploma Thesis  
IAL-LE October 2013

Miljanovic, M.:  
Stromharmonischen-Regelung eines  
dreiphasigen, netzseitigen Wechsel-  
richters mit dSPACE zur Verbesserung der  
Netzqualität.  
Master Thesis  
IAL-LE June 2014

Müller, D.:  
Untersuchungen zur Entwicklung eines  
Messsystems zur Detektion von  
brechenden Wellen im Wellenbecken.  
Master Thesis  
IPI/FI November 2012

Schmitt, B.M.:  
Analysis of energy characteristics of freak  
wave events.  
Diploma Thesis  
FI March 2012

Schmitt, H.:  
Untersuchung des Einflusses von  
Geometrieabweichungen auf die aero-  
elastischen Belastungen der Rotorblätter  
von OWEA.  
Diploma Thesis  
TFD March 2012

Schroeder, H.:  
Untersuchung von Messspulensystemen  
in permanent-erregten Synchron-  
maschinen zum Einsatz in Offshore-  
Windenergieanlagen.  
Diploma Thesis  
IAL 2013

Schwanitz, F.:  
Sensitivität einer Jacket-Gründungs-  
struktur gegenüber variierenden Wellen-  
parametern.  
Diploma Thesis  
IfMa November 2012

Seefisch, C.:  
Anwendung unterschiedlicher Lebens-  
dauermodelle unter Berücksichtigung des  
Eigenspannungszustandes.  
Diploma Thesis  
IMKT 2013

Smirnov, A.:  
Simulation eines rauen Wälzkontaktes  
unter Berücksichtigung von Reibung.  
Diploma Thesis  
IMKT 2011

Spiegel, C.:  
Bestimmung der Ausfallwahrscheinlichkeiten  
von Rotorblättern mittels FORM und  
SORM.  
Master Thesis  
TFD September 2013

Streßer, M.:  
Erfassung der Dynamik des Wellen-  
brechens mit einem dopplertisierten Mikro-  
wellenradar.  
Diploma Thesis  
FI March 2013

Tomann, C.:  
Weiterentwicklung und Anwendung einer  
optischen Methode zur Bestimmung von  
Entmischungen in Grout-Materialien.  
Diploma Thesis  
IfB March 2014

Vordoagu, J.:  
Einfluss von Modellfehlern auf die Sicher-  
heit von axial belasteten Offshore-  
Gründungspfählen.  
Master Thesis  
IGtH July 2012

Wendland, J.:  
Modellversuche zur Analyse baustofflicher  
und herstellungsbedingter Einflüsse auf  
Grouted Joints.  
Diploma Thesis  
IfB September 2011

### 5.3.3 Bachelor Theses

Brauer, S.:  
Automatisierter Ermüdungsnachweis sto-  
chastisch verteilter Lasten auf Rohrknoten  
in Jackettragstrukturen von Offshore-  
Windenergieanlagen.  
IfS August 2012

Könecke, N.:  
Bestimmung der Sensitivität von statis-  
tischen Extrapolationsverfahren für die  
Ermittlung von Extremlastungen von  
OWEA.  
Bachelor Thesis  
TFD July 2013

Leonardy, H.:  
Entwicklung eines Excel-Tools zur Durch-  
führung einer FMEA für Offshore-  
Windenergieanlagen.  
Bachelor Thesis  
TFD January 2012

Lerch, B.:  
Sensitivitätsanalysen geometrischer und  
materialbedingter Einflussgrößen auf das  
Schwingverhalten von Tragstrukturen.  
Bachelor Thesis  
ISD June 2014

Munck, H.:  
Zur Berücksichtigung der Nichtlinearität  
der Bernoulli-Gleichung zur Beschreibung  
von Seegängen beim Ermüdungs-  
nachweis von Jacket-Knoten.  
IfS August 2014

Niesen, S.:  
Probabilistische Sicherheitsbewertung von  
Betriebsmitteln für Offshore-Windenergie-  
anlagen.  
Bachelor Thesis  
IEE 2010

### 5.3.4 Seminar / Project Theses

Bank, S.:  
Versuche zur thermografischen Aufnahme  
von Fließwegen verpumpter hochfester  
Mörtel- und Betone.  
Study Thesis  
IfB November 2012

Bremm, G.:  
Langzeitanalyse von Seegangsdaten.  
Project Thesis  
FI November 2011

- Cotardo, D.:  
Optimierung eines Versuchsstandes zur Untersuchung von "early-age-cycling" Effekten auf die Materialeigenschaften von Verfüllmaterial für Grouted Joints.  
Study Thesis  
IfB June 2012
- Ewert, C.:  
Rechtliche Rahmenbedingungen bei der Installation von Offshore-Windenergieanlagen.  
Project Thesis  
IfMa November 2013
- Frerichs, G.:  
FE-Modellierung eines Wälzkontaktes unter Berücksichtigung des Eigenspannungszustandes.  
Project Thesis  
IMKT 2013
- Geeb, A.:  
Validierung von Teilsicherheitsbeiwerten für axial belastete Offshore-Gründungspfähle.  
Project Thesis  
IGtH October 2012
- Gloukh, V.; Halim, S.:  
Einflüsse auf die Verarbeitung von Vergussmörteln und -betonen für Grouted Joints bei OWEAs.  
Project Thesis  
IfB September 2010
- Gossmann, A.:  
Konstruktive Anpassung und Erweiterung eines Prüfstandskonzeptes für Wälzlager eines Windkraftanlagengetriebes  
Project Thesis  
IMKT 2010
- Haberjan, L.:  
Regelung eines Netzpulsstromrichters mit MATLAB/Simulink/dSpace.  
Study Thesis  
IAL-LE November 2012
- Hansen, I.:  
Bestimmung von Ausfallwahrscheinlichkeiten der Rotorblätter für Offshore-Windenergieanlagen durch aerodynamische Lasten.  
Project Thesis  
TFD February 2014
- Hatzopoulos, A.; Supinski, K.:  
Vergleichende Untersuchungen zwischen unterschiedlichen hochfesten Mörteln anhand eines neu entwickelten Prüfstands zur Simulation von Verfüllvorgängen an Grouted Joints.  
Project Thesis  
IfB November 2012
- Hötmann, J.:  
Vergleichende Untersuchungen hochfester Feinkornvergussmörtel für Grouted Joints unter dynamischer Belastung während der Erhärtung.  
Project Thesis  
IfB January 2014
- Kröger, F.:  
Electromagnetical and mechanical design of the rotor of a permanent magnet excited synchronous machine.  
Project Thesis  
IAL 2013
- Kulinski, S.:  
Aufbau einer Messeinrichtung zur Überwachung von Schraubenvorspannkräften.  
Project Thesis  
IMKT 2012
- Meister, S.; Diekmann, H.:  
Auswirkungen von Wassergehalts- und Temperaturschwankungen auf die Frischmörteleigenschaften von Vergussmörtel für Grouted Joints.  
Study Thesis  
IfB May 2011
- Michaely, M.:  
Modellierungstechniken von Boden-Bauwerks-Interaktionen mit Anwendung auf Offshore-Gründungspfähle.

Study Thesis  
ISD May 2014

Munck, H.:  
Zum Knicknachweis von Jacket-Konstruktionen für OWEA.  
Project Thesis  
IfS April 2014

Osterndorf, M. S.:  
Vergleich des statischen und dynamischen Verhaltens einer Jacket-Gründungsstruktur unter Wellenbeanspruchung.  
Project Thesis  
IfMa August 2013

Ötting, G.:  
Focused wave-breaking generated using 1st and 2nd order wave maker theory in the wave flume.  
Study Thesis  
FI Dezember 2012

Otto, S.:  
Konstruktion Wälzlagerprüfstand für Windgetriebelager  
Project Thesis  
IMKT 2009

Pham, D. V.:  
Stabilitätsanalyse dreiphasiger Wechselrichter im Netzverbund mit Hilfe des Nyquistkriteriums.  
Study Thesis  
IAL-LE February 2012

Reichert, A.; Reichert, N.:  
Vergleichende Untersuchungen von Zementleim und hochfestem Mörtel für Grouted Joints.  
Project Thesis  
IfB July 2012

Roppes, S.:  
Vergleich von Netzsynchronisationsverfahren in dreiphasigen Systemen.  
Study Thesis  
IAL-LE June 2012

Schultenkämper, M.:  
Probabilistische Voruntersuchung einer Gründungskonstruktion für Offshore-Windenergieanlagen.  
Study Thesis  
IfMa June 2011

Segelke, M.:  
Erprobung eines piezoelektrischen Sensors zur Schwingungsüberwachung.  
Project Thesis  
IMKT 2014

Spieker, H.:  
Semi-analytische, probabilistische Analyse der Beullast dünnwandiger Faserverbundzylinder.  
Project Thesis  
ISD March 2009

Stein, M.:  
Sensitivität einer Monopilestruktur gegenüber streuenden Wellenparametern.  
Project Thesis  
IfMa November 2012

Tomann, C.:  
Versuche zur Bestimmung der Entmischungsneigung hochfester Mörtel mit optischen und thermografischen Verfahren.  
Study Thesis  
IfB September 2012

Voges, J.:  
Charakterisierung von relevanten produktspezifischen Materialkennwerten hochfester Vergussmörtel und deren Einfluss auf das Verhalten des Grout-Materials unter dynamischer Belastung während der Erhärtung.  
Project Thesis  
IfB August 2014

## 6 References

### 6.1 Safety of Offshore Wind Turbines (WP 1)

- [1.1] Det Norske Veritas: (DNV): Design of Offshore Steel Structures. Offshore Standard DNV-OS-C101. Oslo, Norway, 2004.
- [1.2] Det Norske Veritas (DNV): Design of Offshore Wind Turbine Structures. Offshore Standard DNV-OS-J101. Oslo, Norway, October 2007.
- [1.3] Deutsches Institut für Bautechnik (DIBt): Richtlinie für Windenergieanlagen – Einwirkungen und Standsicherheitsnachweise für Turm und Gründung. Schriften des DIBt, Reihe B, Heft 8. Berlin, Germany, March 2004.
- [1.4] Deutsches Institut für Bautechnik (DIBt): Richtlinie für Windenergieanlagen – Einwirkungen und Standsicherheitsnachweise für Turm und Gründung. Schriften des DIBt, Reihe B, Heft 8. Berlin, Germany, March 2012.
- [1.5] DIN 1045-1: Tragwerke aus Beton, Stahlbeton und Spannbeton – Teil 1: Bemessung und Konstruktion. 2008.
- [1.6] DIN 1055-100: Grundlagen der Tragwerksplanung, Sicherheitskonzept, Bemessungsregeln. Deutsches Institut für Normung (Hrsg.). Berlin, Köln: Beuth, März 2001.
- [1.7] DIN 61400-1:2005: Windenergieanlagen – Teil 1: Auslegungsanforderungen (IEC 61400-1:2005), Deutsche Fassung EN 61400-1:2005.
- [1.8] DIN EN 1990: Grundlagen der Tragwerksplanung; Deutsche Fassung EN 1990:2002 + A1:2005 + A1:2005/AC:2010. Dezember 2010; Deutsche Fassung, Beuth, Oktober 2002.
- [1.9] DIN EN 61400-3: Windenergieanlagen – Teil 1: Auslegungsanforderungen für Windenergieanlagen auf offener See, Januar 2010.
- [1.10] DIN EN ISO 19902: Fixed Offshore Structures. Erdöl- und Erdgasindustrie - Gegründete Stahlplattformen; Engl. Fassung EN ISO 19902:2007. Juli 2008.
- [1.11] Germanischer Lloyd: Guideline for the Certification of Offshore Wind Turbines, Germanischer Lloyd (GL) IV Industrial Services – Part 2, Hamburg, Germany, 2005.
- [1.12] Germanischer Lloyd: Guideline for the Certification of Wind Turbines, Germanischer Lloyd (GL) IV Industrial Services – Part 1, Hamburg, Germany, 2010.
- [1.13] Germanischer Lloyd: Guideline for the Certification of Offshore Wind Turbines. Germanischer Lloyd Industrial Services (GL), Hamburg, Germany, June 2005.
- [1.14] Joint Committee on Structural Safety (JCSS): Background Documentation, Eurocode 1 (ENV 1991), Part 1: Basis of Design. Working Document, March 1996.
- [1.15] Joint Committee on Structural Safety. (JCSS): Probabilistic Model Code. Part I – Basis of Design. 12th draft, November 2000. [www.jcss.ethz.ch](http://www.jcss.ethz.ch)
- [1.16] Safety factors – IEC 61400-1 – MT01 Background document, Draft, 16.12.2012.
- [1.17] Biegert, U.: Ganzheitliche modellbasierte Sicherheitsanalyse von Prozessautomatisierungssystemen. Dissertation, Universität Stuttgart, 2003.
- [1.18] BSH Standard „Konstruktion“, AG „Sicherheitsniveau“, Protokoll der Besprechung am 20.3.2012 in Hannover.
- [1.19] Ditlevsen, O.: Stochastic model for joint wave and wind loads in offshore structures. Structural safety 24 (2002), 139-163.
- [1.20] Faber, M. H.: Risk and Safety in Civil Engineering. Lecture notes on Risk and Safety in Civil Engineering. Swiss Federal Institute of Technology, 2001.
- [1.21] FINO-Forschungsplattform: [www.fino-offshore.de](http://www.fino-offshore.de)
- [1.22] Gigawind: [www.gigawind.de](http://www.gigawind.de)
- [1.23] Gomez de las Heras, E.; Gutierrez, R.; Azagra, E.; Sorensen, J. A.: Assessment of wind turbines for site-

specific conditions using probabilistic methods. EWEA Event 2013, 5.2.2013.

[1.24] Grünberg, J.: Comments on EN 1990 „Basis of Structural Design“, Guidelines for implementation and application. Beuth Verlag, Berlin 2007

[1.25] Grünberg, J.: Sicherheitskonzept und Einwirkungen nach DIN 1055 neu. In Avak/Goris: Stahlbetonbau aktuell - Jahrbuch 2001 für die Baupraxis. Beuth, Werner, 2001.

[1.26] Grünberg, J.: Grundlagen der Tragwerksplanung – Sicherheitskonzept und Bemessungsregeln für den konstruktiven Ingenieurbau, Erläuterungen zu DIN 1055-100. Praxis Bauwesen, Hrsg.: DIN Deutsches Institut für Normung e.V., Beuth Verlag, Berlin, Wien, Zürich, 2004.

[1.27] Hansen, M.: Monitoringgestützte Risikobewertung bestehender Massivbauwerke. Habilitationsschrift, Leibniz Universität Hannover, 2014.

[1.28] Hansen, M.: Zur Auswirkung von Überwachungsmaßnahmen auf die Zuverlässigkeit von Betonbauteilen. PhD thesis, Universität Hannover, 2004.

[1.29] Institut für Massivbau: Bericht Nr. 1149 Teil 1: Bestimmung der Windbedingungen für Offshore-Windenergieanlagen am Standort der *FINO 1* Messplattform. Interner Bericht, Leibniz Universität Hannover, 23.5.2011.

[1.30] Institut für Massivbau: Bericht Nr. 1149 Teil 2: Zielzuverlässigkeiten, Systemwahrscheinlichkeiten und Kombination der Einwirkungen Wind und Welle – Grundlagen. Interner Bericht, Leibniz Universität Hannover, 22.12.2011.

[1.31] Institut für Massivbau Bericht Nr. 1149 Teil 3: Langzeitstatistik von Wellenhöhen am Standort der *FINO 1* Messplattform. Interner Bericht, Leibniz Universität Hannover, 2.4.2013.

[1.32] Institut für Massivbau Bericht Nr. 1149 Teil 4: Anpassung der Wellenhöhenverteilung am Standort der *FINO 1* Messplattform an einen Standort mit 50 m Wassertiefe. Interner Bericht, Leibniz Universität Hannover, 30.8.2013.

[1.33] Institut für Massivbau Bericht Nr. 1149 Teil 5: Zusammenfassung der bilateralen Gespräche zwischen Teilprojekt 1 und allen weiteren Teilprojekten. Interner Bericht, Leibniz Universität Hannover, November 2013.

[1.34] Melchers, R.E.: Structural reliability analysis and prediction. Wiley, 1999.

[1.35] Neumann, T.; Emeis, S.; Illig, C.: Report on the Research Project OWID – Offshore Wind Design Parameter. DEWI Magazin Nr. 28, Germany, 2006.

[1.36] OptiSLang©: Version 3.2.1, optiSLang Documentation. DYNARDO GmbH, Weimar, Germany, July 2011.

[1.37] Oumeraci, H. (Hrsg): Probabilistic Design Tools for Vertical Breakwaters. ISBN-13: 978-9058092489. A A Balkema Publishers, Oktober 2001.

[1.38] PSB-OWEA – Annual Report 2010. Hannover, 2011. [www.psb.uni-hannover.de](http://www.psb.uni-hannover.de).

[1.39] PSB-OWEA – Annual Report 2011. Hannover, 2012. [www.psb.uni-hannover.de](http://www.psb.uni-hannover.de).

[1.40] PSB-OWEA – Annual Report 2012. Hannover, 2013. [www.psb.uni-hannover.de](http://www.psb.uni-hannover.de).

[1.41] PSB-OWEA – Annual Report 2013. Hannover, 2014. [www.psb.uni-hannover.de](http://www.psb.uni-hannover.de).

[1.42] PSB-OWEA – Workshop „Antriebsstrang“, 14.6.2012, Hannover.

[1.43] PSB-OWEA – Workshop „Konstruktion“, 31.5.2012, Hannover.

[1.44] Rakesh, K. S.; Dolan, D.; Der Kiureghian, A.; Campo, T.; Smith, Ch. E.: Comparison of Design Guidelines for Offshore Wind Energy Systems. Offshore Technology Conference OTC 18984-PP, Houston, Texas, USA, 2007.

[1.45] Reuter, A.: Impulsvortrag zum Workshop PSB-OWEA „Konstruktion“ am 31.5.2012.

[1.46] Seidel, M.: Critical remarks regarding requirements for design of axially loaded piles. REpower System AG. Tagung „Offshore – Wind-, Wellen- und

Strömungskraftwerke“ 4./5.10.2011 TU Hamburg-Harburg.

[1.47] Sørensen, J. D.: MT1 – SC 'Safety factors': Proposal for informative annex on 'Design assisted by testing'. Roskilde, 22.10.2012.

[1.48] Sørensen, J. D.; Tarp-Johansen, N. J.: Reliability based optimization and optimal reliability level of offshore wind turbines. *J. Offshore Polar Engineering* 2005, 15, 1-6.

[1.49] Sørensen, J. D.; Toft, H. S.: Probabilistic Design of Wind Turbines. *Energies* 2010, 3, 241-257; doi: 10.3390/en3020241.

[1.50] Spaethe, G.: Die Sicherheit tragender Baukonstruktionen. Wien, New York: Springer, 1992.

[1.51] Tadich; J. K.; Ronold, K. O.; Feld, T.: Revision of DNV Standard for Offshore Wind Turbine Structures. 2007.

[1.52] Tarp-Johansen, N. J.: Partial safety factors and characteristic values for combined extreme wind and wave load effects. *J. Solar Energy Engineering* 2005, 127, 242-252.

[1.53] Tarp-Johansen, N. J.; Madsen, P. H.; Frandsen, S. T.: Calibration of partial safety factors for extreme loads on wind turbines. In: Proceedings of the European Wind Energy Conference and Exhibition (EWEC), Madrid, Spain. June 2003.

[1.54] Thöns, S.: Monitoring based condition assessment of offshore wind turbine support structures. Thesis, ETH Zürich, 2011.

[1.55] Turkstra, C. J.: Theory of Structural Design Decisions. Solid Mechanics Study No. 2, University of Waterloo, 1970.

[1.56] Veldkamp, D.: A Probabilistic Evaluation of Wind Turbine Fatigue Design Rules. *Wind Energy* 2008, 11, 655-672.

[1.57] Veldkamp, H. F.: Chances in Wind energy: A Probabilistic Approach to Wind Turbine Fatigue Design. PhD thesis, Delft Technical University, 2006.

[1.58] Vrouwenvelder, T.: Reliability based code calibration. The use of the

JCSS probabilistic model code. Joint Committee on Structural Safety, Workshop on Code Calibration. <http://jcss.ethz.ch>, 2002.

[1.59] Wissenschaftlicher Beirat der Bundesregierung Globale Umweltveränderungen. Welt im Wandel: Strategien zur Bewältigung globaler Umweltrisiken. Jahresgutachten 1998. <http://www.wbgu.de>.

[1.60] [www.dena.de](http://www.dena.de)

## 6.2 Action Effects of Wind and Waves (WP 2)

[2.1] Germanischer Lloyd: *Guideline for the Certification of Offshore Wind Turbines*. Germanischer Lloyd Windenergie GmbH, Edition 2012.

[2.2] International Electrotechnical Commission: IEC 61400-1: Wind turbines part 1: Design. 3<sup>rd</sup> edition, 2005.

[2.3] International Electrotechnical Commission: IEC 61400-3: Wind turbines part 3: Design Requirements for Offshore Wind Turbines. IEC, 1<sup>st</sup> edition, 2009.

[2.4] International Electrotechnical Commission: IEC TS 61400-13: Wind Turbine Generator Systems Part 13: Measurement of Mechanical Loads; 1<sup>st</sup> edition, 2001.

[2.5] Babanin, Alexander V. (2011): Breaking and dissipation of ocean surface waves. Cambridge, UK,, New York: Cambridge University Press.

[2.6] Babanin, Alexander V.; Chalikov, Dmitry; Young, Ian R.; Savelyev, Ivan (2010): Numerical and laboratory investigation of breaking of steep two-dimensional waves in deep water. In: *Journal of Fluid Mechanics* 644, S. 433–463.

[2.7] Bir G.S.: User's Guide to BModes (Software for Computing Rotating Beam Coupled Modes). NREL/TP-500-39133. Golden, Colorado, USA: National Renewable Energy Laboratory, 2005.

- [2.8] Bir, G.; Jonkman, J.: Aeroelastic Instabilities of Large Offshore Wind Turbines Journal of Physics: Conference Series 75, 2007.
- [2.9] Blum, J.R.; Kiefer, J.; Rosenblatt, M.: Distribution free tests of in-dependence based on the sample distribution function. Ann. Math. Stat. 1961, 32, 485-498.
- [2.10] Bonmarin, P.; Rochefort, R.; Bourguel, M. (1989): Surface wave profile measurement by image analysis. In: *Experiments in Fluids* 7 (1), S. 17–24. DOI: 10.1007/BF00226592.
- [2.11] Drela, M.; Youngren, H.: XFOIL 6.94 User Guide, Cambridge, MA, USA: Massachusetts Institute of Technology, 2001.
- [2.12] Ernst, B.; Schmitt, H., Seume, J.R.: Effect of Geometric Uncertainties on the Aerodynamic Characteristic of Offshore Wind Turbine Blades. Presentation: The Science of Making Torque from Wind, October 9-12, 2012, Oldenburg, Germany.
- [2.13] Ernst, B.; Seume J.R.: Investigation of Structural Uncertainty of Wind Turbine Rotor Blades. 6. Dresdner Probabilistik-Workshop, 10.-11. Oktober 2013, Technische Universität Dresden.
- [2.14] Ernst, B.; Seume, J.R.: Modelling Structural Uncertainty of Wind Turbine Rotor Blades for Aeroelastic Investigations. Seventh M.I.T. Conference on Computational Fluid and Solid Mechanics - Focus: Multiphysics & Multiscale, June 12-14, 2013, Massachusetts Institute of Technology, Cambridge, MA 02139 USA.
- [2.15] Ernst, B; Seume, J.R.: Investigation of Site-Specific Wind Field Parameters and Their Effect on Loads of Offshore Wind Turbines. Energies 2012, 5, 3835-3855, doi: 10.3390/en5103850.
- [2.16] Ghanem, R.G.; Spanos, P.D.: Stochastic Finite Elements: A Spectral Approach. Springer-Verlag, New York, 1991.
- [2.17] Gómez de las Heras, E.; Gutiérrez, R.; Azagra, E.; Sørensen, J.D.: Assessment of Wind Turbine for Site-specific Conditions Using Probabilistic Methods. Proceedings of the EWEA Annual Event 2013, 4-7 February, Vienna, Austria.
- [2.18] Griffin, O.; Peltzer, D.; Wang, T. (1996): Kinematic and dynamic evolution of deep water breaker waves. Journal of geophysical Research, 101, C7, 16, 515-16, 531.
- [2.19] Hansen, I.: Bestimmung von Ausfallwahrscheinlichkeiten der Rotorblätter für Offshore-Windenergieanlagen durch aerodynamische Lasten. Project thesis, Institute of Turbomachinery and Fluid Dynamics, Leibniz Universität Hannover, 2014.
- [2.20] Huang, N.E.; Shen, Z.; Long, S.R.; et al. (1998): The empirical mode decomposition and the Hilbert spectrum for nonlinear and non-stationary time series analysis. Proc. R. Soc. Lond. A454, 903-995.
- [2.21] Jonkman, B.J.: TurbSim User's Guide: Version 1.50. National Renewable Energy Laboratory: NREL/TP-500-46198, 2009.
- [2.22] Jonkman, J.; Butterfield, S.; Musial, W.; Scott, G.: Definition of a 5-MW Reference Wind Turbine for Offshore System Development. National Renewable Energy Laboratory: NREL/TP-500-38060, 2009.
- [2.23] Jonkman, J.M.; Buhl Jr., M.J.: FAST User's Guide. National Renewable Energy Laboratory: NREL/TP-500-38230, 2005.
- [2.24] Könecke, N.L.: Bestimmung der Sensitivität von statistischen Extrapolationsverfahren für die Ermittlung von Extrembelastungen und OWEA. Bachelor thesis, Institute of Turbomachinery and Fluid Dynamics, Leibniz Universität Hannover, 2013.

- [2.25] Lafon, C.; Piazzola, J.; Forget, P.; Le Calve, O.; Despiau, S. (2004): Analysis of the Variations of the Whitecap Fraction as Measured in a Coastal Zone. *Boundary-Layer Meteorology*, 111(2):339-360, April 2004.
- [2.26] Naess, A.; Gaidai, O.: Estimation of extreme values from sampled time series. *Struct. Saf.* 2009, 31, 325-334.
- [2.27] Naess, A.; Gaidai, O.: Monte Carlo Methods for Estimating the Extreme Response of Dynamical Systems. *J. Eng. Mech.* 2008, 134, 628--636.
- [2.28] Perlin, M.a; Choi, W.b c; Tian, Z.c (2013): Breaking waves in deep and intermediate waters. In: *Annual Review of Fluid Mechanics* 45, S. 115–145. DOI: 10.1146/annurev-fluid-011212-140721.
- [2.29] Probabilistic Safety Assessment of Offshore Wind Turbines. Annual report 2011, Leibniz Universität Hannover, February 2012.
- [2.30] Schmidt, B., Ernst, B., Wilms, M., Hildebrandt, A., Hansen, M. (2014): Messdatenbasierte Empfehlungen von Wind- und Wellenparametern für die Auslegung von Offshore-Windenergieanlagen, *Bautechnik* 91 (2014), Heft 8, pp. 533-542. (german)
- [2.31] Sriram, V.: Finite element simulation of nonlinear free surface waves. Doctoral thesis, Department of Ocean Engineering, Indian Institute of Technology Madras, Chennai, April 2008.
- [2.32] Stramska, M. and T. Petelski (2003): Observations of oceanic whitecaps in the north polar waters of the Atlantic. *J. Geophys. Res.*, 108(C3), 3086.
- [2.33] Sugihara, Y.; Tsumori, H.; Ohga, T.; Yoshioka, H.; Serizawa, S. (2006): Variation of whitecap coverage with wave-field conditions. *Journal of Marine Systems*, 66, 47–60.
- [2.34] Thomsen, K.: The Statistical Variation of Wind Turbine Fatigue Loads. Technical Report Risø-R-1063(EN), Risø National Laboratory, Roskilde, Denmark, September 1998.
- [2.35] Toft, H.S.; Naess, A.; Saha, N.; Sørensen, J.D.: Response Load Extrapolation for Wind Turbines During Operation Based on Average Conditional Exceedance Rates. *Wind Energy* 2011, 14, doi: 10.1002/we.455.
- [2.36] Türk, M.; Emeis, S.: The dependence of offshore turbulence intensity on wind speed. *Journal of Wind Engineering and Industrial Aero-dynamics*, 98 (2010) 466-471, 2010.
- [2.37] Veldkamp, D.: Chances in Wind Energy – A Probabilistic Approach to Wind Turbine Fatigue Design. PhD thesis, Delft University Wind Energy Research Institute, Delft, 2006.

### 6.3 Soil (WP 3)

- [3.1] API Errata and Supplement 3: API Recommended Practice 2A-WSD, Recommended Practice for Planning, Designing, Constructing Fixed Offshore Platforms – Working Stress Design, 2007
- [3.2] API: Recommended Practice for Planning, Designing and Constructing Fixed Offshore Platforms- Working Stress Design, API (RP2A-WSD); Dallas: American Petroleum Institut, 21st edition, 2006
- [3.3] Deutsche Gesellschaft für Geotechnik: EA-Pfähle – Empfehlungen des Arbeitskreises "Pfähle", 2. Auflage, 2012
- [3.4] DIN 1054: Baugrund – Sicherheitsnachweise im Erd- und Grundbau, Berlin: Deutsches Institut für Normung, 2010
- [3.5] DIN EN 1990: Eurocode 0: Grundlagen der Tragwerksplanung; Berlin: Deutsches Institut für Normung, 2010
- [3.6] DIN EN 1997: Eurocode 7: Entwurf, Berechnung und Bemessung in der Geotechnik – Teil 1: Allgemeine Regeln; Berlin: Deutsches Institut für Normung, 2009

[3.7] Achmus, M. Müller, M.: Evaluation of pile capacity approaches with respect to piles for wind energy foundations in the North Sea, In S. Gourvenec, D. J. White (eds), *Frontiers in Offshore Geotechnics Two*, CRC Press: Balkema, 2010

[3.8] Ellingwood, B.; Galambos, T.V.: Probability based criteria for structural design; *Structural Safety* 1, pp. 15–26, 1982

[3.9] Holicky, M., Markova, J. & Gulvanessian, H.: Code Calibration Allowing for Reliability Differentiation and Production Quality. In Kanda, Takada & Furuat (eds), *Application of Statistics and Probability in Civil Engineering: Proceedings of the 10th International Conference*. London: Taylor & Francis, 2007

[3.10] Huber, M.: Soil variability and its consequences in geotechnical engineering, *Mitteilung 69 des Instituts für Geotechnik*, Universität Stuttgart, Germany, 2013

[3.11] Jardine, R., Chow, F.C., Overy, R. & Standing, J.: *ICP Design Methods for Driven Piles in Sands and Clays*. London: Thomas Telford, 2005

[3.12] Kuo, Y.S. (2008). "On the behavior of large-diameter piles under cyclic lateral load". Ph.D. thesis. Institute for Geotechnical Engineering, Leibniz University of Hanover, Book 65

[3.13] Nottrodt, H. P.: Einige Aspekte der stochastischen Modellierung der effektiven Scherparameter, In: Savidis, S. A. (ed.); *Beiträge zur Probabilistik in der Geotechnik*, Veröffentlichungen des Grundbauinstitutes der Technischen Universität Berlin, Heft 20, pp. 81-104, 1991

[3.14] Phoon, K. K.; Kulhawy, F. H.: Characterization of geotechnical variability, *Canadian Geotechnical Journal*, 36, pp. 612-624, 1999a

[3.15] Vanmarcke, E. H.: *Random fields: analysis and synthesis*, MIT Press, Cambridge, 1983

## 6.4 Foundation and Support Structure (WP 4)

[4.1] American Petroleum Institute: *Recommended Practice for Planning, Designing and Constructing Fixed Offshore Platform – Working Stress Design*. API (RP2A-WSD), 21st edition, Dallas, 2007.

[4.2] Bundesamt für Seeschifffahrt und Hydrographie (ed.): *Standard – Konstruktive Ausführung von Offshore-Windenergieanlagen*. Hamburg und Rostock, 2007.

[4.3] Deutsches Institut für Normung: *Hot-rolled steel plates 3 mm thick or above - Tolerances on dimensions and shape; German version EN 10029:2010*.

[4.4] DNV-OS-J101: *Design of Offshore Wind Turbine Structures*. Det Norske Veritas (DNV), Høvik, Norway, 2010.

[4.5] DNV-RP-C203: *Fatigue Design of Offshore Steel Structures*. Det Norske Veritas (DNV), Høvik, Norway, 2010.

[4.6] DNV-RP-C205: *Environmental Conditions and Environmental Loads*. Det Norske Veritas (DNV), Høvik, Norway, 2010.

[4.7] Germanischer Lloyd: *Guideline for the certification of Offshore Wind Turbines*, Germanischer Lloyd Industrial Services (GL), Hamburg, Germany, 2012.

[4.8] Germanischer Lloyd: *Guideline for the Certification of Wind Turbines*. Germanischer Lloyd Industrial Services (GL), Hamburg, 2010.

[4.9] IEC 61400-3: *Wind turbines - Part 3: Design requirements for offshore wind turbines*. Genf, 2010.

[4.10] Joint Committee on Structural Safety: *Probabilistic Model Code. Part III – Resistance Models*. <http://www.jcss.byg.dtu.dk/Publications/Pr>

- obabilistic\_Model\_Code (accessed on Nov 3rd, 2014), 2001.
- [4.11] ANSYS®: Release 13.0, Documentation ANSYS, SAS IP, Inc ed., USA, 2010.
- [4.12] Bericht Nr. 1149 Teil 1: Bestimmung der Windbedingungen für Offshore-Windenergieanlagen am Standort der *FINO 1* Messplattform. Interner Bericht, Institut für Massivbau, Leibniz Universität Hannover, Mai 2011.
- [4.13] Bericht Nr. 1149 Teil 3: Langzeitstatistik von Wellenhöhen am Standort der *FINO 1* Messplattform. Interner Bericht, Institut für Massivbau, Leibniz Universität Hannover, April 2013.
- [4.14] Bericht Nr. 1149 Teil 5: Stand der Forschung zur Korrelation und Richtungsabhängigkeit von Wind und Welle. Interner Bericht, Institut für Massivbau, Leibniz Universität Hannover, November 2013.
- [4.15] Böker, C.: Load simulation and local dynamics of support structures for offshore wind turbines. Dissertation, Leibniz Universität Hannover, 2009.
- [4.16] Coastel Engineering Research Center: Shore Protection Manual, U.S. Government Printing Office, Washington D.C., 1984.
- [4.17] Dean, R.G.: Stream Function Representation of Nonlinear Ocean Waves. *Journal of Geophysical Research* (70), pp. 4561-4572, 1965.
- [4.18] Goretzka, J.; Rolfes, R.: Modal and Robustness Analysis of the Support Structure of an Offshore Wind Turbine with Scattered Soil Parameters. *Proceedings of 8th PhD Seminar on Wind Energy in Europe*, ETH Zürich, 2012.
- [4.19] Hapel, K.-H.: Festigkeitsanalyse dynamisch beanspruchter Offshore-Konstruktionen. Vieweg, Braunschweig, 1990.
- [4.20] Jonkman, J.; Butterfield, S.; Musial, W.; Scott, G.: Definition of a 5-MW Reference Wind Turbine for Offshore System Development. NREL/TP-500-38060. NREL, Golden, CO, 2009.
- [4.21] Jonkman, J.; Butterfield, S.; Passon, P.; Larsen, T.; Camp, T.; Nichols, J.; Azcona, J.; Martinez, A.: Offshore Code Comparison Collaboration within IEA Wind Annex XXIII: Phase II Results Regarding Monopile Foundation Modeling. NREL/CP-500-42471. NREL: Golden, CO, 2007.
- [4.22] Jonkman, J.; Musial, W.: IEA Wind Task 23 Offshore Wind Technology and Deployment – Subtask 2 The Offshore Code Comparison Collaboration (OC3) – Final Report. NREL: Golden, CO, 2010.
- [4.23] Kelma, S.; Schaumann, P.: Probabilistic Fatigue Design of Jacket Support Structures for Offshore Wind Turbines Exemplified on Tubular Joints. *Proceedings of EERA DeepWind'2015*, Trondheim, 2015 (accepted).
- [4.24] Kelma, S.; Schmoor, K.A.; Goretzka, J.; Hansen, M.: Sicherheitsaspekte der Tragstruktur von Offshore-Windenergieanlagen. *Bautechnik* (91), issue 8, Ernst&Sohn, Berlin, pp. 543-553, 2014.
- [4.25] Mittendorf, K.: Hydromechanical Design Parameters and Design Loads for Offshore Wind Energy Converters. PhD thesis, Leibniz Universität Hannover, 2006.
- [4.26] Mittendorf, K.; Nguyen, B.: WaveLoads – A computer program to calculate wave loading on vertical and inclined tubes. User manual, Hannover, 2005.
- [4.27] Neumann, T.; Herklotz, K.: Erste Betriebserfahrungen mit der *FINO 1*-Forschungsplattform in der Nordsee, DEWI Magazin Nr. 24, Germany, 2004.
- [4.28] optiSLang®: Version 3.2.1, optiSLang Documentation, DYNARDO GmbH, Weimar, Germany, 2011.

[4.29] Probabilistic Safety Assessment of Offshore Wind Turbines. Annual report 2010, Leibniz Universität Hannover, 2011.

[4.30] Probabilistic Safety Assessment of Offshore Wind Turbines. Annual report 2011, Leibniz Universität Hannover, 2012.

[4.31] Probabilistic Safety Assessment of Offshore Wind Turbines. Annual report 2012, Leibniz Universität Hannover, 2013.

[4.32] Reuter, M.: Modellbildung für den Entwurf stählerner Rahmentragwerke. 17.DASt-Kolloquium, Bauhaus Universität Weimar, 2010.

[4.33] Rüschi, H.; Sell, R.; Rackwitz, R.: Statistische Analyse der Betonfestigkeit. Schriftenreihe des Deutschen Ausschusses für Stahlbeton, issue 206, Ernst&Sohn, Berlin, 1969.

[4.34] Schaumann, P.; Kelma, S.: Probabilistic Design of Extreme Loads Acting on the Foundation Piles of a Jacket during an 1-Year Storm. Proceedings of 9th PhD Seminar on Wind Energy in Europe, Uppsala University Campus Gotland, 2013.

[4.35] Schmidt, B.; Ernst, B.; Wilms, M.; Hildebrandt, A.; Hansen, M.: Messdatenbasierte Empfehlungen von Wind- und Wellenparametern für die Auslegung von Offshore-Windenergieanlagen. Bautechnik 91 (8), August 2014.

[4.36] Seidel, M.: Substructures for offshore wind turbines - Current trends and developments. In: Schaumann, P. (ed.): Festschrift Peter Schaumann, Hannover, pp. 363-368, 2014. doi: 10.2314/GBV:77999762X

[4.37] Seidel, M.; Kelma, S.: Stochastic modelling of wind and wave induced loads on jacket piles. Stahlbau (81), issue 9, pp. 705-710, Ernst&Sohn, Berlin, 2012.

[4.38] Sørensen, J.D.; Tarp-Johansen, N.J.: Reliability-based Optimization and Optimal Reliability Level of Offshore Wind Turbines. International Journal of Offshore

and Polar Engineering (15), issue 2, pp. 141-146, 2005.

[4.39] Sørensen, J.D.; Toft, H.S.: Probabilistic Design of Wind Turbines. Energies (3), pp. 241-257, 2010.

[4.40] Thöns, S.: Monitoring Based Condition Assessment of Offshore Wind Turbine Support Structures. PhD thesis, ETH Zürich, 2011.

[4.41] Vorpahl, F.; Popko, W.; Kaufer, D.: Description of a basic model of the "Upwind reference jacket" for code comparison in the OC4 project under IEA Wind Annex XXX. Technical Report, Fraunhofer Institute for Wind Energy and Wind System Technology (IWES), 2011.

## 6.5 In Situ Assembly (WP 5)

[5.1] Anders, S.; Erhardt, T.: "Offshore-Windenergie – Neue Chancen für die Bautechnik in Beton". Beton (2010), 12/2010.

[5.2] Anders, S.; Lohaus, L.; Lindschulte, N.: „Opportunities and risks of steel fibres in Grouted Joints“. Proceedings of the EWEC, Warsaw 2010.

[5.3] Domone, P.L.J.; Jefferis, S.A.: "Structural Grouts". Blackie Academic & Professional, Glasgow 1993.

[5.4] Hümme, J.; Lohaus, L.: "Fatigue Behaviour of High-Strength Grout in Dry and Wet Environment". Proceedings of the International Wind Engineering Conference, Hanover 2014.

[5.5] Lohaus, L.; Werner, M.: Probabilistic aspects of Offshore Wind Turbines: Influence of in situ assembly of grouted Joints. In Life-Cycle and Sustainability of Civil Infrastructure Systems. CRC Press/Balkema, Leiden 2013.

[5.6] Lohaus, L.; Cotardo, D.; Werner, M.: "A test system to simulate the influence of early age cycling on the properties of grout materials". Proceedings of the 24th International Ocean and Polar Engineering Conference, Busan 2014.

- [5.7] Lohaus, L.; Cotardo, D.; Werner, M.: "The Early Age Cycling and its Influence on the Properties of hardened Grout Material". Proceedings of the International Wind Engineering Conference, Hanover 2014.
- [5.8] Lohaus, L.; Lindschulte, N.; Scholle, N.; Werner, M.: „Betontechnik für Grouted Joints – Baustoffliche und bauausführungstechnische Anforderungen“. Stahlbau 81 (2012), Heft 9.
- [5.9] Lohaus, L.; Werner, M.: "In-Situ Assembly (WP5)". In: Probabilistic Safety Assessment of Offshore Wind Turbines, Annual Report 2011, 2012.
- [5.10] Lohaus, L.; Werner, M.: "In-Situ Assembly (WP5)". In: Probabilistic Safety Assessment of Offshore Wind Turbines, Annual Report 2012, 2013.
- [5.11] Lohaus, L.; Werner, M.: "In-Situ Assembly (WP5)". In: Probabilistic Safety Assessment of Offshore Wind Turbines, Annual Report 2013, 2014.
- [5.12] Lohaus, L.; Werner, M.; Cotardo, D.: "Experimental Test Procedures to Simulate the In Situ Assembly of Grouted Joints. Proceedings of the International Wind Engineering Conference, Hanover 2014.
- [5.13] Schaumann, P.; Lochte-Holtgreven, S.; Lohaus, L.; Lindschulte, N.: „Durchrutschende Grout-Verbindungen in OWEA – Tragverhalten, Instandsetzung und Optimierung“. Stahlbau 79 (2010), Heft 9.
- [5.14] Welham, T.R.; Gilfrin, J.A.: "Installation of Grouted Pile-Sleeve Connections: A State-of-the-Art Review." 25th Annual OTC, Houston 1993.
- [5.15] Werner, M.: „Grouted Joints in Offshore-Windenergieanlagen – Materialverhalten hochfester Vergussmörtel bei unplanmäßigen Ereignissen während des Verfüllvorgangs.“ Tagungsband zur 1. DAfStb Jahrestagung 2013, Bochum 2013.
- [5.16] Werner, M.; Lohaus, L.: "Ausführungstechnische Einflüsse aus Aspekte der Tragsicherheit von Grouted Joints". Bautechnik 91 (2014), Heft 8.

## 6.6 Monitoring of mechanical Components (WP 6)

[6.1] Guideline for the Certification of Condition Monitoring Systems for Wind Turbines, Edition 2007, GL Renewables Certification guidelines.

[6.2] Althen: data sheet load washer ALF207, Version 1.02 03/2010, [http://www.althensensors.com/public/media/PDF\\_Datenblatt/1b\\_Kraftmesstechnik/en/1b-ALF207-loadcell-en.pdf](http://www.althensensors.com/public/media/PDF_Datenblatt/1b_Kraftmesstechnik/en/1b-ALF207-loadcell-en.pdf), requested 24.10.2014.

[6.3] Becker, E.: Measurement locations and diagnostics in WPPs, telediagnose.com, No. 05, 09/2003.

[6.4] Biel, S.; Lüthje, H.; Bandorf, R.; Sick, J.-H.: Multifunctional thin film sensors based on amorphous diamond-like carbon for use in tribological applications, Thin Solid Films, volume 505, issue 3, 2006, pages 1171–1175.

[6.5] Daacke, S.; Overmeyer, L.: InUse – Intelligente Unterlegscheiben zur Messung der Kräfte in Schrauben-Verbindungen, Proceedings of Logistics Journal, 2013, ISSN 2192-9084.

[6.6] Errichello, R.: Microstructural Alterations in Hertzian Fatigue, Wind Turbine Tribology Seminar, Broomfield, Co, USA, November 15-17, 2011.

[6.7] Hacke, B.: Früherkennung von Wälzlagerschäden in drehzahlvariablen Windgetrieben, Phd. Thesis, Leibniz Universität Hannover, Verlag Dr. Hut, 2011

[6.8] Hacke, B.; Radnai, B.; Hinkelmann, K.: Berücksichtigung von Betriebszuständen, Sonderereignissen und Überlasten bei der Berechnung der Wälzlagerlebensdauer in Windenergieanlagen und Großgetrieben; final report FVA 541;

issue 967, Research Association for Power Transmission Engineering, 2010.

[6.9] Hiraoka, K.; Nagao, M.; Tatsuro, I.: Study on Flaking Process in Bearings by White Etching Area Generation, Journal of ASTM International, vol. 3, issue 6, 2006.

[6.10] Pfann, W. G.; Thurston, R. N.: Semiconducting stress transducers Utilizing the transverse and shear piezo-resistance effects, Journal of Applied Physics, volume 32, no. 10, page 2008, 1961.

## 6.7 Diagnostic Systems for Electronic Systems (WP 7)

[7.1] Frohne, H.: Ueber den einseitigen magnetischen Zug in Drehfeld-maschinen. Forschungsbericht ETZ-A, 1966.

[7.2] Fruchtenicht, S.: Analytische und Experimentelle Behandlung von Wicklungsschlüssen in Asynchronmaschinen. Dissertation an der Universität Hannover, 1990. Fortschritt-Berichte VDI, Reihe 21, Nr. 56

[7.3] Kumar, K.V.; Kumar, S.S.; Praveena, B., John, J.P.; Paul, J.E.: Soft computing based fault diagnosis. International Conference on Computing Communication and Networking Technologies (ICCNT), 2010.

[7.4] Lu, Bin; Li, Yaoyu; Wu, Xin: A review of recent advances in wind turbine condition monitoring and fault diagnosis. Power Electronics and Applications, 2009, PEMWA 2009, IEEE.

[7.5] Nandi, S; Toliyat, H.A.; Li, Xiaodong: Condition monitoring and fault diagnosis of electrical motors – a review. Energy Conversion, IEEE Transactions on 20, 2005.

[7.6] Neti, P.; Nandi, S.: Stator Interturn Fault Detection of Synchronous Machines Using Field Current and Rotors Search-Coil Voltage Signature Analysis.

Transactions on Industry Applications, IEEE, 2009.

[7.7] Pittius, E.: Analytische und Experimentelle Behandlung von Erdschlüssen in Asynchronmaschinen. Dissertation an der Universität Hannover, 1989. Fortschritt-Berichte VDI, Reihe 21, Nr. 48

[7.8] Ponick, B.: Fehlerdiagnose bei Synchronmaschinen. Dissertation an der Universität Hannover, 1994

[7.9] Schroeder, H.: Untersuchung von Messspulensystemen in permanent-erregten Synchronmaschinen zum Einsatz in Offshore-Windenergieanlagen, Diploma Thesis, Universität Hannover, 2013.

[7.10] Wehner, M; Probabilistic Safety Assessment of Offshore Wind Turbines, WP7, Annual Report 2013

## 6.8 Reliability of the Grid Connection (WP 8)

[8.1] Andrew, R. Henderson, Lyndon Greedy, Fabio Spinato, Colin A Morgan. Optimising Redundancy of Offshore Electrical Infrastructure Assets by Assessment of Overall Economic Cost. Stockholm : s.n., 14th – 16th September .

[8.2] Bartram M.; Bloh I.; Doncker R.; Doubly-fed-machines in wind turbine systems: Is this application limiting the lifetime of IGBT frequency converters; 35th Annual IEEE Power Electronics Specialists Conference Aachen, 2004.

[8.3] Deicke, M.; Schniedermeier, M.: "Zules: Thermal load of igbt-converters for wind turbines with doubly fed induction generator - final presentation," BMBF-Verbundprojekt with SEG Woodward, 2003 (in german).

[8.4] Fuchs, F.; Mertens, A.: Dynamic modeling of a 2 MW wind turbine for converter issues. Power Electronics and Motion Control (EPE PEMC 2011 ECCE Europe), Proceedings of the 2012-15th

International Conference and Exposition on Novi Sad, Serbia

[8.5] Gasch, R.; Twele, J.: Windkraftanlagen: Grundlagen, Entwurf, Planung und Betrieb. Teubner Verlag, 2007.

[8.6] Hahn, B.: Zuverlässigkeit, Wartung und Betriebskosten von Windenergieanlagen. s.l. : ISET Kassel.

[8.7] Haubrich, Wellßow, Handschin, Seitz, Montebaur, Koglin. AKTR-Seminar Zuverlässigkeit. Mannheim-Rheinau : Forschungsgemeinschaft für Hochspannungs- und Hochstromtechnik e.V., 1994.

[8.8] Held, M.; Jacob, P.; Nicoletti, G.; Scacco, P.; Poech, M.: Fast power cycling test for insulated gate bipolar transistor modules in traction application, Int. J Electron.,vol.86,pp. 1193-1204, 1999.

[8.9] Hühnerbein, B.: Probabilistische Leistungsflussberechnung als Methode zur Bewertung der Einflüsse stochastischer Erzeuger und Verbraucher auf die Netzbelastung. Hannover : Universität Hannover, 2010.

[8.10] ISET Kassel; Windenergiereport 2008 (in german).

[8.11] IWES Fraunhofer. Schadenshäufigkeit und Ausfallzeit je Schaden.

[8.12] IWES, Fraunhofer Institut für Windenergie und Energiesystemtechnik. Abschlussbericht für das Verbundprojekt „Erhöhung der Verfügbarkeit von Windkraftanlagen“ .

[8.13] IWES, Fraunhofer Institut für Windenergie und Energiesystemtechnik. Abschlussbericht für das Verbundprojekt „Erhöhung der Verfügbarkeit von Windkraftanlagen“

[8.14] Krause, G.: Zukunftsenergien. Aachen : s.n., 2009.

[8.15] Lubosny, Z.: Wind turbine operation in electric power systems: advanced modeling and control, Springer, 2003.

[8.16] Neumann, T.; Nolopp, K.: Erste Betriebserfahrungen mit der *FINO 1*-Forschungsplattform in der Nordsee (in german), DEWI Magazin, 2004.

[8.17] Niesen, S.: Probabilistische Sicherheitsbewertung von Betriebsmitteln für Offshore-Windenergieanlagen. Hannover, Universität Hannover, 2010.

[8.18] Ohlhorst, D.: Windenergie in Deutschland. Berlin : Freie Universität Berlin, 2008.

[8.19] Sayas, F. C.; Allan. R. N.: Generation availability assesment of wind farms. Manchester: IEEE, 1996.University Science, 1989.

[8.20] Siemens AG: Zuverlässigkeit: Berechnung der Versorgungszuverlässigkeit in elektrischen Netzen. Erlangen : s.n., 2009.

[8.21] William, P.E.; Bartley, H.: Analysis of Transformer Failures.. Stockholm : The Hartford Steam Boiler Inspection & Insurance Co., 2003.